Advances in Civil Engineering

Concrete in Aggressive Environments: Sustainability and Challenges

Lead Guest Editor: Ramadhansyah Putra Jaya
Guest Editors: Sajjad Ali and Mohd Haziman Wan Ibrahim

Concrete in Aggressive Environments: Sustainability and Challenges

Advances in Civil Engineering

Concrete in Aggressive Environments: Sustainability and Challenges

Lead Guest Editor: Ramadhansyah Putra Jaya
Guest Editors: Sajjad Ali and Mohd Haziman Wan Ibrahim

Contents

Hindawi
Advances in Civil Engineering
Volume 2023, Article ID 9865205, 1 page
https://doi.org/10.1155/2023/9865205

Retraction

Retracted: Experimental Study on Mineral Solid Waste Green Grouting Material Based on Electromagnetic Characteristic Detection

Advances in Civil Engineering

Received 10 October 2023; Accepted 10 October 2023; Published 11 October 2023

This article has been retracted by Hindawi following an investigation undertaken by the publisher [1]. This investigation has uncovered evidence of one or more of the following indicators of systematic manipulation of the publication process:

(1) Discrepancies in scope
(2) Discrepancies in the description of the research reported
(3) Discrepancies between the availability of data and the research described
(4) Inappropriate citations
(5) Incoherent, meaningless and/or irrelevant content included in the article
(6) Peer-review manipulation

The presence of these indicators undermines our confidence in the integrity of the article's content and we cannot, therefore, vouch for its reliability. Please note that this notice is intended solely to alert readers that the content of this article is unreliable. We have not investigated whether authors were aware of or involved in the systematic manipulation of the publication process.

Wiley and Hindawi regrets that the usual quality checks did not identify these issues before publication and have since put additional measures in place to safeguard research integrity.

We wish to credit our own Research Integrity and Research Publishing teams and anonymous and named external researchers and research integrity experts for contributing to this investigation.

The corresponding author, as the representative of all authors, has been given the opportunity to register their agreement or disagreement to this retraction. We have kept a record of any response received.

References

[1] X. Wang, J. Hu, X. Zhang, K. Wang, D. Shen, and C. Liang, "Experimental Study on Mineral Solid Waste Green Grouting Material Based on Electromagnetic Characteristic Detection," *Advances in Civil Engineering*, vol. 2022, Article ID 6261429, 19 pages, 2022.

Hindawi
Advances in Civil Engineering
Volume 2023, Article ID 9856964, 1 page
https://doi.org/10.1155/2023/9856964

Retraction

Retracted: Study on Seismic Performance of Recycled Steel Fibers Locally Reinforced Cruciform Concrete Frame Beam-Column Joint

Advances in Civil Engineering

Received 10 October 2023; Accepted 10 October 2023; Published 11 October 2023

This article has been retracted by Hindawi following an investigation undertaken by the publisher [1]. This investigation has uncovered evidence of one or more of the following indicators of systematic manipulation of the publication process:

(1) Discrepancies in scope
(2) Discrepancies in the description of the research reported
(3) Discrepancies between the availability of data and the research described
(4) Inappropriate citations
(5) Incoherent, meaningless and/or irrelevant content included in the article
(6) Peer-review manipulation

The presence of these indicators undermines our confidence in the integrity of the article's content and we cannot, therefore, vouch for its reliability. Please note that this notice is intended solely to alert readers that the content of this article is unreliable. We have not investigated whether authors were aware of or involved in the systematic manipulation of the publication process.

Wiley and Hindawi regrets that the usual quality checks did not identify these issues before publication and have since put additional measures in place to safeguard research integrity.

We wish to credit our own Research Integrity and Research Publishing teams and anonymous and named external researchers and research integrity experts for contributing to this investigation.

The corresponding author, as the representative of all authors, has been given the opportunity to register their agreement or disagreement to this retraction. We have kept a record of any response received.

References

[1] Y. Li, R. Zhao, D. Li, and C. Qu, "Study on Seismic Performance of Recycled Steel Fibers Locally Reinforced Cruciform Concrete Frame Beam-Column Joint," *Advances in Civil Engineering*, vol. 2022, Article ID 8155038, 19 pages, 2022.

Hindawi
Advances in Civil Engineering
Volume 2023, Article ID 9898510, 1 page
https://doi.org/10.1155/2023/9898510

Retraction

Retracted: Energy Evolution Characteristics and Performance Parameter Degradation of Rubber-Mixed Concrete in Sulfate Attack Environment

Advances in Civil Engineering

Received 10 October 2023; Accepted 10 October 2023; Published 11 October 2023

This article has been retracted by Hindawi following an investigation undertaken by the publisher [1]. This investigation has uncovered evidence of one or more of the following indicators of systematic manipulation of the publication process:

(1) Discrepancies in scope
(2) Discrepancies in the description of the research reported
(3) Discrepancies between the availability of data and the research described
(4) Inappropriate citations
(5) Incoherent, meaningless and/or irrelevant content included in the article
(6) Peer-review manipulation

The presence of these indicators undermines our confidence in the integrity of the article's content and we cannot, therefore, vouch for its reliability. Please note that this notice is intended solely to alert readers that the content of this article is unreliable. We have not investigated whether authors were aware of or involved in the systematic manipulation of the publication process.

Wiley and Hindawi regrets that the usual quality checks did not identify these issues before publication and have since put additional measures in place to safeguard research integrity.

We wish to credit our own Research Integrity and Research Publishing teams and anonymous and named external researchers and research integrity experts for contributing to this investigation.

The corresponding author, as the representative of all authors, has been given the opportunity to register their agreement or disagreement to this retraction. We have kept a record of any response received.

References

[1] X. Chen, "Energy Evolution Characteristics and Performance Parameter Degradation of Rubber-Mixed Concrete in Sulfate Attack Environment," *Advances in Civil Engineering*, vol. 2022, Article ID 5692655, 10 pages, 2022.

Hindawi
Advances in Civil Engineering
Volume 2023, Article ID 9894575, 1 page
https://doi.org/10.1155/2023/9894575

Retraction

Retracted: Performance of High Strength Concrete Containing Palm Oil Fuel Ash and Metakaolin as Cement Replacement Material

Advances in Civil Engineering

Received 10 October 2023; Accepted 10 October 2023; Published 11 October 2023

This article has been retracted by Hindawi following an investigation undertaken by the publisher [1]. This investigation has uncovered evidence of one or more of the following indicators of systematic manipulation of the publication process:

(1) Discrepancies in scope
(2) Discrepancies in the description of the research reported
(3) Discrepancies between the availability of data and the research described
(4) Inappropriate citations
(5) Incoherent, meaningless and/or irrelevant content included in the article
(6) Peer-review manipulation

The presence of these indicators undermines our confidence in the integrity of the article's content and we cannot, therefore, vouch for its reliability. Please note that this notice is intended solely to alert readers that the content of this article is unreliable. We have not investigated whether authors were aware of or involved in the systematic manipulation of the publication process.

Wiley and Hindawi regrets that the usual quality checks did not identify these issues before publication and have since put additional measures in place to safeguard research integrity.

We wish to credit our own Research Integrity and Research Publishing teams and anonymous and named external researchers and research integrity experts for contributing to this investigation.

The corresponding author, as the representative of all authors, has been given the opportunity to register their agreement or disagreement to this retraction. We have kept a record of any response received.

References

[1] M. H. Ismail, M. A. Megat Johari, K. S. Ariffin, R. P. Jaya, M. H. Wan Ibrahim, and Y. Yugashini, "Performance of High Strength Concrete Containing Palm Oil Fuel Ash and Metakaolin as Cement Replacement Material," *Advances in Civil Engineering*, vol. 2022, Article ID 6454789, 11 pages, 2022.

Hindawi
Advances in Civil Engineering
Volume 2023, Article ID 9856915, 1 page
https://doi.org/10.1155/2023/9856915

Retraction

Retracted: Simulation of Migration Law of Organic Pollutants in Circulating Wells

Advances in Civil Engineering

Received 3 October 2023; Accepted 3 October 2023; Published 4 October 2023

This article has been retracted by Hindawi following an investigation undertaken by the publisher [1]. This investigation has uncovered evidence of one or more of the following indicators of systematic manipulation of the publication process:

(1) Discrepancies in scope
(2) Discrepancies in the description of the research reported
(3) Discrepancies between the availability of data and the research described
(4) Inappropriate citations
(5) Incoherent, meaningless and/or irrelevant content included in the article
(6) Peer-review manipulation

The presence of these indicators undermines our confidence in the integrity of the article's content and we cannot, therefore, vouch for its reliability. Please note that this notice is intended solely to alert readers that the content of this article is unreliable. We have not investigated whether authors were aware of or involved in the systematic manipulation of the publication process.

Wiley and Hindawi regrets that the usual quality checks did not identify these issues before publication and have since put additional measures in place to safeguard research integrity.

We wish to credit our own Research Integrity and Research Publishing teams and anonymous and named external researchers and research integrity experts for contributing to this investigation.

The corresponding author, as the representative of all authors, has been given the opportunity to register their agreement or disagreement to this retraction. We have kept a record of any response received.

References

[1] X. Li, J. Zhang, and Z. Yang, "Simulation of Migration Law of Organic Pollutants in Circulating Wells," *Advances in Civil Engineering*, vol. 2022, Article ID 7342604, 12 pages, 2022.

Hindawi
Advances in Civil Engineering
Volume 2023, Article ID 9767238, 1 page
https://doi.org/10.1155/2023/9767238

Retraction

Retracted: Control System of Fire Rescue Robot for High-Rise Building Design

Advances in Civil Engineering

Received 22 August 2023; Accepted 22 August 2023; Published 23 August 2023

This article has been retracted by Hindawi following an investigation undertaken by the publisher [1]. This investigation has uncovered evidence of one or more of the following indicators of systematic manipulation of the publication process:

(1) Discrepancies in scope
(2) Discrepancies in the description of the research reported
(3) Discrepancies between the availability of data and the research described
(4) Inappropriate citations
(5) Incoherent, meaningless and/or irrelevant content included in the article
(6) Peer-review manipulation

The presence of these indicators undermines our confidence in the integrity of the article's content and we cannot, therefore, vouch for its reliability. Please note that this notice is intended solely to alert readers that the content of this article is unreliable. We have not investigated whether authors were aware of or involved in the systematic manipulation of the publication process.

Wiley and Hindawi regrets that the usual quality checks did not identify these issues before publication and have since put additional measures in place to safeguard research integrity.

We wish to credit our own Research Integrity and Research Publishing teams and anonymous and named external researchers and research integrity experts for contributing to this investigation.

The corresponding author, as the representative of all authors, has been given the opportunity to register their agreement or disagreement to this retraction. We have kept a record of any response received.

References

[1] J. Yu, "Control System of Fire Rescue Robot for High-Rise Building Design," *Advances in Civil Engineering*, vol. 2022, Article ID 7867533, 10 pages, 2022.

Hindawi
Advances in Civil Engineering
Volume 2023, Article ID 9064645, 12 pages
https://doi.org/10.1155/2023/9064645

Research Article

Potential of Palm Oil Fuel Ash as a Partial Replacement of Fine Aggregates for Improved Fresh and Hardened Mortar Performance

Siti Adriana Zaimi,[1] Muhd Norhasri Muhd Sidek,[2] Nor Hafida Hashim,[3] Hamidah Mohd Saman,[1] Ramadhansyah Putra Jaya,[2,4] and Nur Ashikin Marzuki[3]

[1]*School of Civil Engineering, Universiti Teknologi MARA Shah Alam, Shah Alam 40450, Selangor, Malaysia*
[2]*Institute for Infrastructure Engineering and Sustainable Management (IIESM), Universiti Teknologi MARA Shah Alam, Shah Alam 40450, Selangor, Malaysia*
[3]*School of Civil Engineering, Universiti Teknologi MARA Cawangan Pulau Pinang, Permatang Pauh 13500, Pulau Pinang, Malaysia*
[4]*Faculty of Civil Engineering Technology, Universiti Malaysia Pahang, Gambang 26300, Kuantan, Malaysia*

Correspondence should be addressed to Muhd Norhasri Muhd Sidek; muhdnorhasri@uitm.edu.my

Received 27 April 2022; Revised 22 July 2022; Accepted 23 August 2022; Published 29 March 2023

Academic Editor: Adewumi Babafemi

The growth of Malaysia has caused many industries to grow rapidly, especially construction industries due to the demand for more homes, buildings, and infrastructure. The production of concrete and mortar is highly requested. Therefore, the demand for fine aggregate becomes higher because fine aggregate is one of the main elements in concrete and mortar production. The high demand for fine aggregates will create a worrying situation where the fine aggregate crisis will worsen. An alternative was introduced to replace the fine aggregate known as palm oil fuel ash (POFA) in order to reduce the use of natural resources such as fine aggregates and lead to the reduction of fine aggregate mining activity. POFA produced from palm oil fibre, palm oil shell, and mesocarp at high temperature has no benefits in the commercial return. Thus, POFA that has accumulated in landfill has the ability to create environmental pollution. Due to the pozzolanic behaviour of POFA, it could be relevant when POFA is used in the production of mortar as a partially fine aggregate replacement. There is a limited study on the effects of POFA as a partially fine aggregate replacement in the production of mortar. The aim of this research is to study the effects of POFA on the workability of fresh mortar, and for the hardened mortar, compressive strength and microstructural analysis will be analysed. A total of 45 cubes with dimensions of 100 mm × 100 mm × 100 mm were cast at different percentages of POFA at 0%, 2.5%, 5%, 7.5%, and 10% by the weight of fine aggregates. Slump and flow table tests were conducted during the casting process to determine the workability. All the specimens were water cured at days 3, 7, and 28 before being tested with a compression test and scanning electron microscope (SEM) on the hardened mortar. It was discovered that 0% POFA recorded the highest workability. Furthermore, the laboratory results showed that the 2.5% POFA in the mortar recorded the highest compressive strength compared to other specimens. Moreover, the microstructure of the mortar specimen was observed to be denser, and the pores were refined with the presence of POFA, compared to the control specimen. Based on the findings, this research enables us to give an understanding of the effect of POFA incorporated in mortar as a partially fine aggregate replacement in terms of workability, compressive strength, and microstructural analysis. Based on the results from this research, the advantage of POFA can be fully utilized and can help reduce the environmental problems.

1. Introduction

The growing development in Malaysia has caused many industries to grow rapidly including the construction industry. In this industry, the demand for cement and fine aggregates were growing drastically for construction activities [1]. Thus, the use of materials obtained from the fine aggregate mining activities and cement production for mortar manufacture increases massively. This will lead to environmental deterioration and depletion of natural resource materials for future generations. In addition, this practice will also lead to a reduction in sustainable development and will not allow the materials from natural resources to be renewed in the future.

The construction industry is facing a critical challenge in concrete and mortar manufacturing due to the need of natural resources [2]. Besides, fine aggregate mining in a large-scale affects rivers and coastal habitats, induces sediment suspension that will lead to major problems such as soil erosion, and causes certain areas to be vulnerable to flooding reported in [2]. Thus, an alternative must be provided to prevent worsening situations and ensure that the construction industry can contribute to sustainable development.

Palm oil products in Malaysia are one of the largest export companies to other countries. Palm oil fuel ash (POFA) is an unwanted substance usually disposed of in an open area. Disposal of this material led to soil and air pollution concerns, which can cause worse environmental problems [2]. A product that is produced through the burning of palm oil waste such as palm oil fibre, palm oil shell, and mesocarp at high temperature in order to generate power in palm oil factory can be named POFA. The amount of disposed of POFA has resulted in accumulated toxic gases by contaminating the air in open areas and landfills [3]. In [4] the authors had stated that more wastes of palm oil was produced and need to manage as the palm oil industry continues to expand. Researchers in this field must focus on the use of sustainable, renewable resources, such as palm oil waste, in order to achieve greater sustainability in the construction industry [2].

Thus, research regarding the use of POFA as a partially fine aggregate replacement needs to be done in order to minimise the demand and the use of fine aggregates in the construction industry. In addition, partially replacing POFA in concrete and mortar will help minimise the environmental issues such as abundant waste materials in the palm oil industry so that the disposal of these waste products can be mitigated.

2. Materials and Methods

2.1. Materials. POFA is known as waste in landfills, which needs to be managed, as it will cause environmental problems. POFA is obtained in the form of ash when the fibre, shell, and empty fruit bunch of the palm oil trees are burnt as fuel to generate electricity and extract the palm oil [5]. The raw POFA was gained from the United Palm Oil Mill, Nibong Tebal, Pulau Pinang, as shown in Figure 1(a). In this study, the collected POFA was dried for 24 hours at a temperature of 100°C in the oven as shown in Figure 1(b). This is to ensure that the raw POFA is free from moisture content. The dried POFA was then sieved by 212 μm after 24 hours to remove any waste or unwanted materials and larger-sized particles. In [6], the authors added that POFA that have sieved into 212 μm is much finer than the raw POFA that is able to improve the strength.

Then, the type of cement chosen throughout this study was ordinary Portland cement (OPC), the common type of cement being used. It acts as a binder that mixes with fine aggregates and POFA in the mortar mixture, and according to [7], the standard strength for day 28 was ≥32.5 MPa. The OPC must be kept in an airtight container to prevent contact with air moisture. Furthermore, fine aggregates, water, and Master Glenium Ace 8538 super plasticizer (SP) will be prepared accordingly based on the mix design.

2.2. Mixing and Curing. In this study, in order to determine mix design, a modified mix design was used instead of the mortar standard ratio 1 : 3 of cement to fine aggregates as stated in [8]. The number of cubes used in this study is 45 cubes with standard cubes sized 100 mm. For each mix that has different amount of POFA, 9 cubes were used. The fine aggregate was partially replaced by POFA at 0%, 2.5%, 5%, 7.5%, and 10% by the weight of filler, as shown in Table 1.

The process of curing is very important in gaining the strength for the mortar specimens through the hydration process and preventing the occurrence of shrinkage cracks. Moreover, this curing process helps in increasing the durability of the concrete. In this study, the specimens were cured in the water tank for 24 hours to ensure the mortar specimens had hardened on days 3, 7, and 28.

2.3. Tests and Methods

2.3.1. Slump Test. The slump test was performed according to the specified standard[9] to determine the consistency of fresh concrete. The slump value can be determined by measuring the difference between the height of the slump cone and the highest point of the slumped test specimen, as shown in Figure 2.

2.3.2. Flow Table Test. The flow table test was done by referring to the specified standard which is [10]. Figure 3 shows the flow table test conducted after the casting process.

2.3.3. Compression Test. Using compression machine, a compression test was performed to determine the compressive strength of mortar at different percentage of POFA as a partially fine aggregate replacement. The test was carried out in accordance with [11]. Before the test was conducted, all the specimens must be dried after they were taken from the curing tank. The specimen is placed centrally on the machine and placed in a position where the surface is perpendicular to the load applied. An axial load with a specified rate of loading 3.00 kN/s was applied to the 100 mm cube until failure happened. The average values of

(a) (b)

Figure 1: Raw POFA (a) and oven-dried POFA (b).

Table 1: Mix proportion of mortar cubes.

Mixture	*Materials*					*Total samples for curing (days)*		
	Fine aggregate (kg/m^3)	POFA (kg/m^3)	Cement (kg/m^3)	Water (kg/m^3)	SP (kg/m^3)	3	7	28
Control	11.28	—	4.87	2.43	0.0097	3	3	3
2.5% POFA	11.00	0.28	4.87	2.43	0.0097	3	3	3
5% POFA	10.72	0.56	4.87	2.43	0.0097	3	3	3
7.5% POFA	10.44	0.85	4.87	2.43	0.0097	3	3	3
10% POFA	10.15	1.13	4.87	2.43	0.0097	3	3	3

Figure 2: Slump test.

Figure 3: Flow table test.

the three specimens were taken as a compressive strength of the cube. Figure 4 shows the compression test machine.

2.3.4. Microstructural Analysis. Microstructural image analysis was conducted by the mean of scanning electron microscope (SEM). The analysis is to analyse the morphological properties of POFA as a partially fine aggregate replacement in mortar. Hitachi TM3030 Plus was used for this microstructure study. The cube specimen for each different percentage of POFA used as a partially fine aggregate replacement was crushed into small pieces to do the microstructure analysis and kept in an airtight container to avoid moisture. The SEM was carried out at different ages, which were on day 3, 7, and 28, and a 1500 magnification was used for the analysis. Figure 5 shows the SEM that was used for this study.

3. Results and Discussion

3.1. Fresh Mortar. The quality of the fresh mortar incorporated with POFA as a partially fine aggregate

Figure 4: Compression test machine.

Figure 5: Scanning electron microscope.

replacement in terms of workability can be measured by conducting a slump test. During casting, a slump test was carried out on the fresh mortar and the slump value was measured by the distance of the fresh mortar that has slumped. Figure 6 shows the outcome obtained from the slump test.

Figure 6 shows the results of the slump value of fresh mortar at different percentages of POFA which were 0%, 2.5%, 5%, 7.5%, and 10%. Based on the findings, mortar with 0%, 2.5%, 5%, 7.5%, and 10% of POFA was recorded as 40 mm, the highest slump value, 15 mm, 0 mm, 0 mm, and 0 mm, respectively, which showed a decreasing pattern. By considering the slump value of 2.5%, 5%, 7.5%, and 10%, it was recorded that the workability was reduced compared to the control specimen with the amount of super plasticizer (SP) that work to improve the workability was the same. Then, the slump value of mortar that contains POFA at 2.5%

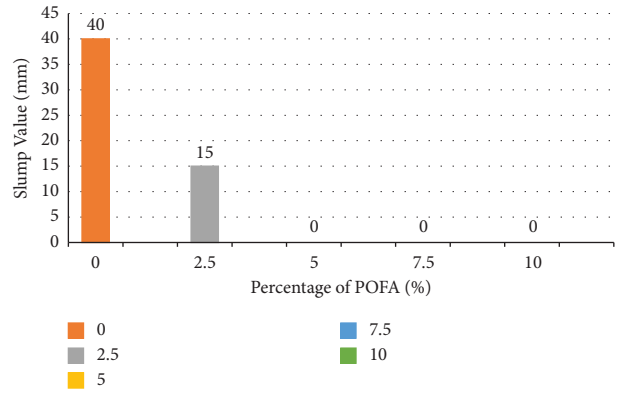

Figure 6: Slump value results on different percentages of POFA.

was recorded as the second highest compared to other percentage with 15 mm of the slump value. Mortar specimens with POFA at 5%, 7.5%, and 10% can be categorized as true slump with zero slump value and can be concluded as having the least workability.

In order to determine the flow value of the mortar, the flow table test was conducted on the fresh mortar with different percentages of POFA. The flow value can be obtained by measuring the diameter of the mortar spread on the flat surface. Figure 7 shows the results obtained from the flow table test.

Figure 7 shows the pattern of the flow value of fresh mortar at different percentages of POFA which were 0%, 2.5%, 5%, 7.5%, and 10%. According to Figure 3, POFA at 0%, known as a control specimen, the recorded flow value was 403 mm, which was higher compared to mortar incorporated with POFA as a partially fine aggregate replacement at 2.5%, 5%, 7.5%, and 10%. Then, POFA at 2.5% and 5% recorded the flow value of 385 and 380 mm, respectively. Moreover, the flow value of 7.5% of POFA as a partially fine aggregate replacement showed 328 mm, and the 10% of POFA, which had the highest percentage of POFA, showed the least flow value of 315 mm.

Based on the findings, it can be observed that the workability of the mortar with different percentages of POFA as a partially fine aggregate replacement reduced with a higher percentage of POFA being used in the mortar mixture compared to the control specimen that contains 0% of POFA. According to [1], POFA particles are spherical with coarse and agglomerate surfaces that could increase the high-water demand, thus reducing the workability.

Furthermore, the relationship between a slump and flow value of mortar incorporated with POFA at different percentages as a partially fine aggregate replacement, which were 0%, 2.5%, 5%, 7.5%, and 10%, as can be seen in Figure 8.

Based on the observation in Figure 8, it is obvious that both values brought a downturn value with an increase in POFA percentage in mortar. In terms of percentage difference, it can be clearly seen that the higher the percentage of POFA as a partially fine aggregate replacement used in mortar, the higher the percentage difference. This was due to the workability for each of the percentage of POFA decreases compared to the control specimen.

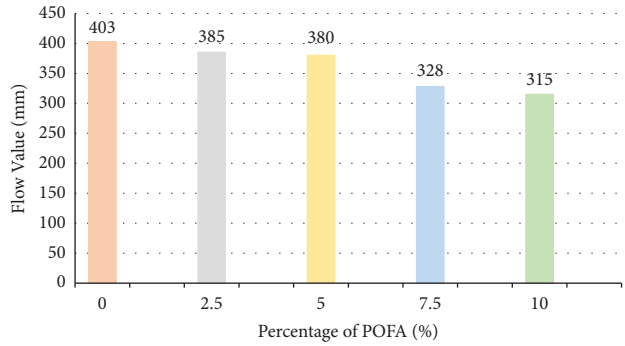

Figure 7: Flow value results on different percentages of POFA.

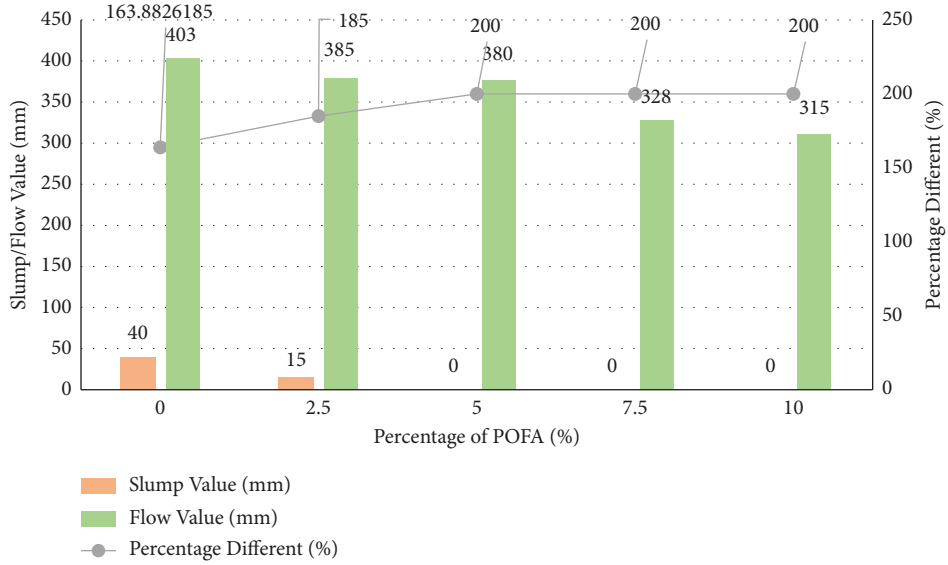

Figure 8: Relationship between the slump value and flow value of mortar.

From Figure 8, it shows the percentage difference between slump and flow values for 0%, 2.5%, 5%, 7.5%, and 10% specimens recorded difference at 164%, 185%, 200%, 200%, and 200%, respectively. It can be concluded that the lowest percentage difference between slump and flow values was the control specimen mortar while the highest percentage difference was mortar with 5%, 7.5%, and 10% since it had a zero-slump value. Thus, it indicated that the inclusion of POFA at every level of replacement did not improve the workability of mortar.

According to Figure 8, it can be seen that the higher the percentage of POFA used in the mortar will result in lower workability. This can be proven through studies conducted in [12] that the higher the amount of POFA will result in low workability compared to the control specimen. This statement can be supported by [13] which had expressed that the workability of concrete with the inclusion of POFA declined as the percentage of POFA rise in the mixture.

3.2. Hardened Mortar. A compression test was carried out on mortar specimens after being cured in water at days 3, 7, and 28 using the compression test machine. The compressive strength was recorded by taking the maximum load of the specimen that can be sustained. Figure 8 illustrates the results of the compressive strength of mortar incorporated with POFA as a partially fine aggregate replacement on the effect of age.

Figure 8 shows the results of compressive strength of mortar at different percentage of POFA, which were 0%, 2.5%, 5%, 7.5%, and 10% as a partially fine aggregate replacement. According to the results of Figure 8, it is shown that the compressive strength was increasing from day 3 to day 28 for POFA at 0%, 2.5%, 7.5%, and 10%. Meanwhile, compressive strength of mortar with 5% POFA as a partially fine aggregate replacement was increased from day 3 to day 7 with 20.37 MPa and 24.49 MPa, respectively, but suddenly reduced to 10.53 MPa on day 28.

In this study, it can be noticed that the highest compressive strength on day 3 is the mortar with the inclusion of 5% of mortar. Results on day 7 showed POFA at 0% contributes the highest compressive strength with 26.31 MPa followed by 2.5% with 25.79 MPa. Overall, based on the findings during the mature age of the concrete which is on day 28, it can be marked that 2.5% was the optimum strength with 37.70 MPa compared to the control specimen with 6% of percentage difference.

The possible effect of that particular 2.5% was that the optimum percentage of POFA comes from a good filler effect. POFA is a good filler effect that can fill in between voids. A study by Hamada et al. [14] confirmed that using POFA with fine particles will improve the compressive strength compared to the control specimen. The fineness of the POFA is the main aspect that can contribute to the compressive strength, which can be supported by [15]. In this study [15], the authors stated that the specimen that contains POFA as a partially replacement for cement or fine aggregates will be improved towards their age. This was due to the high fineness of POFA that can fill in the voids. This can be determined from the results obtained by POFA at 2.5%. The compressive strength is increasing starting from 19.87 MPa, 25.79 MPa, and 37.70 MPa on day 3, 7, and 28, respectively.

Figure 9 also shows the equation of the relationship between compressive strength and age of mortar incorporated with POFA together with the coefficients of determination (R^2). In addition, the highest value R^2, as shown in Figure 9, was mortar with 5% POFA as a partially fine aggregate replacement with 0.998. Therefore, the value was used to determine the compressive strength in improving the study of replacing POFA at longer curing age. In the study in [16], the determination of the strength to improve at a longer curing age was based on the R^2, and it was recorded that 10% POFA was the optimal percentage for the study.

POFA used in this study was taken from the same source as [2], which was from the United Palm Oil Mill, Nibong Tebal at Pulau Pinang with a high amount of silica. According to [6], the high silica content in the POFA will affect the compressive strength and make the water absorption become lesser, and it can be confirmed by [17] through XRF that had been conducted. In [17], the authors stated that waste materials which are POFA showed the highest amount of silica with 51%, as shown in Table 2, followed by CaO and other elements. In accordance with [18], a standard POFA fits the criteria for being pozzolanic and can be categorized within Class C and Class F, as shown in Table 2, which reveals the reactive oxide of POFA with 59.03% that was composed from $SiO_2 + Al_2O_3 + Fe_2O_3$.

In addition, the microstructural analysis will be analysed on the specimens of mortar with different percentage of POFA at curing ages of days 3, 7, and 28. The change in morphology was due to the different percentages of POFA incorporated in the mortar which was examined by using SEM. Figure 10 shows the SEM micrographs of mortar on day 3 at 50-micron scale with 1500 magnification at different percentages of POFA, which were 0%, 2.5%, 5%, 7.5%, and 10%.

Figure 10(a) shows the control specimen for this research at day 3 which is without inclusion of POFA. It was obvious that the control specimen has a higher volume of voids and is more porous compared to the mortar incorporated with POFA due to the large particles of fine aggregates. It can be observed that there was a formation of a tiny needle action called ettringites, as illustrated in Figure 10(a). Furthermore, the formation of $Ca(OH)_2$ was done in the mortar with 0% POFA creating more voids in the mortar. This happened during the hydration process when there was a rapid action of the cement in contact with the water, thus producing a high quantity of $Ca(OH)_2$.

Mortar with POFA at 2.5%, 5%, 7.5%, and 10% are illustrated in Figures 10(b)–10(e), respectively. It can be clearly seen that the voids in the mortar specimens were reduced. The presence of POFA in specimens helps in reducing the porous structure [19]. It shows that the main factors of the reduction come from the good filler effect caused by the POFA itself. It can be noticed that the needle action or ettringites started to disappear. Moreover, the amount of $Ca(OH)_2$ will become lesser as the percentage of POFA is higher. This can be shown from the figure below for POFA at 2.5%, 5%, 7.5%, and 10% which helps to fill in the voids and make them less porous.

Moreover, the higher the amount of POFA used in the mixture, the lesser the voids of the specimen. As illustrated in Figure 10(c), which contains 5% of POFA, it can be verified that it has less void compared to the 2.5% and control specimen. This was due to the amount of POFA being used in the mixture. When there is a presence of POFA in the mixture, the process named as the refining process will occurr. The refining process will close all the voids in the specimen, and if there are any of the voids, it is not significant as the control specimen and 2.5% of POFA. This had proven that the inclusion of POFA act as microfiller. In [20], the authors had declared that the microfilling ability and pozzolanic activity of POFA are satisfactory.

Observation on 7.5% POFA as a partially fine aggregate replacement makes the specimen become incomplete bonding. This incomplete bonding is shown in Figure 10(d). The incomplete bonding may be due to agglomeration. Due to its agglomeration, the POFA particles cannot easily roll over one another, thus increasing the interparticle friction. For Figure 10(e), which consists of 10% POFA in mortar as a partially fine aggregate replacement, there was an internal cracking between the particles, although the voids are improved through the refining process. This can be due to too much POFA incorporated in the mortar which will reduce the strength. Besides, the mixture of mortar will need a higher water requirement since the fineness of the particles increases. Hence, a study conducted by Saffuan et al. [13] had proved the appearance of the internal cracking that happened at the specimen of 10% of POFA.

POFA is high with silica and alumina which contributes to the pozzolanic activity. This can be proved by a study revealed in [12] that stated POFA is a good pozzolanic material and can be considered as a good supplementary cementing material (SCM). Figure 11 illustrates the SEM micrographs of mortar on day 7 at 50 micron scale with 1500 magnification at different percentages of POFA, which were 0%, 2.5%, 5%, 7.5%, and 10%.

One of the POFA's behaviour can improve strength due to its characteristic that can act as a good SCM. As can be seen in Figure 11(a), which represents the control specimen of mortar, it can be noticed that there was no SCM since it has 0% inclusion of POFA, thus the amount of $Ca(OH)_2$ will be higher. Although the 0% POFA contains $Ca(OH)_2$, it does

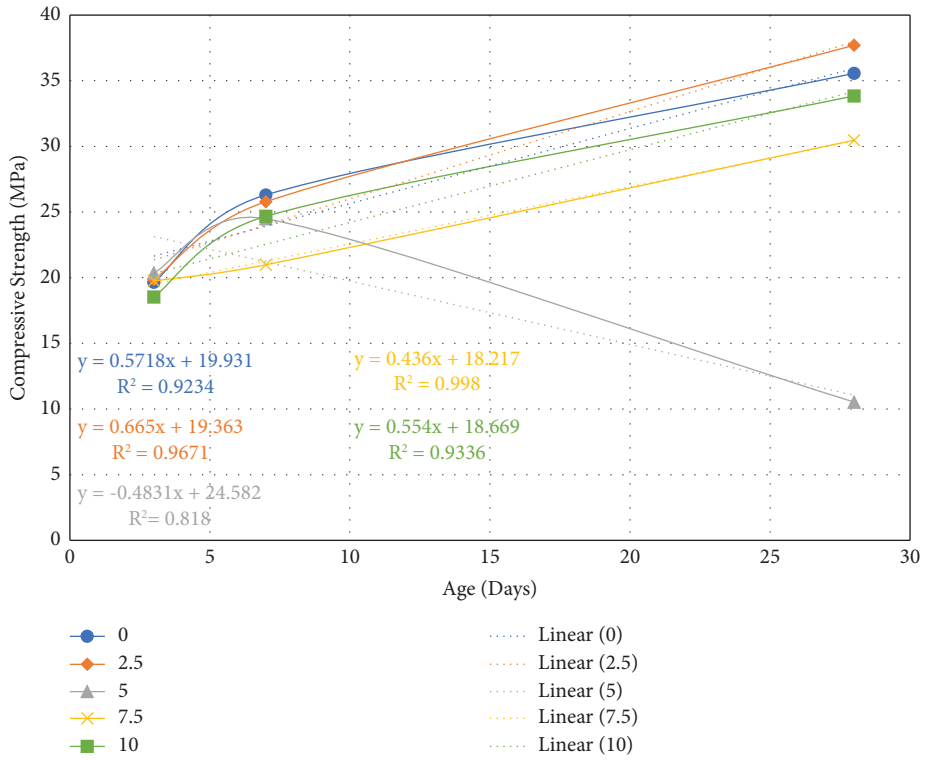

Figure 9: Compressive strength of mortar on the effect of age.

Table 2: Chemical composition of POFA (adopted from reference [17]).

Chemical composition (%)	POFA
SiO_2	51.00
Al_2O_3	4.61
Fe_2O_3	3.42
CaO	6.93
MgO	4.02
Na_2O	0.06
K_2O	5.52
SO_3	0.36
LOI	21.60

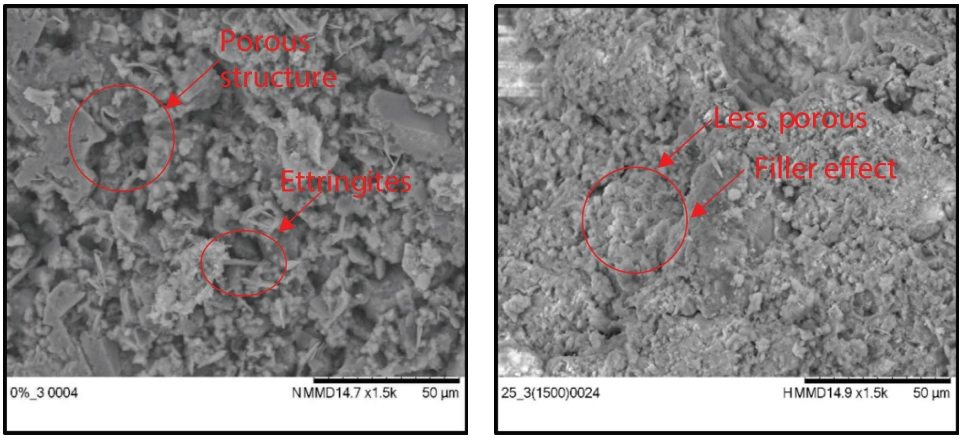

(a) (b)

Figure 10: Continued.

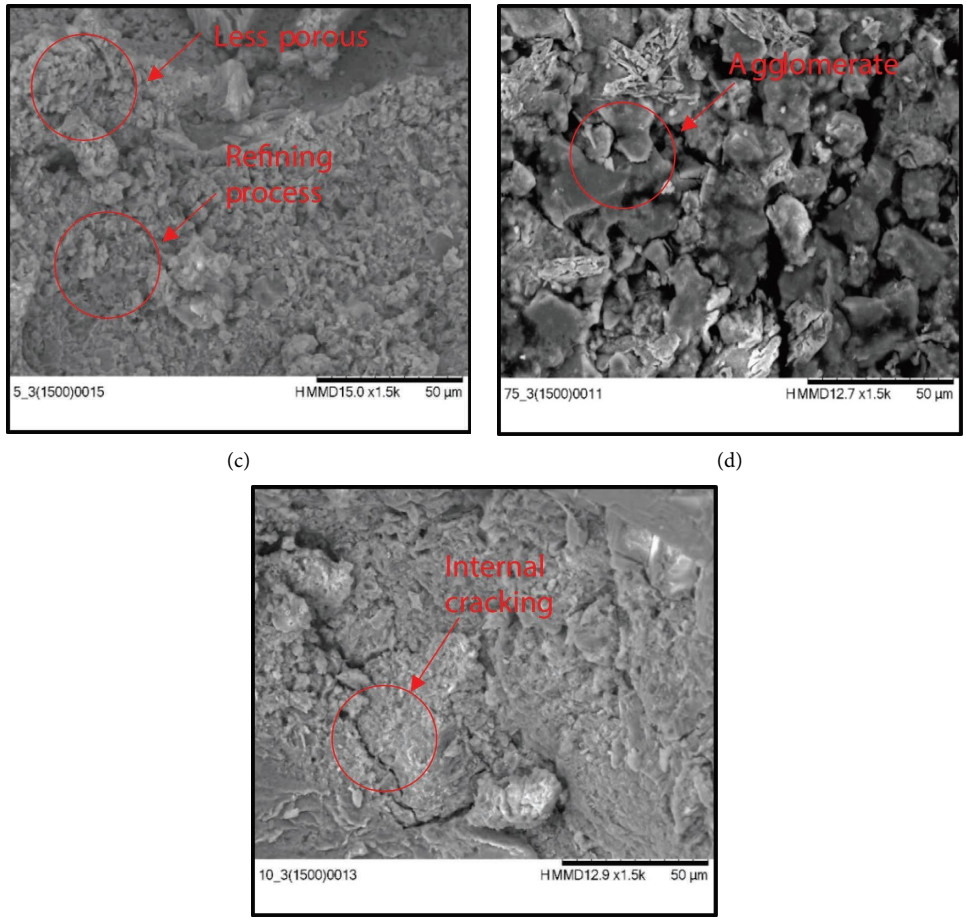

Figure 10: SEM micrographs of mortar on day 3 at 50 micron scale with 1500 magnification: (a) 0% POFA, (b) 2.5% POFA, (c) 5% POFA, (d) 7.5% POFA, and (e) 10% POFA.

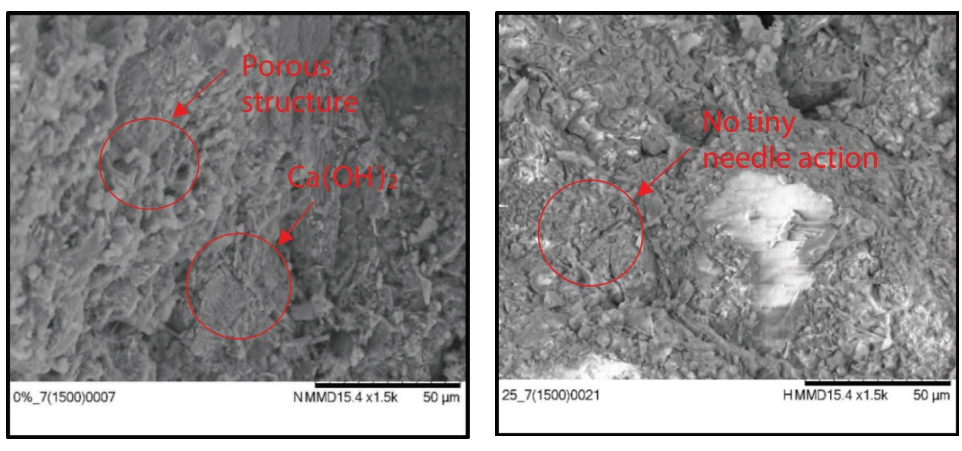

Figure 11: Continued.

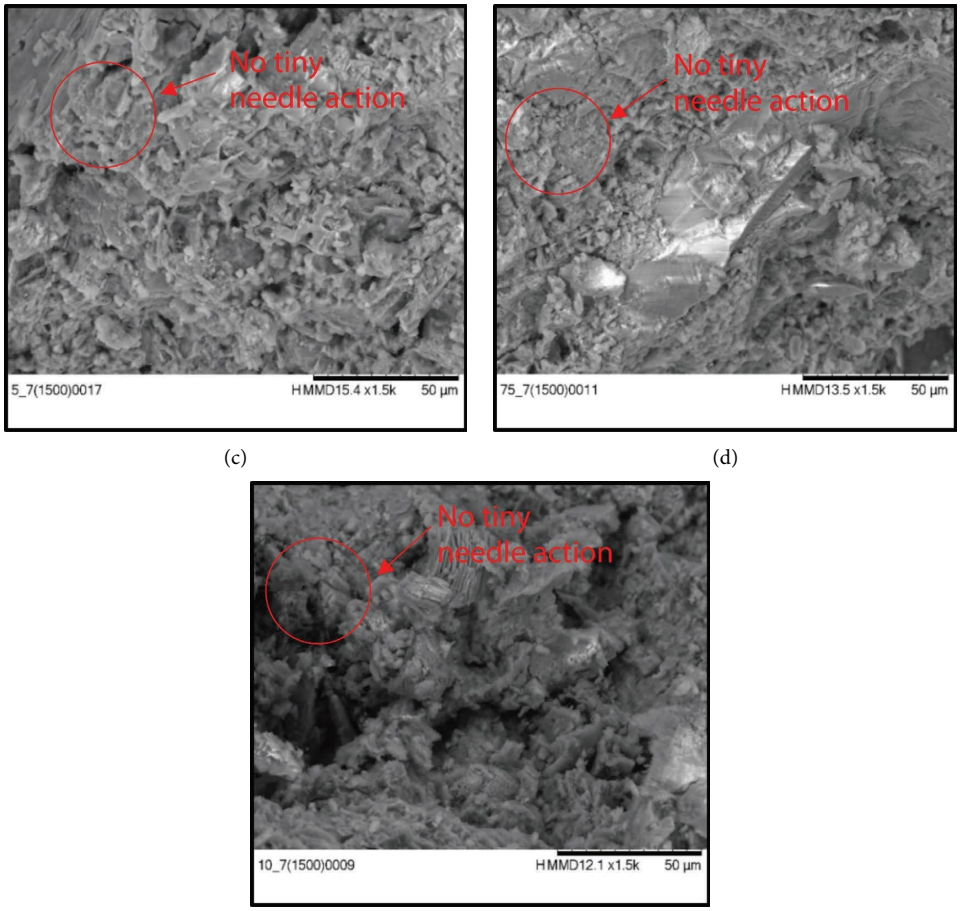

Figure 11: SEM micrographs of mortar on day 7 at 50 micron scale with 1500 magnifications: (a) 0% POFA, (b) 2.5% POFA, (c) 5% POFA, (d) 7.5% POFA, and (e) 10% POFA.

not notice as much as on day 3. Furthermore, the SEM images showed a porous structure, as illustrated in Figure 11(a). The porous structure of the specimen is improved compared to earlier ages at day 3.

Based on Figures 11(b)–11(e), it shows the specimen of mortar with 2.5%, 5%, 7.5%, and 10% of POFA, respectively. Due to the presence of POFA, which can be classified as a good SCM by [12], the amount of $Ca(OH)_2$ can be reduced. The higher the usage of SCM, which in this study is POFA, the lower the value of $Ca(OH)_2$, and this statement was supported by [21]. Moreover, it can be observed that there is no formation of tiny needle action as a result of $Ca(OH)_2$ present in the specimen at POFA at 2.5%, 5%, 7.5%, and 10%.

POFA has a higher amount of silica and alumina. The pozzolanic activity can be enhanced due to the presence of silica in the POFA composition [3]. The oven-dried POFA used in this study has a high fineness particle that could improve the strength of mortar. Moreover, due to high fineness and less unburned carbon in POFA particles, it will increase the rate of the pozzolanic activity. In [17], the authors added that SiO_2 will increase with increasing POFA fineness. The unique behaviour of POFA was due to pozzolanic behaviour making it resistant to other chemicals [12]. Figure 12 shows the result of the microstructural analysis on day 28.

The SEM images on the inclusion of 0% POFA show that the mortar specimen is less dense than others, as evidenced in Figure 12(a). Since mortar at 0% POFA has no existence of POFA, then the pozzolanic activity could not be encouraged in the mixture. This was because the POFA content has a high amount of silica that helps in improving the pozzolanic activity.

Based on Figures 12(b)–12(e), the amount of the pozzolanic material was higher as compared to the control specimen since it contains POFA as a partially fine aggregate replacement in the mixture. Thus, the amount of C-S-H gel produced due to high silica in the mixture was also high. In addition, the additional C-S-H produce makes the microstructure much denser and able to improve the interfacial bond between aggregates and binder paste. Thus, it will help in improving the strength [19]. This can be proved based on Figure 8 which shows the SEM images of POFA at different percentages were much denser compared to 0% POFA at the mature age of mortar.

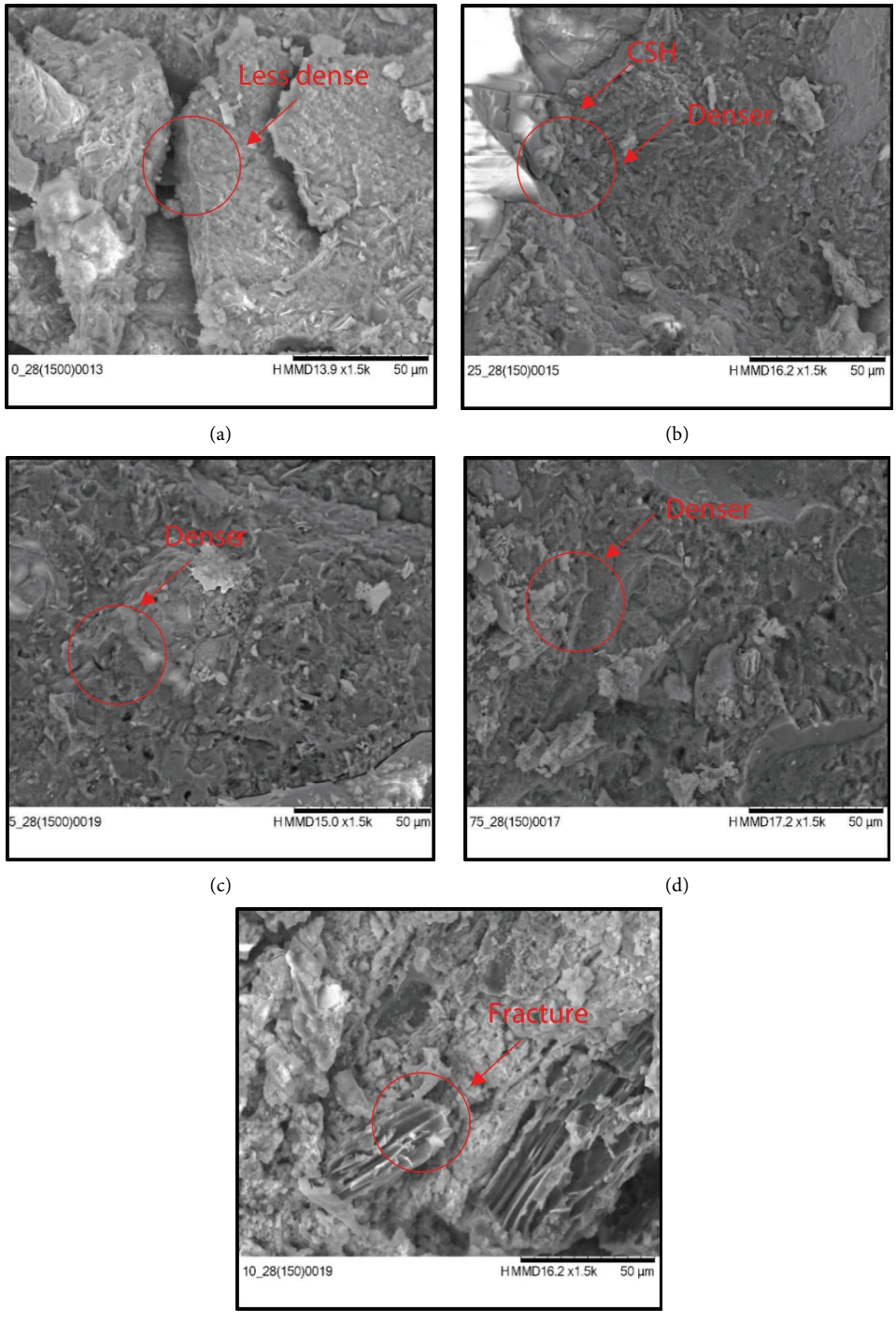

Figure 12: SEM micrographs of mortar on day 28 at 50 micron scale with 1500 magnification: (a) 0% POFA, (b) 2.5% POFA, (c) 5% POFA, (d) 7.5% POFA, and (e) 10% POFA.

The highest compressive strength on day 28 was achieved by POFA at 2.5%. This was due to the high fineness of the POFA itself, which contributes to the strength and high amount of SiO_2. As a result of high SiO_2 in the specimen, the reaction between $Ca(OH)_2$ and SiO_2 was improved, thus resulting in a large quantity of C-S-H gel that helps to improve the compressive strength [19]. In [19], the authors also added in the research that the optimum percentage that improved the strength was due to the maximum amount of C-S-H on the specimen which was fully used, and it produced low permeable porosity by filling microvoids with C-S-H.

4. Conclusions

The following conclusions can be drawn from the laboratory results according to the respective objectives specified at the beginning of this study.

(1) Mortar with 0% of POFA as a partially fine aggregate replacement recorded the highest slump and flow value with 40 mm and 403 mm, respectively. This is because no inclusion of POFA has the ability to absorb water.

(2) Mortar with 5%, 7.5%, and 10% recorded as true slump in the zero slump value. Meanwhile, mortar with 10% recorded the lowest flow value.

(3) Mortar incorporated with POFA requires high water demand due to high fineness in particles that increases the surface area and contains a high amount of carbon.

(4) Mortar with 2.5% inclusion of POFA recorded the highest compressive strength, making it the optimum percentage of POFA as a partially fine aggregate replacement to the mortar specimen at mature age at day 28.

(5) Mortar having 5% of POFA measured the lowest compressive strength at mature age which is at day 28.

(6) Due to the POFA acting as a filler in the void of mortar, the compressive strength was improved.

(7) During the water curing process, the pozzolanic reaction of the mortar produced by silica in the POFA helps to enhance the compressive strength of the mortar.

(8) Microstructural analysis on day 3 had successfully shown that POFA acts as a filler between the voids in mortar mixture and reduces the formation of calcium hydroxide ($Ca(OH)_2$) that produced a tiny needle action.

(9) Microstructural analysis on day 7, POFA can be classified as a good supplementary cementing material (SCM) that produces calcium silicate hydrate (C-S-H) gel and results in the reduction of $Ca(OH_2)$.

(10) Some future recommendations are listed below so that future researchers can refer to this study to achieve better results:

(a) Increase the fineness of the POFA particles in mortar mixture
(b) Observed the physical properties of POFA as a partially fine aggregate replacement in mortar through the particle size distribution
(c) Discover the microstructural analysis on the material of POFA

(11) This study intends to highlight the usage in the IBS industry since it can produce a lighter structure due to the incorporation of POFA as a partially fine aggregate replacement.

Data Availability

The data used to support the findings of this study are included within the article.

Conflicts of Interest

The authors declare that there are no conflicts of interest regarding the publication of this paper.

Acknowledgments

The authors' gratitude and thanks go to their supervisor, Nor Hafida Hashim, and cosupervisor, Dr.Muhd Norhasri Bin Muhd Sidek. The authors thank them for their support, patience, and ideas throughout the study, which have led to the smooth finishing of this study. The authors also would like to express their gratitude to Dr. Nur Ashikin Binti Marzuki for the guidance that had been provided during the completion of this study. The authors also would like to thank the staff of Heavy Structural Lab and Mechanical Lab, Encik Habibullah Bin Mahmud, Encik Mohd Salleh Bin Abdullah, and Encik Amir Shahrul Bin Ishak, respectively. A word of gratitude is extended to United Palm Oil Mill, Nibong Tebal, Pulau Pinang, for the supply of palm oil fuel ash (POFA) and their colleagues. Lastly, the authors thank the Research Management Centre (RMC) for providing grant entitled "A Potential of Palm Oil Fuel Ash as Partially Fine Aggregate Replacement with an Additional of Gfrp in Improving the Performance of Mortar" (RMC/GP/GIP2021).

References

[1] F. Mulizar, A. Iskandar, and A. Fauzi, "Effect of POFA as a replacement material on fly ash based geopolymer mortar," *IOP Conference Series: Materials Science and Engineering*, vol. 854, no. 1, Article ID 012012, 2020.

[2] N. H. Hashim, M. N. Muhd Sidek, N. M. Noor, S. R. Roselli, M. A. Mohd Yusoff, and M. F. S. Saiful Bahari, "Utilisation of palm oil fuel ash (Pofa) as sand replacement for fresh and hardened concrete by using powder and liquidation method," *Journal of Physics: Conference Series*, vol. 1349, no. 1, Article ID 012055, 2019.

[3] H. M. Hamada, G. A. Jokhio, F. M. Yahaya, A. M. Humada, and Y. Gul, "The present state of the use of palm oil fuel ash (POFA) in concrete," *Construction and Building Materials*, vol. 175, pp. 26–40, 2018.

[4] S. Wan Ahmad, K. Muthusamy, M. H. Hashim, A. M. Albshir Budiea, and N. F. Ariffin, "Effect of Effect of Unground Palm Oil Fuel Ash as Partial Sand Replacement on Compressive Strength of Oil Palm Shell Lightweight Concretenground palm oil fuel ash as partial sand replacement on compressive strength of oil palm shell lightweight concrete," *IOP Conference Series: Materials Science and Engineering*, vol. 712, no. 1, Article ID 012034, 2020.

[5] P. Chindaprasirt, S. Homwuttiwong, and C. Jaturapitakkul, "Strength and water permeability of concrete containing palm oil fuel ash and rice husk-bark ash," *Construction and Building Materials*, vol. 21, no. 7, pp. 1492–1499, 2007.

[6] S. R. Rosseli, M. N. M. Sidek, N. I. Halim, N. H. Hashim, M. S. A. Hamid, and N. Tutur, "Effect on consistency and

performance of POFA concrete," *Journal of Physics: Conference Series*, vol. 1349, no. 1, Article ID 012067, 2019.

[7] Bs En 197-1:2000, *Cement Part 1: composition, specifications and conformity criteria for common cements*, vol. 3, British Standard, British, UK, 2000.

[8] Bs En 197-1:2000, "Methods of testing cement Part 1: determination of strength," *Part 1 Determ. strength*, vol. 196, no. 1, p. 36, 2005.

[9] Bs En 12350-2:2019, *BSI Standards Publication Testing Fresh concrete Part 2: Slump Test*, BSI Stand. Publ, British, UK, 2010.

[10] Bs En 12350-5:2019, *BSI Standards Publication Testing Fresh concrete Part 5: Flow Table Test*, British Standard, British, UK, 2019.

[11] Bs En 12390-3:2019, *BSI Standards Publication Testing hardened concrete Part 3: compressive strength of test specimens*, BSI Standard Publication, British, UK, 2019.

[12] A. A. Awal and I. A. Shehu, "Evaluation of heat of hydration of concrete containing high volume palm oil fuel ash," *Fuel*, vol. 105, pp. 728–731, 2013.

[13] W. A. Saffuan, K. Muthusamy, N. A. M. Salleh, and N. Nordin, "Properties of concrete containing ground palm oil fuel ash as fine aggregate replacement," *IOP Conference Series: Materials Science and Engineering*, vol. 264, no. 1, Article ID 012008, 2017.

[14] H. M. Hamada, G. A. Jokhio, F. M. Yahaya, and A. M. Humada, "Properties of fresh and hardened sustainable concrete due to the use of palm oil fuel ash as cement replacement," *IOP Conference Series: Materials Science and Engineering*, vol. 342, no. 1, Article ID 012035, 2018.

[15] M. Rezaul Karim, M. F. M. Zain, M. Jamil, and M. Nazrul Islam, "Strength of concrete as influenced by palm oil fuel ash," *Australian Journal of Basic and Applied Sciences*, vol. 5, no. 5, pp. 990–997, 2011.

[16] W. Y. Wan Yusof, S. H. Adnan, Z. Jamellodin, and N. S. Mohammad, "Strength Strength Development of Fine Grained Mortar Containing Palm Oil Fuel Ash as a Partial Cement Replacementevelopment of fine grained mortar containing palm oil fuel ash as a partial cement replacement," *Applied Mechanics and Materials*, vol. 773-774, no. 774, pp. 964–968, 2015.

[17] E. S. R. Abdullah, A. K. Mirasa, and H. Asrah, "Review on the effect of palm oil fuel ash (POFA) on concrete," *Journel of Industrial Engineering and Research.*vol. 1, no. 7, pp. 1–4, 2015.

[18] Astm C618, *Standard Specification for Coal Fly Ash and Raw or Calcined Natural Pozzolan for Use in concrete*, ASTM International, Pennsylvania, Philadelphia, 2015.

[19] Z. Jumaat, M. Safiuddin, and M. A. Salam, "Microstructure of self-consolidating high strength concrete incorporating palm oil fuel," *Physical Review and Research International*, vol. 3, no. 4, pp. 674–687, 2013.

[20] M. Safiuddin, M. A. Salam, and M. Z. Jumaat, "Utilization of palm oil fuel ash in concrete: utilization of palm oil fuel ash in concrete: a review," *Journal of Civil Engineering and Management*, vol. 17, no. 2, pp. 234–247, 2011.

[21] N. A. S. M. Azhar, N. H. Hashim, M. N. M. Sidek, N. A. I. A. Halim, A. Newman, and M. A. M. Fauzi, "Effect of low inclusion of palm oil fuel ash (POFA) as a partially sand replacement to the performance of mortar," *Journal of Building Pathology and Rehabilitation*, vol. 7, no. 1, 2022.

Hindawi
Advances in Civil Engineering
Volume 2023, Article ID 9767238, 1 page
https://doi.org/10.1155/2023/9767238

Retraction

Retracted: Control System of Fire Rescue Robot for High-Rise Building Design

Advances in Civil Engineering

Received 22 August 2023; Accepted 22 August 2023; Published 23 August 2023

This article has been retracted by Hindawi following an investigation undertaken by the publisher [1]. This investigation has uncovered evidence of one or more of the following indicators of systematic manipulation of the publication process:

(1) Discrepancies in scope
(2) Discrepancies in the description of the research reported
(3) Discrepancies between the availability of data and the research described
(4) Inappropriate citations
(5) Incoherent, meaningless and/or irrelevant content included in the article
(6) Peer-review manipulation

The presence of these indicators undermines our confidence in the integrity of the article's content and we cannot, therefore, vouch for its reliability. Please note that this notice is intended solely to alert readers that the content of this article is unreliable. We have not investigated whether authors were aware of or involved in the systematic manipulation of the publication process.

Wiley and Hindawi regrets that the usual quality checks did not identify these issues before publication and have since put additional measures in place to safeguard research integrity.

We wish to credit our own Research Integrity and Research Publishing teams and anonymous and named external researchers and research integrity experts for contributing to this investigation.

The corresponding author, as the representative of all authors, has been given the opportunity to register their agreement or disagreement to this retraction. We have kept a record of any response received.

References

[1] J. Yu, "Control System of Fire Rescue Robot for High-Rise Building Design," *Advances in Civil Engineering*, vol. 2022, Article ID 7867533, 10 pages, 2022.

Hindawi
Advances in Civil Engineering
Volume 2022, Article ID 7867533, 10 pages
https://doi.org/10.1155/2022/7867533

Research Article

Control System of Fire Rescue Robot for High-Rise Building Design

Junfang Yu

College of Intelligent Security, Zhejiang College of Security Technology, Wenzhou 325016, Zhejiang, China

Correspondence should be addressed to Junfang Yu; junfangyu@zjcst.edu.cn

Received 19 April 2022; Revised 23 May 2022; Accepted 13 July 2022; Published 10 August 2022

Academic Editor: Ramadhansyah Putra Jaya

In recent years, with the steady and rapid growth of the national economy, various industries have developed rapidly and the resulting fire accidents have also been on the rise. This study mainly discusses the control system of a fire rescue robot for a high-rise building design. Robot fire detection method involves obtaining the video image of the fire detection area through a high-definition camera, performing image preprocessing on the current frame image of the video in the robot operating system to obtain the image; and performing the flame area segmentation based on the Ohta color space and the Otsu threshold segmentation algorithm on the image, to obtain the segmented image; through the interframe difference method, the preprocessed image of the previous frame is subtracted from the current frame image and the moving area of the image is segmented to obtain the segmented image; the obtained segmented image is combined with the segmented image in the robot operating system and images are intersected to obtain a segmented image with the characteristics of flame motion; based on other characteristics of the flame, flame recognition is performed on the area in the segmented image. Fires in high-rise buildings are increasing gradually, which seriously endangers the safety of human life and property. The firefighting robot and its control system play an important role in the fire protection of high-rise buildings. The purpose of this study is to analyze the disaster relief effect of a firefighting robot and control system in high-rise buildings. In this study, we use MATLAB software to model and simulate the rescue situation of a firefighting robot in high-rise buildings. The fuzzy control system established in the fuzzy logic toolbox of MATLAB can easily replace human field work and can change the control rules and membership function in the FIS editor. The results show that the rise time and adjustment time of the system are basically the same under the condition of variable load stiffness. The maximum overshoot is 0.59%, and the steady-state error is 0.19%. The maximum overshoot is 1.0148%, and the stability error is 0.46%. It is concluded that the expert PID algorithm is efficient and practical. It can be concluded that the robot position control system adopts PID control algorithm, and the attitude control system adopts expert PID control algorithm. This research provides some value for the development and design of firefighting robots in high-rise buildings in the future and also brings important significance.

1. Introduction

The development of modern cities is accelerating, and more and more high-rise buildings are erected. While people enjoy modern life, they are also faced with a life-threatening problem, that is, high-rise fire protection and rescue. For these problems, people have come up with many countermeasures, but they have encountered great difficulties. One is that it is difficult to observe the fire situation in the high-rise buildings and the internal fire scene. There are certain height restrictions, high-pressure water guns on the ground, limited range of fire-fighting projectiles, and inability to accurately locate, so people think of using special firefighting robots. In the face of the development of modern high-rise buildings, people are increasingly enjoying the problems related to life and safety. In view of these problems, although many countermeasures have been taken, it is difficult to see the high-rise buildings and the internal firefighting scene, and the use of the previous firefighting methods has been greatly restricted, facing great difficulties. There are certain height restrictions, high-pressure water guns on the ground, limited range of fire bombs, that cannot be correctly configured. So I thought about the use of special fire robots. In the actual production and operation of modern industry,

there are many control loops, including PID control of basic loop and advanced control suitable for complex working conditions. Considering some robustness in PID controller design, some uncertain information contained in the model will be considered. This makes the PID controller maintain acceptable performance and good quality within the range of uncertain information, so as to overcome the shortcomings of traditional PID implementation. Therefore, it is of great theoretical and engineering significance how to keep the good performance of the PID controller and the advanced controller in the actual industrial control.

The whole system of the robot is a control system. As a product of the development of modern science and technology, robots have begun to penetrate into various fields of human activities, working in unstructured environments that human beings cannot reach or cannot reach. Firefighting robots can go deep into the accident scene, predict the existence of danger in time, ensure personal safety, complete data processing and feedback, and provide on-site information and intelligence. In addition, the rescue work of firefighters and toxic gas inspection can also be carried out. The fire environment of high-rise buildings is more complex than that on the ground, with high risk and difficult rescue. In order to protect the safety of life and equipment, it is very important to study the fire rescue and firefighting robots of high-rise buildings.

Many experts and scholars have researched and analyzed the design and method of firefighting robots and their control systems. Lee et al. introduced a new rescue robot, which is composed of a multipurpose dual intelligent robot and a mobile platform with variable structure, including rescuing the wounded and transporting dangerous goods. In order to solve the composition and balance characteristics of the robot, a rescue strategy based on the whole technique is proposed. In order to study the security and stability of the robot in the rescue process, it reflects the specific constraints with different priorities in the redundant domain of the robot. In order to achieve stable motion control in various situations, he uses the unique Robert reverse movie feature and modifies it to make the robot's motion more stable. By comparing with other methods, the robustness of the control method is tested numerically, which replaces the rescue robot which is being developed with a small simulator. The firefighting robot in their method cannot effectively control the fire situation, and its function is not enough [1]. Hong et al. proposed a practical hardware design strategy and control method of rescue robot in disaster environment. The safety of firefighting robot in their method is not enough [2]. Madhevan et al. designed and developed autonomous fire rescue robots. The robot is designed to move even in case of fire or danger; he also established a mathematical model to describe the kinematics and dynamics of the robot. V-rep is used to create a robot simulation in a fire environment of fire simulation. His method is only based on the model, there is no actual experimental operation, and the persuasion is not strong [3]. The method proposed in this paper is a great progress of robot intelligent control technology and computer technology. Compared with other methods, it can further realize autonomous decision-making, autonomous action, and self-protection.

Advanced controls have achieved practical results in complex industrial processes. In these practical applications, the system generally cannot maintain good performance continuously. The main reason is the lack of effective detection methods for the control system, the poor robustness of the designed controller, and the poor self-healing. The high-rise building firefighting robot developed in this study uses a core coin support mechanism. The mechanism uses an inner steel cable to separate and fix it into an inverted triangle at the top of the building, and uses a nonlinear infinite climbing device instead of traditional traction. Under the action of the system and the driving motor, the body can move flexibly in the two-position space, and has static stability after losing power. Firstly, this paper introduces the working principle of firefighting robot system and the related characteristics of a BIM high-rise building. At the same time, the main classification and application of fire robots are described in detail. The PID control principle used in this research includes a classical PID control algorithm, an expert PID control algorithm, and an attitude controller design. The main functions of the upper computer software, the principle of ultrasonic sensor, and the design of control system module are explained in the experiment. Through the experimental results, the simulation analysis of the firefighting robot control system, the rescue analysis of the firefighting robot under the wind disturbance, the load state analysis of the firefighting robot, the simulation of the rescue process of the fire robot, and the effect analysis of the PID control algorithm of the firefighting robot are carried out.

2. High-Rise Building and Firefighting Robot Control System

2.1. Characteristics of BIM for High-Rise Buildings. BIM is a three dimensional building information model. This model contains the information data of all building processes [4–6].

2.1.1. Visualization. Visualization can be understood as "what you see can be obtained." If it can be applied to commercialization in construction engineering, its effect will be very great. Today, the architectural design industry also has 3D rendering, which only includes the location, size, and color of building components, and lacks other information about the connection between building components and different components. The visualization of BIM Technology is to visualize the connection between various parts of the building. That process is all visualized. The results of BIM visualization can not only be displayed in a 3D rendering, but can also automatically generate report data information. The most important thing is that the design, construction, and operation of construction projects can be discussed, communicated, and decided in the visual state [7, 8].

2.1.2. Coordination. Adjustment is an important part of the construction industry. If there are problems in the actual construction process of the project, it is necessary to

organize all relevant professional and technical personnel to hold a coordination meeting to find out the causes of the problems in the actual construction, and propose solutions for the change in project. Finally, in order to solve the problem, the corresponding improvement measures are adopted. In the process of designing drawings, due to the lack of communication and communication between professional engineering designers, the various drawings designed have problems of intersection and conflict [8].

2.1.3. Simulation. Simulation can not only simulate the shape of buildings but can also simulate things that cannot be operated in the real world. In architectural design, BIM can simulate the functional requirements of design simulation. For example, energy saving simulation, lighting simulation, etc.; in the construction phase of buildings, 4D simulation of buildings (time maintenance based on bim3d model) can be carried out. In this way, the progress of site construction can be simulated according to the design documents of project construction organization. A more reasonable construction plan can be made.

2.1.4. Optimization. The decision-making stage, design stage, construction stage, and operation stage of a construction project are all a continuous optimization process. Of course, there is no specific inevitable relationship between optimization and BIM, but better project optimization can be performed based on BIM. Optimization is mainly controlled by information, complexity, and time. If there is no clear information about the building, high-quality optimization results cannot be obtained. BIM provides information about the actual components of a building, including geometric, physical, and limiting information of the components, and also provides real-time presence information after changes to the building [9]. In the case of high building complexity, the technical personnel related to the construction project have limited ability and cannot master all the information [10, 11].

2.2. Main Classification of Firefighting Robots. In order to facilitate the research, from the point of view of actual combat, according to the corresponding requirements, firefighting robots can be divided into the following categories:

(1) According to their different executive functions, they are divided into fire detection robot, dangerous goods leakage detection robot, disassembly robot, emergency robot, multifunctional robot, etc.

(2) According to the different walking modes, it can be divided into walking robots with wheels, crawling robots, crawling wheels walking robots, sucker walking robots, etc.

(3) According to the different control methods, it can be divided into line control robot, wireless remote control robot, adaptive robot, etc. [12–14].

(4) According to the different degree of intelligence, it can be divided into program control robot, computer support control robot with sensory calculation function, intelligent robot, etc.

(5) According to the difference of sensory function, it can be divided into vision robot, smell robot, temperature robot, smoke robot, tactile robot, etc. [15].

2.3. Working Principle of the Firefighting Robot Control System. The rear part of the aerial firefighting robot is composed of an air support system and a human-computer interaction system, while the robot body control system and the monitoring system constitute the front part. The monitoring system sends back the image and sound information of the scene, and the robot body control system is responsible for firefighting and first aid. When the robot host is released to the designated position of the helicopter, the host first receives the information and scene from the temperature sensor and optical sensor. The image is used to determine the fire source scene. Next, the position of the robot head is adjusted according to the position information recorded by the position sensor, so that the fire bomb is the same as the fire source. After the setting is successful, the fire extinguisher is ignited: extinguish the fire. By adjusting the position, the robot approaches the attic, locates the exact location of the trapped person, and rescues them through the emergency shelter. In the whole process, it is necessary to keep the balance of the main body of the robot in the air [16, 17].

2.4. Application Fields of the Firefighting Robot Control System. The firefighting robot carries a small robot and 360. The advantages of an omni-directional rotary table are fully compatible with the advantages of a multirotary flying robots and ground mobile robots, and can overcome the disadvantages of both. The realization of firefighting robot can provide good help for disaster rescue and other applications. Some applications are as follows:

(1) Explosion proof: for example, explosives will be placed on high ground such as roofs. The ordinary explosion-proof robots in these places cannot be reached and it is very inconvenient to move. For explosive-related work, land-based robots and aerial robots can fly near the explosives and then move the ground to the explosives. Or, for some explosives that need manual explosion, the land robot can be used to move to the side of the explosives. After picking up the explosives, they can fly to high places or open spaces for explosive operation. Of course, it is possible to damage the land robots now, but compared with the victims of explosions, the damage to land robots should be kept to a minimum.

(2) Earthquake relief: for collapsed buildings or damaged bridges, land robots or aerial robots can be used to fly on the damaged bridges to search and rescue the injured after reaching the rubble. After searching and rescuing the wounded, the land robot will

quickly feedback the location coordinates and status of the wounded to the emergency center, so that the emergency personnel can be rescued in the shortest time. At the same time, land robots and aerial robots can also be used to investigate the overall situation of the earthquake affected areas. This helps the emergency team to customize the first aid plan [18, 19].

(3) Fire rescue: the disaster situation can be photographed in the fire scene. Or the infrared detector of human body is loaded on the land and air robots to go deep into the disaster room, search for the injured and transmit the result data to the control center, or use a small aerial robot to shut down or provide sleep for the receiver, use no smoking and wet towel for people with smoke, or land and air robots to guide the people trapped in the smoke to escape [20].

(4) Military reconnaissance: when the wing aircraft is flying, the sound of propeller is relatively loud, which is easy to be detected by airborne radar. Land robots and aerial robots initially fly to the enemy, and then switch to ground mobile mode for secret detection.

(5) Nuclear area operation: if there is a nuclear leakage in a nuclear radiation place such as a nuclear power plant, it is very dangerous for workers to enter that place. At this point, it is not a human, but a land-based robot that invades the leakage area, and the cause can be found out. People can operate remotely through the robot arm of the land robot [21, 22].

(6) Agricultural application: equipped with a special camera, it can not only obtain low altitude information of diseases, pests, and weeds but also drive small-scale pests and diseases. In addition, after landing, the farmland soil can be moved to collect comprehensive soil information such as pH value, moisture content, and electrical conductivity, and send it back to the control center. In addition, problematic crops can be obtained and returned to the control center for user analysis.

(7) In terms of rescue, the intelligent machine of land robot can grasp the light buoy and fly to the people who fall into the water to seek help. This rescue method greatly exceeds the speed of manual rescue, and the success rate will also be improved [23].

2.5. PID Control Principles. Proportional integral differential (PID) control is a common control algorithm in the industry. It has a history of more than 70 years. There are many advantages such as simple structure, stability, reliability, and easy adjustment [24].

2.5.1. Classical PID Control Algorithm. The principle block diagram of PID control system is shown in Figure 1.

Here, $r(t)$ is the target value, $c(t)$ is the output value, $e(t) = r(t) - c(t)$ is the input error of the controller, and $u(t)$ is the total output control amount of the controller [25]. The ideal PID controller is as follows:

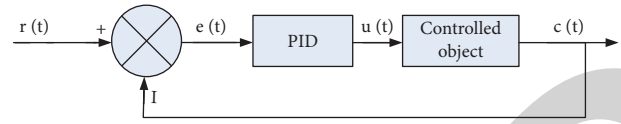

Figure 1: PID control principle.

$$u(t) = K_p\left[e(t) + \frac{1}{T_1}\int e(t)dt + T_d\frac{de(t)}{dt}\right], \quad (1)$$

where K_P is the proportional coefficient; T_i is the integral time constant; T_d is the differential time constant. Discretization is needed. In discretization, let

$$t = kT, (k = 0, 1, 2...). \quad (2)$$

Approximate transformation:

$$u(t) \approx u(kT), \quad (3)$$

$$e(t) \approx e(kT), \quad (4)$$

$$\int e(t)dt \approx T\sum_{j=0}^{k} e(jT) = T\sum_{j=0}^{k} e(j), \quad (5)$$

$$\frac{de(t)}{dt} \approx \frac{e(kT) - e(kT - T)}{T} = e(k) - e(k-1), \quad (6)$$

where T is the sampling period, which must be very short; $e(kT)$ is omitted as $e(k)$. After substituting the above approximate transformation into the formula, the PID formula of the discrete system is as follows:

$$u(k) = K_p e(k) + K_i\sum_{j=0}^{k} e(j) + K_d[e(k) - e(k-1)], \quad (7)$$

where K_i is the integral coefficient ,$K_i = K_pT/T_i$; K_d is the differential coefficient, and $K_d = K_pT_d/T$.

2.5.2. Expert PID Control Algorithm. The essence of expert control is to use knowledge to understand all kinds of knowledge and control rules of the control object, and design parameters of the PID algorithm based on expert experience to realize the intelligent design of the control and carry out expert PID control [26, 27].

$e(k)$ is the discretization error value of the current sampling time, and $e(k-1)$ and $e(-2)$are the error values of the first and second sampling times, respectively:

$$\begin{cases} \Delta e(k) = e(k) - e(k-1) \\ \Delta e(k-1) = e(k-1) - e(k-2) \end{cases}. \quad (8)$$

According to the change of $e(k)$, $\Delta e(k)$, $\Delta e(k-1)$ and their relationship, the expert PID controller can be designed.

2.5.3. Design of Attitude Controller. All the points that meet the requirements constitute the working space of the fire-fighting robot, which is a fan-shaped area [28]. Reducing the inner diameter of the area can appropriately increase the

working space of the robot. The problem is transformed into finding the minimum distance between two points under certain constraints. The attitude controller adopts expert PID control algorithm:

(1) When the error $e_\gamma(k) \neq 0$, the output of the controller is as follows:

$$\begin{cases} U_\gamma(k) = 4\left|e_\gamma(k)\right|/e_\gamma(k), \left(150^\circ < \left|e_\gamma(k)\right| \leq 180^\circ\right) \\ U_\gamma(k) = 2.5\left|e_\gamma(k)\right|/e_\gamma(k), \left(100^\circ < \left|e_\gamma(k)\right| \leq 150^\circ\right) \\ U_\gamma(k) = 1.5\left|e_\gamma(k)\right|/e_\gamma(k), \left(60^\circ < \left|e_\gamma(k)\right| \leq 100^\circ\right) \\ U_\gamma(k) = \left|e_\gamma(k)\right|/e_\gamma(k), \left(20^\circ < \left|e_\gamma(k)\right| \leq 60^\circ\right) \end{cases}. \tag{9}$$

(2) When $e_\gamma(k)\Delta e_\gamma(k) > 0$ or $\Delta e_\gamma(k) = 0$, the output of the controller is as follows:

$$\begin{cases} U_\gamma(k) = U_\gamma(k-1) + 1.2K_p\Delta e_\gamma(k) + 1.5K_i e_\gamma(k), \left(\left|\Delta e_\gamma(k)\right| > 20\right) \\ U_\gamma(k) = U_\gamma(k-1) + 0.4K_p\Delta e_\gamma(k) + 0.5K_i e_\gamma(k), \left(\left|\Delta e_\gamma(k)\right| \leq 10\right) \end{cases}. \tag{10}$$

(3) When $e_\gamma(k)\Delta e_\gamma(k) < 0$, $\Delta e_\gamma(k)\Delta e_\gamma(k-1) > 0$ or $e_\gamma(k) = 0$, the output of the controller is as follows:

$$\begin{cases} U_\gamma(k) = U_\gamma(k-1) \\ U_\gamma(k) = 0 \end{cases}, \left(\left|e_\gamma(k)\right| < 60^\circ, \left|\Delta e_\gamma(k) > 2^\circ\right|\right). \tag{11}$$

(4) When $e_\gamma(k)\Delta e_\gamma(k) < 0$, $\Delta e_\gamma(k)\Delta e_\gamma(k-1) < 0$, the output of the controller is as follows:

$$\begin{cases} U(k) = U(k-1) + 2K_p\Delta e_\gamma(k), \left(\left|e_\gamma(k)\right| > 10^\circ\right) \\ U(k) = U(k-1) + 0.6K_p\Delta e_\gamma(k), \left(\left|e_\gamma(k)\right| \leq 10^\circ\right) \end{cases}. \tag{12}$$

(5) When $|e_\gamma(k)|<2^\circ$, the output of the controller is as follows:

$$U_\gamma(k) = U_\gamma(k-1) + 0.5K_p\Delta e_\gamma(k) + 0.01K_i e_\gamma(k). \tag{13}$$

3. Simulation Experiment of the Firefighting Robot Control System

3.1. System Software Simulation and Function Realization Requirements

3.1.1. Basic Parameter Setting. The basic parameters are as follows: *PID* parameter setting, position, and position *P*, *I*, *D* parameters need to be set separately. To adjust the positioning parameters, it is necessary to adjust the position and the individual implementation of the position.

3.1.2. Basic Control Functions. The basic control functions that must be installed on the host are as follows. Algorithm parameters and algorithm parameter settings should be sent to a lower order computer. The fire source should be identified and the robot controlled to determine the location of the fire source. The position of the robot should be adjusted. Bomb launch, robot control, bomb launch. Roll until you reach your destination and control the robot. End the command and control the robot to return.

3.1.3. Processing Function. It mainly includes sensor data processing and serial communication data processing.

3.1.4. Display and Save Function. It mainly includes monitoring image, sensor data, basic parameters, and display of common task execution.

3.1.5. Help Function. It mainly includes system description.

3.2. Ultrasonic Sensors. Distance sensors mainly include ultrasonic, laser, and infrared distance sensors. The working principle of the laser clearing instrument is that the laser diode first emits laser pulses to the target. The laser is reflected by the target and scattered in different directions and returned by some light sensors. After receiving light from the receiving sensor optical system, it acts on the avalanche photodiode. The built-in photoelectric sensor of avalanche photodiode can detect weak optical signals, record the time from laser pulse emission to receiving, and determine the distance to the destination. Laser distance sensor is usually used for long distance measurement, its resolution is very high, can reach 1 mm, but the price is relatively expensive.

The distance sensor has a pair of infrared light-emitting diodes and receiving diodes. Infrared light-emitting diodes are used to emit infrared light. After the infrared beam irradiates the object, the infrared beam is reflected by the infrared receiving diode and processed by CCD image. The sending time is different from the receiving time. The signal processor processes the data to obtain the distance of the target object. Infrared distance sensors can be used not only for natural surfaces but also for reflectors. It has the characteristics of long measuring distance and excellent RF performance. It is suitable for harsh industrial environment, but the precision is not high.

3.3. Module Design of the Robot Control System

3.3.1. Power Circuit. The power chip upc2933 t is a 3-terminal low pull-down voltage regulator with 1A output current and on-chip current protection functions. The diode D13 is used to protect the chip from high back voltage. 47 UF electrolytic capacitor is used to ensure the stability of output voltage.

3.3.2. Clock Circuit. The system uses 10 MHz external crystal oscillator as the clock source. Through the powerful

clock management module of f28m35, the clock source is divided and frequency doubled, which can provide 100 MHz and 150 MHz system clock to m3 and C28 cores, respectively.

3.3.3. Reset Circuit. In order to improve the reliability of the control circuit, an independent external watchdog reset circuit is used. The reset chip xc6121e which has the function of low voltage detector and monitor dog reset is selected. The chip consists of a reference voltage source, a delay circuit, a comparator, and an output driver.

3.3.4. Memory Circuit. In the process of operation, the system needs to save important data such as fault information and position information of robot manipulator, so an external storage circuit will be added. There are flash, EEPROM, fram (ferroelectric memory), and other nonvolatile memories. Among them, EEPROM (power on programmable read-only memory) is a special form of flash memory, which can use a higher voltage than usual to rewrite the internal program without disassembly. It is mostly used for interface card and storage hardware. Fram uses the strong dielectric effect of ferroelectric crystals to store data. The operation speed is fast and the power consumption of reading and writing is very low. The maximum number of writes is OK, but the maximum number of accesses is limited. The system selects the serial ferroelectric memory FM 25cl64b with SPI interface. The storage space is 64 kB and the maximum read-write speed is 20 MBps. The position and posture of the robot arm are displayed on the screen, which is convenient for the controller to control and adjust it according to the scene situation. As the central part of the control system, the lower computer not only receives the action commands from the upper computer to control the opening and closing of the motor driver and other components but also collects the analog signals from the sensor, and also controls the transmission of audio information back to the upper computer.

4. Operation Analysis of the Firefighting Robot

4.1. Simulation Analysis of Control System of the Firefighting Robot. Based on the principle of classical PID controller and expert PID controller, the attitude PID control system of high altitude rescue and firefighting robot is established, and then the expert PID control system of attitude is established, and the performance of the two is compared. The system adopts software PID control mode, the given value is the motor speed, and the relationship between the given value and the actual speed is measured by adjusting parameters.

The whole system is a negative feedback structure. Firstly, the PID controller obtains the angle difference between the given yaw angle and the actual yaw angle, and then converts it into the input voltage of the rotating motor with paddle through the algorithm calculation processing, so as to generate the rotation torque and make the robot reach the required attitude angle. Since the air drag coefficient will always change in the air, in order to make the simulation more accurate, we let selenium change randomly in the range of [0.1, *l*]. In Figure 2, the K_I change curve is shown.

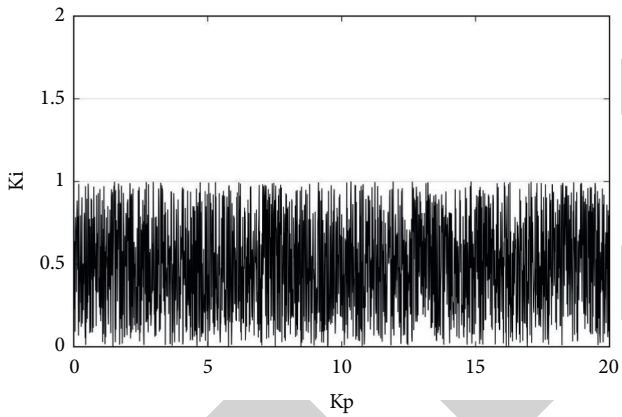

Figure 2: K_I variation curve.

According to Figure 2, the simulation of attitude PID controller can be divided into four situations:

When $V = 0$ m/s, $\Phi = 60^\circ$, $K_p = 20$, $K_i = 0.2$, $K_d = 9.8$ and target angle $\gamma = 2$, the output curve of yaw angle γ is obtained

When $V = 2$ m/s, $\Phi = 60^\circ$, $K_p = 20$, $K_i = 0.2$, $K_d = 9.8$ and target angle $\gamma = 2$, the output curve of yaw angle γ is obtained

When $V = 5$ m/s, $\Phi = 60^\circ$, $K_p = 20$, $K_i = 0.2$, $K_d = 9.8$ and target angle $\gamma = 2$, the output curve of yaw angle γ is obtained

When $V = 10$ m/s, $\Phi = 60^\circ$, $K_p = 20$, $K_i = 0.2$, $K_d = 9.8$ and target angle $\gamma = 2$, the output curve of yaw angle γ is obtained

In Figure 3, the yaw angle output curve of the attitude control system is shown.

It can be seen from Figure 3 that with the increase in wind speed, although the attitude angle of the robot can reach a certain steady value, the deviation from the given value also increases slowly, which indicates that with the increase in the external wind speed, the role of the proportion link should be gradually weakened.

Using the attitude expert PID control system, the convergence speed of the system is faster; the experiment shows that the steady-state value of the system output will deviate from the given value when the external environment changes in the attitude PID control system, and the attitude expert PID control system can still reach the given value when the external environment changes; the attitude expert PID control system has stronger expansibility in the actual test You can add your own test experience.

4.2. Rescue Analysis of Firefighting Robot under Wind Disturbance. Shown in Table 1 are the relevant parameters of position control experiment.

It can be seen from Table 1 that the angle between the direction of the external wind speed and the positive

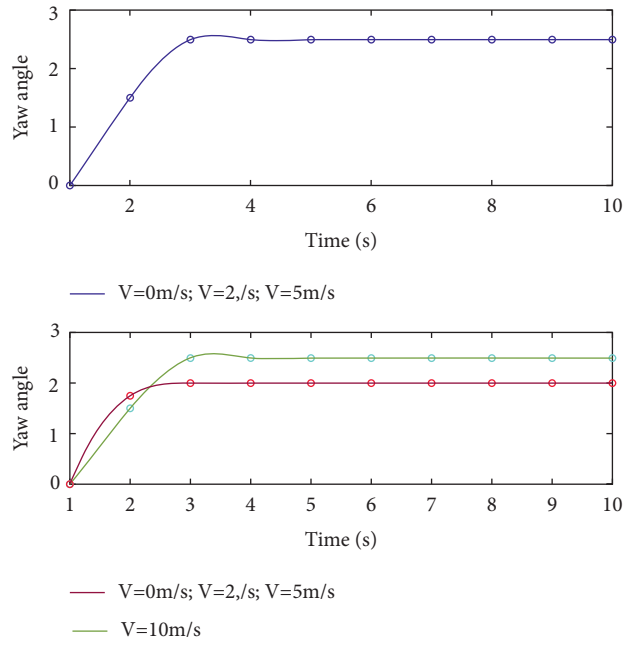

Figure 3: Yaw angle output curve of the attitude control system.

Table 1: Relative parameters of position control experiment under external wind disturbance.

Serial number	External wind speed V (m/s)	Adjustment time (s)	Error (mm)
1	−10	12.5	27
2	−5	10.7	24
3	−2	9.6	19
4	2	8.2	17
5	5	6.6	22
6	10	4.5	20

direction of the x-axis is an acute angle, then the external wind force will promote the position control of the machine, and the adjustment time will be reduced. On the contrary, if the angle between the direction of the external wind speed and the positive direction of the x-axis is acute, the external wind force will hinder the position control of the machine, and the adjustment time will increase, but the error is basically kept within 30mm. According to the working principle of the system, the translation error should not exceed the distance of a normal person, which is generally 500 mm. However, the error of the experimental results is within 30 mm. Therefore, the position control algorithm is effective.

4.3. Load State Analysis of Firefighting Robot. For the experimental platform of the firefighting robot control system, the experiment shows that under the condition of constant load stiffness and load quality, the BP neural network PID control curve based on the optimization algorithm is compared with the PID control curve, and the conclusions are as follows. Figure 4 is the experimental diagram of sine signal ($M1$).

It can be seen from Figure 4 that when $M = M1$, the rapidity is improved by 0.079 s, the time to reach stability is increased by 0.144s, the maximum overshoot is 1.0148%, and the steady-state error is 0.46%. The maximum lag time is 0.081 s, which meets the force control requirements of firefighting robot. The trend of experimental results is the same as that of simulation results;

When $M = M2$, the rapidity is improved by 0.076 s, the time to reach stability is increased by 0.109 s, the maximum overshoot is 0.9867%, and the steady-state error is −0.46%. The maximum lag time is 0.082 s, which meets the force control requirements of firefighting robot. The trend of experimental results is the same as that of simulation results;

When $M = M3$, the rapidity is improved by 0.077 s, the time to reach stability is increased by 0.07 s, and the steady-state error is 0.9306%. The maximum lag time is 0.081 s, which meets the force control requirements of the firefighting robot. The trend of experimental results is the same as that of simulation results.

4.4. Analysis of Simulated Disaster Relief Process of the Firefighting Robot. The robot end is composed of a robot control rod and other hardware components. With the help of these components, the operator inputs the action command into the upper computer and communicates between the upper and lower computers. The upper computer transmits the action command to the lower computer wirelessly. At the same time, the upper computer receives the real-time working status information from the lower computer. The camera installed on the robot will transmit the working scene to the console in time, and the position and posture of the robot arm will be displayed on the screen. It is convenient for the control personnel to control and adjust it according to the site conditions. As the central link of the control system, the lower computer not only receives the action command from the upper computer but also collects the analog signal from the sensor. In addition, it also controls the transmission of audio information to the upper computer.

Since the sensor obtains the distance d between the robot and the high-rise building, if the initial distance between the robot and the high-rise building is selected, then the translation distance of the robot is $x = do - d$; the premise of the position control experiment is that the posture has been kept constant, so we carry out the position control experiment after the attitude control experiment, and in the process of position control, the posture needs to be adjusted in real-time. The robot maintains attitude balance. Figure 5 is the control chart of firefighting robot.

In order to meet the needs of the fire scene, the robot needs to reach the fire scene in the shortest time, which requires accurate control of the climbing speed of the robot along the steel cable. In the last chapter, we have established the control model of the system and simulated it. In fact, the scientific computing function provided by Kingview is very limited, so it can be extended by Matlab. In this study, the fuzzy logic toolbox provided by Matlab is used to control the climbing speed. The fuzzy control system based on Matlab

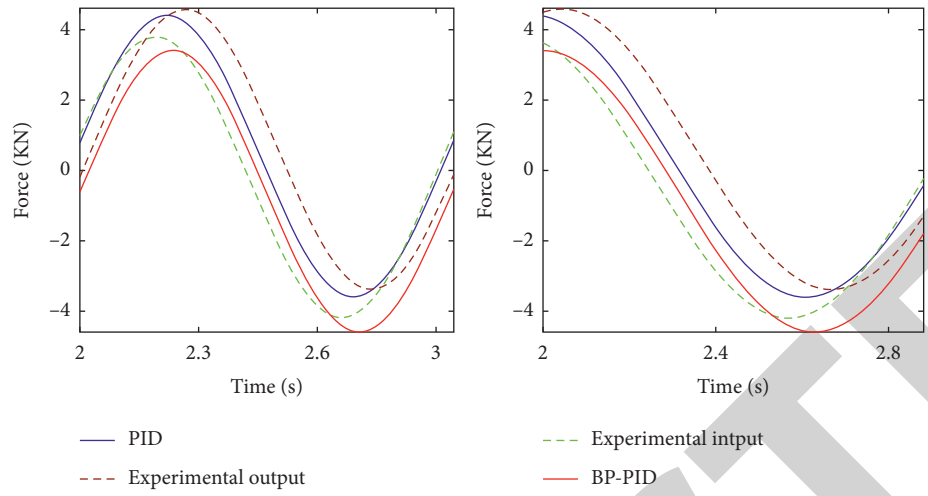

Figure 4: Experimental diagram of sine signal ($M1$).

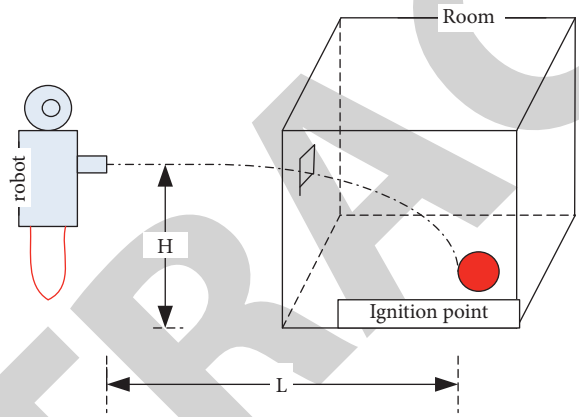

Figure 5: Firefighting robot control chart.

Table 2: Performance index of step signal.

Curve	Rise time (s)	Adjustment time (s)	Overshoot (%)	Steady-state error (%)
Experience group	0.065	3.286	7.909	1.1
PID	0.066	0.098	3.7988	0.35
BP-PID	0.054	0.08	2.5987	−0.25

Fuzzy Logic Toolbox replaces the original control algorithm query table programming, and can easily change the control rules and membership functions in the Matlab FIS editor.

4.5. Effect Analysis of PID Control Algorithm for Firefighting Robot. The classical PID control algorithm and expert PID control algorithm are used to control the position and attitude of the robot. According to the working principle of the aerial rescue and firefighting robot, the rotation speed difference of the rotary motor can realize the attitude control of the robot, and the position control of the robot depends on the thrust generated by the translation motor and the change in the robot's attitude. Therefore, the robot control system is divided into position control system and attitude control system, and the controller is designed, respectively. The robot position control system adopts PID control algorithm, and the attitude control system adopts expert PID control algorithm.

Through the simulation experiment, the performance index parameters of experimental curve, PID control curve, and BP neural network PID controller based on optimization algorithm are obtained. The performance index table of input signal is step function as shown in Table 2.

For the hydraulic position drive unit, the BP neural network PID control curve based on the optimization algorithm is compared with the PID control curve, the rapidity is improved by 0.009 s, the adjustment time is increased by 0.017 s, and the maximum overshoot and steady-state error

are also reduced. However, the maximum delay time is 0.006 s, which significantly improves the tracking performance of the system. The simulation results show that when the BP neural network PID controller based on the optimization algorithm is adopted, the hydraulic position driving unit experimental platform has the advantages of short rise time and adjustment time, small overshoot, small steady-state error, and good tracking performance. It meets the position control requirements of the fire robot. Compared with the simulation results, there is the same trend.

5. Conclusion

According to the working principle of the firefighting robot system, the software and hardware platform of the firefighting robot control system is developed and designed. The attitude control of the firefighting robot is realized. The robot posture controller is researched and designed, and the robot is controlled by simulation. The whole system will be designed and verified. The experimental platform of high rescue and firefighting robot is established, and the experimental program is developed. The experimental pose verification algorithm of high altitude rescue and firefighting robots is tested under the condition of increasing external wind interference. The experimental results show that the proposed algorithm has more advantages and better effect than other algorithms.

The firefighting robot uses neural network PID controller based on optimization algorithm. Under various load conditions, the increase time and adjustment time of the system are basically the same, the maximum overshoot is 0.59%, and the stability error is 0.19%. The experiment was carried out under the condition of load quality variation. The maximum overshoot is 10148%, and the stability error is 0.46%, which meets the performance requirements of the firefighting robot control system.

According to the advantages and limitations of the existing multirotor aircraft and mobile robot, the idea of small-scale four rotor land-air firefighting robot is innovatively proposed. This kind of land-air firefighting robot can perfectly overcome the shortcomings of multirotor aircraft unable to move in narrow space and mobile robot cannot cross large obstacles. When the ground air firefighting robot encounters the position that cannot be reached by land walking, it can start the flight mode to reach the target point, and then start the land walking mode for remote fire rescue. Although the prototype of the high-altitude firefighting robot has been trial produced, there are still many gaps between the prototype and its system from the actual fire scene, such as the presetting and fixing of the climbing steel cable, and the ground climbing support system. Although these are not the specific research content of this topic, they will play a crucial role in the real application, so this will also be the main content and direction of further research.

Data Availability

No data were used to support this study.

Conflicts of Interest

The author declares no conflicts of interest.

References

[1] W. Lee, Y. Lee, G. Park, S. Hong, and Y. Kang, "A whole-body rescue motion control with task-priority strategy for a rescue robot," *Autonomous Robots*, vol. 41, no. 1, pp. 243–258, 2017.

[2] S. Hong, G. Park, Y. Lee et al., "Development of a tele-operated rescue robot for a disaster response," *International Journal of Humanoid Robotics*, vol. 15, no. 04, p. 1850008, 2018.

[3] B. Madhevan, R. Sakkaravarthi, G. M. Singh, R. Diya, and D. K. Jha, "Modelling, simulation and mechatronics design of a wireless automatic fire fighting surveillance robot," *Defence Science Journal*, vol. 67, no. 5, p. 572, 2017.

[4] A. Kulkarni, P. Limbhore, and D. Londhe, *IoT BASED FIRE RESCUE ROBOT*, vol. 6, no. 3, pp. 25–27, 2017.

[5] N.'A. Yusof, S. S. M. Ishak, and R. Doheim, "An exploratory study of building information modelling maturity in the construction industry," *International Journal of BIM and Engineering Science*, vol. 1, no. 1, pp. 06–19, 2018.

[6] M. H. Hamma-adama, T. Kouider, and H. Salman, "Analysis of barriers and drivers for BIM adoption," *International Journal of BIM and Engineering Science*, vol. 3, no. 1, pp. 18–41, 2020.

[7] A. Athira, "Fire and rescue robot," *International Journal of Computer Application*, vol. 182, no. 45, pp. 18–21, 2019.

[8] X. Xue, X. Cao, X. Zhang, C. Wang, H. Ma, and H. Fan, "Electromagnetic wave attenuation mechanism and distribution strategy for coal mine rescue robot under the typical obstacle environment," *Radio Science*, vol. 55, no. 3, pp. 1–5, 2020.

[9] B. Zaarour, "BIM adoption around the world," *International Journal of BIM and Engineering Science*, vol. 4, no. 2, pp. 31–44, 2021.

[10] C. S. . Thaventhiran, "An efficient microcontroller based bore well rescue robot," *Indian Journal of Pure and Applied Mathematics*, vol. 119, no. 15, pp. 127–134, 2018.

[11] B. C. Min, E. T. Matson, and J. W. Jung, "Active antenna tracking system with directional antennas for enhancing wireless communication capabilities of a networked robotic system," *Journal of Field Robotics*, vol. 33, no. 3, pp. 391–406, 2016.

[12] S. Y. Choi, "Agent-based human-robot interaction simulation model for the analysis of operator performance in the supervisory control of UGVs," *International Journal of Precision Engineering and Manufacturing*, vol. 19, no. 5, pp. 685–693, 2018.

[13] R. A. Sowah, A. R. Ofoli, S. N. Krakani, and S. Y. Fiawoo, "Hardware design and web-based communication modules of a real-time multi-sensor fire detection and notification system using fuzzy logic," *IEEE Transactions on Industry Applications*, vol. 53, no. 1, pp. 559–566, 2017.

[14] M. Schwarz, T. Rodehutskors, D. Droeschel et al., "NimbRo rescue: solving disaster-response tasks with the mobile manipulation robot momaro," *Journal of Field Robotics*, vol. 34, no. 2, pp. 400–425, 2017.

[15] D. Sloggett, "Robot wars: future firefighting challenge arrives today," *Fire*, vol. 114, no. 1416, pp. 22-23, 2019.

[16] M. V. Shenoy and K. R. Anupama, "Dtta - distributed, time-division multiple access based task allocation framework for

Hindawi
Advances in Civil Engineering
Volume 2023, Article ID 9856915, 1 page
https://doi.org/10.1155/2023/9856915

Retraction

Retracted: Simulation of Migration Law of Organic Pollutants in Circulating Wells

Advances in Civil Engineering

Received 3 October 2023; Accepted 3 October 2023; Published 4 October 2023

This article has been retracted by Hindawi following an investigation undertaken by the publisher [1]. This investigation has uncovered evidence of one or more of the following indicators of systematic manipulation of the publication process:

(1) Discrepancies in scope
(2) Discrepancies in the description of the research reported
(3) Discrepancies between the availability of data and the research described
(4) Inappropriate citations
(5) Incoherent, meaningless and/or irrelevant content included in the article
(6) Peer-review manipulation

The presence of these indicators undermines our confidence in the integrity of the article's content and we cannot, therefore, vouch for its reliability. Please note that this notice is intended solely to alert readers that the content of this article is unreliable. We have not investigated whether authors were aware of or involved in the systematic manipulation of the publication process.

Wiley and Hindawi regrets that the usual quality checks did not identify these issues before publication and have since put additional measures in place to safeguard research integrity.

We wish to credit our own Research Integrity and Research Publishing teams and anonymous and named external researchers and research integrity experts for contributing to this investigation.

The corresponding author, as the representative of all authors, has been given the opportunity to register their agreement or disagreement to this retraction. We have kept a record of any response received.

References

[1] X. Li, J. Zhang, and Z. Yang, "Simulation of Migration Law of Organic Pollutants in Circulating Wells," *Advances in Civil Engineering*, vol. 2022, Article ID 7342604, 12 pages, 2022.

Hindawi
Advances in Civil Engineering
Volume 2022, Article ID 7342604, 12 pages
https://doi.org/10.1155/2022/7342604

Research Article

Simulation of Migration Law of Organic Pollutants in Circulating Wells

Xiaojie Li, Jianwei Zhang, and Zhuojing Yang

Center for Hydrogeology and Environmental Geology, China Geological Survey, Baoding 071051, Hebei, China

Correspondence should be addressed to Jianwei Zhang; chegs_jianwei@st.btbu.edu.cn

Received 6 May 2022; Revised 21 June 2022; Accepted 30 June 2022; Published 20 July 2022

Academic Editor: Ramadhansyah Putra Jaya

Groundwater resources are one of the most important freshwater resources for human beings. The protection of groundwater resources is an important measure for human survival. Therefore, it is extremely important to discuss the treatment of pollutants in groundwater. The purpose of this paper is to simulate and analyze the migration law of organic pollutants using the experimental circulating well. In the analysis, this paper uses the gas-liquid-solid three-state model to simulate the pollutants for organic pollutants. It independently analyzes pollutants in different states. For the movement law, this paper not only simulates the vertical transition circulation well in the laboratory but also simulates the transport law of pollutants in the well. The experimental results show that in the laboratory environment, the simulated value of the circulation well designed in this paper is not far from the actual value, and the accuracy rate is more than 90%. And according to the movement law of organic pollutants, it is found that the variable flow rate and the dispersion, porosity, and thickness of the skin have a great influence on the migration of pollutants.

1. Introduction

Groundwater is one of the most valuable natural resources supporting human health, economic development, and ecosystem diversification. In dry and semiarid areas with relatively few surface water sources, groundwater plays an irreplaceable role as an important source of water resources. However, in the process of industrialization and urbanization, with the depletion of groundwater and the deterioration of water quality, especially serious groundwater pollution, various pollutants attached to the surface infiltrate into groundwater from circulating wells. Pollutants in the groundwater seep in. The problem of organic pollution directly endangers the survival and safety of human beings.

In recent years, the organic pollution of groundwater has become a hot spot in groundwater scientific research, attracting the attention of scholars. The only way for contaminants to intrude into groundwater is through circulation wells, so organic contaminants in circulation wells are becoming more and more noticeable. Volatile organic pollutants are different from inorganic pollutants. They have high toxicity, fire resistance, and volatility. Their movement, metamorphism, and form are affected by their properties and the surrounding geological environment, and repair work is extremely difficult. The innovation of this paper is to simulate the mechanical energy of the organic pollutants' migration law in the circulating well and find out the organic pollutants' migration law. It plays an important role in the scientific simulation and prediction of groundwater pollution, effective governance and improvement of groundwater pollution status, and the maintenance of sustainable economic and social development and protection of the ecological environment.

2. Related Work

With the rapid development of economy, the increasing intensity of industrial and agricultural production and human activities, the problem of soil and groundwater pollution has become increasingly prominent. Organic

contamination of soil and groundwater is of great concern to researchers and governments. Liu et al. G found that the radical-based advanced oxidation process (AOP) has received increasing attention in water and wastewater treatment, and its radicals face the challenges of high operating costs and potential secondary pollution [1]. Liang et al. found that the detection of organic contaminants in water media is essential to ensure the quality and safety of water resources. Here, they described a sticky nanomat made of crystallizable fluorescent polymers for easy detection of toxic contaminants in water. Adhesive nanomats can rapidly detect organic contaminants within seconds [2]. Novikov analyzed long-term observational data (2003–2018) from 625 stations to determine the relationship between organochlorine pesticides and pollutants in the entire ocean and six selected regions. He used mathematical statistics and GIS analysis methods to process the data and presented the concentration distribution map of the inspected pollutants [3]. Shi et al. found that antibiotics have become the dominant organic pollutants in water resources, and efficient removal of antibiotics is the primary task of protecting the water environment. They synthesized various photocatalysts using a combination of hydrothermal synthesis and partial annealing. The results show that the removal rate is about 80% [4]. Lakshmi et al. found that the global population is increasing, and the world may experience severe freshwater shortages. Water treatment and recycling methods are the only options for obtaining fresh water for decades to come. Therefore, there is an urgent need to develop a suitable, inexpensive, and rapid wastewater treatment technology and reuse or conservation method in this century [5]. Scholars have discovered the shortage of water resources and the threat of organic pollutants to water resources, but they have not given specific and effective methods on how to remove organic matter.

For the study of groundwater resources, most scholars focus on the study of circulating wells. Zeng et al. found that groundwater has been increasingly used in open-loop soil-coupled heat pump systems as an alternative to realizing environmentally friendly geothermal systems for space heating and/or cooling [6]. Kurtul and Duran studied the application of circulating wells in water resource restoration [7]. Sulikowska et al. aimed to describe the temporal and spatial characteristics of extreme warm days (WDs) and warm periods (WSs) in summer and extremely cold days (CDs) and cold periods (CSs) in winter in Alaska from 1951 to 2015. They also determined the role of atmospheric circulation in its occurrence [8]. Morozov considered groundwater flow near vertical circulation wells. He presented a solution to the problem of steady-state and transient groundwater flow near vertical circulation wells in anisotropic aquifers, taking into account both skin and wellbore storage effects at pumping and injection intervals [9]. However, it can be found that many scholars have a wide range of research, focusing on the regulation of the overall environment of water resources, and there is still a lack of research on the establishment of pollutant transport models.

3. Calculation Based on the Migration Law of Organic Pollutants in Circulating Wells

3.1. Status and Harm of Organic Pollutants

3.1.1. Status of Organic Pollutants. With the continuous development of China's economy and society and the continuous improvement of urbanization level, the impact of human activities on groundwater resources has become more and more serious [10]. Compared with the "water quantity type" water shortage, the "water quality type" water shortage due to the pollution of groundwater or the poor quality of natural water resources is gradually becoming an important factor of water shortage. Organic chemical products will leak in the processes of refining, use, and storage, coupled with the random discharge of human beings, which makes the problem of organic pollution in soil and groundwater continue to aggravate. The main sources of groundwater organic pollution include the use of pesticides and fertilizers, oil spills, and seepage, and the random placement and discharge of organic wastes by factories and enterprises. Organic pollutants refer to pollutants composed of natural organic substances in the form of carbohydrates, proteins, amino acids, and fats and some other biodegradable synthetic organic substances [11]. Developed countries have attached great importance to the problem of organic pollution of groundwater and invested a lot of money in investigation and research. It has successively carried out investigations on organic pollution of drinking water, and developing countries are still in their infancy [12]. Water pollution caused by organic pollutants is shown in Figure 1.

As shown in Figure 1, after the end of the 20th century, scholars mainly investigated the polluted areas in the region. After the investigation of residual organic pollutants in the region, they gradually carried out risk assessment, remediation, research on treatment technology, and the transfer and conversion mechanism of organic pollutants. Through the sampling analysis of the Geological Survey, the results show that VOC can be detected almost in the water-bearing layer [13].

At present, the research on the migration and transformation mechanism of VOCs in China mainly focuses on the adsorption process and the degradation process, and the research on groundwater volatile organic pollutants is also gradually carried out. The research on organic pollution of groundwater is still in its infancy, and the research on the migration, transformation, and restoration mechanism of organic pollutants is still immature. It mainly studies its migration and transformation law in the geological environment, decontamination prevention and control technology, etc., and its application range is not large [14].

In recent years, due to the increasing influence of human activities and the rapid development of industry and agriculture, the role of petroleum organic pollutants on groundwater pollution has become more and more obvious. A large number of organic chemical products are directly or indirectly derived from the petrochemical industry. On the

Figure 1: Water pollution from organic pollutants.

one hand, petrochemical products provide convenience for human life, and on the other hand, they also bring many pollution problems. In the processes of oil refining, transportation, and use, phenomena such as foaming and liquid leakage will occur, and various organic pollutants with high toxicity will invade the environment and cause extremely serious pollution to soil and groundwater [15].

3.1.2. Harm of Organic Pollutants. Most of the organic pollution are more toxic or potentially toxic to the ecological environment and human health. Polluted soil and groundwater often contain a variety of pollutants, but their physical and chemical properties are different [16]. Organic pollutants can change the chemical composition of water bodies, increase the biological oxygen demand (BOD) and chemical oxygen demand (COD) of water bodies, and change the pH of water bodies [17]. The organic pollutants in the water body are further decomposed by anaerobic organisms and produce hydrogen sulfide, ammonia, mercaptan, and other products with pungent odor [18]. Since organic pollutants contain a variety of highly toxic substances, they are potentially harmful to humans [19]. The harm of organic pollutants to the human body is shown in Figure 2.

As shown in Figure 2, organic pollutants paralyze the human central nervous system, which may lead to cancer in some organs, weaken the function of the nervous system, and reduce their own immunity. Although the toxicity of perchloroethylene is less than that of trichloroethylene, its harm to humans cannot be ignored [20].

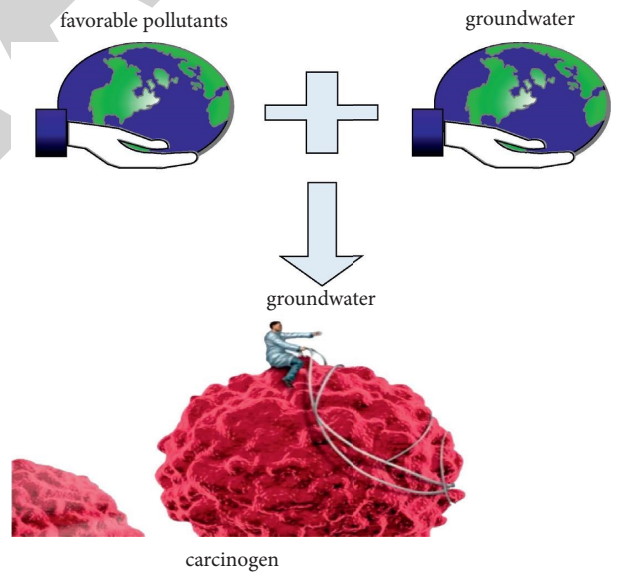

Figure 2: Harm of organic pollutants to human body.

3.2. Substance Exchange between Three Phases of Gas-Liquid-Solid. VOCs migrate in soil through leaching, volatilization, and diffusion and escape into water and atmosphere. It may be absorbed by the ecosystem and migrate out of the geological body, causing great harm to the air, surface water, groundwater, ecosystem, and human life. Therefore, it is extremely important to study the migration and transformation mechanism of volatile organic pollutants in circulating wells [21, 22].

The distribution of volatile organic pollutants in the gas-water-solid three phases includes the distribution of

pollutants between the water phase and the gas phase, the distribution between the water phase and the solid particles, and the accumulation at the interface between the water phase and the gas phase. In the unsaturated state, there is an equilibrium between the three phases of gas, liquid, and solid, mainly the water-gas two-phase distribution equilibrium combined with the water-solid two-phase distribution equilibrium [23]. Henry's law is one of the basic laws of physical chemistry. It can be expressed as follows: at a certain temperature and equilibrium state, the solubility of a gas in a liquid (expressed in mole fraction) is proportional to the equilibrium partial pressure of the gas. Henry's law can be used to express the material exchange balance between the water-gas phase as shown in the following formula:

$$C_a = HC_w. \tag{1}$$

In the formula, C_a is the pollutant concentration in the gas, C_w is the pollutant concentration in the water, and H is the Henry coefficient.

For the exchange of pollutants between the water phase and the solid phase, a linear formula is often used as follows:

$$q_s = K_d C_W, \tag{2}$$

where q_s is the concentration of pollutants on the surface of solid particles.

Soil particles are often of different sizes, different surface areas, and different organic matter contents. Linear formulas cannot realistically describe the material distribution between the water-solid phase. Freundlich equation is a chemical engineering term published in 1995. Therefore, the nonlinear adsorption isotherm formula, Freundlich formula, is used to describe the following formula:

$$q_s = K_F C_W^{1/n}. \tag{3}$$

In the formula, K_F is the distribution coefficient, and the diffusion of pollutants in the gas phase is not considered. Assuming that the gas phase is static, the pollutants migrate with water in the circulating well, which can be expressed by the following formula:

$$R_t \frac{\partial C_W}{\partial_t} = -v_a \frac{\partial C_W}{\partial_a} + D_W \frac{\partial^2 C_W}{\partial_a^2}. \tag{4}$$

In the formula, R_t is the hysteresis coefficient.

The retardation coefficient is the ratio of the velocity of groundwater seepage to the velocity of pollutant migration, and it is an important parameter to calculate and evaluate the migration behavior of pollutants in groundwater. The distribution and material exchange between the water-gas-solid three phases determine the migration of VOCs in the circulating well. When the interphase material exchange is in equilibrium, the retardation coefficient is used to represent the retardation of material exchange, as shown in the following formula:

$$R_t = 1 + \frac{\rho k_d}{\theta_w} + \frac{\theta_a H}{\theta_w}. \tag{5}$$

In the case of different water content and different pollutant transport mediums, the expression of the retardation coefficient is different, and the migration of volatile organic pollutants with the gas phase in the circulating well is as shown in the following formula:

$$R_t = 1 + \frac{\rho k_d}{\theta_w} + \frac{\theta_a H}{\theta_w}. \tag{6}$$

Recent studies have shown that, due to the accumulation of pollutants on the water-air interface, the experimentally measured coefficient values are larger than the predicted values obtained from formula (4). The retardation coefficient represents the retardation caused by the material exchange between water-gas and water-solid particles during the transport of pollutants. After comprehensive consideration, the delay coefficient of pollutants moving with gas is shown in the following formula:

$$R_t = 1 + \frac{\rho k_d}{\theta_a H} + \frac{\theta_W}{\theta_a H} + \frac{K_i A_i}{\theta_a}. \tag{7}$$

K_i is the adsorption coefficient (cm) of VOCs accumulated at the water-air interface, and A_i is the effective water-air interface area.

3.3. Water Infiltration Characteristics. Water infiltration is an important way for pollutants to penetrate the circulation well and enter the aquifer. Understanding the characteristics of water infiltration under the condition of sufficient water supply is extremely important for the study of solute transport in the unsaturated zone [24]. Infiltration is divided into two processes: non-water infiltration and water infiltration: the initial water supply intensity of infiltration is less than the infiltration capacity without water, which is the non-water infiltration stage. With the increase of infiltration amount, when the water supply intensity is equal to the infiltration capacity, it reaches the time of infiltration water accumulation, and the surface begins to accumulate water and enters the accumulation water infiltration stage under pressure conditions.

Some scholars have introduced unsaturated soil-water flow as shown in the following formula:

$$q = -K(\theta \nabla \psi), \tag{8}$$

where ψ is the soil-water potential and ∇ is the nabla operator.

3.3.1. Continuity Formula for Soil Water Movement (Conservation of Mass). Assuming that the soil water is incompressible, and the soil is isotropic, the initial conditions for the studied problem are as follows:

$$\begin{cases} \theta(z,0) = \theta_i(z) \\ h(z,0) = h_i(z). \end{cases} \tag{9}$$

In the case of evaporation intensity as a function of topsoil θ or h, the three types of boundary conditions are as follows:

$$D(\theta)\frac{\partial\theta}{\partial z} - K(\theta) = a\theta + b. \quad (10)$$

The basic formula for water transport in the one-dimensional unsaturated zone is as follows:

$$\frac{\partial\theta}{\partial t} = \frac{\partial}{\partial z}\left[D(\theta)\frac{\partial\theta}{\partial z}\right]. \quad (11)$$

In order to facilitate the application of the above basic formulas, in practical applications, appropriate formula forms are selected according to specific conditions to simplify complex problems.

3.4. Migration Model of Organic Pollutants in Water Circulation Wells. Groundwater Circulation Well (GCW) was called "well aeration and well treatment technology" in the early days. After that, some scholars added a treatment device to the well and developed a special filter for delaying clogging. Groundwater circulating well technology can also be combined with other technologies, such as bioremediation, surfactant technology, and oxidation technology. After it is repaired by GCW technology, the removal rate of trichloroethylene in the polluted groundwater is 90%. By the late 1990s, GCW technology was basically mature and had made great progress. The GCW technology is shown in Figure 3.

As shown in Figure 3, circulating well technology treats volatile organic pollutants in groundwater through groundwater circulation. It is connected with the inner well through the fixing device, and the inner and outer wells are sealed. The method utilizes an aeration pump to aerate the inner well, the gas forms a mixture with the groundwater in the inner well, and the density decreases and migrates upward. When it reaches the upper flower tube of the outer well, it flows back to the aquifer, and the gas carrying pollutants is discharged from the upper tail gas outlet through the gas-water separator. At the lower flower tube, there is a density difference inside and outside the well, and the groundwater outside the well continuously enters the well. Through continuous aeration, dissolved pollutants enter the inner well and are removed by aeration blow-off. The process of oxygen species transfer is shown in Figure 4.

As shown in Figure 4, the vertical circulation of groundwater may promote the disorder of the medium with water layer and promote the desorption of pollutants, and the transfer of oxygen species between the two phases of gas-water will increase the dissolved oxygen content in the groundwater. It has the potential to enhance biodegradation in situ. When the permeability of the aquifer is good, more water can be recharged into the aquifer, and the restoration effect is significantly improved.

The influence area around a single GCW is predicted by establishing a numerical model, and its governing formula is as follows:

$$\frac{\partial}{\partial r}\left(2\pi rK\frac{\partial h}{\partial r}\right) + \frac{\partial}{\partial z}\left(2\pi rK\frac{\partial h}{\partial z}\right) = 0. \quad (12)$$

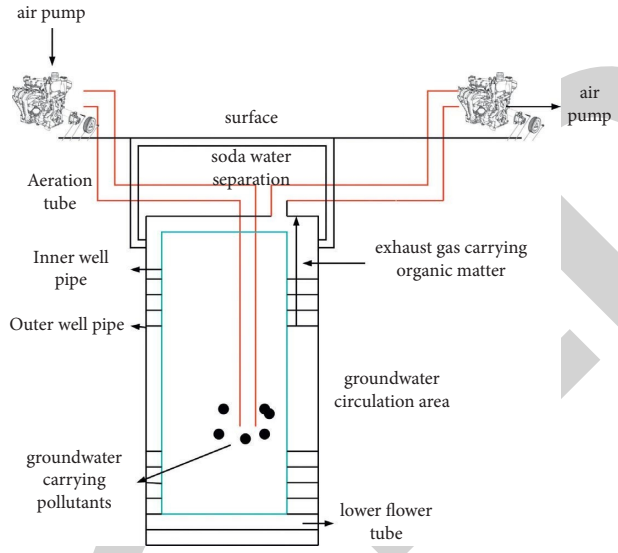

Figure 3: GCW technology.

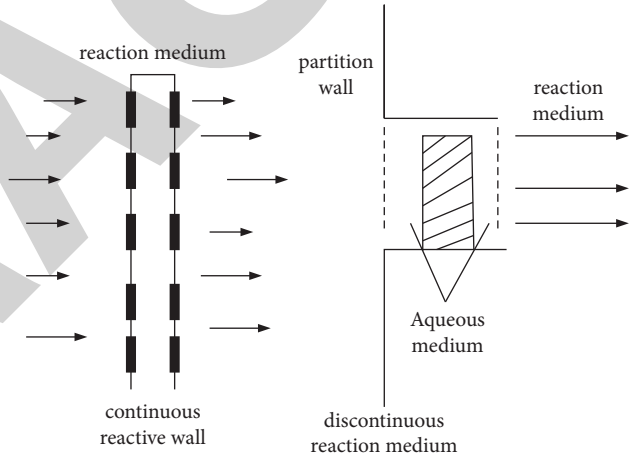

Figure 4: The process of oxygen species transfer.

r represents the influence radius in the horizontal direction; h represents the head of the piezometer; ∂h and ∂z represent the radial and vertical permeability coefficients.

The simulation conditions of the two-dimensional model of the groundwater circulation well are uniform and isotropic steady flow, the thickness of the aquifer and the Darcy velocity are constants, and the basic theoretical formula is the Laplace formula. The capture band width is as follows:

$$\mathrm{CZW} = \frac{Q}{UB}\left(\frac{N}{2} - I_r\right). \quad (13)$$

In the formula, Q is the total flow; B is the thickness of the aquifer; U is the Darcy velocity; N is the number of circulating wells; IT is the total exchange flow of the system. The processing efficiency is as follows:

$$\eta = \frac{\eta_{SP}}{1 - I_{avg}(1 - \eta_{SP})}. \quad (14)$$

In the formula, η_{SP} represents the single-channel pollutant removal rate; I_{avg} represents the average flow exchange.

The three-dimensional model simulation conditions of the circulating well are uniform, anisotropic, and steady flow with zero horizontal groundwater velocity. The theoretical formula is Lagrange's law and Darcy's law. Darcy's law clarifies the equation of steady-state flow energy loss in porous media such as soil, which is the basic law for studying the movement of saturated soil moisture. The flow at any point s is as follows:

$$s(a,b,z) = -J[a\cos(\theta) + b\sin(\theta)]. \tag{15}$$

In the formula, J represents the hydraulic gradient; θ represents the number of the well pipe; b represents the thickness of the aquifer.

The applicability of groundwater circulation well technology is as follows: in contrast to actual on-site treatment technologies (enhanced biomedical technology, etc.), no toxic or partially refractory intermediate compounds are introduced into the aquifer. Under the influence of the water cycle, dissolved oxygen is intensified. The content of groundwater increases, and the decomposition of aerobic microorganisms in that case is enhanced. It does not generate lateral water pressure or cause the spread of pollutants, and the organic removal efficiency of high pollutant concentrations can reach up to 98%.

3.5. Migration Law Based on Multiphase Flow Calculation Principle. Organic pollutants are mainly molecules composed of two elements C and H combined with other elements (N, 0, S). An important feature of organic pollutants is the functional group with basic physical and chemical properties reflected in its molecular structure. Different types of organic pollutants have different functional groups, which determine the basic physicochemical properties of these substances.

Organic pollutants can enter the soil in various ways and infiltrate into the aquifer under the action of gravity and capillary force. After entering the aquifer, organic pollutants usually exist in the form of nonaqueous phase liquids (NAPLs) because of their low solubility, liquids that do not mix with the water in the circulation well and below the water surface. Such liquids are often referred to as nonaqueous liquids. The transformation of NAPLs is shown in Figure 5.

As shown in Figure 5, the existence forms of NAPLs in underground aquifers mainly include free state, dissolved state, gaseous state, and residual state. There is mutual conversion between the four forms, and the residual saturation is closely related to the properties of the medium. It is often the most difficult part of the subsurface medium to repair and remove.

There are many forms of organic pollutants after entering groundwater, among which NAPL phase is the main form of existence in groundwater. Organic pollutants also undergo corresponding transformations between different

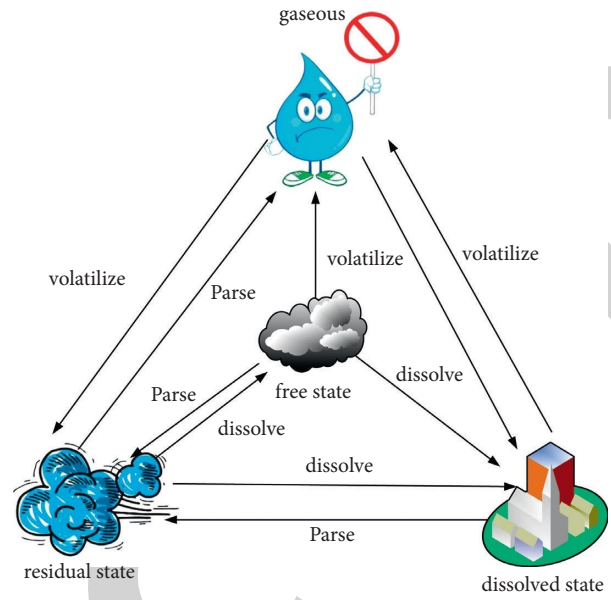

Figure 5: Transformation of NAPLs.

phases. It includes evapotranspiration, dissolution, and adsorption, so that dynamic equilibrium reactions occur among the four states of gaseous state, free state, dissolved state, and residual state. These processes contain many complex influencing factors. Among them, the physical and chemical properties of NAPLs, the heterogeneity of the medium, and the hydraulic conditions of the fluid are all important factors that affect the migration and transformation of NAPLs between phases.

The multiphase flow system in TMVOC software includes three parts: water phase, NAPL phase, and incompressible gas. The software can simulate any combination of single phase, two phases, or three phases among the three components. Due to the differences in the saturation and thermodynamic conditions of the three parts, the migration and distribution process will be accompanied by the mutual transformation between the phases. The expression of its mass and energy conservation formula in TMVOC software is as follows:

$$\frac{d}{d_t}\int_{v_n} M^K dV_n = \int_{r_n} F^K \bullet n d\tau_n + \int_{r_n} q^K dV_n. \tag{16}$$

Among them, V_n represents the unit volume, and τ_n is the area through which the fluid passes.

The total mass of the water and gas phases in a unit volume can be expressed as follows:

$$M^K = \varphi \sum_{\beta} S_\beta \rho_\beta A_\beta^K. \tag{17}$$

Among them, φ is the porosity of the porous medium, and S_β is the saturation of the β phase. The total mass of the NAPL phase per unit volume can be expressed as follows:

$$M^K = \varphi \sum_{\beta} S_\beta \rho_\beta A_\beta^K + M_{ads}^K. \tag{18}$$

Among them, S_β in the above formula is the saturation of the β phase, and M_{ads}^K is the instantaneous reverse adsorption of the K group by the soil medium.

For the numerical simulation of multiphase flow, relative permeability model and capillary pressure model are important factors to determine its migration and distribution in soil-groundwater system. In this paper, the three-phase flow permeability, Stone model, and capillary pressure Parker model are used.

The expression for the relative permeability model is as follows:

$$k_{rg} = \frac{S_g - S_{gr}}{1 - S_{wr}}. \tag{19}$$

Among them, S_g and S_{gr} are the relative permeability of water phase, gas phase, and NAPL phase, respectively. The expression for the capillary pressure model is as follows:

$$S_{wr} = \frac{S_w - S_m}{1 - S_m}. \tag{20}$$

Among them, S_m is the residual saturation of the liquid phase, and S_w is the capillary pressure between the NAPL phase and the gas phase.

The migration behavior of multiphase flow in the underground environment obeys Darcy's law and forms a multiphase flow system under the action of gravity and capillary pressure. In the process of multiphase flow, the components will transform into each other and diffuse in various forms. The diffusion behavior of multiphase flow refers to the distribution method under the condition of variable phase saturation, and the diffusion and transport are carried out in a fully coupled manner.

In this paper, by analyzing the time-space variation of pollutants, the adsorption-desorption mechanism of pollutants was found out. It is combined with the seepage column experiment to simulate the migration law of pollutants with different pollution pathways. In this paper, a groundwater solute migration model is established to predict the migration trend of pollutants. After entering the geological medium, volatile organic pollutants mainly include migration and transformation processes such as convective dispersion, adsorption-desorption, degradation, and volatilization. The main factors affecting its migration are VOCs own characteristics, hydrogeological conditions, geological engineering geological conditions, groundwater, etc.

4. Simulation of Hydrodynamic Field of Circulating Well

4.1. Hydrodynamic Field Model of Vertical Circulation Well. In the confined aquifer, a vertical well with a radius of r_w includes an upper and lower pumping section and a water injection section, and the two sections are sealed with plugs at the same time to form a closed cavity. The upper pumping section maintains the pumping volume of $-Q$ flow rate, the lower water injection section maintains the water injection volume of $+Q$ flow rate, and a pressure difference is formed in the cavity, thereby forming a circulation field from bottom to top. The mathematical model of vertical circulation well established in this paper is established based on the following assumptions:

(1) The vertical circulation well device is installed in the confined aquifer

(2) The aquifer is laterally unbounded

(3) The thin-wall effect of vertical circulation wells is not considered

(4) Under natural conditions, groundwater in the aquifer does not flow, that is, there is no background flow of groundwater

This paper uses the ModelMuse software developed by the United States Geological Survey (USGS) to simulate a groundwater numerical model. ModelMuse is a software for simulating groundwater flow based on GoPhast. The software includes MODFLOW-2005, MODPATH, ZONEBUDGET, and other parts, and ModelViewer is a bundled software for postprocessing of the software. It enables graphic output and analysis of postsimulation results. The operating object is a three-dimensional model, and the operability for meshing and boundary condition setting of the model is flexible. The formula can be used to specify the spatial data value of the global and individual objects. And the specified value has nothing to do with the spatial and temporal discretization of the model, and the user can redefine it. The setting for the aquifer can be restricted, unrestricted, or a combination of restricted and unrestricted, which can well satisfy the user's operation setting for the model.

In this paper, combined with the scale of the laboratory experiment and the characteristics of the selected research unit, a numerical model of the laboratory experiment of the indoor vertical circulation well is established. It takes the bottom as the 0 reference plane, the model length is 1.02 m, the width is 0.06 m, and the height is 0.9 m. The main boundary conditions involved in the model are the injection and pumping sections in the vertical circulation well. They are given flow boundaries, which are generalized by the Flow and Head Boundary package (FHB) module in ModelMuse. Both sides of the model are defined as fixed head boundaries. Using the Time-Variant Specified-Head package (CHD) module in ModelMuse to generalize, the initial head height of the model is defined as 94 cm. On the plane, the circulation well is arranged at the center, and the model is divided into 6 rows, 61 columns, and 18 layers. The grid size of the model gradually transitions from the outer periphery of the well axis, from cell1: $0.005\,\text{m} \times 0.005\,\text{m}$ to cell2: $0.03\,\text{m} \times 0.03\,\text{m}$, and then to cell3: $0.035\,\text{m} \times 0.035\,\text{m}$, and the subdivision is divided into three levels. The parameter settings of the reference model for laboratory experiments are shown in Table 1.

4.2. Model Numerical Verification. In order to determine the accuracy of the numerical model, it needs to be verified and compared with the analytical solution under the same parameters. It provides the numerical simulation results of the

Table 1: Value list of model parameters.

Parameter	Value	unit
Well radius r_w	0.05	m
Thickness of aquifer D	0.94	m
Radius of influence r'	0.5	m
Extract that distance d between the upper and lower bottom of the section and the surface of the aquifer d, d_e	0.19, 0.29	m
The distance l between the upper and lower bottoms of the injection section and the aquifer surface, l, l_e	0.64, 0.74	m
Distance between center points of extraction section and injection section ∇L	0.45	m
Q flow	0.1	m^3/h
Horizontal and vertical hydraulic conductivity K_r, K_z	3×10^{-3}	m/s
Anisotropy ratio K_r/K_z	1	

water head of the reference model at a depth of $z = 0.575$ m and 0.675 m at different horizontal distances. It is compared with the analytical solution of the head value calculated by the formula under the same conditions. Under the numerical model, some parameters are determined, and the accuracy of the model is analyzed by software. The results are shown in Figure 6.

Uncertainty analysis of the magnitude of the numerical simulation flow should be made, keeping all parameters of the numerical model the same as those of the experimental model. It only changes the flow rate and finally selects numerical simulation parameters that are close to the actual flow rate. A scatter plot of the simulated water head height and the experimental water head height is drawn, respectively, to observe the correlation between the two, as shown in Figure 7.

4.3. Hydrodynamic Field Results. In the establishment of the numerical model under the indoor scale, the flow parameter is set as the actual flow rate, and the water head monitoring points are set up in the model, and the number of the monitoring points is larger than the number of the water head monitoring points in the experimental model tank. It also includes the location of the experimental water head monitoring point, which is calculated by numerical simulation. It obtains the water head height in each monitoring point, and the monitoring results are shown in Figure 8. The variation law of the water head at different depths is the same, and the fitting effect of the head reduction at $z = 0.8$ and $z = 0.7$ is better. As the depth from the aquifer surface increases, the experimental water head height value is lower than the numerical simulation water head height value.

The vertical circulation well device forms an elliptical groundwater circulation field with the pumping section as the central axis during operation. In order to quantitatively calculate the groundwater circulation velocity of the circulation wells in the area, this paper takes the position of the straight line where the center points of the monitoring holes A4~F4 of the model tank are located as the x-axis. The position of the straight line where the central axis of the vertical circulation well is located is the y-axis, which establishes a Cartesian coordinate system. The water head monitoring holes of the entire model tank are divided into four areas according to the location of the pumping section, and at the same time, in each area, three points are selected to mark the monitoring points of the known water level. It calculates the average groundwater flow velocity in each area of the hydrodynamic field separately. The head heights of the selected monitoring points in the divided areas are shown in Table 2.

The groundwater flow velocity at the center point of each triangle is obtained, as shown in Table 3.

From Table 3, it can be concluded that the average groundwater flow rates in areas 1, 3, 2, and 4 are approximately the same. It is left-right symmetrical with the position of the central axis of the drawing section as the symmetrical axis. $V_y > V_x$ in areas 1 and 3, $V_x > V_y$ in areas 2 and 4, and the average velocity of groundwater in areas 1 and 3 is greater than that in areas 2 and 4, a difference of about 3 times. This paper analyzes the causes of $V_y > V_x$ in areas 1 and 3, and the vertical circulation well device forms reverse flow during operation. It circulates back from the bottom injection section to the position where the upper extraction section is located, and there is a partial head loss.

5. Simulation of Migration Law of Organic Pollutants in Circulating Wells

According to the derivation and calculation of the above model, this section mainly discusses the influence of variable flow rate and the dispersion, porosity, and thickness of the skin region on the contamination of the tandem layer based on the semianalytical model. For the following research analyses, the default model parameters are shown in Table 4.

5.1. Influence of Variable Flow on Pollutant Transport. In this section, $k1 = 1$ and $k2 = 1$ are set in the semianalytical model calculation, which means that the influence of variable flow on the transport of pollutants under the action of the skin is not considered. Figure 9(a) shows the penetration curves of pollutants at $r = 2$ m when λ takes different values, and the MO solution (steady flow) is also included in the figure for comparative analysis. It can be seen from the figure that the larger the attenuation index λ of the flow, the smaller the concentration of the pollutant breakthrough curve. It shows that the larger the decay index is, the slower the pollutants move. This is mainly due to the fact that the larger the flow decay index, the faster the flow decay, resulting in a faster decrease in the radial groundwater velocity. In addition, by comparing the breakthrough curve of variable flow rate with the solution of steady flow of MO, it can be found that the concentration of breakthrough curve under the condition of variable flow rate is lower than that of steady flow. It shows

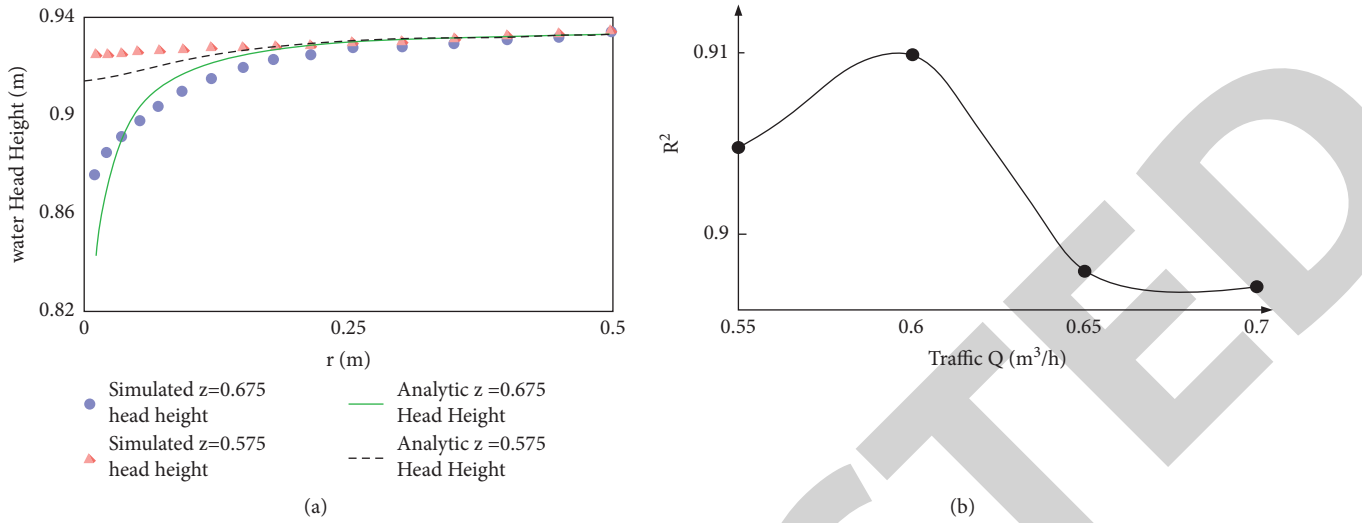

Figure 6: Numerical verification analysis of the model. (a) Comparison of the simulated and analytical solutions of the water head values at different depths of the reference model. (b) Flow rate Q vs. R graph.

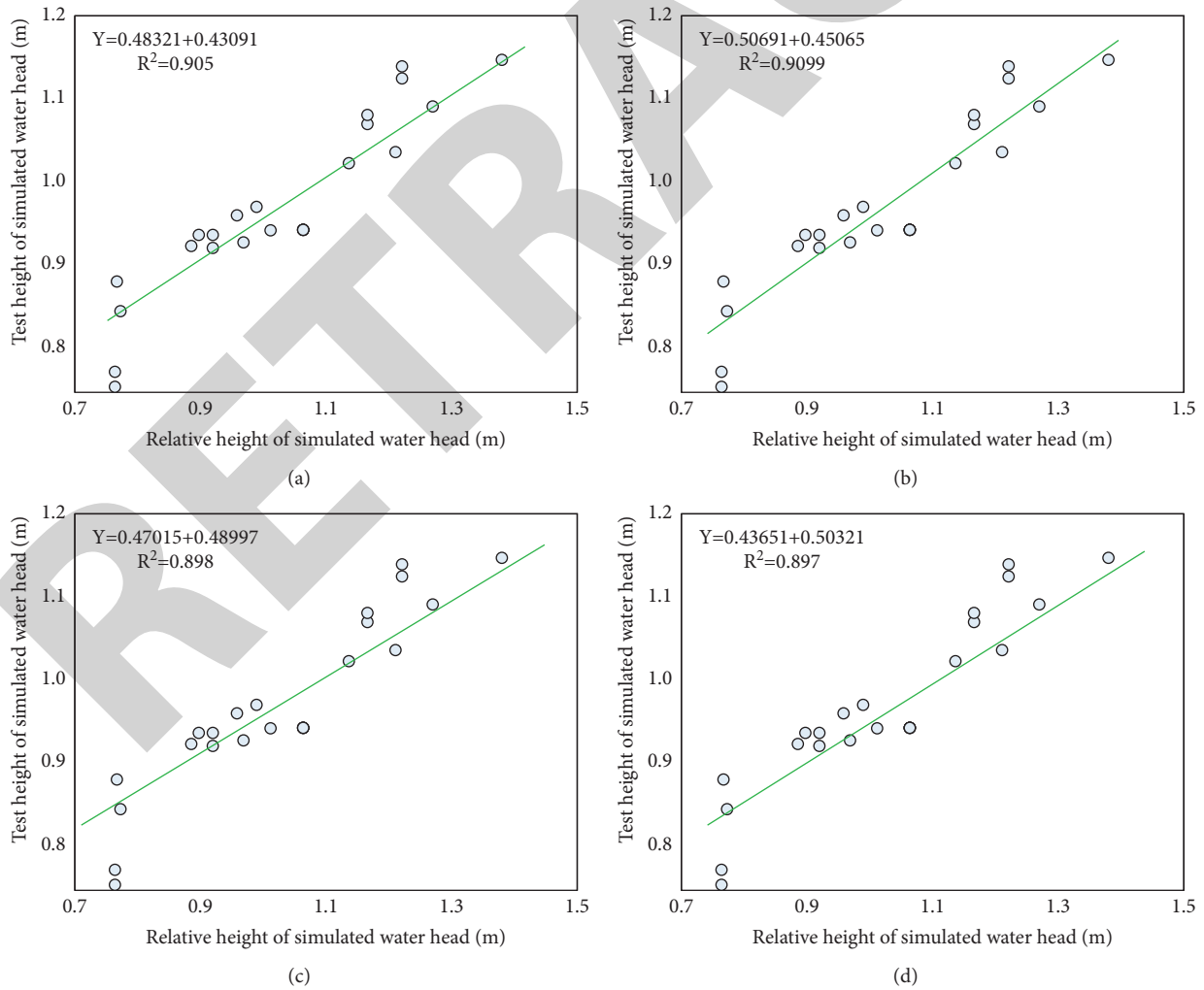

Figure 7: Scatter plot of R^2 analysis with different flow sizes. (a) $Q = 0.55\ m^3/h$. (b) $Q = 0.6\ m^3/h$. (c) $Q = 0.65\ m^3/h$. (d) $Q = 0.7\ m^3/h$.

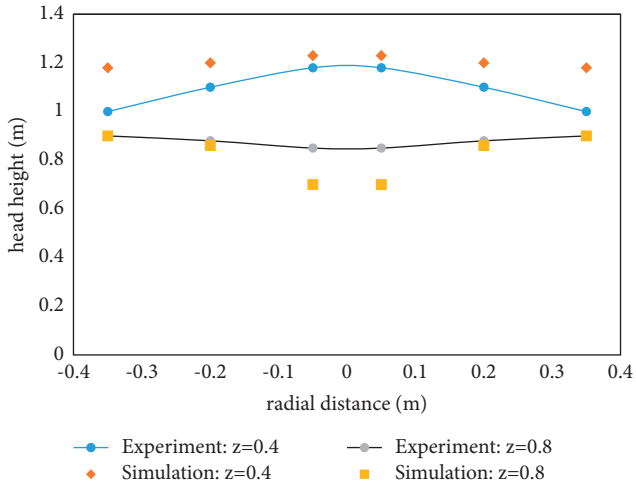

Figure 8: Fitting diagram of experimental head value and numerical simulation head value.

Table 2: Head height values of water head monitoring points in different areas.

Zone	Water head height monitoring point	Height of water head (cm)
1	H1	84.33
	H2	76.9
	H3	96.5
2	H4	113.97
	H5	115.17
	H6	102.7
3	H7	84.63
	H8	74.67
	H9	95.77
4	H10	112.73
	H11	115.17
	H12	102.27

Table 3: Water velocity at the center point.

Central point	V_x (m/h)	V_y (m/h)	V (m/h)
1	1.78	2.54	3.10
2	1.14	0.18	1.15
3	2.13	3.02	3.69
4	1.06	0.37	1.12

that variable flow has a greater impact on the radial transport of pollutants; especially for cascade pollution, the attenuation of flow will lead to a smaller range of pollutant transport. This has played a positive role in protecting groundwater resources.

Figure 9(b) shows the penetration curves of pollutants at $r = 2$ m when $Q2$ takes different values. It can be seen from the figure that the smaller the final stable flow rate $Q2$ is, the smaller the concentration of the breakthrough curve of pollutants is, indicating that the smaller the $Q2$ is, the slower the pollutants migrate. This is mainly because the smaller the final steady flow, the greater the attenuation of the radial groundwater velocity, so the speed of pollutant transport is

Table 4: Parameter values in the model.

Parameter	Value
Aquifer thickness (m)	10
Well radius (m)	0.1
Epidermal area radius (m)	1
The porosity of the movable zone of the aquifer	0.3
Porosity in the movable zone of the epidermis	0.3
Radial dispersion of aquifer (m)	0.5
Radial dispersion of epidermis (m)	0.5

smaller. For example, the permeability of the epidermal region near the well tube is reduced due to microbial clogging. The final steady flow rate of the tandem is also reduced, especially when the dissolved oxygen content is higher, the less permeable the skin area near the well tubing, the smaller the final tandem flow rate. Therefore, reducing the final interlayer flow is also of positive significance for the protection of groundwater resources.

Among them, A is the influence of different flow attenuation exponents on the penetration curve under the condition of variable flow; B is the influence of the final steady flow on the penetration curve.

5.2. Influence of Skin Dispersity and Porosity on Radial Pollutant Transport. This section analyzes the influence of skin effect on radial pollutant transport under variable flow rate conditions. Figure 10(a) shows the penetration curves of pollutants at $r = 2$ m when $k1$ takes different values. The dimensionless parameters $k1$ are 0.2, 1, and 5, respectively, and $k2 = 1$. Here, if $k1 < 1$ means $\alpha1 < \alpha2$, and the smaller the $k1$ is, the smaller the dispersion of the epidermis is. If $k1 = 1$ and $k2 = 1$, it represents the case of no epidermis. Other parameters in the model are $Q1 = 30\ m^3/d$, $Q2 = 15\ m^3/d$, $\lambda = 0.5/d$. Comparing the penetration curves in the three cases, the value of the solution of this model is smaller than that of the MO solution in the middle and late stages, which is mainly caused by the decrease of the flow rate. At the same time, it is also found that, with the increase of the dispersion of the epidermal region, the concentration of the penetration curve also increases. It shows that the dispersity in the epidermis area has a great influence on the radial pollutant migration, and if the dispersity is greater than that of the aquifer, it will promote the contamination of the tandem layer. However, it has an inhibitory effect on the case where the dispersion is less than that of the aquifer.

Figure 10(b)shows the pollutant penetration curves (BTCs) at $r = 2$m when $k2$ takes different values. In addition, the figure also considers the other two cases as a comparison, which is the solution of MO steady flow without skin. The dimensionless parameters $k2$ are 3/5, 1, and 3, respectively, and $k1 = 1$. Here, if $k2 < k1$ means $\theta1 > \theta2$, the smaller the $k2$, the greater the porosity of the epidermis. Other parameters in the model are $Q1 = 30/d$, $Q2 = 15/d$, $\lambda = 0.5/d$. It can be seen from Figure 10 that the value of the solution of this model in the middle and late stages is smaller than that of the MO solution, which is mainly caused by the decrease in flow. It shows that the

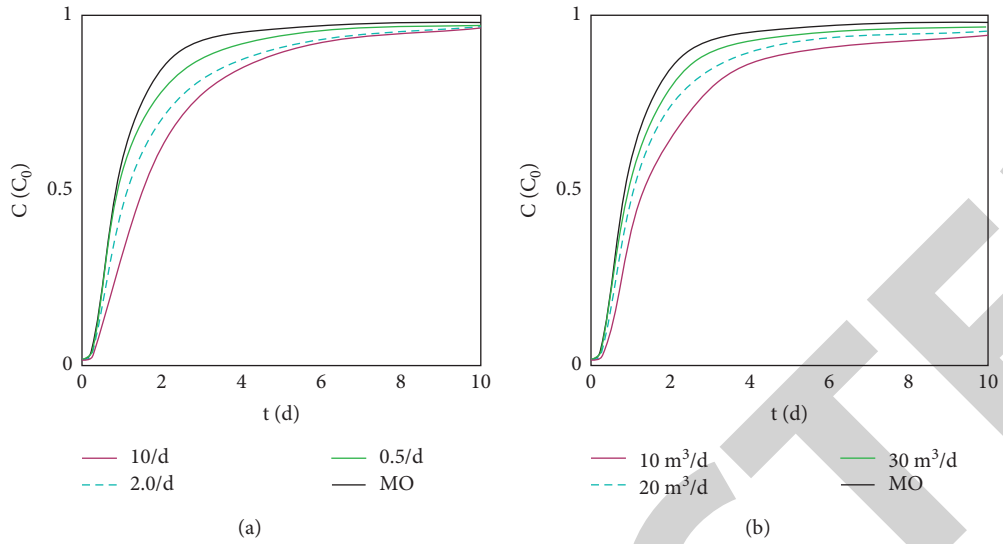

Figure 9: Effect of variable flow rate on pollutant transport.

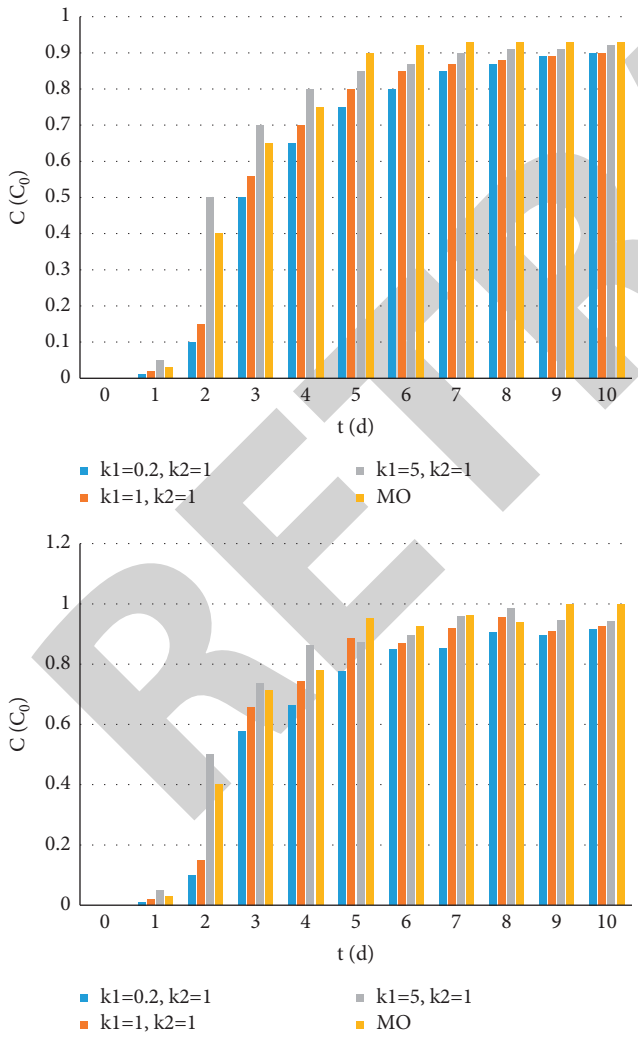

Figure 10: Effects of skin dispersity and porosity on radial pollutant transport. (a) A Effect of different dispersions on penetration curves under variable flow conditions. (b) The effect of different porosity on the penetration curve of radial pollutants under the condition of variable flow.

decrease of flow rate has a great influence on radial pollutant transport. In addition, as $k2$ increases, the value of the penetration curve also increases gradually. This indicates that changes in the porosity of the skin region can affect the penetration curve of pollutants. This is because the larger the $k2$ is, the smaller the porosity of the skin area is, and the larger the groundwater flow rate is. This in turn results in faster contaminant transport and causes and increases breakthrough curve concentration values.

5.3. Influence of Skin Thickness on Radial Pollutant Transport. The previous two sections have analyzed the variation of the contaminant concentration distribution curve and the penetration curve caused by the variable flow rate as well as the dispersion and porosity of the skin region. This section mainly analyzes the influence of the thickness of the skin on the transport of pollutants under the condition of variable flow. Contaminant breakthrough curves (BTCs) at a distance of $r = 2$ m from the water injection well when r1 takes different values. Dimensionless parameters $k1 = 0.2$, 1, 5, $k2 = 3/5$, 1, 3, other parameters are $r1 = 0.5$ m, 1 m, $Q1 = 30/$ d, $Q2 = 15$/d, $\lambda = 0.5$/d. When $k1 = 5$ and $k2 = 3$, as $r1$ increases, the concentration of pollutants in the penetration curve increases. However, when $k1 = 0.2$ and $k2 = 3/5$, as $r1$ increases, the concentration of solute becomes smaller. The experimental results show that different thicknesses also have a certain influence on the transport of pollutants.

6. Conclusion

In this paper, a theoretical model of radial cascading pollution considering the skin effect is established under the condition of variable flow rate. The semianalytical solution of the model is obtained by Laplace transform and Stehfest numerical reversal method. This paper can effectively control the repair scope and repair effect of the vertical circulation well by studying the influencing factors of the hydrodynamic field of the vertical circulation well, which provides a basic reference

Hindawi
Advances in Civil Engineering
Volume 2022, Article ID 7196446, 13 pages
https://doi.org/10.1155/2022/7196446

Research Article

Durability Studies on Fly Ash Based Geopolymer Concrete Incorporated with Slag and Alkali Solutions

S. Nagajothi,[1] S. Elavenil,[1] S. Angalaeswari,[2] L. Natrayan,[3] and Wubishet Degife Mammo[4]

[1]*School of Civil Engineering, Vellore Institute Technology, Chennai, Tamil Nadu, India*
[2]*School of Electrical Engineering, Vellore Institute Technology, Chennai, Tamil Nadu, India*
[3]*Department of Mechanical Engineering, Saveetha School of Engineering-SIMATS, Chennai, Tamil Nadu, India*
[4]*Mechanical Engineering Department, Wollo University, Kombolcha Institute of Technology, Kombolcha, South Wollo 208, Amhara, Ethiopia*

Correspondence should be addressed to S. Elavenil; elavenil.s@vit.ac.in, S. Angalaeswari; angalaeswari.s@vit.ac.in, L. Natrayan; natrayanphd@gmail.com, and Wubishet Degife Mammo; wubishetdegife7@gmail.com

Received 20 February 2022; Revised 15 May 2022; Accepted 27 June 2022; Published 11 July 2022

Academic Editor: Ramadhansyah Putra Jaya

This study explores the durability of green cementitious material of geopolymer concrete. Geopolymer concrete is produced from the polycondensation reaction of aluminosilicate materials (fly ash, Ground Granulated Blast furnace Slag (GGBS)) with alkaline activator solutions. Geopolymer concrete has excellent mechanical properties and its production requires low energy and results in low levels of CO_2 emission. Due to the high demand for river sand, manufactured sand is used as a replacement material in geopolymer concrete under ambient curing conditions. In this study, the durability of G30 grade geopolymer concrete has been investigated using tests acid resistance, water absorption, sulphate resistance, Rapid Chloride Penetration Test (RCPT), and rate of absorption (Sorptivity) test. The sulphuric acid, sodium sulphate, and water absorption tests were carried out at 28 days, 56 days, and 90 days for both the geopolymer and the conventional concrete. The reduction percentage in water absorption and compressive strength loss was found to be better in geopolymer concrete than in conventional concrete. Geopolymer concrete's chloride penetrability and rate of absorption were analogous to conventional concrete. Regression analysis for geopolymer and conventional concretes in the rate of absorption test showed a good relationship between absorption and the square root of time.

1. Introduction

In the cement industry, the production of the clinker by heating calcium carbonate ($CaCO_3$) in a rotary kiln requires a lot of energy. The process also releases a large quantity of carbon dioxide into the atmosphere due to the complex chemical reactions (Intergovernmental Panel on Climate Change [IPCC] Guidelines). As per the account of 2005, the global carbon dioxide emission is roughly 28.3 gigajoules per tonne (Gt/y), out of which the production of cement accounts for about 1.8 gigajoules per tonne (Gt/y) [1]. The cement production industries contributed roughly 7% of the worldwide carbon dioxide emission [2]. This ecological impact needs to be reduced by using cement production in a lesser manner. Finding eco-friendly and environmentally substitute materials instead of ordinary Portland cement is the main way to curb the discharge of CO_2. Incorporating waste byproduct materials as cement replacement in concrete is the main alternative for Portland cement concrete [3]. The source materials such as GGBS, rice husk ash, fly ash, and silica fume, which is affluent in silica and alumina ar, are geopolymer concrete, a newly emerged material and one of the possible substitutes materials for cement to be used in the building material in the construction industry. A huge quantity of industrial byproduct materials of fly ash (FA) and Ground Granulated Blast furnace Slag (GGBS) is generated from thermal power plants during the burning of coal and iron production from a ground blast furnace in steam or water [4]. This waste byproduct material creates disposal and storage problems. Based on global statistics

data, the unutilized and packed landfill quantity of fly ash is 176 million tonnes, and that of GGBS is 200 million tonnes [5]. Several researchers have employed fly ash as the main base material for replacing the cement in geopolymer concrete for manufacturing railway sleepers [6] and concrete columns [7]. A few studies have also been carried out using other materials like GGBS [8], rice husk ash [9], silica fume [10], and metakaolin [11] in geopolymer concrete.

Baburao et al. studied the durability of ordinary Portland cement concrete containing varying amounts of manufactured sand that replaced natural sand and inferred that 70% replacement by manufactured sand showed good durability properties [12]. Farooq et al. developed a multilayer feed-forward neural network model for finding the durability properties of high-performance concrete and concluded that 10% metakaolin + 10% silica fume + 20% bottom ash replacement of cement showed good performance in terms of strength as well as durability properties [13]. Kumar et al. replaced the coarse aggregate, fine aggregate, and cement with the concrete of oil palm shell manufactured sand and GGBS. They inferred that oil palm shell concrete with 40% GGBS replacement showed enhanced compressive strength in the long term [14]. Thangapandi et al. investigated the strength and durability of conventional concrete incorporated with manufactured sand instead of natural sand. The results revealed that 60% replacement of natural sand with m-sand showed optimum percentage for both strength and durability of the conventional concrete [15].

Sallehan et al. examined the mechanical and durability properties of Recycled Concrete Aggregates (RCA) in a treated way under different curing conditions such as normal water curing, open-air environment, and seawater exposure conditions. The authors concluded that seawater exposure caused a detrimental effect on the compressive strength of untreated RCA compared to normal water curing and open-air environment curing conditions. RCA showed poor porosity and permeability in the open-air environment curing conditions [16]. Dimitriou et al. inferred that recycled aggregate concrete showed improved strength and durability properties compared to the natural aggregate [17]. Ortega-lópez et al. studied fibre-reinforced Electric Arc Furnace (EAF) slag under wet-dry tests, as well as freeze-thaw, sulphate, and industrial environments. They proved that fibre-reinforced EAF slag exhibited better durability [18]. Nath and Sarker studied the durability of high-strength concrete containing a high volume of fly ash and observed that the high-strength concrete mixes showed less shrinkage and ion permeation and rate of absorption at 28 days. Even after six months, the rate of absorption and chloride iron permeation were lower [19]. Saha partially replaced cement with fly ash in conventional concrete and inferred that the concrete containing fly ash exhibited lower chloride permeability and water rate of absorption. Later, drops were observed with increasing curing time [20]. Bakharev investigated the durability properties of geopolymer concrete (fly ash) with an alkali activator solution immersed in acetic acid solutions and discussed the parameters of weight loss, compressive strength, and others [21]. Simatupang valuated class F and class C fly ash-based mortar characteristics on alkaline activated material when immersed in 10% sulphuric acid solution for 65 days [22]. Yong et al. stated the procedure for the rate of absorption test and obtained a 0.109 mm/min 0.5 rate of absorption value for lightweight OPS geopolymer concrete [23].

However, only limited studies are available on rapid chloride penetration and rate of absorption tests on fly ash and slag-based geopolymer concrete under ambient curing conditions using manufactured sand. In the present investigation, a more sustainable green geopolymer concrete is produced by replacing GGBS with fly ash and river sand with manufactured sand under ambient curing conditions. While previous investigations have dealt with the mechanical properties, validation, modulus of elasticity, and impact resistance test, this research focuses on the durability properties of geopolymer concrete under ambient curing conditions such as sulphuric acid and sodium sulphate, water absorption, rapid chloride penetration test, and rate of absorption tests. The research work aims to study the influence of slag content using alkali activator solutions on the durability properties and compare the performance of geopolymer concrete with that of ordinary Portland cement concrete.

2. Materials and Mix Proportions

2.1. Materials. Geopolymer concrete is a member of a family of inorganic polymers that do not use Portland cement as a binder for making concrete. Its properties are mainly formed by reacting an alkaline liquid with an aluminosilicate source material (rich in silica and alumina). This study used calcium class F fly ash and GGBS fly ash, which were procured from North Chennai Thermal Power Plant station and Astra Chemicals, respectively. The chemical constituents of fly ash and GGBS used for this research are given in Table 1. Coarse aggregates of sizes 8, 12, and 20 mm were used. Manufactured sand and natural sand were used as fine aggregate. The aggregates (fine and coarse) were used in Saturated Surface Dry (SSD) conditions. The specific gravity values of coarse aggregate, river sand, and m-sand are 2.73, 2.66, and 2.72, respectively.

Alkali solutions of sodium silicate (Na_2SiO_3) and sodium hydroxide (NaOH) in the ratio of 2.5 were used. Sodium silicate solution was used in the ratio of SiO_2/Na_2O by mass of 2.0, and an 8M concentration of NaOH solution was used. A superplasticizer (naphthalene based) was used in the geopolymer concrete.

A three-dimensional polymeric chain is formed during the polymerization process by the fast chemical reaction on silicon-aluminium minerals under alkaline conditions with the formula (empirical) $Mn[-(SiO_2)z-AlO_2]n.wH_2O$, where M is an alkali cation such as K^+ or Na^+, w is the water content, z is the Si/Al molar ratio, and n is polymerization degree [24]. The schematic form of geopolymerization is shown in Figure 1.

2.2. Mix Proportions of Geopolymer and Conventional Concrete. Twenty geopolymer concrete mixes were studied for optimizing G30 geopolymer concrete, and comparison studies were carried out with five conventional concrete

Table 1: Chemical constitution (in %) of fly ash and GGBS.

Constituents	SiO_2	Al_2O_3	CaO	Fe_2O_3	MgO	Na_2O	K_2O	SO_4	LOI[a]
Fly ash	63.32	26.76	2.49	5.55	0.29	0.0004	0.0002	0.36	0.97
GGBS	35.05	12.5	34.64	0.3	6.34	0.9	0.6	0.38	0.26

[a]Loss of ignition.

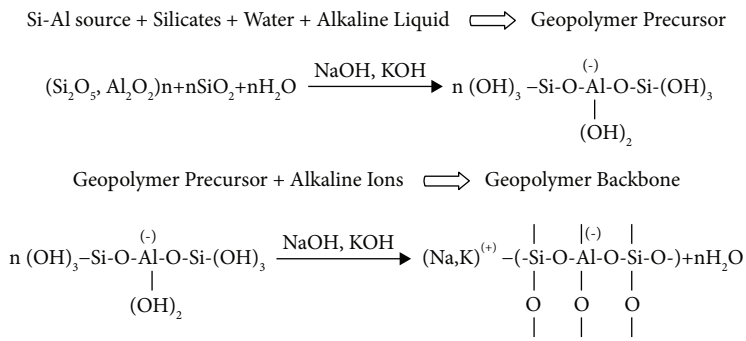

Figure 1: Schematic form of geopolymerization.

mixes as per IS 10262 [25]. This investigation's geopolymer concrete mix proportion is 1 : 2.22 : 3.86 : 6.95 by mass of alkaline activator solutions, aluminosilicate binder, fine aggregate, and coarse aggregates. The ratio between the alkaline activator solutions and the binder was 0.45. The quantity of the superplasticizer (Conplast SP430) used was 1% of the binder content (GGBS and FA) in the geopolymer concrete. For geopolymer concrete, river sand was partially or fully replaced with m-sand.

In the mixing process, fine and coarse aggregates were first mixed in Saturated Surface Dry (SSD) conditions in a mixer machine. Then, the binder contents were mixed with the aggregates. The mixing was continued for about 3 minutes. The already prepared alkali-activated solution was poured into the mixer machine, and the mixing was continued for about 4 minutes. Finally, the superplasticizer was added to the mixture until the concrete appeared homogenous and had the desired consistency. The geopolymer concrete was poured into the moulds in a new state. After demoulding the specimens, the samples were cured under ambient temperature for 28 days. The mechanical properties of the geopolymer and the conventional concrete can be found in previous studies.

Based on the mechanical properties of the prepared geopolymer concrete mixes, three concrete mixes that achieved G30 grade were chosen, and their durability-related properties were investigated and compared with conventional concrete. The mechanical properties were validated using MATLAB software using the Levenberg-Marquardt training algorithm. The mechanical properties of the geopolymer concrete (binder (80% fly ash + 20% GGBS) and 100% replacement of river sand with manufactured sand) and conventional concrete are shown in Table 2.

The stress-strain curves for the conventional and geopolymer concrete from an average of the three values and the failure patterns of these types of concrete tested under uniaxial compression are shown in Figure 2.

The mixed proportions of the G30 grade of geopolymer concrete studied for durability are given in Table 3. For comparative analysis, a mixed proportion of conventional concrete is also provided.

The proportions of coarse aggregate, superplasticizer, and alkali-activated solutions used in the geopolymer concrete mixes were 1189 kg/m^3, 3.8 kg/m^3, and 171 kg/m^3, respectively. The coarse aggregate and water used in the conventional concrete mix were 1189 kg/m^3 and 171 kg/m^3, respectively. From Table 3, it is observed that G20M0 indicates that the mixes have 20% GGBS, 80% fly ash, and 0% manufactured sand. In the same way, G20M100 indicates 20% GGBS, 80% fly ash, and 100% manufactured sand in the mix.

3. Microstructural Analysis and Experimental Procedures

3.1. Scanning Electron Microscopy (SEM) with Energy-Dispersive X-Ray Spectroscopy (EDX) Analysis. The Scanning Electron Microscope equipped with an Energy-Dispersive X-ray spectrometer was used to characterize the microstructure of the geopolymer concrete. The SEM measurements were performed using EVO 18 research microscope and LaB6 filaments electron source to find the surface morphology of the concrete mixes.

The images were obtained at a resolution of 8 kV. The samples were evaluated in the system vacuum technique. The SEM images of fly ash and GGBS are shown in Figures 3(a) and 3(b), respectively. The SEM image of m-sand is shown in Figure 3(c). The results showed that fly ash and GGBS have high silica and alumina content. Fly ash particles are viewed as spherical, while GGBS is granular, and m-sand is angular in shape.

3.2. Experimental Procedures

3.2.1. Acid Resistance Test. The testing requirements include preparing a curing tank separately by mixing 5% concentrated sulphuric acid solution with the required water level to immerse the specimens. The tanks are made isolated from other laboratory areas as the handling of acids needs care.

Table 2: Mechanical properties of geopolymer concrete and conventional concrete.

Mechanical properties	Geopolymer concrete (GC)	Conventional concrete (CC)
Compressive strength (MPa)	40.35	38.95
Split tensile strength (MPa)	3.32	3.17
Flexural strength (MPa)	4.69	4.46
Modulus of elasticity (GPa)	19.10	22.19

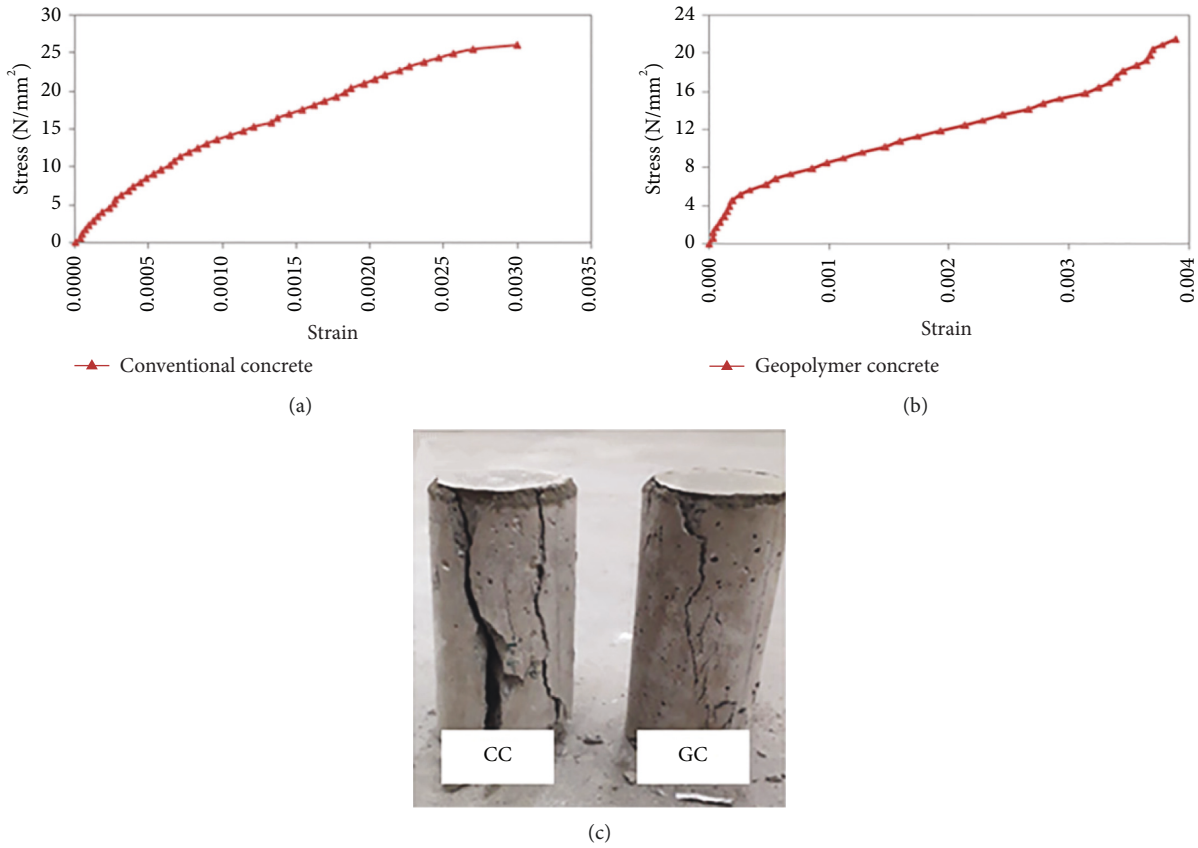

Figure 2: Stress-Strain curve for (a) conventional concrete and (b) geopolymer concrete. (c) Failure patterns of CC and GC were tested under uniaxial compression.

Table 3: Details of mix proportions of concrete specimens.

Mixes	ID	Fly ash	GGBS	Cement	M-sand	River sand
G20M0	GC1	304	76	—	0	660
G20M50	GC2	304	76	—	330	330
G20M100	GC3	304	76	—	660	0
C100R100	OPC	—	—	380	0	660

All units are in kg/m^3.

The specimens are to be placed with care inside the proposed area without splattering the acid solution. Nine specimens each for GC1, GC2, GC3, and OPC were tested for the acid tests as per the procedure given in ASTM C 642 [21]. Initially, the ambient cured geopolymer concrete samples cured for 28 days of size 150 mm × 150 mm × 150 mm were cast to conduct an acid resistance test. After 28 days, water cured conventional concrete cube samples were taken out from the water curing tank. After cleaning, the weights of the cube samples were recorded as W_1. The cube samples were then immersed in 5% sulphuric acid solution with a minimum of 30 mm depth of acid present above the top surface of the concrete specimens. Three samples were taken out from the containers after 28 days, 56 days, and 90 days to carry out the testing. Variation in compressive strength and mass has been recorded before and after immersion. The cube specimens were washed with tap water and weighed using a digital weighing balance with an accuracy of 0.1 mg. The average weight of cube samples was noted as W_2. The variation in mass was calculated as shown in the following equation:

$$\%\ \text{weight loss} = \left[\frac{\text{Initial weight}\ (W_1) - \text{Final weight}\ (W_2)}{\text{Initial weight}\ (W_1)}\right] \times 100. \quad (1)$$

3.2.2. Sulphate Resistance Test. The acid attack test was followed by sulphate curing to understand the resistance of the specimens towards sulphate attack. The specimens were

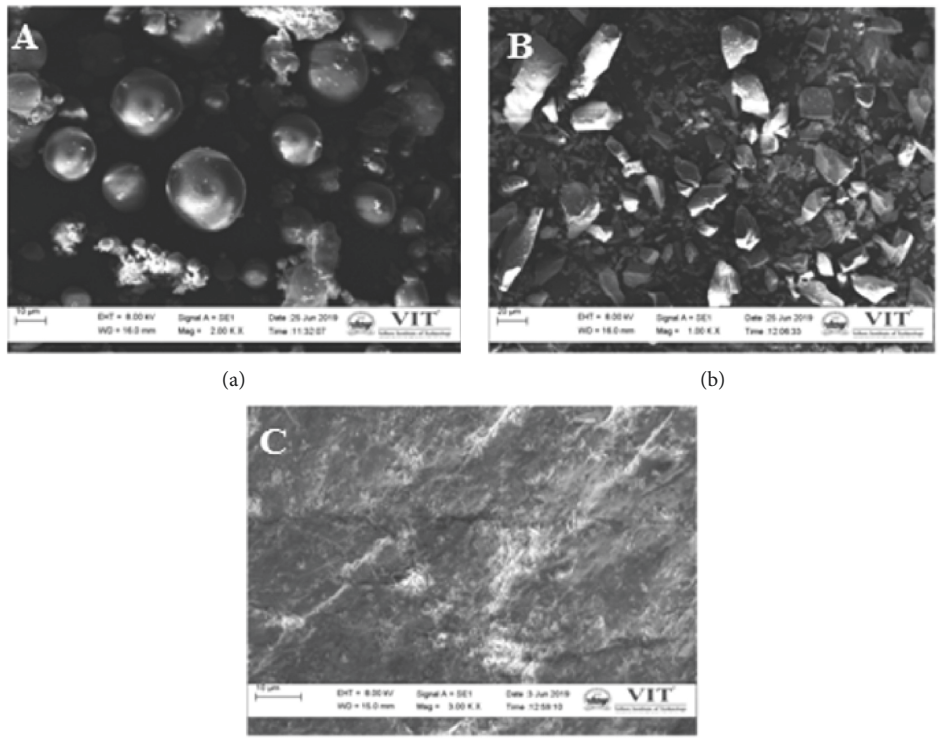

(a) (b)

(c)

Figure 3: SEM images of (a) fly ash, (b) GGBS, and (c) M-sand.

immersed in a solution made of 5% sodium sulphate powder and the required quantity of water to immerse them fully. Unlike acid curing, sulphate curing does not require special handling equipment as it does not cause harm directly. The sulphate intrusion into the specimen was determined by measuring the loss in weight and compression values of the immersed specimens after the proposed curing periods of 28 and 56 days. Nine specimens each for GC1, GC2, GC3, and OPC were tested for sulphate resistance test as per the procedure given in ASTM C 642 [26]. The ambient cured geopolymer concrete cube samples cured for 28 days were subjected to an acid resistance test. After 28 days, water-cured conventional concrete cubes were taken out from the water curing tank. After cleaning the surfaces of the cubes, they were placed in a 5% sodium sulphate solution. The containers were closed to minimize the evaporation and falling of dust particles. The new solutions were maintained every month to regulate the pH value of the solution. The solutions were stirred every week to avoid deposits at the base of the containers. Three samples were taken out from the containers after 28 days, 56 days, and 90 days to carry out the testing. Variations in compressive strength and mass were recorded before and after immersion. The cube samples were tested in a compression testing machine.

3.2.3. Water Absorption Test. Water absorption was determined by measuring the hike in weight recorded over an oven-dried sample when immersed in water for 24 hours. The surface water was removed before measuring the weight. The ratio of the increase in weight to the weight of the dry sample expressed in percentage is termed absorption. Nine specimens each for GC1, GC2, GC3, and OPC were tested for water absorption test as per the procedure specified in ASTM C 642 [9]. The saturated weights of the cube samples measured after being taken from the water curing tank are denoted as W_s. The drying process was continued in the oven at a temperature of 105°C. The drying process was stopped when the difference between two successive measurements was small. The dry weights of the samples were recorded as W_d. The absorbed water was calculated using the following equation:

$$\text{Water Absorption} = \left[\frac{W_s - W_d}{W_d}\right] \times 100, \tag{2}$$

where W_s is weight of the samples at fully saturated condition (kg) and W_d is weight of samples at oven-dried condition (kg).

3.2.4. Rapid Chloride Penetration Test (RCPT). Concrete structures are mainly affected by chloride penetration in seawater and groundwater having high concentrations of chloride salts. The Rapid Chloride Penetration Test is fast and is the main indicator of chloride ion penetration into the concrete structures. The RCPT test was performed per the procedure given in ASTM C 1202-1997 [16]. Concretes of sizes of 100 mm diameter × 50 mm thickness were sliced from the top portion of the cylinders with 100 mm diameter × 200 mm height. After the curing period, the samples

were tested for chloride permeability. Before testing, the samples were dried to ensure that they were free of moisture. The samples were preconditioned as per standards, wherein two halves of the samples were sealed in the container. One container side was packed with 0.3 N sodium hydroxide solution and linked to the anode terminal. In contrast, on the other side, 3% sodium chloride solution was poured and the cell was connected to the cathode terminal. The dried samples were subjected to 60-volt electric potential for about 6 hours and the current passing was recorded every 30 minutes. The RCPT test setup is shown in Figure 4.

3.2.5. Rate of Absorption. The rate of absorption (Sorptivity) characteristic is a concrete's ability to absorb or transmit water through the capillary action like a homogenous material. Water was used as a test fluid for carrying out the rate of absorption test. The procedure for the rate of absorption test was adapted from [26, 27]. The arrangement for the rate of absorption (Sorptivity) test is shown in Figure 5. ASTM C1585 Standard was considered for rate of absorption test (Sorptivity) [27].

The 100 mm cube samples cured for 28 days were used for the rate of absorption test. Ambient cured samples were dried in an oven at a temperature of 105 ± 5°C for about 48 hours until no variation in sample weight was achieved. After that, the samples were cooled at room temperature. The nonabsorbent solutions were prepared using resin and Methyl Ethyl Ketone Peroxide (MEKP) as the catalyst and Cobalt Octoate (CO) as the promoter. The sides of the cube samples were coated with the already prepared nonabsorbent solutions to avoid the penetration of water through the sides of the cube samples. The prepared tubes were positioned in a tray such that the bottom of the cube samples got in touch with the water to a height of 5 mm. The samples were taken from the tray, wiped off with dampened tissue, and then weighed using a weighing balance with 0.1 mg accuracy every 10 minutes.

Since the square root of time increases, the water absorption (cumulative) will also increase. The rate of absorption has been calculated using the following equation:

$$I = s_t^{0.5}, \tag{3}$$

where S is rate of absorption (mm), t is elapsed time (minutes), and absorption, $I = \Delta w/\mathrm{Ad}$, Δw = difference between the mass of the sample after 30 minutes of capillary suction of water and the mass of the oven-dried sample (grams). A is surface area of the sample and d is density of water.

4. Results and Discussions

4.1. Scanning Electron Microscopy (SEM) with Energy-Dispersive X-Ray Spectroscopy (EDX) Analysis of Geopolymer Concrete. The SEM images and the EDX spectra of the geopolymer and conventional concrete samples are shown in Figures 6 and 7. These microstructural images of the samples GC3 (G20M100) and OPC (C100R100) of geopolymer concrete were obtained at 28 days.

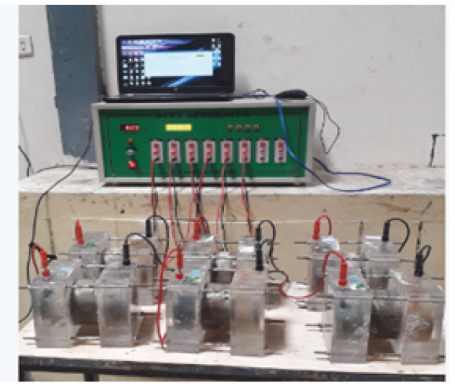

Figure 4: Test setup for RCPT test.

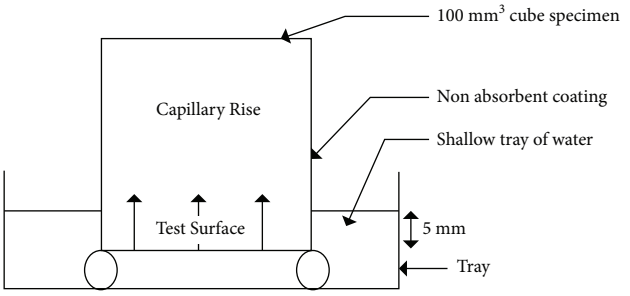

Figure 5: Arrangement for the rate of absorption (Sorptivity) test.

While using GGBS in fly ash-based geopolymer concrete, calcium aluminosilicate hydrate (C-A-S-H) is a reaction product when calcium compound rises in geopolymer concrete [28]. Meanwhile, in ordinary Portland cement concrete, calcium silicate hydrate (C-S-H) gel is the reaction product. The density and homogeneity could be improved by adding the fine particles as an additive in geopolymer concrete.

4.2. Acid Resistance. The weight loss in percentage and compressive strength for GC1, GC2, GC3, and OPC concrete mixes at 28 days, 56 days, and 90 days are presented in Figure 8 and Tables 4 and 5.

From Figure 8(a), it is observed that the percentage weight loss of all the concrete mixes increases with the curing period. The percentage of weight loss between 28 days and 90 days of immersion for the GC1, GC2, and GC3 mixes is lower when compared to that of the OPC. The percentage of weight loss in geopolymer concrete is low due to sodium content and the low permeability of the solution when compared. The test results implied that the GC1, GC2, and GC3 specimens showed better resistance to acid attack when compared with OPC × geopolymer concrete possessing strong resistance to acid attack due to the generation of calcium aluminium silicate gel (C-A-S-H) and sodium aluminosilicate gel (N-A-S-H). The OPC concrete is highly susceptible to acid attack due to the formation of calcium silicate hydrate gel (C-S-H) gel [2PC].

The compressive strength reductions for GC1, GC2, GC3, and OPC concrete mixes for 28 days, 56 days, and 90

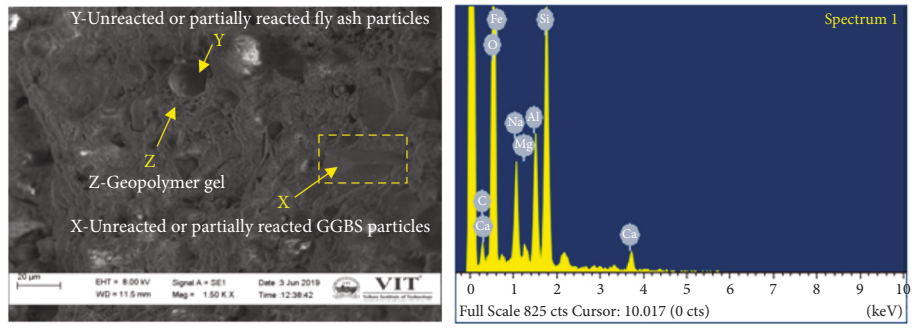

Figure 6: SEM image and EDX spectrum of mix GC3 (G20M100).

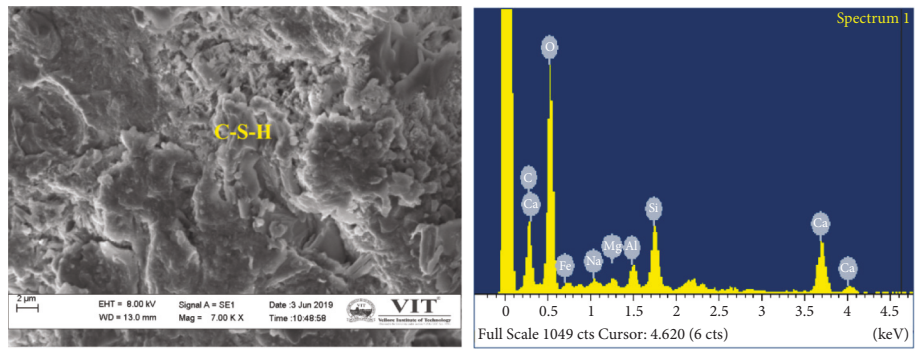

Figure 7: SEM image and EDX spectrum of mix OPC (C100R100). X: unreacted or partially reacted GGBS particles. Y: unreacted or partially reacted fly ash particles. Z: geopolymer gel.

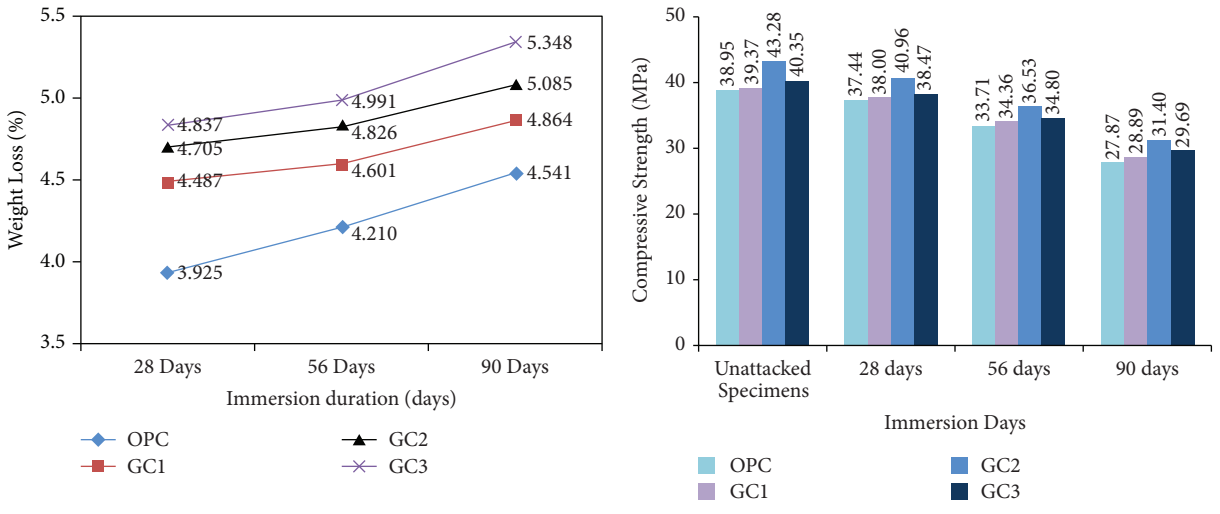

Figure 8: Variation of (a) percentage weight loss and (b) compressive strength after the acid test as a function of curing period.

Table 4: Weight loss in the geopolymer and OPC concrete mix percentage after the acid test for different curing periods.

Mix ID	28 days	56 days	90 days
OPC	37.44	33.71	27.87
GC1	38.00	34.36	28.89
GC2	40.96	36.53	31.40
GC3	38.47	34.80	29.69

Table 5: Compressive strength values of the geopolymer and OPC concrete mixes after the acid test for different curing periods.

Mix ID	Unattacked specimens	28 days	56 days	90 days
OPC	38.95	37.44	33.71	27.87
GC1	39.37	38.00	34.36	28.89
GC2	43.28	40.96	36.53	31.40
GC3	40.35	38.47	34.80	29.69

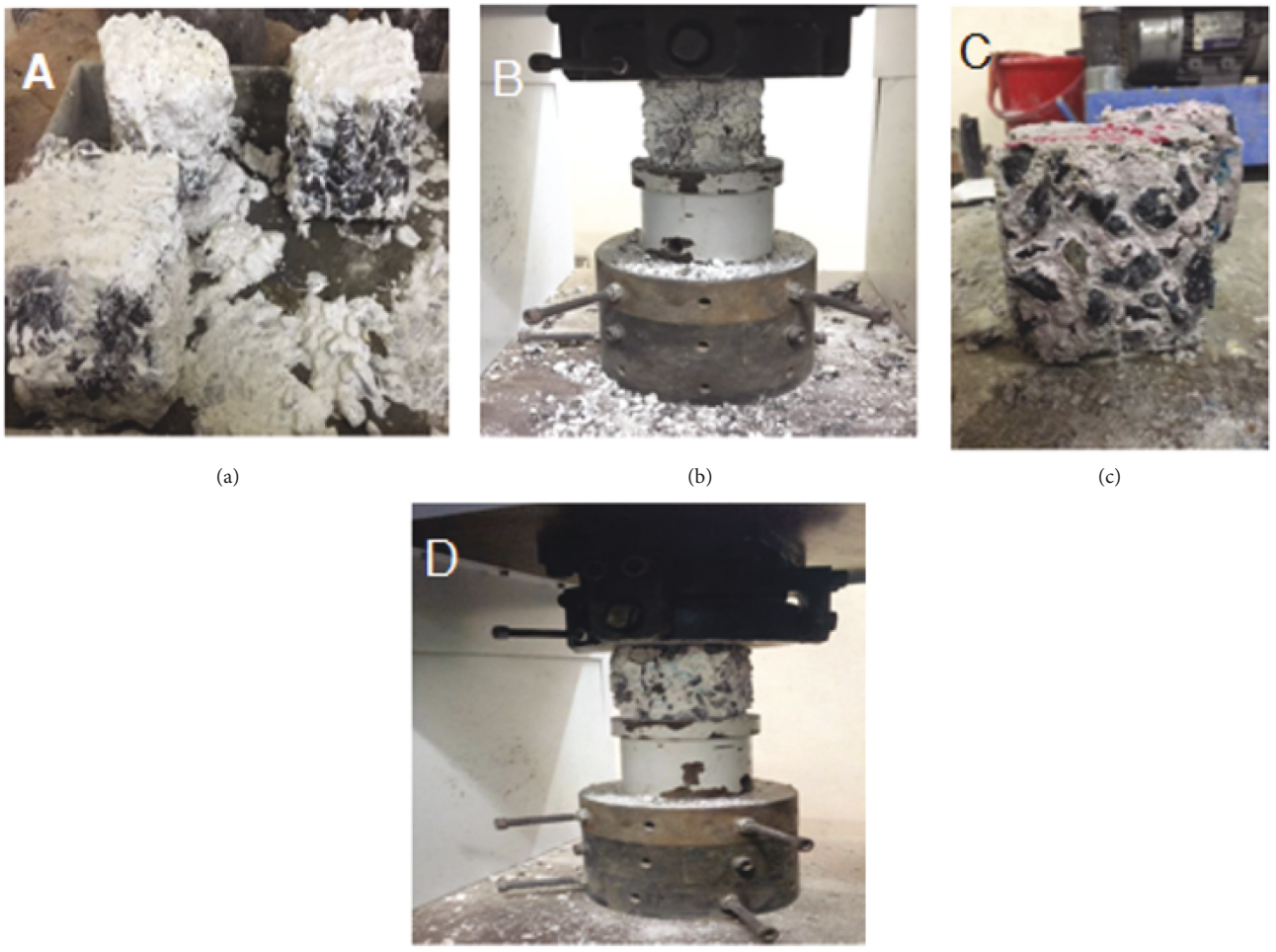

(a) (b) (c)

(d)

Figure 9: (a) Cubes of the conventional mix (OPC) after removal from acid curing; (b) compressive testing of acid cured conventional cube specimen; (c) cubes of geopolymer mix (GC-3) after removal from acid curing; (d) compressive testing of acid cured geopolymer cube specimen.

days are presented in Figure 8(b). It is noted from Figure 8(b) that the compressive strengths for the mixes OPC, GC1, GC2, and GC3 were 27.87 MPa, 29.09 MPa, 31.40 MPa, and 29.69 MPa, respectively, at 90 days. The equivalent percentage losses in compressive strength were 25.56%, 23.45%, 23.34%, and 22.82%. The test results revealed that OPC experienced maximum strength loss, whereas GC1, GC2, and GC3 experienced minimum strength loss. The compressive strength loss was in the order of OPC > GC1 > GC2 > GC3. The decalcification of C-S-H was detected, which, alongside the dissolution of calcium hydroxide, results in a very porous corroded layer and a decrease in compressive strength. On the other hand, the decalcification of the C-A-S-H type gel in geopolymer concrete results in a dense highly siliceous layer that is more resistant to acid attack [29]. Cubes of the conventional and geopolymer concrete mixes after removal from acid curing and compressive testing are shown in Figure 9.

In an acidic environment, geopolymer concrete's better performance than conventional concrete is attributed to the lower calcium content in fly ash, since geopolymer concrete does not depend on lime-like ordinary Portland cement concrete. Geopolymer concrete does not allow ingress of sulphuric acid, since it does not have a transition zone. Hence, geopolymer concrete has a higher durability factor [30].

4.3. Sulphate Resistance Test. The weight loss in percentage and compressive strength for GC1, GC2, GC3, and OPC concrete mixes at 28 days, 56 days, and 90 days are presented in Figure 10 and Tables 6 and 7.

From Figure 10(a), it is noted that the percentage weight loss of all mixes increases with the curing period. The percentage of weight loss is higher in OPC concrete than in geopolymer concrete during 28 days and 90 days of immersion in a sulphate solution. When geopolymer concrete samples were immersed in sulphate solution, the transmission of sulphate ions caused by the disintegration of siloxane bonds (-Si-O-Si-bonds) decreased the Si/Al atomic ratio and leaching of Si in the geopolymer gel structure.

Compressive strength reductions for GC1, GC2, GC3, and OPC concrete mixes at 28 days, 56 days, and 90 days are

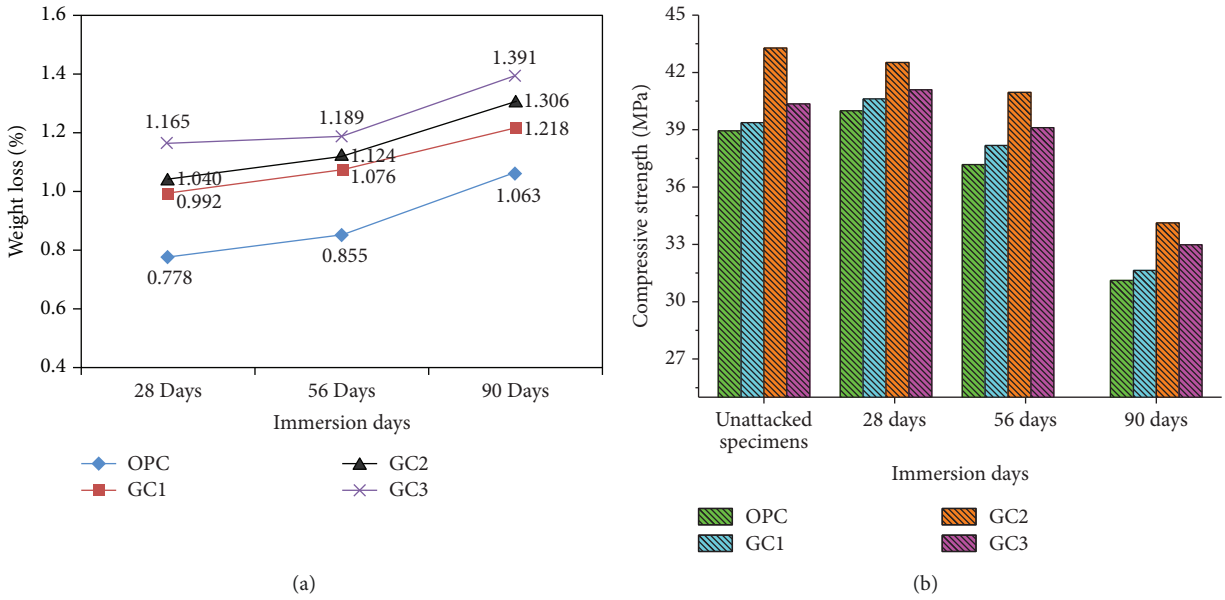

Figure 10: Variation of (a) percentage weight loss and (b) compressive strength after sulphate test as a function of curing period.

Table 6: Weight loss in percentage of the geopolymer and OPC concrete mix after sulphate test for different curing periods.

Mix ID	28 days	56 days	90 days
OPC	0.778	0.855	1.063
GC1	0.992	1.076	1.218
GC2	1.040	1.124	1.306
GC3	1.165	1.189	1.391

Table 7: Compressive strength values of the geopolymer and OPC concrete mixes after sulphate test for different curing periods.

Mix ID	Unattacked specimens	28 days	56 days	90 days
OPC	40	37.18	31.11	40
GC1	40.62	38.18	31.64	40.62
GC2	42.52	40.96	34.13	42.52
GC3	41.09	39.11	32.98	41.09

presented in Figure 11(b). The compressive strengths of OPC, GC1, GC2, and GC3 mixes were 31.11 MPa, 32.44 MPa, 34.13 MPa, and 32.98 MPa, respectively. The equivalent percentage losses in compressive strengths were 22%, 20%, 19.73%, and 19.73%. The test results indicated that OPC experienced maximum strength loss, whereas GC1, GC2, and GC3 experienced minimum strength loss. Figure 11 shows the compressive testing of sulphate cured conventional and geopolymer concrete cube specimens. The authors reported that low calcium fly ash concrete showed higher resistance to sulphate attack [31]. It was also reported that AAS concrete has better sulphate resistance than OPC [32]. The compressive strength of geopolymer concrete had a minimum deteriorating effect due to sulphate ions $(SO_4)^{-2}$ [33]. It could be observed that the presence of GGBS additives led to the minimum strength loss in geopolymer concrete (fly ash-based) compared with conventional concrete.

4.4. Water Absorption Test. The water absorption percentages for GC1, GC2, GC3, and OPC concrete mixes at 28 days, 56 days, and 90 days are presented in Figure 12 and Table 8.

It is noted from Figure 12 that the increase in the percentage of water absorption for geopolymer concrete is lower than that for OPC concrete. The percentage loss in water absorption is taken between 28 days and 90 days. The percentage loss in water absorption for geopolymer concrete decreases from 28 days to 90 days compared to control concrete. The authors found that the fine slag particles fill the pores, leading to lower water absorption values for alkali-activated fly ash blend with slag (AAFS) binders compared to ordinary Portland cement concrete [34].

4.5. Rapid Chloride Penetration Test. The Rapid Chloride Penetration Test (RCPT) value indicates chloride penetration (permeability) into the concrete specimens. It is expressed as the total charge passing in the coulomb during the test period. The RCPT values for GPC and OPC concrete mixes are given in Table 9. The total charge passing through the concrete specimens of geopolymer concrete and conventional concrete at 28 days is shown in Figure 13. The average values for the three specimens for each mix were also obtained.

It is observed from Figure 13 that the penetration level of chloride in the geopolymer concrete falls under the "low level" against the "very low level" in ordinary Portland cement concrete. Cl^- ion penetration was reduced when the FA content increased in the concrete mixtures. Hence, FA concrete showed better resistance to Cl^- ion.

4.6. Rate of Absorption Test. The rate of absorption (Sorptivity) measurement is usually performed for short periods. Hall (1989) suggested that two hours is sufficient for performing the rate of absorption measurements. Martys (1997)

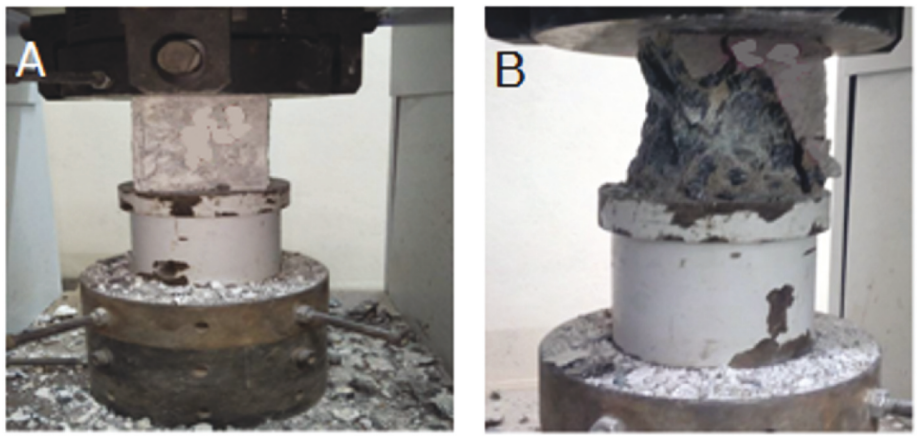

(a) (b)

Figure 11: Compressive testing of sulphate cured (a) conventional and (b) geopolymer concrete cube specimens.

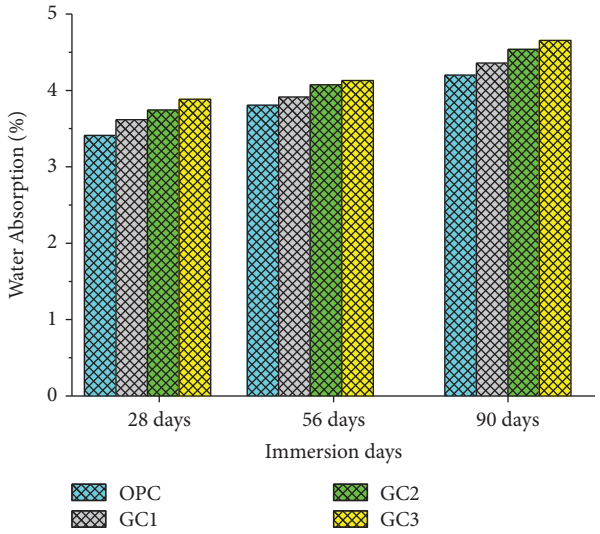

Figure 12: Water absorption percentage as a function of curing period for different concrete mixes.

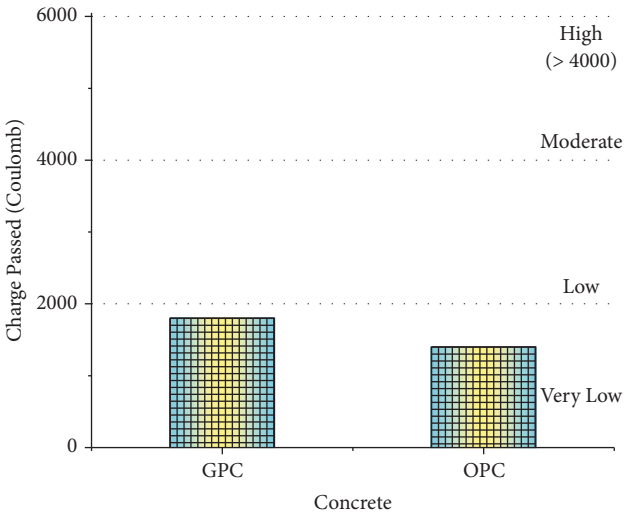

Figure 13: Rapid Chloride Permeability Test results for GPC and OPC mix.

Table 8: Water absorption percentage for different concrete mixes at different curing periods.

Mix ID	28 days	56 days	90 days
OPC	0.778	0.855	1.063
GC1	0.992	1.076	1.218
GC2	1.040	1.124	1.306
GC3	1.165	1.189	1.391

Table 9: RCPT values for different concrete mixes.

Mix ID	Charge passing (coulombs)	Charge passing (coulombs)
GPC 1	1206	
GPC 2	1676	1662 (avg)
GPC 3	2104	
OPC 1	758	
OPC 2	873	847 (avg)
OPC 3	911	

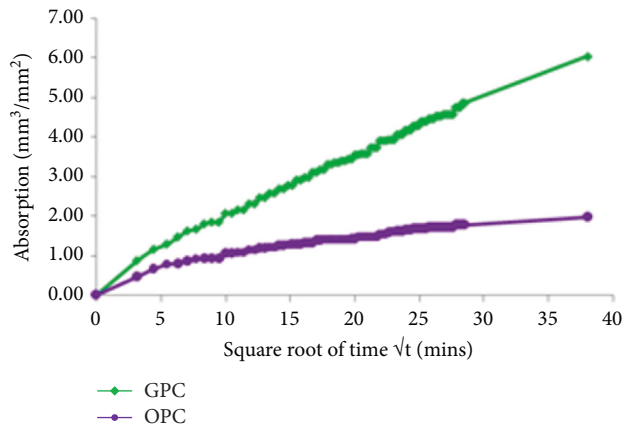

Figure 14: Absorption versus square root of time for GPC and OPC mixes.

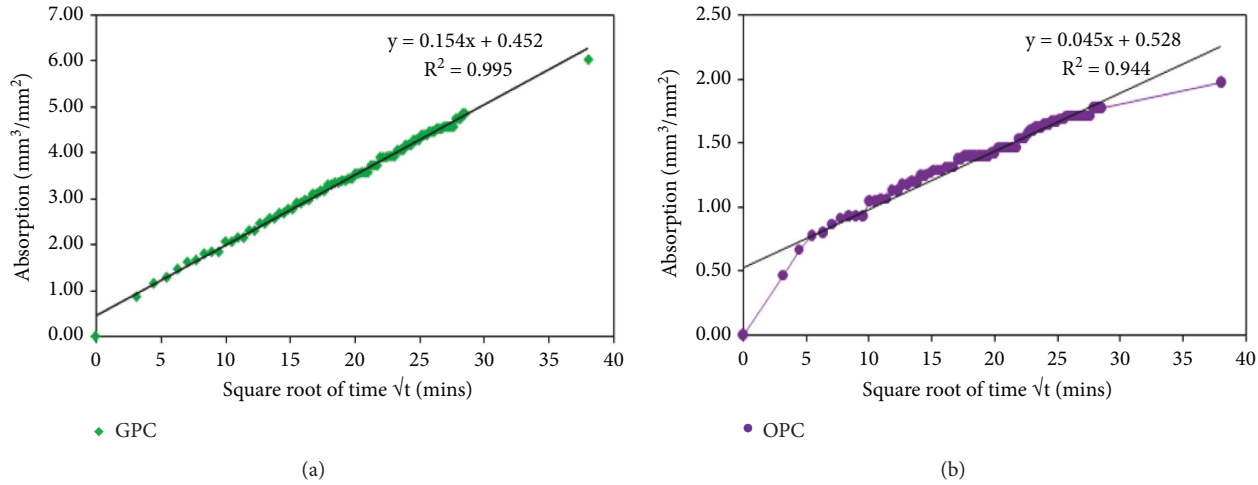

Figure 15: Regression analysis-absorption versus square root of time for (a) GPC and (b) OPC.

Table 10: Rate of absorption (Sorptivity) values for different concrete mixes.

Mix ID	Rate of absorption (mm/min$^{0.5}$)
GPC	0.16
OPC	0.05

claimed that two rate of absorption coefficients characterize mortars and concrete. For large-age rate of absorption coefficients, longer than one day is accredited other than suction such as slow filling of sir voids and water interactions with cement gel due to capillary pore network. Hence, the rate of absorption test was conducted for one day and the readings were noted every 10 minutes' interval. The absorption values for geopolymer concrete and conventional concrete plotted against the square root of time are illustrated in Figure 14. Regression analysis for absorption versus square root of time (t) for GPC and OPC concrete is illustrated in Figures 15(a) and 15(b).

The regression analysis on two parameters, time and GPC absorption (Figure 15(a)), clearly indicates an excellent relationship between absorption and the square root of time with an R^2 value nearing 1 (99% accuracy) and a minimal standard error of 0.075. The regression analysis on two parameters, time and OPC absorption (Figure 15(b)), also indicates an excellent relationship between absorption and the square root of time with an R^2 value nearing 1 (95% accuracy) and minimal standard error of 0.080.

The rate of absorption (Sorptivity) values for OPC and GPC mixes are shown in Table 10. The rate of absorption value of geopolymer concrete mixes is 0.164 (mm/min$^{1/2}$), which is slightly higher than the rate of absorption value of 0.053 for OPC (mm/min$^{1/2}$). This may be due to the addition of 20% GGBS as a replacement material of 80% fly ash in eco-friendly geopolymer concrete.

5. Conclusions

Twenty geopolymer concrete mixtures were designed with FA and GGBS as the binder source materials and the replacement of river sand with m-sand as the fine aggregates. Five conventional concrete mixtures were designed using m-sand as an alternative material to river sand as the fine aggregate. The durability properties of three geopolymer concrete mixes (among the twenty mixes) have been studied and compared with conventional concrete mixes. Optimized geopolymer concrete mix has been selected to carry out future studies of flexural strength of geopolymer beam using fibre-reinforced polymer rebar reinforced concrete beam.

The following points were observed from the experimental test results:

(i) From the investigation of the mechanical properties, it is observed that concrete mixes with 80% FA and 20% GGBS along with m-sand as a full or partial replacement in mix proportions, namely, G20M0, G20M50, and G20M100, achieve the strength of G30 grade and can be used as an alternative material for conventional concrete.

(ii) The percentage of weight loss is higher in conventional concrete than in geopolymer concrete owing to sulfuric acid and sulphate attacks.

(iii) The percentage loss in compressive strength due to sulfuric acid and sulphate attack in geopolymer concrete is lower when compared to that in ordinary Portland cement concrete at 28 days, 56 days, and 90 days.

(iv) The percentage loss in water absorption of geopolymer concrete is lower when compared with that of ordinary Portland cement concrete at 28 days, 56 days, and 90 days.

(v) In geopolymer concrete, the penetrability of chloride ion (Cl^-) falls in the "low level" against the "very low level" in ordinary Portland cement concrete.

(vi) The rate of absorption (Sorptivity) value for geopolymer concrete is slightly higher than that of the ordinary Portland cement concrete when considered for one day, that is, large age rate of absorption coefficient.

6. Disclosure

This study was performed as a part of the Employment of Kombolcha Institute of Technology, Wollo University, Kombolcha, Amhara, Ethiopia.

Data Availability

The data used to support the findings of this study are included in the article. Should further data or information be required, these are available from the corresponding author upon request.

Conflicts of Interest

The authors declare that there are no conflicts of interest regarding the publication of this paper.

Acknowledgments

The authors would like to thank the Management and Dean-School of Civil Engineering, Vellore Institute of Technology, Chennai, India, for providing such a wonderful platform to do their research on time and necessary support to carry out this research.

References

[1] M. Lehtveer and M. Lehtveer, "Bioenergy with carbon capture and storage (BECCS): global potential, investment preferences, and deployment barriers," *Energy Research & Social Science*, vol. 42, pp. 155–165, 2018.

[2] M. B. Ali, R. Saidur, and M. S. Hossain, "A review on emission analysis in cement industries," *Renewable and Sustainable Energy Reviews*, vol. 15, no. 5, pp. 2252–2261, 2011.

[3] M. F. Alnahhal, U. J. Alengaram, M. Z. Jumaat, F. Abutaha, M. A. Alqedra, and R. R. Nayaka, "Assessment on engineering properties and CO2 emissions of recycled aggregate concrete incorporating waste products as supplements to Portland cement," *Journal of Cleaner Production*, vol. 203, pp. 822–835, 2018.

[4] K. Yin, A. Ahamed, and G. Lisak, "Environmental perspectives of recycling various combustion ashes in cement production - a review," *Waste Management*, vol. 78, pp. 401–416, 2018.

[5] P. R. Rao, M. Momayez, K. A. Runge, and K. Muralidharan, "Recent developments in thermally insulating materials based on geopolymers-a review article," *Mining, Metallurgy & Exploration*, vol. 37, no. 4, pp. 995–1014, 2020.

[6] B. Rai, L. B. Roy, and M. Rajjak, "A statistical investigation of different parameters influencing compressive strength of fly ash induced geopolymer concrete," *Structural Concrete*, vol. 19, no. 5, pp. 1268–1279, 2018.

[7] R. Saxena, T. Gupta, R. K. Sharma, and N. L. Panwar, "Influence of granite waste on mechanical and durability properties of fly ash-based geopolymer concrete," *Environment, Development and Sustainability*, vol. 18, Article ID 0123456789, 2021.

[8] A. Mini and K. M. Mini, "Strength and durability studies of SCC incorporating silica fume and ultra fine GGBS," *Construction and Building Materials*, vol. 171, pp. 919–928, 2018.

[9] S. Divvala and M. S. Rani, "Strength properties and durability studies on modified geopolymer concrete composites incorporating GGBS and metakaolin," *Applied Nanoscience*, vol. 15, Article ID 0123456789, 2021.

[10] K. T. Tong, R. Vinai, and M. N. Soutsos, "Use of Vietnamese rice husk ash for the production of sodium silicate as the activator for alkali-activated binders," *Journal of Cleaner Production*, vol. 201, pp. 272–286, 2018.

[11] R. Budarayavalasa, S. Budarayavalasa, Solidification and stabilization of hazardous wastes using geopolymers as sustainable binders," *Journal of Material Cycles and Waste Management*, vol. 23, no. 5, pp. 1699–1725, 2021.

[12] A. Baburao, S. Amit, and B. M. D. Neeraja, "Sustainable alternatives in concrete along with the use of medicinal plant Sapindus Mukoross i as a green workability agent," *Innov. Infrastruct. Solut.*vol. 6, no. 4, pp. 1–10, 2021.

[13] F. Farooq, W. Ahmed, A. Akbar, F. Aslam, and R. Alyousef, "Predictive modeling for sustainable high-performance concrete from industrial wastes: a comparison and optimization of models using ensemble learners," *Journal of Cleaner Production*, vol. 292, Article ID 126032, 2021.

[14] V. R. P. Kumar, K. Gunasekaran, and T. Shyamala, "Characterization study on coconut shell concrete with partial replacement of cement by GGBS," *Journal of Building Engineering*, vol. 26, Article ID 100830, 2019.

[15] K. Thangapandi, R. Anuradha, P. O. Awoyera et al., "Durability phenomenon in manufactured sand concrete: effects of zinc oxide and alcofine on behaviour," *Silicon*, vol. 13, no. 4, pp. 1079–1085, 2021.

[16] American Society for testing and materialsAstmC, *Standard Test Method for Electrical Indication of concrete's Ability to Resist Chloride Ion Penetration*, Am Soc Test Mater, Philadelphia, 1997.

[17] G. Dimitriou, P. Savva, and M. F. Petrou, "Enhancing mechanical and durability properties of recycled aggregate concrete," *Construction and Building Materials*, vol. 158, pp. 228–235, 2018.

[18] V. Ortega-lópez, J. A. Fuente-alonso, A. Santamaría, and J. T. San-josé, "Durability studies on fiber-reinforced EAF slag concrete for pavements," *Construction and Building Materials*, vol. 163, pp. 471–481, 2018.

[19] P. Sarker and P. Sarker, "Effect of fly ash on the durability properties of high strength concrete," *Procedia Engineering*, vol. 14, pp. 1149–1156, 2011.

[20] A. K. Saha, "Effect of class F fly ash on the durability properties of concrete," *Sustainable Environment Research*, vol. 28, no. 1, pp. 25–31, 2018.

[21] American Society of Testing and Materials, *ASTM C642. Standard Specification for Fly Ash and Raw or Calcined Natural Pozzolana for Use as a mineral Admixture in Portland Cement concrete*, Am Soc Test Mater, Philadelphia, 1989.

[22] P. H. Simatupang, "Characteristics of alkali activated material (geopolymer) in sulfuric acid solution characteristics of alkali activated material (geopolymer) in sulfuric acid solution," in *Proceedings of the AIP Conference Proceedings*, vol. 1887, Article ID 0200281–8, Bahasa Indonesia, Septeber 2017.

[23] M. Yong, J. Liu, U. J. Alengaram, M. Z. Jumaat, and K. H. Mo, "Evaluation of thermal conductivity, mechanical and

transport properties of lightweight aggregate foamed geopolymer concrete," *Energy and Buildings*, vol. 72, pp. 238–245, 2014.

[24] A. Palomo, M. W. Grutzeck, and M. T. Blanco, "Alkali-activated fly ashes," *Cement and concrete Research*, vol. 29, no. 8, pp. 1323–1329, 1999.

[25] K R C Naga Dheeraj, L. Natrayan, and W. Degife Mammo, "Seismic fragility and life cycle cost analysis of reinforced concrete structures with a hybrid damper," *Advances in Civil Engineering*, vol. 2021, pp. 1–17, Article ID 4195161, 2021.

[26] American Society for Testing and Materials, *Sample Size to Estimate the Average Quality of a Lot or Process*, Am Soc Test Mater, Philadelphia, ASTM C1585-13. Standard recommended practice for choice of, 1972.

[27] K. Mo, U. Alengaram, M. Y. J. Jumaat, and J. Lim, "Assessing some durability properties of sustainable lightweight oil palm shell concrete incorporating slag and manufactured sand," *Journal of Cleaner Production*, vol. 112, pp. 763–770, 2016.

[28] K. H. Yang, J. Song, K. S. Lee, and A. F. Ashour, "Flow and compressive strength of alkali activated mortars," *ACI Material journal*, vol. 106, no. 1, pp. 50–58, 2009.

[29] T. A. Aiken, J. Kwasny, W. Sha, N. Soutsos, and Soutsos, "Effect of slag content and activator dosage on the resistance of fly ash geopolymer binders to sulfuric acid attack," *Cement and Concrete Research*, vol. 111, pp. 23–40, 2018.

[30] F. N. Okoye, S. Prakash, and N. B. Singh, "Durability of flyash based geopolymer concrete in the presence of silica fume," *Journal of Cleaner Production*, vol. 149, pp. 062–1067, 2017.

[31] S. K. Maganti, M. Sandeep Kauthsa Sharma, S. Umadevi et al., "Mechanical behavior of silica fume concrete filled with steel tubular composite column," *Advances in Materials Science and Engineering*, vol. 2021, pp. 1–9, Article ID 3632991, 2021.

[32] M. Chi, Y. Liu, and R. Huang, "Mechanical and microstructural characterization of alkali-activated materials based on fly ash and slag," *International Journal of Engineering and Technology*, vol. 7, no. 1, pp. 59–64, 2015.

[33] K. Komnitsas, D. Zaharaki, and G. Bartzas, "Effect of sulphate and nitrate anions on heavy metal immobilisation in ferronickel slag geopolymers," *Applied Clay Science*, vol. 73, pp. 103–109, 2013.

[34] J. L. Provis, R. J. Myers, C. E. White, V. Rose, and J. S. van Deventer, "X-ray microtomography shows pore structure and tortuosity in alkali-activated binders," *Cement and Concrete Research*, vol. 42, no. 6, pp. 855–864, 2012.

Hindawi
Advances in Civil Engineering
Volume 2023, Article ID 9894575, 1 page
https://doi.org/10.1155/2023/9894575

Retraction

Retracted: Performance of High Strength Concrete Containing Palm Oil Fuel Ash and Metakaolin as Cement Replacement Material

Advances in Civil Engineering

Received 10 October 2023; Accepted 10 October 2023; Published 11 October 2023

This article has been retracted by Hindawi following an investigation undertaken by the publisher [1]. This investigation has uncovered evidence of one or more of the following indicators of systematic manipulation of the publication process:

(1) Discrepancies in scope
(2) Discrepancies in the description of the research reported
(3) Discrepancies between the availability of data and the research described
(4) Inappropriate citations
(5) Incoherent, meaningless and/or irrelevant content included in the article
(6) Peer-review manipulation

The presence of these indicators undermines our confidence in the integrity of the article's content and we cannot, therefore, vouch for its reliability. Please note that this notice is intended solely to alert readers that the content of this article is unreliable. We have not investigated whether authors were aware of or involved in the systematic manipulation of the publication process.

Wiley and Hindawi regrets that the usual quality checks did not identify these issues before publication and have since put additional measures in place to safeguard research integrity.

We wish to credit our own Research Integrity and Research Publishing teams and anonymous and named external researchers and research integrity experts for contributing to this investigation.

The corresponding author, as the representative of all authors, has been given the opportunity to register their agreement or disagreement to this retraction. We have kept a record of any response received.

References

[1] M. H. Ismail, M. A. Megat Johari, K. S. Ariffin, R. P. Jaya, M. H. Wan Ibrahim, and Y. Yugashini, "Performance of High Strength Concrete Containing Palm Oil Fuel Ash and Metakaolin as Cement Replacement Material," *Advances in Civil Engineering*, vol. 2022, Article ID 6454789, 11 pages, 2022.

Hindawi
Advances in Civil Engineering
Volume 2022, Article ID 6454789, 11 pages
https://doi.org/10.1155/2022/6454789

Research Article

Performance of High Strength Concrete Containing Palm Oil Fuel Ash and Metakaolin as Cement Replacement Material

Mohd Hanif Ismail,[1] **Megat Azmi Megat Johari**,[2] **Kamar Shah Ariffin**,[3] **Ramadhansyah Putra Jaya**,[4,5] **Mohd Haziman Wan Ibrahim**,[1] **and Yugashini Yugashini**[1]

[1]*Faculty of Civil Engineering and Built Environment, Universiti Tun Hussein Onn Malaysia, Parit Raja, Batu Pahat 86400, Johor, Malaysia*
[2]*School of Civil Engineering, Engineering Campus, Universiti Sains Malaysia, Nibong Tebal 14300, Pulau Pinang, Malaysia*
[3]*School of Materials and Mineral Resources Engineering, Engineering Campus, Universiti Sains Malaysia, Nibong Tebal 14300, Pulau Pinang, Malaysia*
[4]*Faculty of Civil Engineering Technology, Universiti Malaysia Pahang, Gambang 23600, Pahang, Malaysia*
[5]*Institute for Infrastructure Engineering and Sustainability Management, Universiti Teknologi MARA, Shah Alam 40450, Selangor, Malaysia*

Correspondence should be addressed to Mohd Hanif Ismail; mohdhanif@uthm.edu.my

Received 9 March 2022; Revised 24 April 2022; Accepted 18 May 2022; Published 31 May 2022

Academic Editor: Andreas Lampropoulos

The release of carbon dioxide (CO_2) from the cement industry into the atmosphere and the increasing amount of oil palm waste from industrial plants lead to the problem of the greenhouse effect and environmental pollution. Studies on palm fuel ash (POFA) and metakaolin (MK) as a semi-substitute for cement can reduce the problem of the greenhouse effect and environmental pollution, as well as increase and improve the level of strength of concrete. Using mechanical and transport test methods as well as assisted by comparative X-ray Diffraction (XRD) analysis can prove the use of pozzolanic material as a catalyst to the compressive strength of concrete. In this study, slump test, compressive strength test, and water absorption test were conducted on samples containing total cement substitution up to 40% of POFA and MK as cement substitutes. The partial replacement of cement with MK and POFA reduced the workability of the concrete. However, binary and ternary blended concrete containing MK and POFA provide better compressive strength compared to OPC concrete up to 9.5% after 28 days age. Moreover, it was found that, the compressive strength of concrete containing POFA was better than the concrete containing MK up to 4%.

1. Introduction

The Portland cement is produced from finely ground clinker. The finely ground clinker is a substance composed mainly by hydraulically active calcium silicate minerals. This substance is formed via high temperature burning of limestone and other materials in kiln [1]. During the process of producing cement, it demanded about 1.7 tons of raw materials per ton of clinker, and the process discharges approximately 1 ton of carbon dioxide to the atmosphere. Therefore, this horrifying carbon dioxide discharge causes the cement industry to become main sources of greenhouse gases in the aspect of industrial manufacturer [2, 3]. Rapid economic growth has increased cement production in the construction industry sector, thus causing problems to the environment [4]. The cement industry is facing a lot of struggles including environmental issue and sustainable issue [4]. This is because the cement manufacture will not only discharge carbon dioxide but also nitrogen oxides (NO_2), sulfur dioxide (SO_2), and grey dust to the atmosphere [5]. The activities that lead to air pollution in cement manufacture including excavation activities, crushing mills, and kiln emissions. A survey regarding the air pollutants emission in Kuala Lumpur was carried out and the result clearly observes that the respirable

dust (PM10) emission from the cement industry is the highest among the other pollutants [6]. Thus, cement industry can cause severe air pollution if no proper solution is taken.

Besides, the study carried out by Sharma et al. [7] proved that the cement industry pollutant can cause 5% to 17% of reduction in Forced Expiratory Volume (FEV). Thus, it could lead to severe respiratory diseases if the person is exposed to the pollutant for a long time. Therefore, a method was proposed to reduce the negative effect toward the environment and increase the quality of concrete, which is applied certain type of material for partial replacement for the manufacture of Portland cement. This material can be industrial or agriculture wastes. The blending between Portland cement and this waste will produce a mixture known as "composite cement" or "blended cement" [8]. The performance of composite cement will still be similar with the general Portland cement as they will react when mixed with water and become harder, in which finally the same hydration products are formed. The most common material used as the replacement material is pozzolanic material such as fly ash, condensed silica fume, and rice husk ash [3, 8]. When the Portland cement is used to carry out the hydration reaction, a chemical substance $Ca(OH)_2$ will produce as one of the by-products and lead to the deterioration of concrete. However, by using pozzolanic material which is composed of amorphous silica to carry out the hydration process of cement, additional calcium silicate hydrate (CSH) will produce, which is also the dominant cementing component. Thus, it is obvious that the application of pozzolanic material can significantly increase the quality of concrete, however, a study from Zeyad et al. [9] stated that the replacement of pozzolanic material should not contain more than 60% of cement as the excess replacement will cause increasing demand for superplasticiser, water, and reduce the workability [9]. Therefore, in this project, treated palm oil fuel ash and metakaolin were chosen as the pozzolanic material. Palm oil fuel ash (POFA) was chosen to use as the pozzolanic material in this project because palm oil industry is one of the most developed agriculture industry in Malaysia. According to the global palm oil production research in 2017, Malaysia was known as the second most in the production of palm oil [10].

According to the research from the United States Department of Agriculture, the combination of palm oil production globally in year 2016 and 2017 will be about 64.5 million metric tons [10]. Large quantity of waste in the form of remnants of fibers and kernels will be produced after the extraction of palm oil. According to the research, about 3.14 million tons of palm oil fuel ash was produced in Malaysia annually, while Indonesia produced about 3.7 million tons of POFA annually [11]. Thus, we can conclude that our country can supply large amount of palm oil fuel ash. Furthermore, accumulation of large amount of palm oil fuel ash may lead to several environmental issues and health problem if failed to maintain or dispose it properly. Besides, the palm oil fuel ash is also being applied to enhance the durability characteristic of concrete. Another reason for choosing palm oil fuel ash in this project is that research stated that 40% of microfine palm oil fuel ash replacement can enhance the workability and viscosity of concrete [12]. Moreover, the POFA also proved that it can decrease heat emission throughout the hydration process as it can be applied to treat the thermal cracking due to drastic increase in temperature in mass mortar [13]. POFA also can improve the resistance of concrete toward acidic and sulfate environment. The POFA also have the advantage of the capability to increase shrinkage of concrete and decrease the heat development [13].

The metakaolin was chosen as the pozzolanic material in this project because it can bring several advantages to the concrete including increase the compressive strength, increase the flexural strength, and increase the resistance toward chemicals. The metakaolin can also decrease shrinkage that is caused by particle packing and indirectly raising the strength and density of concrete [14]. The properties of metakaolin stated above were related to this project which is effect toward workability and compressive strength. According to the research, concrete composed of metakaolin was proved to decrease the expansion caused from alkali-silica reaction and chloride ions penetration process [15]. It also proved that the metakaolin can refine the pore structure of cement paste of concrete by forming a secondary CSH [15]. The application of metakaolin as pozzolanic material can also bring advantages such as improving the resistance of concrete toward acidic and sulfuric environment. The other reason for selecting metakaolin as pozzolanic material applied in this project is that it can decrease porosity as an addition of 2% of metakaolin and result in the decrease of porosity by 10% [16].

The research regarding application of palm oil fuel ash has been studied and investigated deeply since the late nineteenth century. The optimum percentages of palm oil fuel ash replacement for cement would be 10% to 20% as the higher percentage of POFA will decrease the compressive strength of concrete [17]. There was also much research showing that the ground POFA can be used as supplementary cementing material in high strength concrete due to its excellent pozzolanic property. The POFA will be sieved before being applied in the experiment because fine POFA produced will form a more precise result and indirectly increase the strength of concrete. The purpose of the application of metakaolin is to enhance the compressive strength of the concrete. However, the accurate percentage of the application of POFA and metakaolin was also an issue.

The outcome of this research will summarize the application of palm oil fuel ash, superplasticiser, and metakaolin together with their effectiveness in the compressive strength of concrete. From this finding, it could help the other researchers in this field in having more understanding and information about the application of POFA and MK and how it affects the compressive strength of sustainable high strength concrete. The information can be used for further study in this scope.

2. Materials and Method

The primary materials of this study were ordinary Portland cement (OPC), POFA, MK, sand, gravel, water, and superplasticiser. POFA and MK wastes used as semi-cement

substitutes were ensured that their fineness was below 10 micrometres and was heat-treated at 500°C and 700°C for one hour, respectively. The POFA and MK are Class F and Class N, respectively, based on ASTM 618 [18]. The sizes of the fine and coarse aggregates used averaged under 2.36 mm and 14 mm, respectively. The superplasticiser used is compliant with the ASTM C494 type F [19] admixture which improves the workability of concrete.

Table 1 shows the properties of the materials used through the particle size analyser and air permeability methods. Specific surface area and particle size were obtained from the particle size analyser while Blaine surface area was obtained using BS EN 196 [20]. Table 2 shows the chemical composition of the binders used in this study. OPC contains a total amount of silicon dioxide, aluminum oxide, and iron oxide of 28.86%. In comparison, POFA and MK were 73.43% and 93.23%, respectively. Figures 1–3 shows element analysis using Scanning Electron Microscope Energy Dispersive X-ray Analysis (SEM-EDX), particle size analysis for POFA, MK, fine aggregate, and coarse aggregate.

2.1. Specimen. The mixing of concrete containing semi-substitute cement is carried out based on the substitution of the cement mass with the mass of cement substitute material. Eight concrete mixtures containing semi-substitute cement and a control concrete mixture were conducted for the success of this study. These nine mixtures were conducted to prepare the samples for workability testing, compression strength testing, water absorption testing, and microstructural analysis. Slump test was carried out on fresh concrete mix before the concrete mix was put into 100 mm × 100 mm × 100 mm cube mould and 500 mm × 100 mm × 100 mm prism for compressive strength test samples and water absorption test. The fresh concrete mixture was also sieved using a 2.36 mm sieve to separate the coarse aggregate and fresh mortar. The fresh mortar is then placed in an ice cube mould for the use of a microstructure analysis sample. Table 3 shows the design of the mixture according to the density of each material used within 1 m^3 of concrete.

After the concrete and mortar mixture placed in each mould is compacted, the concrete and mortar were removed from the mould and fully immersed in a tank filled with water for 180 days for the curing process. Samples of 7, 28, 60, 90, and 180 days old were subjected to a compressive strength test and a water absorption test. For mortar samples, mortar samples of 7, 28, and 90 days old were soaked in acetone until completely dry to stop the hydration process of the cement and the samples were crushed into dust. The dust from the mortar sample was analysed using an XRD scan to identify compounds formed following a hydration and pozzolanic reaction in the concrete.

2.2. Testing and Analysis Method. Slump tests were conducted to measure the workability of fresh concrete based on BS EN 12350-5 [21]. The density of concretes was determined based on BS EN 12350-7 [21]. Compressive strength tests were performed on 100 mm × 100 mm × 100 mm cube samples of sufficient age based on BS EN 12390-3 [22]. Concrete water absorption tests were also conducted on mature samples using 55 mm diameter and 40 mm thickness concrete cores extracted from 500 mm × 100 mm × 100 mm prism concrete and the tests were performed based on RILEM CPC11.3 [23]. The compound phrases in the dust samples were characterised using XRD equipment that complied with BS EN 13925-1 [24] and then analysed using X'Pert HighScore Plus software. Based on the analysis, portlandite or calcium hydroxide (CH) and tobermorite or calcium silicate hydrate compounds were detected in most of the dust samples in zones 1 and 2 as shown in Figure 4. Counts of CH in zones 1 were analysed to understand the concrete mechanisms in this study that contribute to concrete strength, and for counts of CSH analysed in zone 2 on dust samples aged 7, 28, and 90 days as in Figure 5. Zone 1 is between 34° and 35° and zone 2 is between 51° and 52° of °2Θ. Nima et al. [25] studied that there is a CH intensity value in the scan range 34°. Haider et al. [26] also stated that there is portlandite material at scan range 34°. The study of Bamaga et al. [27] also showed portlandite material at scan range 34°. Data for scan range 51° has been found to have minerals such as quartz which with the addition of chemical components such as SiO_2 can give more compressive strength to concrete. Yusof et al. [28] stated in their research of POFA samples also found that quartz is a chemical composition found in the scan range 51°. Elahi et al. [29] found similar results on the MK sample that said the chemical composition of quartz on the scan range 51°. Research from Haider et al. [26] also said that the chemical composition for OPC control in the scan range 51° is quartz. The increase in value for each sample indicates CSH formation at scan range 51°.

3. Results and Discussion

3.1. Slump Test. Results from a slump test conducted on nine fresh concrete mixes found that the partial replacement of cement with MK and POFA reduced the workability of the concrete. The partial replacement of cement with 10% MK reduced the workability of concrete by 61.7%, while the partial replacement of cement with POFA by 40% only experienced a workability reduction of 29.4%. The workability of concrete containing POFA is better than concrete containing MK by 32%. The Blaine surface area of MK (0.881 m^2/g) which is wider than POFA (0.79 m^2/g) causes the concrete containing MK to absorb higher water than the concrete containing POFA, hence the concrete containing MK experiences a higher reduction in workability. Apart from this, Zoe et al. [30] stated that fine MK acts as a filler filling the spaces between binder, sand, and coarse aggregate causing fresh concrete to be more stiff and lower workability. The workability of concrete binaries containing MK and POFA is very low, and the slump difference is very high compared to concrete binaries containing only MK or POFA. Therefore, using a higher superplasticiser is required to improve the workability of concrete ternary (Figure 6).

Table 1: Properties of material.

Material	Type/properties	Specific surface area (m^2/g)	Particle size mean (μm)	Blaine surface area (m^2/g)
Cement	Normal Portland cement	1.16	16.4	0.32
POFA	POFA passing sieve 300 μm, refined for 8 hours in ball mill and Heat treatment 500°C for 1 hours	1.72	9.64	0.79
MK	Kaolin via heat treatment 700°C for 1 hours	1.48	8.36	0.881
Coarse aggregate	Passing sieve 14 mm	—	—	
Fine aggregate	Passing sieve 5 mm	—	—	
Water	Tap water	—	—	

Table 2: Chemical composition of materials.

	Chemical composition (%)		
	OPC	POFA	MK
Silicon dioxide (SiO_2)	20.63	60.78	55.04
Aluminum oxide (Al_2O_3)	4.71	6.96	37.44
Iron oxide (Fe_2O_3)	3.52	5.69	0.75
Calcium oxide (CaO)	60.98	5.20	0.02
Magnesium oxide (MgO)	0.98	4.17	0.81
Sodium oxide (Na_2O)	0.06	0.10	—
Potassium oxide (K_2O)	1.09	5.40	2.31
Sulfur trioxide (SO_3)	4.97	0.22	—
Loss of ignition (LOI)	2.38	3.00	2.50
SiO_2+Al_2O_3+Fe_2O_3	28.86	73.43	93.23

3.2. Slump Flow Table Test. The results of the slump flow test of concrete mix containing MK and POFA are better than the slump test. The results of the slump flow test for nine fresh concretes are shown in Figure 7. The test results found that the partial replacement of cement with POFA and MK reduced the workability of fresh concrete by reducing the diameter of fresh concrete. Partial replacement of cement with 10% MK reduced the diameter of fresh concrete by 25.4%, while partial replacement of cement with POFA by 20% and 40% showed a reduction in the diameter of fresh concrete by 26% and 25.4%, respectively. The ternary diameter of concrete also experienced a reduction in workability between 15.9% and 31% compared to OPC concrete.

3.3. Density. Figure 8 shows the density of concrete in this study from the age of 7 days to 180 days. Partial replacement of cement with MK and POFA lowers the overall concrete density. Thus, the density of concrete containing MK and POFA is lower than that of ordinary concrete. Concrete containing a total of 40% cement substitute material showed the lowest concrete density compared to other concretes in this study. All concretes in this study experienced an increase in density from the age of 7 days to 180 days. The increase in concrete density from the age of 7 days to 180 days indicates the increase of mass in the concrete due to the reaction between cement, MK, POFA, and water that causes the addition of cement hydration and secondary hydration products. Sofri et al. [31] also experience the same situation where total concrete densities decreases when cement is replaced by POFA.

3.4. Water Absorption of Concrete. From Figure 9 concrete containing MK and POFA cement substitutes has lower water absorption than ordinary concrete. Concrete containing more cement substitutes shows lower water absorption. Concrete in the group of total cement substitutes of 40% showed the lowest water absorption followed by the group of total cement substitutes of 20%, 10%, and 5%. The pores of the concrete become smaller or smaller causing the water absorption in the concrete to decrease. The cause of reduced water absorption is from the addition of hydration cement and secondary hydration product in concrete in parallel with the increase in concrete density from the age of 7 days to 180 days. In addition, there is a strong trend in the absorption of water that reduces as POFA material increases [32].

3.5. Compressive Strength. Table 4 and Figure 10 are the results of compressive strength tests for nine different types of concrete from the age of 7 days to 180 days. M5 concrete containing 5% MK and 95% cement was the strongest concrete at 7 days concrete age with 11% stronger than OPC concrete, while P40 concrete containing 40% POFA and 60% cement was the weakest concrete in this study at 7 days age with 11% weaker than OPC Concrete. Next is P15M5 concrete containing 15% POFA and 5% MK, i.e., the strongest ternary concrete at the age of 7 days with 0.8% stronger than OPC concrete. The study of Ahmad et al. [33] obtained the same result, whereby the replacement of POFA with 15% has obtained the highest optimum compressive strength. The finer MK than cement acts as a filler to reduce the pores in the concrete and the aluminum Oxide content in the MK influences the hydration reaction by increasing the initial strength of the M5 and P15M5 concrete. To add on, Arslan et al. [34] mentioned that MK in cement functions as a filler, accelerating cement hydration at the early age of 3 days. By speeding up the hydration process, more CH is formed, and this CH combines with the active silica and aluminate phases of pozzolans, resulting in secondary calcium aluminosilicate hydrates at an early stage. The study by Narmatha & Felixkala [35] also obtained similar results, where the replacement of cement with MK increased the early strength of the concrete. MK concrete strength increases are effective only at the early age of concrete and the strength increase is only marginal in the long term [35].

Excessive cement replacement inhibits the hydration reaction resulting in a reduction of the early strength of P40 concrete. Studies also state that the compressive strength of

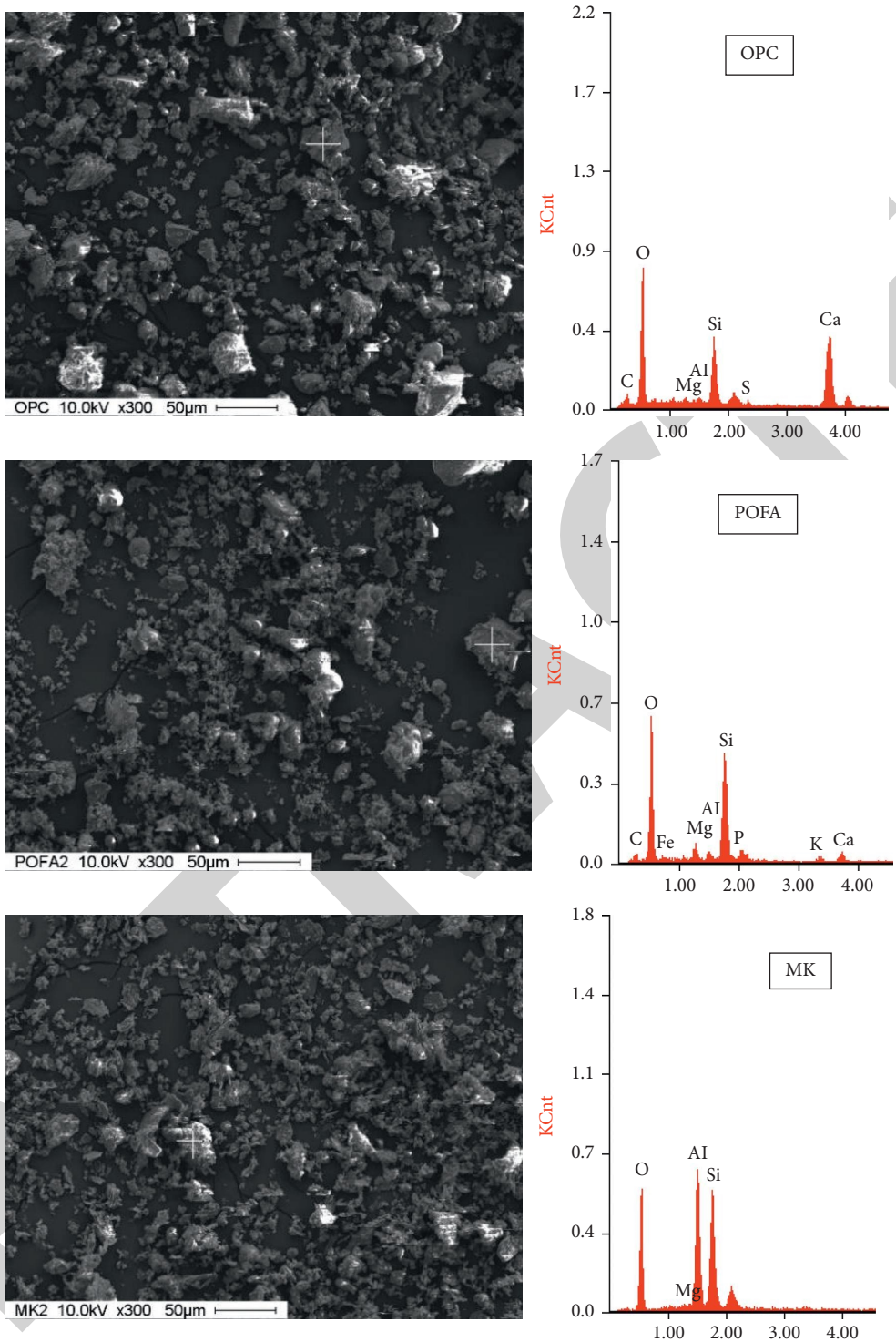

Figure 1: OPC, POFA, and MK element analysis using SEM –EDX.

POFA at an early age is lower than OPC [32]. Conditions changed when the concrete age reached 28 days, P40 concrete underwent a high strength change with a strength increase of 36% from 56 MPa to 76.5 MPa. P40 concrete at 28 days of age was 6% stronger than OPC concrete.

M5 concrete which is the strongest concrete at the age of 7 days experienced a strength increase at a low rate of 9% from 69.9 MPa to 76.5 MPa at the age of 28 days. M5 concrete was 6.3% stronger than OPC concrete at 28 days of age. For ternary concrete, P35M5 concrete showed a better increase in strength than other ternary concretes and P35M5 concrete was 3.6% stronger than OPC concrete at 28 days. Ismail et al. [36] obtained a similar result as well, whereby the replacement of POFA partially in cement increases the

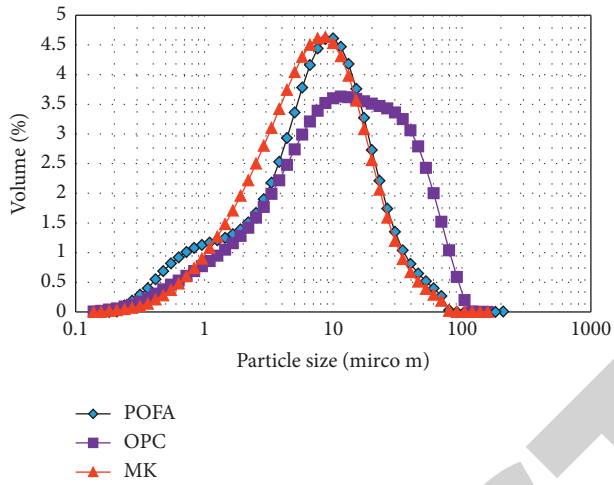

Figure 2: Particle size analysis of OPC, POFA, and MK (Mastersizer 2000 Ver 5.4, Malvern Instruments Ltd).

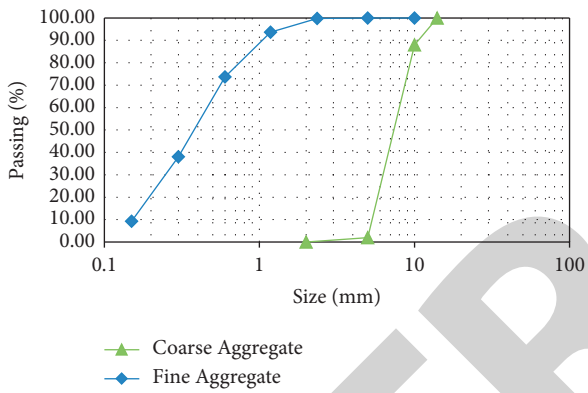

Figure 3: Coarse and fine aggregate sieve analysis.

compressive strength. It also highlights that higher compressive strength is achieved due to its fines [36].

Concrete containing heat-treated POFA contains high silica content that begins to be reactive after the concrete age of 7 days. The high silica content in concrete and the smaller size of POFA than cement led to an increase in hydration and pozzolanic reactions which resulted in an increase in strength in concrete containing POFA at 28 days.

After 28 days of concrete age, concrete containing MK cement substitute showed a decreasing pattern of increasing concrete strength. In comparison, binary and ternary concretes containing POFA and MK cement substitutes continue to show a pattern of continuous increase in strength. Sam et al. [37] documented that the progressive strength of concrete containing POFA and MK increases due to the pozzolanic response, which usually improves over age. The synergetic effect of POFA and MK in concrete can be seen in ternary concrete where the increase in strength of ternary concrete continues to increase with the age of concrete.

3.6. X-Ray Diffraction Analysis. Figure 11 shows the counts of CH in zone 1(Figure 5), while Figure 10 shows the counts of CSH in zone 2 (Figure 5) analysed from XRD scan results up to a concrete age of 90 days. Substitution of cement with POFA and MK causes the CaO content to decrease in concrete causing the hydration product of CH to decrease [38]. The results of zone 1 analysis found that concrete containing POFA and MK as cement substitutes contained less CH content than OPC concrete in line with the study [38]. However, CH content continued to increase in parallel with hydration reaction until the concrete age of 90 days. No increase in CH content was recorded for P40, CH content for P40 continued to decrease with concrete age. The decrease in CH content in concrete containing more than 5% cement substitute material at 28 days of concrete age is the effect of the reaction of CH with silicon dioxide and aluminum oxide to form more CSH and calcium aluminosilicate hydrates (CASH) in concrete. The synergetic effect of POFA and MK can be seen in ternary concrete with higher CH content for ternary concrete containing 20% cement substitute material compared to ternary concrete containing 40% cement substitute material. The unhydrated CaO in POFA and unhydrated cement reacts with the water present promoting the growth of CH content in concrete. This is because, when the degree of hydration of the mineral admixture is low and the amount of CH that has not reacted with the mineral admixture is significant, the consumption rate of CH increases due to a large number of mineral admixtures [39].

The results of zone 2 analysis in Figure 12 found that the replacement of cement with silica -rich cement substitute increased the CSH content in concrete. Concrete containing more than 5% cement substitutes experienced a decrease in CSH content at an early stage compared to OPC. Replacement of cement with POFA or MK resulted in a decrease in CaO content in concrete resulting in a reduction in CSH production compared to OPC concrete [40]. Nevertheless, the CSH content in concrete continues to increase with the pozzolanic reaction in which silicon dioxide reacts with CH to form more CSH between the concrete ages of 7 to 90 days. However, the CSH content in concrete containing POFA and MK could not match the CaO-rich OPC concrete. The CSH content of M5 concrete was higher than OPC concrete at 7 days, but the production of CSH content of M5

Table 3: Mix design proportion.

Mix	OPC (kg/m^3)	POFA (kg/m^3)	MK (kg/m^3)	Total (kg/m^3)	Sand (kg/m^3)	Gravel (kg/m^3)	Water (kg/m^3)	SP (kg/m^3)
OPC	500	—	—	500	750	1250	150	15
M5	475	—	25	500	750	1250	150	15
M10	450	—	50	500	750	1250	150	15
P20	400	100	—	500	750	1250	150	15
P40	300	200	—	500	750	1250	150	15
P15M5	400	75	25	500	750	1250	150	15
P35M5	300	175	25	500	750	1250	150	15
P10M10	400	50	50	500	750	1250	150	15
P30M10	300	150	50	500	750	1250	150	15

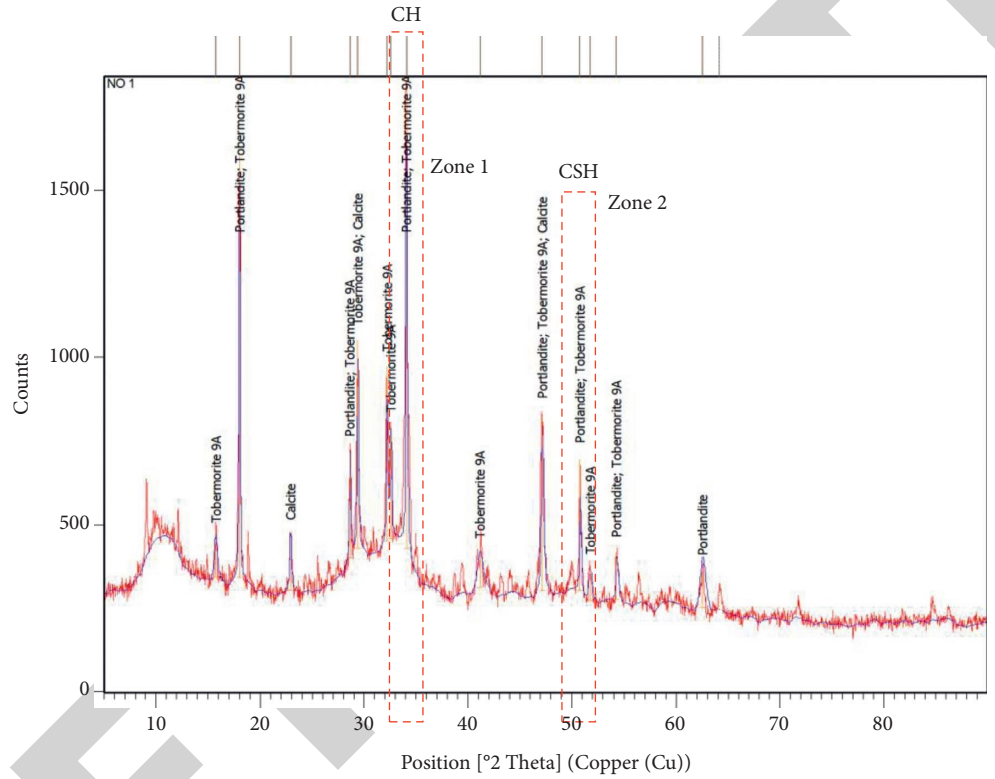

Figure 4: Compound scanning using X′ pert highscore software.

concrete decreased after 7 days. M5 concrete containing MK is more likely to react in the early stages of the hydration process. The high CSH production for P40 and P30M10 concretes after 28 days of concrete age is due to the result of a pozzolanic reaction in concrete, in which CH reacts with silicon dioxide to form more CSH. According to Ash et al. [38], the pozzolanic reactions involve a secondary reaction whereby the CH and silica content integrate to form the strength by contributing CSH. This will develop the strength of concrete beyond 28 days.

3.7. Influence of Water Absorption, Calcium Hydroxide, and Calcium Silicate Hydrate on Compressive Strength. The strength of concrete is influenced by the rate of absorption of water, CH, and CSH in the concrete. OPC concrete experiences high water absorption compared to other concretes. OPC concrete also contains high CH and CSH compared to other concretes. Although the CSH content of OPC concrete is high, it does not contribute to a higher strength than other binary and ternary concrete because OPC concrete contains high porosity, which contributes to high water absorption. High porosity of OPC concrete results in low strength of OPC concrete. Cement replacement with POFA and MK over 5% substitution causes the concrete to contain less CaO, which is required in the hydration process to produce CH and CSH. The lack of CaO in concrete causes the production of CH, and CSH is to be reduced. Nevertheless, the presence of more silicon dioxide than POFA and MK contributes to the pozzolanic reaction which increases the CSH content in concrete. This unhydrated silicon dioxide reacts with CH to produce CSH in concrete which causes a decrease in CH content in concrete. Like OPC concrete, the strength of these binary and ternary concretes is influenced by the porosity of the concrete, CH, and CSH content. Binary and ternary concretes with a low water absorption rate, lower CH

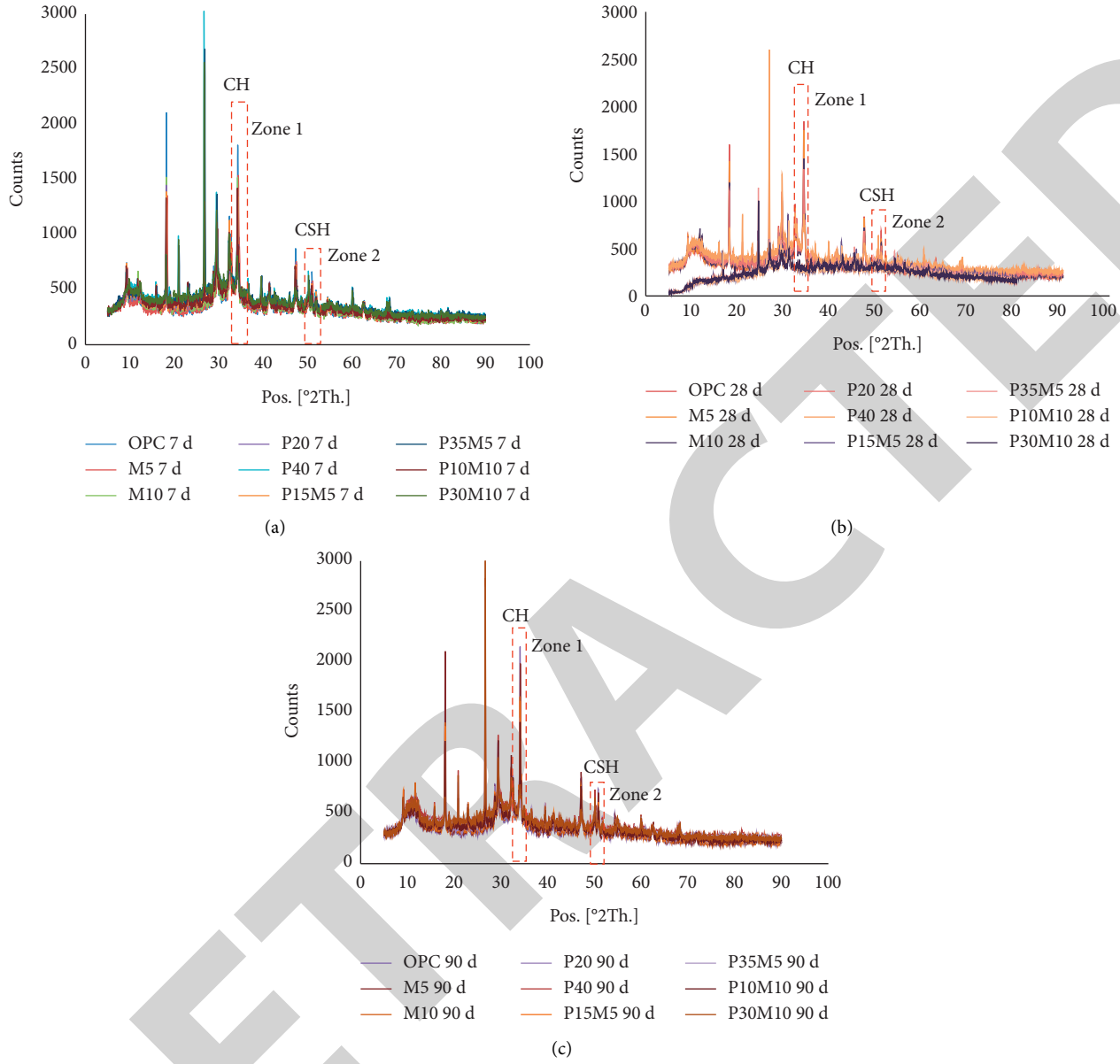

Figure 5: Samples counts analysis by zone for 7 to 90 days age.

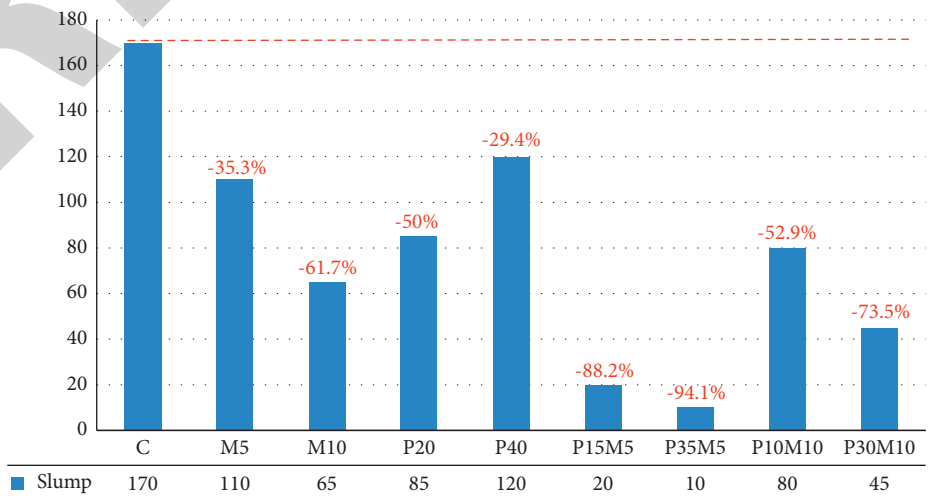

Figure 6: Concrete slump test results.

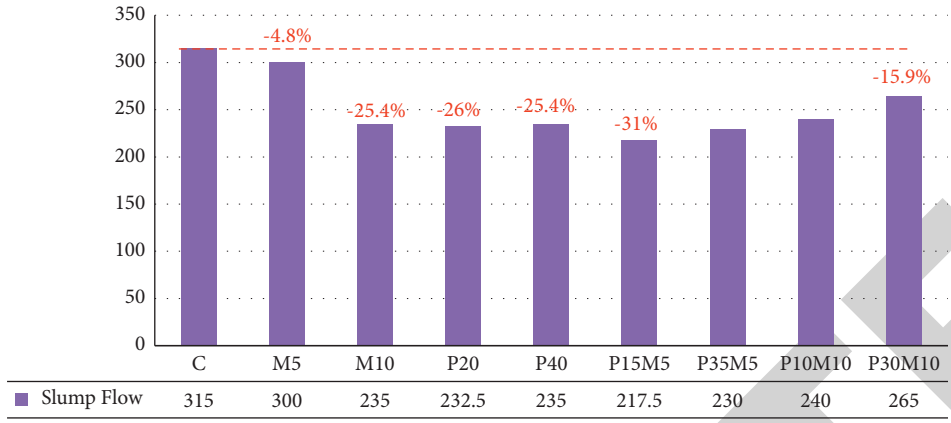

Figure 7: Concrete slump flow table results.

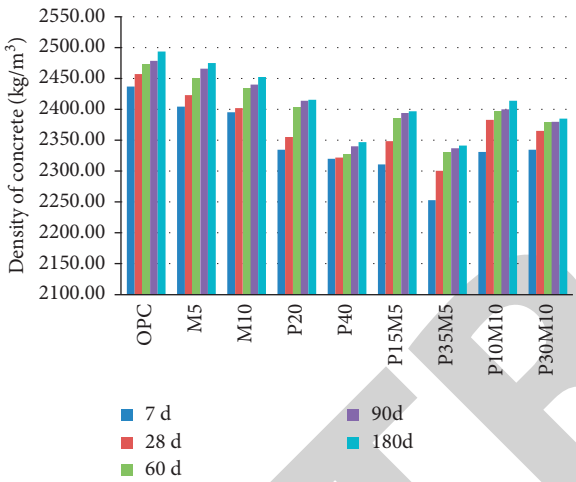

Figure 8: Density of concrete.

Table 4: Compressive strength of concrete.

	7 d	28 d	60 d	90 d	180 d
OPC	63.0	72.0	79.0	82.0	85.0
M5	69.9	76.5	80.5	83.0	86.0
M10	65.8	78.5	84.0	86.7	88.0
P20	60.3	75.6	85.0	87.9	88.9
P40	56.0	76.5	86.0	89.8	91.5
P15M5	63.5	73.7	83.0	86.7	89.0
P35M5	62.4	74.6	84.8	88.4	90.8
P10M10	61.0	73.2	81.0	85.0	89.7
P30M10	60.1	73.5	82.0	86.7	89.9

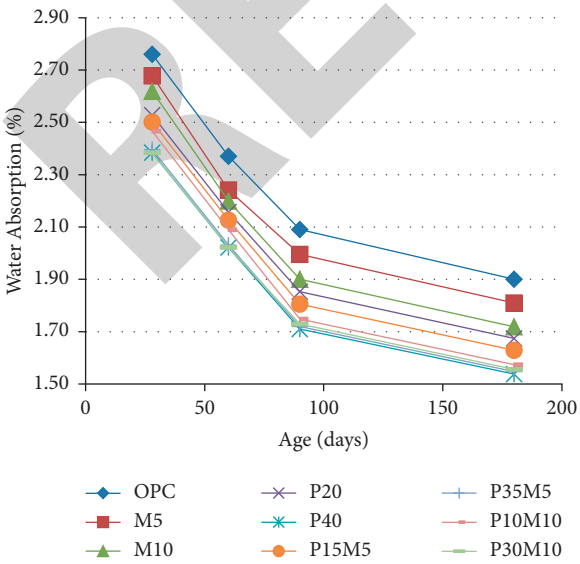

Figure 9: Water absorption of concrete.

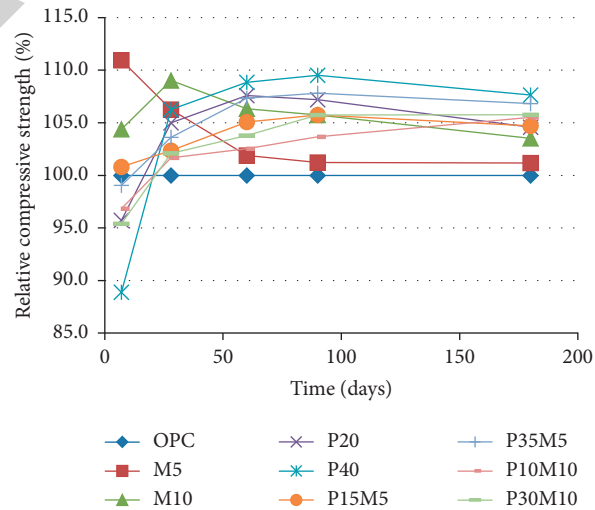

Figure 10: Relative compressive strength of concrete.

content than OPC concrete, and have high CSH production increase contributes to higher concrete strength. P40 concrete showed low water absorption results, in low CH content but increased in high CSH production resulting in P40 concrete being stronger than other concretes. Adebayo et al. [41] also explained in their research that the compressive strength of concrete is influenced by the presence of CH and CSH in the pozzolanic reaction.

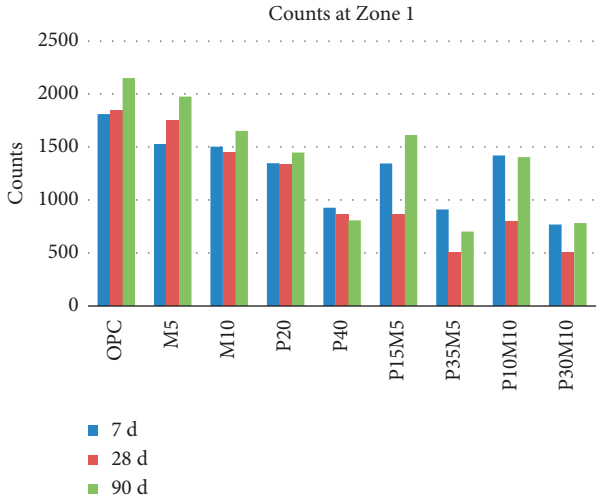

Figure 11: XRD analysis at zone 1 (Figure 5).

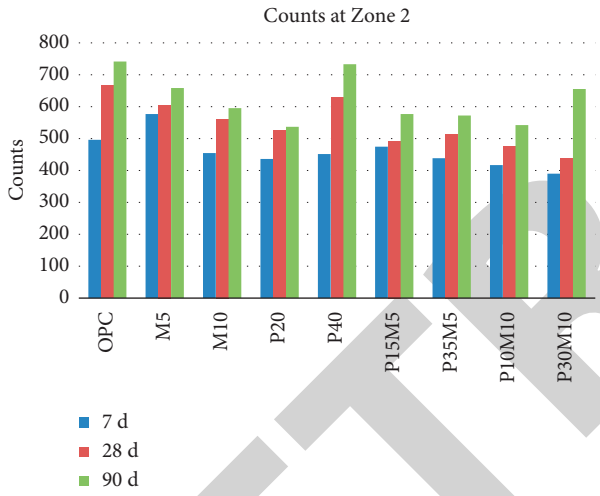

Figure 12: XRD analysis at zone 2 (Figure 5).

4. Conclusion

Concrete containing POFA and MK has lower workability compared to OPC concrete. By adding superplasticiser content, the workability of concrete containing POFA and MK can be improved. In addition, concrete containing POFA and MK has a lower density of concrete than OPC. Concrete containing POFA and MK also has a lower water absorption rate than OPC concrete, wherethe high-water absorption in concrete is the cause of the low strength of concrete. Meanwhile, concrete containing POFA and MK has lower CH and CSH content than OPC concrete. Nevertheless, the increase in high CSH production contributed to the increase in the strength of concrete containing POFA and MK.

Data Availability

The data used to support the findings of this study are included within the article.

Conflicts of Interest

The authors declare that they have no conflicts of interest.

Acknowledgments

This research was supported by the Ministry of Higher Education (MOHE) through Fundamental Research Grant Scheme (FRGS/1/2021/STG05/UTHM/03/2). The authors also would like to thank the Universiti Tun Hussein Onn Malaysia staff in the laboratory of Faculty of Civil Engineering and Built Environment, where the research was conducted, and would like to thank Bandung Palm Oil Mill Sdn. Bhd., for providing POFA in this research.

References

[1] M. Bustillo Revuelta, "Cement," in *Construction Materials*, Springer Textbooks inEarth Sciences, Geography and Environment, pp. 117–165, Springer, Cham, 2021.

[2] B. Bakhtyar, T. Kacemi, and M. A. Nawaz, "A review on carbon emissions in Malaysian cement industry," *International Journal of Energy Economics and Policy*, vol. 7, no. 3, pp. 282–286, 2017.

[3] S. Ali, T. Behzad, and K. K. Reza, "Effect of fly ash and silica fume on transition zone, pore structure and permeability of concrete," *Magazine of Concrete Research*, vol. 70, no. 10, pp. 519–532, 2018.

[4] K. S. Devi, V. V. Lakshmi, and A. Alakanandana, "Impacts of cement industry on environment-an overview," *Asia Pac. J. Res*, vol. 1, pp. 156–161, 2017.

[5] K. Sivaguru, "Air pollutant emission and control techniques for the cement manufacturing industry," *International Journal of Information and Computing Science*, vol. 6, 2019.

[6] A. Azhari, N. D. Abdul Halim, M. Othman et al., "Highly spatially resolved emission inventory of selected air pollutants in Kuala Lumpur's urban environment," *Atmospheric Pollution Research*, vol. 12, no. 2, pp. 12–22, 2021.

[7] B. P. Sharma, D. G. Gopal Purohit, and S. K. Singh, "Effect of air pollution from cement manufacturing plants on "Forced Expiratory Volume of Lungs" of children," *American International Journal of Research in Formal, Applied & Natural Sciences*, vol. 19, no. 1, pp. 13–17, 2017.

[8] A. A. Raheem, R. Abdulwahab, and M. A. Kareem, "Incorporation of metakaolin and nanosilica in blended cement mortar and concrete-A review," *Journal of Cleaner Production*, vol. 290, Article ID 125852, 2021.

[9] A. M. Zeyad, A. H. Khan, and B. A. Tayeh, "Durability and strength characteristics of high-strength concrete incorporated with volcanic pumice powder and polypropylene fibers," *Journal of Materials Research and Technology*, vol. 9, no. 1, pp. 806–818, 2020.

[10] A. M. Zeyad, M. A. Megat Johari, B. A. Tayeh, and M. O. Yusuf, "Pozzolanic reactivity of ultrafine palm oil fuel ash waste on strength and durability performances of high strength concrete," *Journal of Cleaner Production*, vol. 144, pp. 511–522, 2017.

[11] S. G. D. Iya, M. Z. Noh, N. A. A. Kutty et al., "Effect of palm oil fuel ash treatment on physico-mechanical properties of porcelain," in *AIP Conference Proceedings*, vol. 2068, no. 1, Article ID 020093, AIP Publishing LLC, Melville, February 2019.

Hindawi
Advances in Civil Engineering
Volume 2022, Article ID 2919167, 10 pages
https://doi.org/10.1155/2022/2919167

Research Article

Effect of Coral Aggregates of Blended Cement Concrete Subjected to Different Water Immersion Condition

Bunyamin Bunyamin,[1] **Febrina Dian Kurniasari**,[1] **Reza Pahlevi Munirwan**,[2] **and Ramadhansyah Putra Jaya**[3,4]

[1]*Department of Civil Engineering, Faculty of Engineering, Universitas Iskandar Muda, Banda Aceh 23234, Indonesia*
[2]*Department of Civil Engineering, Faculty of Engineering, Universitas Syiah Kuala, Banda Aceh 23111, Indonesia*
[3]*Faculty of Civil Engineering Technology, Universiti Malaysia Pahang, Kuantan 26300, Pahang, Malaysia*
[4]*Institute for Infrastructure Engineering and Sustainability Management, Universiti Teknologi MARA, Shah Alam 42300, Selangor, Malaysia*

Correspondence should be addressed to Reza Pahlevi Munirwan; r.munirwan@unsyiah.ac.id

Received 14 January 2022; Revised 4 April 2022; Accepted 6 May 2022; Published 14 May 2022

Academic Editor: Abdulkadir Cuneyt Aydın

The increasing use of concrete in construction has caused an increase in the need for resources for concrete mixtures and driving wide-scale mining. One alternate material that can be used for aggregates replacement is coral. Coral aggregates (CA) have similar chemical characteristics to cement. The compressive strength and tensile splitting strength tests of concrete coral aggregates were performed based on the ASTM and ACI standards. This study aims are to investigate the usage of CA as a partial replacement of cement and fine aggregate to increase the strength of concrete at substitution percentages of 0, 5, 10, and 15%. Two different water submerged scenarios of distilled water and salt sea water immersion were applied. The concrete strength test was carried out after 28 days of curing time, with the specified concrete quality of 17 MPa. The results showed that immersion in distilled water has a higher concrete strength than immersion in sea water. The maximum compressive strength of concrete for distilled and sea water immersion is for 0% CA content of 18.47 and 14.89 MPa, respectively. Moreover, the highest value of the split tensile strength of concrete with distilled and sea water immersion is for CA substitution of 5% of 2.52 and 2.5 MPa, respectively. The addition of 5% coral aggregates to cement and fine sand is the optimum combination since it increases the maximum split tensile strength of concrete.

1. Introduction

Global production of cement is over 12 billion tons per year, which equals nearly 1 m^3 per person per year, making it one of the world's major consumers of natural resources [1–3]. By 2025, concrete consumption is expected to exceed 7.5 billion m^3 (approximately 18 billion tons) per year [4, 5]. Concrete is a fundamental component that is regularly utilized in the construction of buildings [6–8]. Concrete is made up of cement, aggregates, chemical and mineral admixtures, and water and contains a large proportion of artificial components [9, 10]. The amount of concrete consumed on our entire Planet is measured in billions of tons [1, 11, 12]. The extensive use of concrete in the building has increased the demand for concrete materials, resulting in large-scale mining for raw materials [13–15]. The consequences of this condition include a decline in the availability of materials such as cement for concrete production, which is directly proportionate to the increase in costs and material shortages [16, 17].

With the marine industry rapid development, marine engineering infrastructure projects such as island construction, reclamation, and massive floating structures are rising [18]. Due to the remoteness of the island from the near mainland and accompanying transportation challenges, materials like aggregates and water supplies are scarce on-site [19]. Coral debris is a unique organic sedimentary rock that contains more than 96% calcium carbonate and is abundant on the sea island [20]. Coral debris is primarily formed of coral reef alga and marine species bone debris [21]. It is the result of channel digging and harbor dredging, as well as natural weathering, which take up valuable island

space and have a detrimental effect on ecological systems [20]. As a result, maximizing the utilization of this coral debris is necessary to meet the marine industry's material requirements. Additionally, Aceh-Indonesia has one of the highest rates of seismic activity in the world [22, 23]. Notably in the aftermath of multiple historic big earthquakes in Aceh, such as the 8.9 Mw earthquake-tsunami of 2004 that caused death and destroyed numerous structures [24], it is critical to conduct a comprehensive analysis of the concrete used in construction [25].

Coral aggregates (CA) are a type of undersea environment comprised of coral invertebrates that produce a calcium carbonate structure, a form of limestone. CA is typically composed of limestone, which means that the aggregates formed from coral have the most chemical content in the form of $CaCO_3$, which is classified as limestone [26]. CA may be used in the replacement of fine aggregate in concrete as a substitute ingredient [18, 19, 27, 28]. By and large, CA is composed of limestone. This is because these rocks contain a high concentration of CaO [29]. Geologically defined, limestone-containing rock is also referred to as crystalline limestone. Meanwhile, coral reefs degrade when they are damaged. As a result, this form of rock is known as coral limestone [26]. CA is formed when coral reef-building organisms deposit vast amounts of calcium carbonate ($CaCO_3$). Calcium carbonate ($CaCO_3$), which contains a similar chemical composition to cement, can be used in place of some of the cements in concrete [30–32].

The extensive usage of rock fragments as a cement substitute will affect the chemical composition of cement [33]. When used with cement, CA can enhance the binding capacity by acting as a more homogenous binder throughout the hydration process. CA can be used as a common aggregate; however, it is light and porous, with a rough surface, lack of adhesion, and high sea salt concentrations. These parameters affect the resulting workability, mechanical capabilities, volume stability, and durability of concrete [34, 35]. Numerous researcher findings indicate that the CA used to replace a portion of the conventional aggregates has physical qualities similar to river aggregates [21, 36–39].

There are several external forces of concrete failure such as weathering, high-temperature variation, wetting-drying cycles, abrasion, and exposure to extreme environments [40]. The effect of pozzolanic materials added to concrete when exposed to highly humid marine environments or the tropical climate has yet to be fully investigated [41]. As a consequence, it is essential to investigate the effect of strength and workability of CA on the durability characteristics of concrete exposed to an extreme sea water environment. Thus, it is vital to determine the extent to which the $CaCO_3$ content of CA affects the ability of CA to react homogeneously with cement and fine sand in concrete.

Recent research on the usage of CA has included the use of coral as a partial alternative for cement and gravel. This study employs a higher percentage of CA as a partial alternative for cement and fine sand, to lower CO_2 emissions caused by increased cement production and also reduce cement scarcity. The previous study has shown that immersion with solely distilled water is effective. Other novel immersion methods were evaluated in this study, specifically with sea water and in comparison to distilled water. CA was used in place of conventional aggregates and sands for concrete production subjected to two different water conditions. Following casting, the concrete specimens were submerged for 28 days in distilled and sea water conditions. Furthermore, the compressive strength and tensile splitting strength tests of concrete CA were investigated. The results of an experimental inquiry into the strength and workability of concrete including CA substitution subjected to different water immersion conditions are reported in this article.

2. Material and Methods

2.1. Materials. For this investigation, ordinary Portland cement (OPC) was obtained from an Andalas cement factory, Aceh, with a specific gravity of 3.15 according to ASTM C595 [42]. When coupled with water, Portland cement is made of calcium silicates and calcium aluminates that hydrate to generate the cementing components calcium silicate hydrate (CSH) and calcium aluminate hydrate (CAH), along with excess calcium hydroxide [7].

The processing of CA into granular and ash is depicted in Figure 1. The CA are cleaned and immersed in distilled water for one day after they are collected from the coast. Then, it is dried in the sun until it is ready to be used.

The used natural CA was obtained in Lamreh beach. The white sand beach region of Lamreh village, Aceh Besar, Aceh Province, is abundant life, with coral reefs on the seafloor. Some dead coral reefs are washed away by the waves and end up as a pile of boulders on the beach. These coral fragments come in a variety of sizes, with some being comparable to sand. CA is often constituted of limestone, which implies that coral aggregates have the highest chemical composition in the form of $CaCO_3$ and SiO_2, as illustrated in Figure 2. In addition, CA is utilized in place of cement and fine sand in the concrete.

The study incorporated fine and coarse aggregate from Jantho, Aceh Besar District. The fine sand passed through a 4.76-mm sieve, coarse sand passed through a 9.52-mm sieve, and gravel passed through a sieve size of 31.5 and remained in a sieve size of 4.76 mm. In this study, the test object was treated with distilled water and sea water. The typical tropical sea water chemical composition can be seen in Table 1. Each treatment involves the use of twenty concrete cylinder specimens. The distilled water used is safe for drinking. Furthermore, sea water was taken from Cermin Beach, Banda Aceh of Ulee Lheue Sea.

2.2. Mix Proportion and Specimen Preparation. The ASTM [43] and ACI 211.1-91 [44] standards were used to design concrete mixes. The concrete is mixed using a forced mixer in the order of cement, sand, coarse aggregates, and water. The whole time required for mixing was 15 minutes. The substitution material is fine sand that passes through a number 200 sieve and is used to replace a portion of the fine sand that passes through a 4.75-mm sieve [45]. The concrete compressive strength machine was applied in this study.

(a) (b)

Figure 1: Coral aggregates: (a) natural form; (b) after crushing to fine sand size.

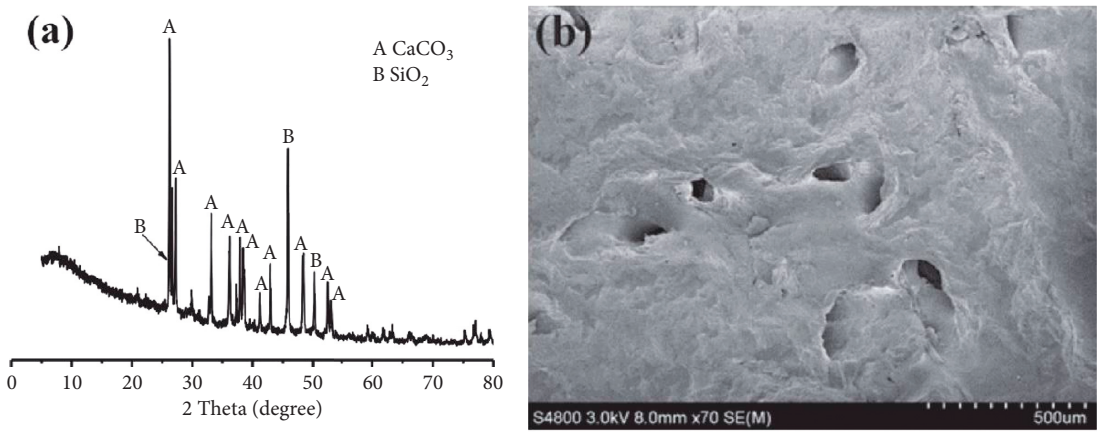

Figure 2: The XRD pattern (a) and the SEM picture (b) of a common coral aggregate [20].

Table 1: Typical tropical sea water chemical composition [41].

Chemical constituent	Value
Sodium, Na^+: ppm	2000–2400
Potassium, K^+: ppm	375
Calcium, Ca^{2+}: ppm	285
Magnesium, Mg^{2+}: ppm	1055
Chloride, Cl^-: ppm	16 618–18 020
Sulfate, $SO4^{2-}$: ppm	1098
Specific gravity: G/ml	1.025
pH	7.9–8.2
Temperature range: °C	26.5–32.0

Coral from the white sand coast of Lamreh, Aceh Besar District in Aceh Province, was used as a substitute material in this investigation. The CA were substituted for cement and fine sand at rates of 0%, 5%, 10%, and 15%. The ratio of substitute materials to cement and fine sand in concrete is 1 : 1 [46]. The CA was separated into two sections: the first section was utilized as a substitute for cement, while the second section was used in place of fine sand. The ratio of CA substituted in cement and fine sand was equal.

CA collected along the coast are transported to the laboratory and washed to remove any clinging sand. The CA are then submerged in distilled water for 24 hours. After 24 hours of saturation with water, CA is dried in the sun and then crushed. It produces 5 kg of coarse grain-sized rock powder from the Los Angeles machine. The rock powder was sieved using a 4.75-mm sieve and utilized in place of fine sand. According to the sieve results, it can obtain coarse grains for sand up to 3 kg. The remaining rock powder on a 4.75-mm sieve was then crushed with an iron stick until it formed fine grains that went through the No. 200 sieve. By using sieve number 200, it got a total of up to 2 kg of fine coral grains. The fine grains are next roasted until they take on an almost blackish color. The color shift occurs at a temperature of 200°C for ten to fifteen minutes. CA possess the chemical properties of $CaCO_3$ in high quantities and, when burned, changes this substance which behaves as a binder in concrete and can behave like cement.

2.3. Testing Details. Compressive strength and split tensile strength of concrete tests were used for predicting concrete cracks and maximum tensile strength. A compressive

strength test was conducted with a 15 cm × 30 cm cylindrical test object. The cylinder compression experiment was performed by gradually applying a force vertically or parallel to the cylinder height until the sample reaches its maximum compressive strength. The split tensile strength of concrete with a cylindrical test object is the value of the test object's indirect splitting tensile strength as determined by loading the test object horizontally parallel to the compression testing machine's surface [47]. The tensile strength of concrete is quite modest, representing around 9% to 15% of the compressive strength. This strength is more difficult to measure and the findings vary depending on the experimental material used.

The designing of the concrete mix begins with determining the compressive strength of concrete, which is 17 MPa with a slump design of (75–150) mm. The amount of water used for each 1 m^3 of concrete is based on the ACI standard, which indicates that the maximum diameter of aggregate is 31.5 mm. The amount of cement used was derived using the water F02D cement ratio value from the ACI standard. The normal weight of concrete is determined using the ACI, with cement, fine sand, coarse sand, and water being the projected normal arrangement of concrete. The results of the concrete mix design calculation are shown in Table 2. Figure 3 illustrates the gradation curve of the mixed materials.

The preparation for the concrete mix starts with the preparation of cement, fine sand, sifted coarse sand and gravel, water, and rock that has been processed to perform as a substitute for cement and fine sand. Then, before the start of the mold, each material is weighed following the mixture ratio determined by the concrete mix design. The test specimen mold is covered with oil to assist in its removal once the concrete has hardened. The mixer utilized has a capacity of 50 liters/mix and is propelled by an electric dynamo. Before casting, the concrete mix machine and mortar storage container are saturated with water. This prevents the concrete mortar from sticking to the container, making it easy to remove. After the preparations are complete, the concrete mortar was mixed by sequentially incorporating the concrete-forming ingredients, including coarse aggregate, fine aggregate, fine and coarse grains of rock, cement, and water. The stirring duration is around 15 minutes with the concrete mix machine axis tilted approximately 45°. After thoroughly mixing the materials, the mortar is placed into a steel mortar storage container. After the mixing process is complete, the mortar mixture is slump tested to determine the workability and viscosity parameters.

Concrete cylindrical specimens are made by filling the cylindrical mold with mortar in three layers. Each layer was compacted by dropping a steel rod with a diameter of 16 mm and a length of 60 cm from a height of 30 cm, with 25 compactions per layer. After filling the mold to the maximum, tap the side of the mold with a rubber mallet to densify the mortar. As in Figure 4(a), after 24 hours, the test object is removed from the mold and each is assigned a number/code accordingly.

For compressive and split tensile strength tests, fresh concrete is poured into cylindrical molds. The samples consisted of 80 cylindrical specimens measuring 15 cm × 30 cm. 40 of which were immersed in distilled water and 40 of which were immersed in sea water (Table 3). Cement usage was replaced by 5%, 10%, and 15% of CA, respectively. The fine sand was also replaced by 5%, 10%, and 15% fine CA. The purpose of reducing the cement concentration is to determine if the chemical composition of $CaCO_3$ in the CA has an effect, primarily as a binder for concrete. Furthermore, assess whether an extra additive is still required to ensure that the bonding power created during the hydration process is more consistent. The influences of a marine ecosystem on cement and CA-blended concrete were investigated in a field study and compared with the neutral ecosystem. The treatment of test specimens with distilled water begins with the specimens being immersed in a shielded immersion tube in the laboratory for 28 days as in Figure 4(b). The distilled water used is completely safe to drink. Furthermore, sea water immersion begins with the direct immersion of a concrete cylinder test object for 28 days in sea water at the Cermin beach, Aceh, as in Figure 4(c).

Table 2: Design of a concrete mix for 1 m^3.

Material	Required amount	Unit
Water	193.00	
Cement	288.06	
Gravel	1201.31	kg/m^3
Coarse sand	184.72	
Fine sand	512.91	
Total	2380.00	kg/m^3

The concrete specimen was tested for compressive and split tensile strength after 28 days of immersion. The laboratory-scale test was used to measure and record the dimensions and weight of the test object. The test object is then positioned vertically on a compressive strength tester machine to determine the compressive and split tensile strength of concrete, and the machine speed was gradually increased until the test object reaches the maximum strength, at which point the test object becomes cracked or broken.

3. Results and Discussion

3.1. Slump Test. The slump test is the most often used method for determining the workability of concrete. It can be performed in the laboratory or on-site. It is not appropriate for either wet or extremely dry concrete. Indonesia standard of SNI 1972 : 2008 was used for slump test procedures. Sea water was employed in this study for immersion of the samples only. While the water used to fabricate concrete test items for each scenario was distilled. Slump is a term that refers to the ability of fresh concrete to work or is one of the properties. Slump is determined after the concrete mixture has been thoroughly mixed. The amount of the slump is the fall in the value of the concrete mixture poured into the test cone. The results indicated that the slump varied, as it was evaluated on each of the test objects. The test findings indicate that the slump obtained in the laboratory remains within the ideal range of 75 to 100 mm.

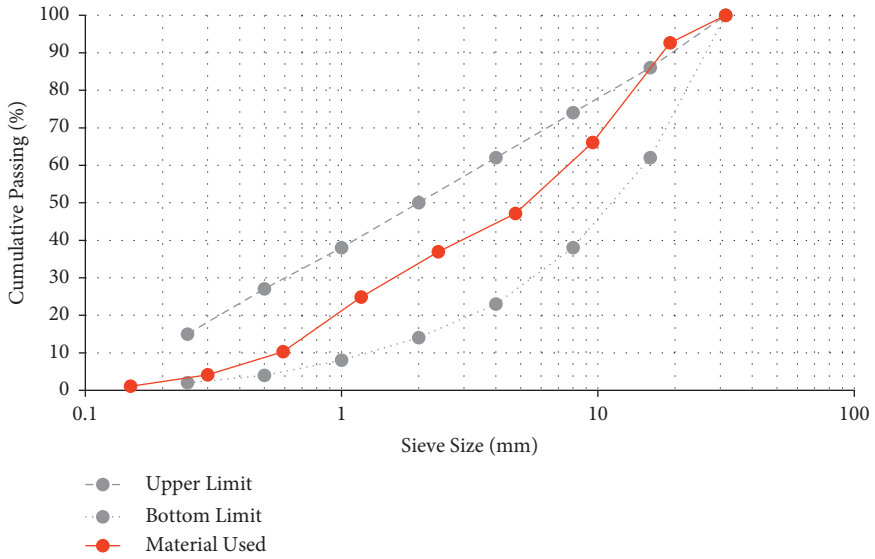

Figure 3: The gradation of concrete-CA material used.

(a) (b) (c)

Figure 4: Sample preparation: (a) sample after 24 hours casting, (b) sample in distilled water immersion, and (c) sample in sea water immersion.

Table 3: The design of specimens for the experiment.

Test	Mixes	OPC (%)	CA-OPC (%)	CA-FS (%)	Submerged distilled	Submerged sea water
Compressive strength	Control	100	—	—	5	5
	CA5FS5	90	5	5	5	5
	CA10FS10	80	10	10	5	5
	CA15FS15	70	15	15	5	5
Splitting tensile strength	Control	100	—	—	5	5
	CA5FS5	90	5	5	5	5
	CA10FS10	80	10	10	5	5
	CA15FS15	70	15	15	5	5
Total specimens					40	40

Note. CA = coarse aggregates, FS = fine sand, OPC = ordinary Portland cement.

The workability of CA-concrete was tested utilizing a variety of replacement levels. Figure 5 illustrates the workability values in terms of the slump test. As illustrated in Figure 5, the slump test result varies between 75 and 85 mm. This is consistent with the proposed slump of (75–100) mm. The results indicate that, except for 5% sea water submerged, the workability of concrete built with CA as fine aggregate and cement declined as the proportion of substitution and water F02D cement ratio increased even though the slump test results obtained are still within the acceptable range.

Similarly, Althoey et al. [48] reported that the slump values appear to decrease linearly as the fine aggregate content of the concrete is increased. Furthermore, the reduced slump could be a result of the roughness and heterogeneity of the CA particles, which contribute to the mixtures' fluidity. Additionally, the slump test results correspond to the finding of Mangi et al. [49], which workability declines as the proportion of substitute material in the concrete mix increases. This could be because of the fineness of the particles, which increases surface area; as a result, the concrete mix absorbed more water.

3.2. Compressive Strength. The compressive strength test was conducted on cylindrical specimens of 150 mm in diameter and 300 mm in length. This test was used to determine the compressive strength of CA concrete samples. SNI 1974 : 2011 was used for compressive strength test procedures. A 28-day-old concrete cylinder specimen was subjected to the test. Concrete's compressive strength was measured under two different conditions, namely sea water immersion and distilled water immersion.

Figure 6 displays the compressive strength test results of concrete after 28 days of curing. The compressive strength curve of concrete when immersed in distilled water and sea water exhibits the same pattern, specifically, the greater CA added to the concrete, the lower the compressive strength. It demonstrates that the salt content of sea water has a negative effect on the overall strength of concrete. Additionally, by immersing the concrete in sea water, it was demonstrated that the maximum strength of concrete with 0% variation in CA provided a compressive strength of 14.89 MPa. Additionally, the result of concrete testing using the distilled water immersion method indicated that the maximum compressive strength of concrete is 18.47 MPa at 0% CA. The results indicated that the addition of CA resulted in a decrease in compressive strength when compared to 0% CA. This demonstrates that when the CA content of the concrete increased, the compressive strength of the concrete decreased. The possible reason for the loss in compressive strength of CA concrete is that a significant percentage of cement was replaced with CA, lowering the cement content of the concrete and thereby limiting cement hydration processes [50]. Additionally, this is because the chemical content of the $CaCO_3$ of CA does not contribute much to the production of cement and fine sand. There may be too saturated lime in the cement F02D CA mixture, reducing the homogeneity of the bonding power. Thus, when the force is applied vertically, parallel to the test object, the upper surface

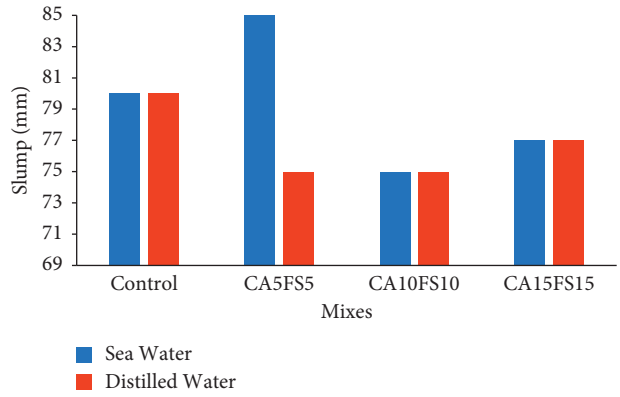

Figure 5: Slump test of CA-concrete.

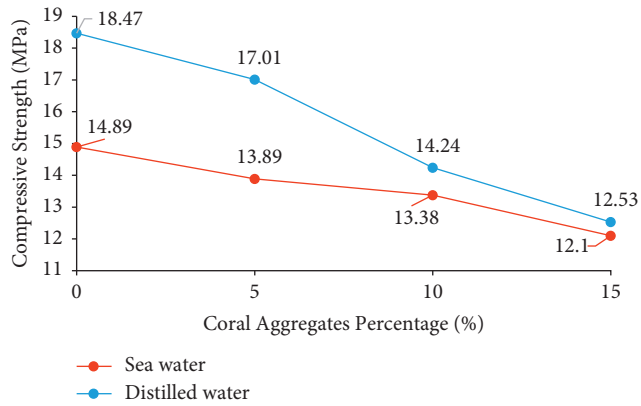

Figure 6: Compressive strength of CA-concrete.

area of the concrete is insufficiently strong to sustain the strain. Apart from the increased CA content, this resulted in a higher water need, resulting in water being unavailable for cement hydration [49].

3.3. Splitting Tensile Strength. The strength of tensile for CA-concrete samples was determined in this test. Cylindrical specimens with a diameter of 150 mm and a length of 300 mm were used for the split tensile test. SNI 03-2491-2002 was used for splitting tensile strength test procedures. The splitting tensile strength test was performed on a 28-day-old concrete cylinder specimen. The splitting tensile strength of concrete was determined for two scenarios namely sea water immersion concrete and distilled water immersion scenarios. Based on the findings, it is confirmed that distilled water immersion has a higher splitting tensile strength than sea water immersion.

The results indicate that substituting CA for a portion of the cement and fine sand can boost the split tensile strength of the concrete. From Figure 7, the split tensile strength of concrete for CA substitution using a sea water immersion method of 0%, 5%, 10%, and 15% is 2.10 MPa, 2.50 MPa, 2.41 MPa, and 2.25 MPa, respectively. Moreover, the split tensile strength of concrete at 0%, 5%, 10%, and 15% CA using the distilled water immersion was 2.23 MPa, 2.52 MPa, 2.14 MPa, and 1.73 MPa, respectively.

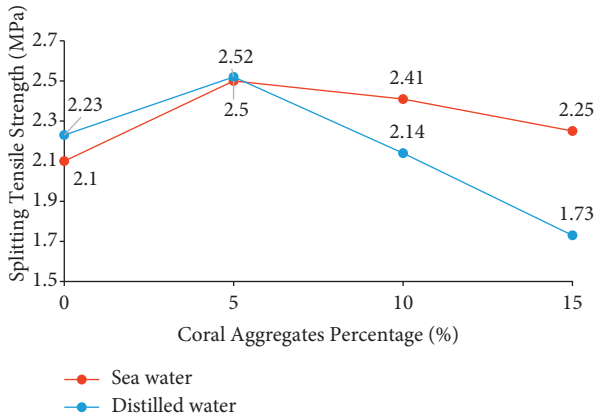

Figure 7: Splitting tensile strength of CA-concrete.

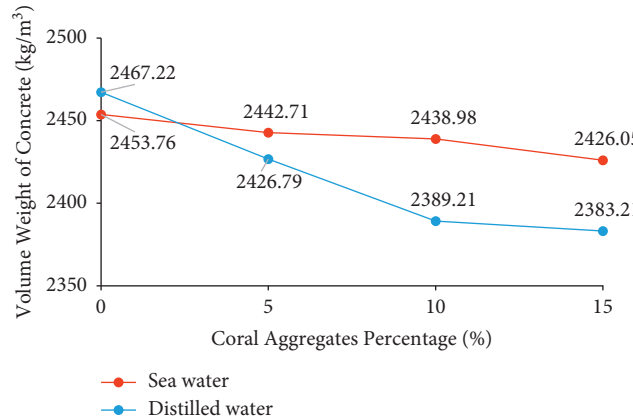

Figure 8: Volume weight of coral aggregates concrete.

The maximum split tensile strength of concrete is obtained when 5% CA was substituted and the least split tensile strength of concrete occurs when regular concrete. The immersion method with sea water and distilled water at a difference of 5% generates the same value of concrete's split tensile strength, which is around 2.50 MPa. This is because CA released moisture continually during cement hydration, which enhanced cement hydration and the reaction of pozzolanic for CA [20].

Additionally, the split tensile strength of concrete increased by 5% due to the perpendicular loading of the test specimen for cylinders. As a result, the surface area that may be retained is increased by 30 cm. When loading occurs, the CA that has been substituted for cement and fine sand is capable of maintaining a 15-cm broad bond on the horizontal side. The tensile strength declined further when the CA substitute was increased to 10% and 15%. This is because the chemical composition of the concrete has saturated to the point where it can no longer maintain its binding capacity on the horizontal side of the test object.

The specimens immersed in sea water, on the other hand, showed a higher average split tensile strength than those immersed in distilled water. This may be because the rock contains $CaCO_3$ (lime substance), which triggers a chemical reaction in the test object during immersion in sea water, which is the rock's natural habitat/environment. The concrete mix contains 5% CA develops strength at a rate of approximately 8% higher than the control mix. This could be an indication of the production of C-S-H gel in the concrete mix as a result of the presence of CA [49]. As a result, a higher split tensile strength value was achieved than when the specimen is soaked in distilled water.

3.4. Volume Weight of Concrete. After the concrete cylinder specimen had been treated for 28 days, the volume weight of the concrete was determined utilizing the dimensions and weight of the concrete cylinder. As illustrated in Figure 8, the weight of the concrete volume was determined for the sea water immersion scenario. The weight values of concrete volume for rock substitution for the sea water immersion scenario are 2453.76 kg/m^3, 2442.71 kg/m^3, 2438.98 kg/m^3, and 2426.05 kg/m^3. Furthermore, the volume of concrete measured using the distilled water immersion with substitutions of 0%, 5%, 10%, and 15% results in 2467.22 kg/m^3, 2426.79 kg/m^3, 2389.21 kg/m^3, and 2383.21 kg/m^3, respectively.

The results of the weight testing of the concrete volume utilizing the sea water and distilled water immersion indicate that normal concrete has the maximum volume weight. Moreover, specimens with 5%, 10%, and 15% substitution experienced a considerable drop in the weight of the concrete volume. The more CA substituted for cement and fine sand, the lighter the concrete [51]. This is because the amount of water (workability) in the concrete mixture is reduced by up to 2%–5% when rock substitution was used. The workability specification attempts to achieve a design slump of 75–100 mm in conformity with ACI standards [52].

According to Figure 8, the weight of the concrete volume fluctuated between 2383.21 kg/m^3 and 2467.22 kg/m^3. This indicates that the weight of the concrete volume obtained is still within the range of 2200 kg/m^3 to 2500 kg/m^3. The volume weight of regular concrete treated with distilled water immersion is somewhat greater than that of sea water-treated concrete. This is owing to the excellent absorption of the test object of distilled water. Meanwhile, sea water is not completely absorbed by other test objects, resulting in the formation of pores. Meanwhile, the weight of the concrete volume when CA was substituted for 5% to 15% of the saltwater immersion test object is more than the weight of the distilled water immersion test object. This is because sea water has higher specific gravity than distilled water and also contains CA that reacts well when dissolved in sea water, hence reducing pores during hydration.

4. Conclusion

Several conclusions can be drawn from this study, including the following: reducing the amount of rock in cement and fine sand by 0%, 5%, 10%, and 15% has a significant effect on the compressive and splitting tensile strength of concrete and the weight of the concrete volume, both when using the

sea water distilled water immersion scenario. The compressive strength of concrete results shows that 0% of CA as the optimum percentage. Moreover, the splitting tensile strength results indicated that the strength increased at 5% CA and subsequently fell significantly at 10% and 15% CA substitution. In terms of volumetric weight, the more CA substituted for cement and fine sand, the lower the volumetric weight of the concrete. Moreover, CA incorporation into concrete has several additional environmental and technological benefits for all associated businesses. Additionally, partial substitution of CA lowers the cost of concrete production.

Immersion of the samples in sea water may affect the quality of the cement-water heat hydration process in concrete. During cement hydration, concrete requires high-quality water to achieve maximum hardness and avoid cracking, swelling, and shrinking. In this investigation, the CA was partially exchanged for cement and fine sand. Even though crushed CA processed as a substitute material does not react properly with cement and water, when submerged in sea water, the volume of the concrete changes, i.e., the weight of the concrete is larger, in comparison to concrete immersed in fresh water. For further research, curing days of concrete after mixing, such as 7 and 90 days, are considered to determine the rate of strength development in the concrete samples. Moreover, a different type of sea water immersion is considered, namely immersing the test object in sea water, with the test object floating and sheltered from the sun to determine the effect of water depth and direct sun exposure.

In brief, distilled water immersion provides a stronger concrete bond than immersion in sea water. Moreover, CA possess excellent pozzolanic abilities, and it has been proven experimentally that concrete comprising 5% cement substitution with CA exhibits reasonable strength performance and is thus designated as the optimum replacement ratio. Thus, the substitution of modified cement concrete for conventional cement has two advantages namely reducing carbon dioxide (CO_2) emissions and may reduce construction costs. As a result, it may be seen as a cost-effective and long-term strategy.

Substituting a portion of the CA for cement and fine sand might decrease the compressive strength of concrete, as the chemical composition of $CaCO_3$ is too high and saturated and is unable to sustain its binding ability with cement and fine sand in the vertical direction. On the other hand, it can improve the split tensile strength of concrete. This is because the chemical composition of $CaCO_3$ in the CA allows it to retain a horizontal direction with cement and fine sand.

Data Availability

The data used to support the findings of this study are included within the article.

Conflicts of Interest

The authors declare that they have no conflicts of interest.

Acknowledgments

This study was supported by the Universitas Syiah Kuala, Banda Aceh, Indonesia, and Universiti Malaysia Pahang under the research grant (RDU/UMP) vote number RDU190339. Furthermore, the authors wish to extend their gratitude to Mr. Bagus and Mr. Siddiqul for assisting in the experimental and data collections.

References

[1] D. Siang Ng, S. C. Paul, V. Anggraini et al., "Influence of SiO_2, TiO_2 and Fe_2O_3 nanoparticles on the properties of fly ash blended cement mortars," *Construction and Building Materials*, vol. 258, Article ID 119627, 2020.

[2] E. Zahraalsadat, N. D. N. Norsyahariati, Z. M. Yusoff, and V. Rostami, "Evaluation of the effects of cement and lime with rice husk ash as an additive on strength behavior of coastal soil," *Materials*, vol. 14, 2021.

[3] R. Palod, S. V. Deo, and G. D. Ramtekkar, "Sustainable approach for linz-donawitz slag waste as a replacement of cement in concrete: mechanical, microstructural, and durability properties," *Advances in Civil Engineering*, vol. 2020, Article ID 5691261, 9 pages, 2020.

[4] B. W. Yifru, B. B. Mitikie, and B. Mitikie, "Partial replacement of sand with marble waste and scoria for normal strength concrete production," *SN Applied Sciences*, vol. 2, no. 12, pp. 1938–2011, 2020.

[5] B. W. Chong, R. Othman, P. J. Ramadhansyah, S. I. Doh, and X. Li, "Properties of concrete with eggshell powder: a review," *Physics and Chemistry of the Earth, Parts A/B/C*, vol. 120, Article ID 102951, 2020.

[6] H. A. Jaber, R. S. Mahdi, and A. K. Hassan, "Influence of eggshell powder on the Portland cement mortar properties," *Materials Today Proceedings*, vol. 20, pp. 391–396, 2020.

[7] J. James and P. K. Pandian, "Industrial wastes as auxiliary additives to cement/lime stabilization of soils," *Advances in Civil Engineering*, vol. 2016, Article ID 1267391, 17 pages, 2016.

[8] M. Song, C. Wang, Y. Cui, Q. Li, and Z. Gao, "Mechanical performance and microstructure of ultra-high-performance concrete modified by calcium sulfoaluminate cement," *Advances in Civil Engineering*, vol. 2021, Article ID 4002536, 9 pages, 2021.

[9] A. P. Gursel and C. Ostertag, "Life-cycle assessment of high-strength concrete mixtures with copper slag as sand replacement," *Advances in Civil Engineering*, vol. 2019, Article ID 6815348, 13 pages, 2019.

[10] G. Abebaw, B. Bewket, and S. Getahun, "Experimental investigation on effect of partial replacement of cement with bamboo leaf ash on concrete property," *Advances in Civil Engineering*, vol. 2021, Article ID 6468444, 9 pages, 2021.

[11] T. A. Kua, A. Arulrajah, S. Horpibulsuk, Y. J. Du, and S. L. Shen, "Strength assessment of spent coffee grounds-geopolymer cement utilizing slag and fly ash precursors," *Construction and Building Materials*, vol. 115, pp. 565–575, 2016.

[12] W. Al-kutti, A. B. M. Saiful Islam, and M. Nasir, "Potential use of date palm ash in cement-based materials," *Journal of King Saud University—Engineering Sciences*, vol. 31, no. 1, pp. 26–31, 2019.

[13] A. Forty, *Concrete and Culture: A Material History*, Reaktion Books, London, UK, 2013.

[14] M. S. Imbabi, C. Carrigan, and S. McKenna, "Trends and developments in green cement and concrete technology," *International Journal of Sustainable Built Environment*, vol. 1, no. 2, pp. 194–216, 2012.

[15] M. Schneider, M. Romer, M. Tschudin, and H. Bolio, "Sustainable cement production-present and future," *Cement and Concrete Research*, vol. 41, no. 7, pp. 642–650, 2011.

[16] J. E. Waani and L. Elisabeth, "Substitusi material pozolan terhadap semen pada kinerja campuran semen," *Jurnal Teoretis dan Terapan Bidang Rekayasa Sipil*, vol. 24, no. 3, pp. 853–2982, 2017.

[17] R. M. Andrew, "Global CO_2 emissions from cement production, 1928–2017," *Earth System Science Data*, vol. 10, no. 4, pp. 2213–2239, 2018.

[18] J. Tang, H. Cheng, Q. Zhang, W. Chen, and Q. Li, "Development of properties and microstructure of concrete with coral reef sand under sulphate attack and drying-wetting cycles," *Construction and Building Materials*, vol. 165, pp. 647–654, 2018.

[19] M. Chen, J. Geng, H. Xiong, T. Shang, C. Xue, and M. Abbas, "Effect of curing on mechanical properties of cement-stabilized coral sand in marine environment," *Advances in Materials Science and Engineering*, vol. 2020, Article ID 4678376, 11 pages, 2020.

[20] Y. Wang, S. Zhang, D. Niu, L. Su, and D. Luo, "Effects of silica fume and blast furnace slag on the mechanical properties and chloride ion distribution of coral aggregate concrete," *Construction and Building Materials*, vol. 214, pp. 648–658, 2019.

[21] H. Shi, Q. Wu, Z. Yu, J. Ma, and X. Shen, "Properties of eco-friendly coral sand powder—calcium sulfoaluminate cement binary system," *Construction and Building Materials*, vol. 263, Article ID 120181, 2020.

[22] R. P. Munirwan, M. Munirwansyah, K. Jamaluddin et al., "Liquefaction potential analysis of reusep prestress bridge in pidie jaya due to 6.4 Mw earthquake," *IOP Conference Series: Materials Science and Engineering*, vol. 712, no. 1, Article ID 12010, 2020.

[23] M. Munirwansyah, R. P. Munirwan, and H. Yunita, "Geotechnical engineering aspect related to pidie jaya-aceh earthquake disaster and mitigation," *International Journal of Advanced Science, Engineering and Information Technology*, vol. 8, no. 3, pp. 870–875, 2018.

[24] M. Munirwansyah, R. P. Munirwan, M. Sungkar, and Z. Melinda, "The effect of soil-structure interaction on multi-storey building resonance and dynamic shear modulus for pidie jaya Aceh earthquake," *IOP Conference Series: Materials Science and Engineering*, vol. 523, no. 1, Article ID 12038, 2019.

[25] M. Munirwansyah, M. A. Fulazzaky, H. Yunita, R. P. Munirwan, J. Jonbi, and K. Sumeru, "A new empirical equation of shear wave velocity to predict the different peak surface accelerations for Jakarta city," *Geodesy and Geodynamics*, vol. 11, no. 6, pp. 455–467, 2020.

[26] H. R. A. Yamin, "Pemanfaatan batu karang keristalin fak-fak umtuk campuran beraspal," *Jurnal Jalan-Jembatan*.vol. 28, pp. 178–192, 2018.

[27] C. Parithra, A. Ratten, and A. Arokiaprakash, "others, Study on use of coral sand as fine aggregates in concrete," *International Journal of Civil Engineering & Technology*, vol. 8, pp. 543–549, 2017.

[28] L. Wang, J. Mei, J. Wu, X. He, H. Li, and Q. Ding, "Mechanical properties and microscopic mechanism of coral sand-cement mortar," *Advances in Materials Science and Engineering*, vol. 2020, Article ID 4854892, 11 pages, 2020.

[29] D. A. T. Sina, *Others, Potensi Penggunaan Batu Karang Pulau Timor Sebagai Agregat Kasar Pada Beton*, Petra Christian University, Surabaya, Indonesia, 2003.

[30] Y. Afrizal, N. Ramahayati, and M. Islam, *Pengaruh Pemanfaatan Abu Pecahan Terumbu Karang Dan Abu Sekam Padi Sebagai Pengganti Semen Terhadap Kuat Tekan Beton*, Universitas Bengkulu, Bengkulu, Indonesia, 2019.

[31] C. Tang, Z. Lu, and H. Yao, "Effect of axial pressure on lime-treated expansive soil subjected to wetting and drying cycles," *Advances in Civil Engineering*, vol. 2019, Article ID 3052932, 8 pages, 2019.

[32] J. Ma, Y. Su, Y. Liu, and X. Tao, "Strength and microfabric of expansive soil improved with rice husk ash and lime," *Advances in Civil Engineering*, vol. 2020, Article ID 9646205, 8 pages, 2020.

[33] R. Nie, Q. Wu, Z. Yu, A. Wang, and X. Shen, "Effect of coral powder and ground-granulated blast-furnace slag on the hydration behavior of cement paste," *Journal of Thermal Analysis and Calorimetry*, vol. 147, pp. 6643–6654, 2021.

[34] A. Wang, B. Lyu, Z. Zhang, K. Liu, H. Xu, and D. Sun, "The development of coral concretes and their upgrading technologies: a critical review," *Construction and Building Materials*, vol. 187, pp. 1004–1019, 2018.

[35] W. Wu, R. Wang, C. Zhu, and Q. Meng, "The effect of fly ash and silica fume on mechanical properties and durability of coral aggregate concrete," *Construction and Building Materials*, vol. 185, pp. 69–78, 2018.

[36] X. Wang, R. Yu, Z. Shui, Q. Song, and Z. Zhang, "Mix design and characteristics evaluation of an eco-friendly Ultra-High Performance Concrete incorporating recycled coral based materials," *Journal of Cleaner Production*, vol. 165, pp. 70–80, 2017.

[37] Y. Yuan, *Mix Design and Property of Coral Aggregate concrete*, Nanjing Univ. Aeronaut. Astronaut, Nanjing, China, 2015.

[38] Q. Wang, P. Li, Y. Tian, W. Chen, and C. Su, "Mechanical properties and microstructure of Portland cement concrete prepared with coral reef sand," *Journal of Wuhan University of Technology-Materials Science Edition*, vol. 31, no. 5, pp. 996–1001, 2016.

[39] Y. Cao, L. Wang, H. Wu, Z. Wang, and Y. Yao, "Effect of coral powder on the properties of cement-based materials," *IOP Conference Series: Materials Science and Engineering*, vol. 563, no. 2, Article ID 22010, 2019.

[40] R. P. Jaya, B. H. A. Bakar, M. A. M. Johari, M. H. W. Ibrahim, M. R. Hainin, and D. S. Jayanti, "Strength and microstructure analysis of concrete containing rice husk ash under seawater attack by wetting and drying cycles," *Advances in Cement Research*, vol. 26, no. 3, pp. 145–154, 2014.

[41] D. S. Jayanti, J. Mirza, R. P. Jaya, B. H. A. Bakar, N. A. Hassan, and M. R. Hainin, "Chloride penetration of RHA concrete under marine environment," *Proceedings of the Institution of Civil Engineers—Maritime Engineering*, vol. 169, no. 2, pp. 76–85, 2016.

[42] Astm-International, "Cements C595/C595M20: Standard Specification for Blended Hydraulic," *American Standards Testing Materials, 2020*, American Standards Testing Materials, West Conshohocken, PA, USA, 2020.

[43] I Standards Worldwide, *Annual Book of ASTM Standards 2004*, Concrete Aggregates, 2004.

[44] A C I, "Standard, Standard practice for selecting proportions for normal, heavyweight, and mass concrete," *ACI Manual of Concrete Practice*, vol. ACI 211.1-91, pp. 1–38, 1996.

[45] B. Bunyamin, N. Hendrifa, and M. Ridha, "Pengaruh substitusi cangkang tiram sebagai pengganti sebahagian semen

dan pasir halus terhadap kuat tarik belah beton," *Teras Jurnal*, vol. 11, no. 2, pp. 272–281, 2021.

[46] B. Bunyamin and A. Mukhlis, "Utilization of oyster shells as a substitute part of cement and fine aggregate in the compressive strength of concrete," *Aceh International Journal of Science and Technology*, vol. 9, no. 3, pp. 150–156, 2020.

[47] S. Mindess and J. F. Young, *Concrete*, Prentice-Hall, Hoboken, NJ, USA, 2002.

[48] F. Althoey and M. A. Hosen, "Physical and mechanical characteristics of sustainable concrete comprising industrial waste materials as a replacement of conventional aggregate," *Sustainability*, vol. 13, no. 8, p. 4306, 2021.

[49] S. A. Mangi, M. H. Wan Ibrahim, N. Jamaluddin, M. F. Arshad, and P. J. Ramadhansyah, "Effects of ground coal bottom ash on the properties of concrete," *Journal of Engineering Science & Technology*, vol. 14, pp. 338–350, 2019.

[50] A. Demissew, F. Fufa, and S. Assefa, "Partial replacement of cement by coffee husk ash for C-25 concrete production," *Journal of Civil Engineering, Science and Technology*, vol. 10, no. 1, pp. 12–21, 2019.

[51] R. S. Mcmanus, N. Archibald, S. Comber, A. M. Knights, R. C. Thompson, and L. B. Firth, "Partial replacement of cement for waste aggregates in concrete coastal and marine infrastructure: a foundation for ecological enhancement?" *Ecological Engineering*, vol. 120, pp. 655–667, 2018.

[52] B. Bunyamin, R. P. Munirwan, M. Ridha, and N. Hendrifa, "Utilization of wood processing dust as a substitute for a part of cement in concrete," *IOP Conference Series: Materials Science and Engineering*, vol. 1087, no. 1, Article ID 12004, 2021.

Hindawi
Advances in Civil Engineering
Volume 2022, Article ID 9674096, 13 pages
https://doi.org/10.1155/2022/9674096

Research Article

Performance of Palm Oil Clinker Lightweight Aggregate Concrete Comprising Spent Garnet as Fine Aggregate Replacement

Nur Farah Aziera Jamaludin[1], **Khairunisa Muthusamy**[1], **Mohd Faizal Md Jaafar**[1], **Ramadhansyah Putra Jaya**[2] **and Mohamed A. Ismail**[3]

[1]*Faculty of Civil Engineering Technology, Universiti Malaysia Pahang, Lebuhraya Tun Razak, 26300, Gambang, Pahang, Malaysia*
[2]*Department of Civil Engineering, College of Engineering, Universiti Malaysia Pahang, Lebuhraya Tun Razak, 26300, Gambang, Pahang, Malaysia*
[3]*Department of Civil Engineering, Miami College of Henan University, Kaifeng, Henan, China*

Correspondence should be addressed to Khairunisa Muthusamy; khairunisa@ump.edu.my

Received 17 January 2022; Revised 22 March 2022; Accepted 24 March 2022; Published 12 April 2022

Academic Editor: Alessandro Rasulo

The increase in building activity as a result of population expansion has resulted in an overexploitation of aggregate, with disastrous environmental consequences. Simultaneously, the disposal of spent garnet by the shipbuilding industry and palm oil clinker by palm oil mills harms the environment and needs a greater amount of landfill space. Therefore, the purpose of this study was to determine the influence of spent garnet as a fine aggregate substitute on the fresh, mechanical, and durability properties of palm oil clinker concrete. Concrete mixes were created using various percentages of spent garnet as a fine aggregate substitute, including 0%, 10%, 20%, 30%, and 40%. The workability, compressive strength, flexural strength, splitting tensile strength, modulus of elasticity, water absorption, and acid resistance of the water cured concrete were all determined. It was determined that using 20% spent garnet increased the compressive strength of lightweight concrete. The positive filler effect of spent garnet resulted in a densely packed internal structure of concrete, allowing it to have the lowest percentage of water absorption. The same mixtures exhibited the least mass change and strength reduction when exposed to acid solution. The results established that ecologically friendly concrete may be manufactured by including considerable volumes of waste from the shipbuilding and palm oil sectors.

1. Introduction

The Sustainable Development Goals (SDGs) of "Goal 7" are aimed to make sure that everyone can have access to affordable and reliable energy by 2030. This includes expanding infrastructure and upgrading technology to make sure that everyone can get modern and sustainable energy services [1]. The construction sector is one of the industries featured in "Agenda 2030," as it is the least sustainable industry in the world, consuming over half of all nonrenewable resources [2]. Concrete is one of the most essential and commonly utilized building materials in the world nowadays [3]. It is an ideal material for construction because it is strong enough to meet the needs for various applications according to the type of concrete. Zareei et al. [4] reported that 25 billion tons of concrete consumption led to sustainability issues due to the scarcity of natural resources, including aggregates. In comparison, sand, and gravel are the world's most mined resources, with between 32 billion tons and 50 billion tons taken each year [5]. Excessive mining of river sand causes changes in the riverbed, water levels, and flood plains and affects the river ecosystems, navigation systems, and salinity levels [6]. Instabilities in the channel and sedimentation caused by instream mining also cause problems on public facilities such as bridges, pipelines, and utility lines [7]. According to Kuhar [8], global demand

for natural aggregates used in concrete manufacturing is expected to expand at an average annual rate of 7.7% through 2022, reaching 66.2 billion metric tons. The rise in aggregate extraction activities from the quarries destroys greenery (which is the habitat of wildlife), changes the natural landscape, and pollutes the environment. The land deprivation causes pollution and affects the biodiversity, posing ecological impact on local neighborhoods and communities [9, 10]. Therefore, utilization of other types of material to function as sand and coarse aggregate in concrete could reduce the quantity of these natural resources reaped from the environment, decrease destruction to green surroundings, and preserve aggregate resources for future use.

Spent garnet waste is a type of waste generated from the shipbuilding industry. Based on the US Geological Survey [11], 140 000 garnets were produced, and 12, 000 tons was exported to other countries, including Malaysia. Garnet is commonly used as an abrasive material for sandblasting ships in Malaysia after the Malaysian shipbuilding industry was recently revealed to be responsible for importing thousands of tons of garnets from outside the country each year [12]. Garnet is an abrasive blasting medium that is a mineral found in crystal metamorphic rocks, and it has a variety of chemical components and colors [13]. Due to its hardness, this material may be recycled several times (between three and five times) for abrasive purposes [14]. The garnet that was no longer useable or practical for blasting purposes would be disposed of as "spent garnet" at landfills [12]. Spent garnet causes many environmental and health hazards because the paint in most ship hulls contains heavy metals like tributyltin (TNT) that leached underground and contaminate soil and underground water [15]. Furthermore, when these products are entered into the rivers through flooding or by run-offs, such garnet wastes cause significant environmental and health dangers such as water pollution [16]. They can threaten the biodiversity of natural ecological environment [12]. An approach that aims to utilize this waste for other purposes rather than disposing it would alleviate this material ending up piled up as an environmental polluting waste.

Malaysia is currently the second-largest producer of palm oil after Indonesia, with the total output accounting for 36% of global demand [17]. In 2019, Malaysia produced 19.86 million tons of palm oil and exported 18.47 million tons [18]. The expansion in the plantation increased the annual production of solid waste such as oil palm shell (OPS), palm oil clinker (POC), and palm kernel fiber [19, 20]. The porous rock-like material known as palm oil clinker (POC) is a by-product obtained during the palm oil and fiber incineration cycle in a boiler at the mill. As palm oil production continues to increase, it is expected that a massive volume of clinker would be produced with little or no commercial value [20, 21]. These waste materials are usually dumped into open fields and landfills [19] and causes water, air, and land pollution [22, 23]. Besides, continuous waste discarding contaminates the soil and impacts the source of groundwater supply [24]. Developing nations such as Malaysia confront several challenges in managing waste sustainably, owing to the rapidly expanding cities and a growing population. Malaysia generated 19,000 tons of debris per day in 2005, with a recycling rate of 5%. The quantity increased to 38,000 tons per day in 2018 even though the recycling rate rose by 17.5% [25]. With limited landfill space and escalating disposal costs, there is an urgent need to address waste management and reduce environmental and human impacts. Hence, integrating POC as coarse aggregate and spent garnet as partial sand replacement in concrete material would reduce the natural aggregate usage and, at the same time, minimize adverse environmental impacts.

Table 1: Physical properties of POC.

Physical properties	POC
Bulk density (kg/m^3)	945.66
Water absorption (%)	10.19
Moisture content (%)	1.87
Aggregate impact value (%)	49.39
Aggregate crushing value (%)	45.54
Los Angeles abrasion value (%)	58.70

Figure 1: Large chunk of POC.

Figure 2: Spent garnet.

2. Materials and Methods

2.1. Materials and Properties. In this study, the binder used was OPC with ASTM C150 [24], classified as Type 1 binder material in the concrete. The properties of POC, which has been used as a lightweight coarse aggregate in this research, are presented in Table 1. Large chunks of POC were collected from a dumping site in a local palm oil mill. POC's large

Table 2: Physical properties of river sand and spent garnet.

Physical properties	River sand	Spent garnet
Bulk density (kg/m^3)	1541	2006
Water absorption (%)	0.85	6.12
Moisture content (%)	0.42	1.06
Specific gravity	2.77	3.75
Fineness modulus	3.85	2.79

Table 3: Chemical composition of spent garnet.

Chemical composition (%)	Spent garnet
Silicon dioxide (SiO_2)	39.04
Aluminium oxide (Al_2O_3)	13.40
Iron oxide (Fe_2O_3)	40.23
Magnesium oxide (MgO)	4.08
Sulfur trioxide (SO_3)	0.38
Potassium oxide (K_2O)	0.32
Calcium oxide (CaO)	-
Manganese (II) oxide (MnO)	1.03
Titanium dioxide (TiO_2)	1.53

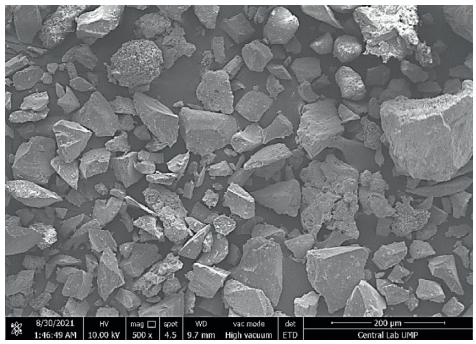

Figure 3: SEM spent garnet.

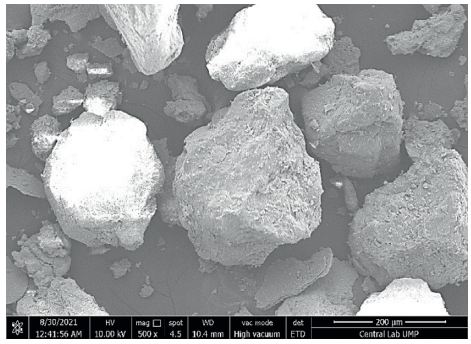

Figure 4: SEM river sand.

chunks (Figure 1) were initially crushed with the required size jaw crusher. Then, POC was sieved by passing 10 mm and retaining 5 mm to get the required size for replacement of coarse aggregate. Air-dried river sand was used as a fine aggregate with particle size passing of 2.36 mm and fineness modulus of 3.85. The spent garnet (Figure 2) was collected from a factory that provides integrated brownfield services for the oil and gas and petrochemical industries in West Malaysia. The waste was oven-dried at a temperature of 105°C ± 5 for 24 hours to remove the moisture content and sieved passing 600 μm. The physical properties of river sand and spent garnet are shown in Table 2, and the chemical composition of spent garnet is tabulated in Table 3. Figures 3 and 4 show the spent garnet and river sand's scanning electron image, respectively. Tap water was used for preparing the specimen for concrete and curing purposes. 1% superplasticizer from cement was used to produce workable mix while keeping low water cement ratio.

Table 4: Mix proportion used (kg/m^3).

Mixes (%)	Sand	Sg	POC	OPC	Water	SP
0	625	—	345	375	158	3.75
10	563	63	345	375	158	3.75
20	500	125	345	375	158	3.75
30	438	188	345	375	158	3.75
40	375	250	345	375	158	3.75

2.2. Mix Design and Preparation. The trial mix method was used to generate a total of five different palm oil clinker lightweight aggregate concrete mixes of grade 50. The percentages of spent garnet used to replace sand in the concrete mixes were 0%, 10%, 20%, 30%, and 40% by weight of fine aggregate. Each mix had the same quantity of cement, POC as coarse aggregate, water, and superplasticizer. The concrete mixture proportions used in this experiment are listed in Table 4. The lightweight concrete aggregate mix was prepared using a mechanical mixer. Sand, POC aggregate, spent garnet, and cement were dry-mixed for three minutes before adding water and superplasticizer. The remaining water and SP were mixed and put into the concrete mix, which was then mixed for 5 minutes. Concrete was cast in cubes and compacted appropriately. The concretes were covered with a damp gunny bag and kept in the mould for 24 hours before being removed. All concrete cubes were 7-, 28-, and 60-day water cured. The compressive strength, splitting tensile strength, flexural strength, modulus of elasticity, water absorption, and acid resistance of the concrete were then determined.

2.3. Test Methods. The slump test was performed in accordance with BS EN 12350–2 [26] to establish the workability of the concrete mix. The dry density of the concrete specimen was determined according to ASTM C 642 [27]. The compressive strength of POC concrete was evaluated using the BS EN 12390–3 [28] standard testing procedure. For the flexural strength measurement, three-point bending tests were conducted according to BS EN 12390-5 [29]. Splitting tensile strength of the concrete cylinders was carried out by referring to ASTM C496-96 [30]. The static modulus elasticity of concrete was established by conducting testing in accordance with BS 1881: Part 121 [31]. The performance of concrete in terms of water absorption and acid resistance was evaluated through testing conducted following the procedure in BS EN 1881-122 [32] and experimental method of Sarıdemir et al. [33], respectively.

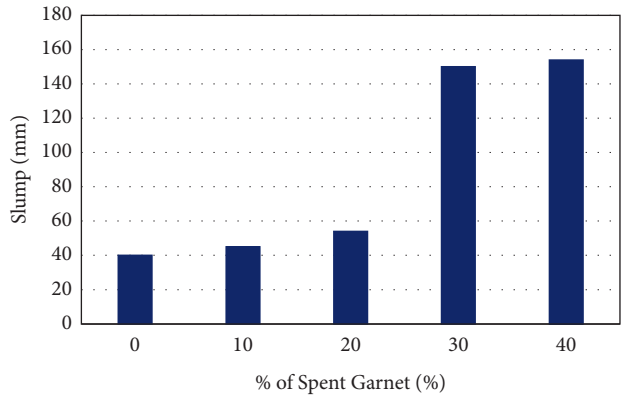

Figure 5: Slump value of POC LWAC containing spent garnet.

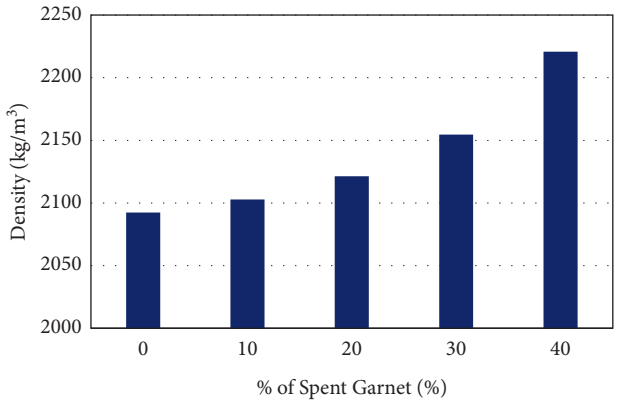

Figure 6: Oven dry density of POC LWAC containing spent garnet.

3. Results and Discussions

3.1. Workability. The effect of spent garnet as partial sand replacement in palm oil clinker lightweight aggregate concrete (POC LWAC) mixes towards slump is shown in Figure 5. As the spent garnet content was increased, the workability of POC LWAC increased. Figure 5 reveals slump values of 40 mm, 45 mm, 54 mm, 150 mm, and 154 mm for POC LWAC, with addition of 0%, 10%, 20%, 30%, and 40% of spent garnet, respectively. Control POC LWAC mixture was the least cohesive among the mixtures consisting of spent garnet. The improvement in the workability of the mix was due to the higher density of spent garnet (2006 kg/m^3) compared to river sand (1541 kg/m^3). The approach of integrating spent garnet to replace sand by weight resulted in smaller volume of this solid waste to be added to the mix, thus resulting in a mixture with enhanced workability. Furthermore, the smaller particle size of spent garnet improved the workability of concrete as the surface bonding between particles increased. A similar trend was also observed by the previous researchers [12, 34, 35] in different types of concrete.

3.2. Oven dry Density. Figure 6 shows that the inclusion of spent garnet increased the density of all mixes. Density of POC LWAC increased from 2091 kg/m^3, 2102 kg/m^3, 2120 kg/m^3, and 2154 kg/m^3 to 2220 kg/m^3 when the replacement levels of river sand by spent garnets were increased from 0% to 10%, 20%, 30%, and 40%, respectively. POC LWAC containing 40% of spent garnet exhibited the largest density value. This occurred because the spent garnet had higher bulk density and specific gravity compared to river sand, which were 2006 kg/m^3 and 3.75, respectively. The effect of using iron ore, which was a waste material with different bulk density, as fine aggregate on density of concrete has also been documented by the previous researchers [12, 35]. According to BS EN 1992-1-1 (2004) [36], lightweight concrete had density not more than 2200 kg/m^3. Therefore, all replacements were categorized as lightweight concrete excluded 40%.

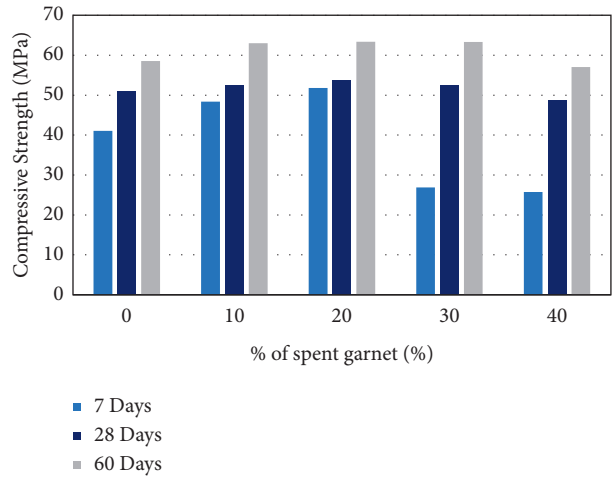

Figure 7: Compressive strength of POC LWAC containing spent garnet.

3.3. Compressive Strength. The compressive strength of POC LWAC with varying percentages of spent garnet as a partial sand replacement is shown in Figure 7. Compressive strength increased steadily over time as the age increased. On Day 60 of curing age, the results indicated that the strength of POC LWAC containing 20% (63.4 MPa) spent garnet was the highest compared to the control specimen (58.6 MPa). The strength decreased as the percentage of spent garnets increased, reaching 63.3 MPa and 57.0 MPa at 30% and 40%, respectively. The mix with 20% of spent garnet demonstrated the highest strength value. The presence of finer aggregates in the particle size passing 600 μm filled in the existing spaces in the concrete, thus forming more compact concrete structure with higher strength. The increase in compressive strength of POC LWAC could partly be attributed to spent garnets' rough and angular texture, and finer particles. According to Muttashar et al. [16], the coarse and angular texture of the spent garnet materials increased bonding at the cement-aggregate contact, resulting in the high strength. The study also stated that a rough and angular surface on the materials improved the grip between the particles and reduced the strength loss that led to higher strength of the concrete [37]. In addition, lower water absorption of spent garnet means fewer pores on the concrete

surface and a stronger bond between cement paste and aggregates [38]. The difference in the internal structure fashion was due to the use of suitable spent garnet content that can be seen in Figures 8 and 9. The microstructure of control specimen is less compact, as illustrated in Figure 8, in contrast to the concrete with 20% spent garnet, which appears well-packed and denser, as in Figure 9. Precaution needed to be taken to not use this waste excessively as the use of spent garnet at 30% and 40% decreases the compressive strength of concrete. However, the mix produced using 30% can still be classified as high strength concrete, whereas the one produced by integrating 40% spent garnet can be used for structural application.

The relationship between compressive strength against spent garnet content and curing days is presented in Figure 10. As suggested from response surface method (RSM), the quadratic model was the best fit to maximize the relationship. The plot shows that the compressive strength improved with prolonged curing days. However, it was obvious that the compressive strength decreased with an increase in the level percentage of spent garnet in POC LWAC, as shown in Figure 10(a). The RSM plots also clearly displayed that inclusion of 20% spent garnet in POC LWAC enhanced the strength performance as compared to plain POC LWAC and those contained 10%, 30%, and 40% spent garnet. The analysis is fit from 0, 10, 20, 30, and 40%, in which the regression analysis (from ANOVA analysis) is approaching to value $R^2 > 0.80$. The strong relation proves the effectiveness of the spent garnet as 20% of replacement towards compressive strength. Figure 10(b) depicts a graphic representation of response surface to visualize the effects. A curvature in the plot indicates the sensitivity of response factors. The curvature of Curve A was more curved than that of Curve B, thus indicating that those different levels of percentages spent garnet were more sensitive than the age of curing to enhance the compressive strength. From ANOVA analysis, the regression indicated that the relationship between compressive strength and those variables was strong, where R^2 value was 0.866. The empirical relationship between compressive strength and multiples factors (% spent garnet and curing days) is presented in the following equation:

$$\mathrm{CS} = -0.0191\mathrm{A}^2 - 0.0060\mathrm{B}^2 + 0.0086\mathrm{AB} + 0.291\mathrm{A} + 0.652\mathrm{B} + 38.902, \quad (1)$$

where CS is compressive strength, A is percentage of spent garnet, and B is curing day.

3.4. Flexural Strength. The results of flexural strengths of POC LWAC containing spent garnet are shown in Figure 11, which illustrates strength at Day 7, Day 28, and Day 60 of concrete age. The flexural strengths of 4.21 MPa, 8.13 MPa, 8.45 MPa, 7.92 MPa, and 7.74 MPa at the age of Day 7 in mixtures of 0%, 10%, 20%, 30%, and 40%. However, at Day 28 and Day 60 of curing age, the flexural strengths of the specimens were 10.98 MPa, 11.09 MPa, 11.10 MPa, 10.95 MPa, 10.66 MPa, and 11.21 MPa, 11.22 MPa, 11.46 MPa, 11.21 MPa, and 11.20 MPa, respectively. Evidently, all specimens demonstrated strength increment as the curing period became longer, resulting from better hydration process. The test results revealed that POC LWAC containing spent garnet in 20% enhanced strength compared to the control POC LWAC at all ages. However, the mixture produced using 30% and 40% replacement of spent garnet showed a decrease in flexural strength, whereby the pattern was similar to the compressive strength result. SOman et al. [39] and Kim and Lee [40] also described similar observations upon the use of high amount of waste material as sand replacement in concrete.

The response surface 3D plot in Figure 12 indicates the relationship between percentage of spent garnet and curing day towards flexural strength. It was found that POC containing higher content of spent garnet had no effect on the flexural strength when compared to plain POC specimens. The plots in Figure 12(a) clearly illustrate that POC incorporating 20% spent garnet attained the highest

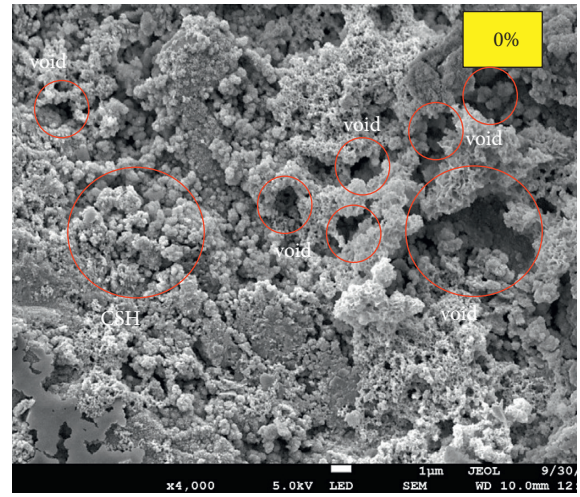

Figure 8: POC control specimen with many voids.

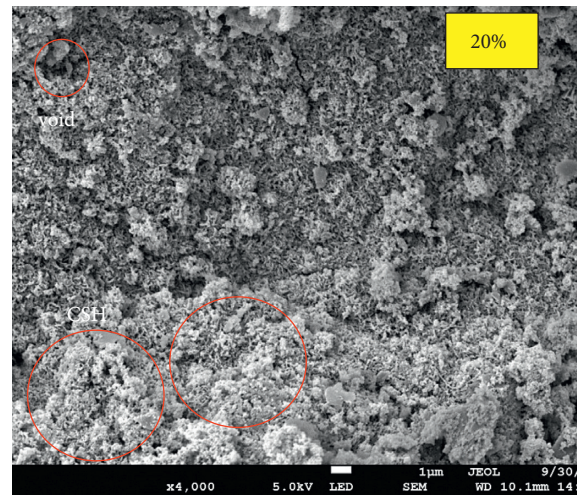

Figure 9: Specimen containing 20% spent garnet with lesser amount of voids.

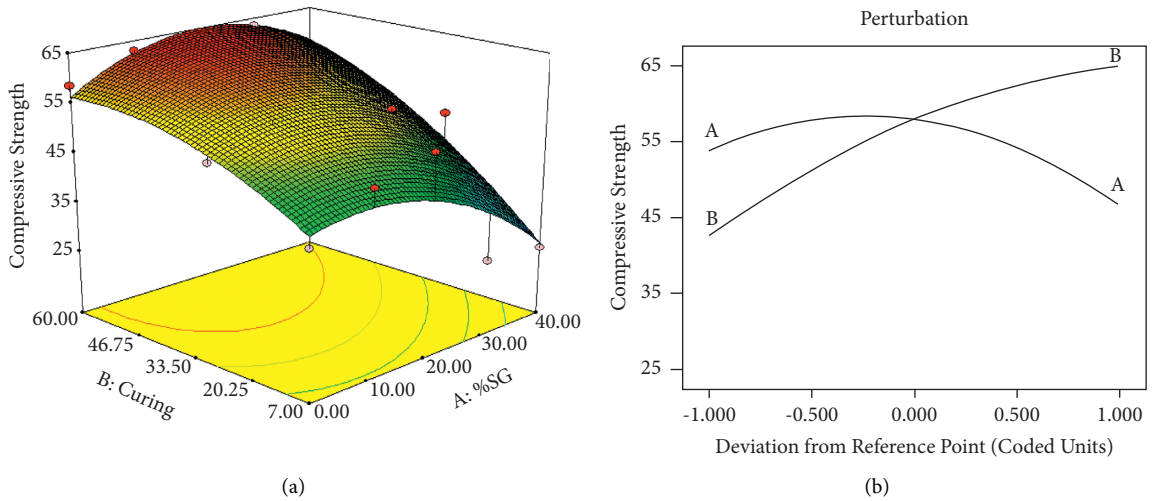

Figure 10: Response surface plots (a) and perturbation plots (b) indicating the relationship between spent garnet content and curing days with respect to compressive strength.

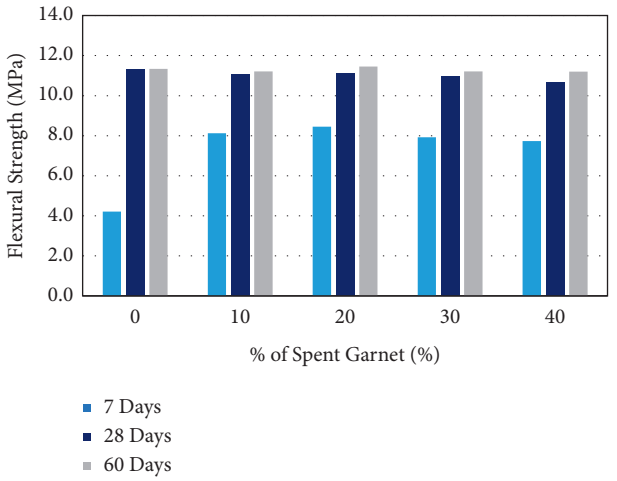

Figure 11: Flexural strength of POC LWAC containing spent garnet.

flexural strength as compared to that plain POC. By using ANOVA analysis, the regression indicated that the effect of different level percentage of spent garnet and curing days towards flexural strength was significant. The quadratic model was selected, and the value of R2 obtained from the analysis was 0.9939. Overall, the analysis is fitting from 0, 10, 20, 30, and 40% as the regression analysis (from ANOVA analysis) is approaching value > 0.80. Thus, the robust relation demonstrates the efficacy of the spent garnet at 20% replacement towards flexural strength of concrete. It is interesting to note that Figure 12(b) demonstrates that Curve B was much curved than Curve A, thus indicating that prolonging the curing day was more sensitive than the content of spent garnet to enhance the flexural strength. From the quadratic regression, the relation equation between spent garnet content and curing day on flexural strength of spent garnet based POC is shown in the following equation:

$$FS = -0.0002A^2 - 0.0024B^2 + 0.0003AB - 0.013A + 0.215B + 7.126, \quad (2)$$

where FS is flexural strength, A is percentage of spent garnet, and B is curing day.

3.5. Splitting Tensile Strength. Figure 13 illustrates the effect of substituting spent garnet for sand on the splitting tensile strength of POC LWAC. The splitting tensile strength of POC LWAC mixes containing 20% spent garnet waste was greater than that of the control sample at all curing ages. This might be because the optimal proportion of finer garnet particles resulted in improved bonding between aggregates and cement paste. Utilizing spent garnet more than 20% resulted in a weaker concrete with a lower splitting tensile strength. The decreased fine aggregate ratio was ascribed to the deterioration of interface between the spent garnet particles and binder paste. Huseien et al. [12] previously observed a decline in concrete strength because of excessive waste material use.

Figure 14 evaluates the relationship between spent garnet content and curing days against splitting tensile strength. The quadratic model was designed by RSM to obtain the best fit for splitting tensile strength relation with the percentage of spent garnet and curing days, as presented in Figure 14(a). The results described that the splitting tensile strength for POC was influenced by the inclusion of spent garnet in POC mixes. Based on the regression analysis (from ANOVA analysis), which is approaching (value $R^2 > 0.80$), it can be deduced that the analysis is fit from 0, 10, 20, 30, and 40% of spent garnet as fine aggregate replacement. The 3D surface response showed that when the content of spent garnet increased, the splitting tensile strength of POC specimens decreased. In contrast, when the curing days increased, the splitting tensile strength increased with decreasing spent garnet content. The quadratic regression analysis revealed that R^2 obtained was 0.9861, which means that about 98.61% of its

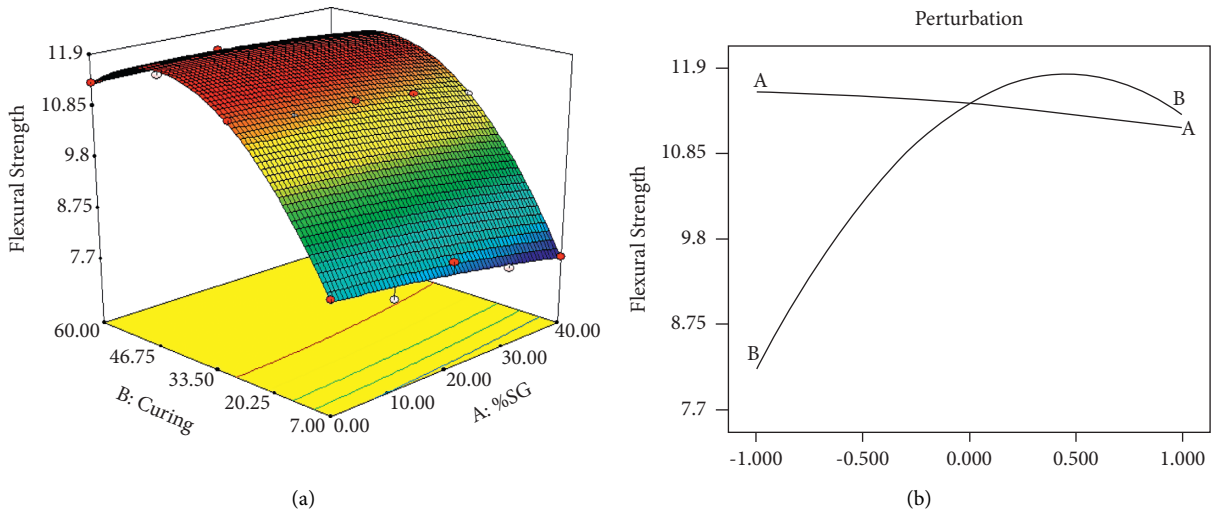

(a) (b)

Figure 12: Response surface plots (a) and perturbation plots (b) indicating the relationship between spent garnet content and curing days with respect to flexural strength.

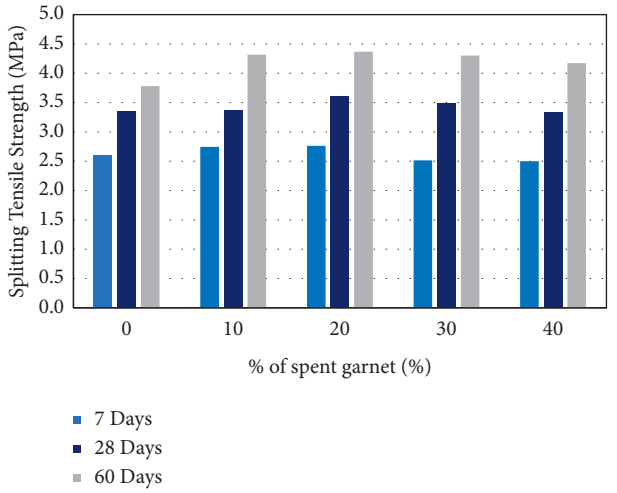

Figure 13: Splitting tensile strength of POC LWAC containing spent garnet.

spent garnet content and curing days contributed to the variation in splitting tensile strength of POC. Instead, the adequacy of the model was also tested by examining the perturbation trends, as depicted in Figure 14(b). The steep slope in the perturbation plots shown in Curve A for the content of spent garnet indicated that the inclusion of different percentages of spent garnet in POC enhanced the strength properties. The relation equation between splitting tensile strength with respect to that spent garnet content and curing days is shown in the following equation:

$$TS = -0.0006A^2 - 0.0003B^2 + 0.0002AB + 0.04A + 0.02B + 2.29, \quad (3)$$

where TS is splitting tensile strength, A is percentage of spent garnet, and B is curing day.

3.6. Modulus of Elasticity. The results of modulus of elasticity at age of 7, 28, and 60-day curing are shown in Figure 15. It can be observed that the variation in the amount of spent garnet used influenced the stiffness of the POC LWAC. The combination of 20% spent garnet as fine aggregate increased the modulus of elasticity by 32%, 59%, and 7.02%, respectively, compared to control mixture at all ages. The positive contribution of 20% spent garnet inclusion to form denser internal structure resulted in the formation of lower deflection of concrete upon subjected to loading. According to Neville [38], an increase in the modulus of elasticity of concrete signified an increase in the stiffness of the concrete element, which may result in less deflection in the structural element. Similar patterns were seen in the compressive strength result obtained in this study. The elastic modulus of concrete was usually directly proportional to its compressive strength (high strength constitutes high elastic modulus) [41]. Upon inclusion of 30 and 40% of spent garnet in the mix, concrete became less stiff and exhibited lower modulus elasticity value.

The effect of numerical factors between spent garnet content and curing days towards modulus of elasticity (MOE) of POC and POC contained spent garnet was found by RSM analysis and presented in Figure 16. In this RSM analysis, the 3D surface response plots displayed that the inclusion of spent garnet in POC mixes significantly affected MOE, as shown in Figure 16(a). POC with 20% spent garnet resulted in higher MOE as compared to those of POC mixes. The 3D surface response plots also demonstrated that when the duration of curing prolonged, MOE also increased. It was observed that the spent garnet content and curing days had a strong relationship with the MOE (R^2 was 0.8486). It can be stated that the different percentages of spent garnet in POC mix were more dominant in prescribing the MOE of concrete. The perturbation plots were drawn to estimate the influence of individual effect of those variables to the MOE of POC and are presented in Figure 16(b). It demonstrates

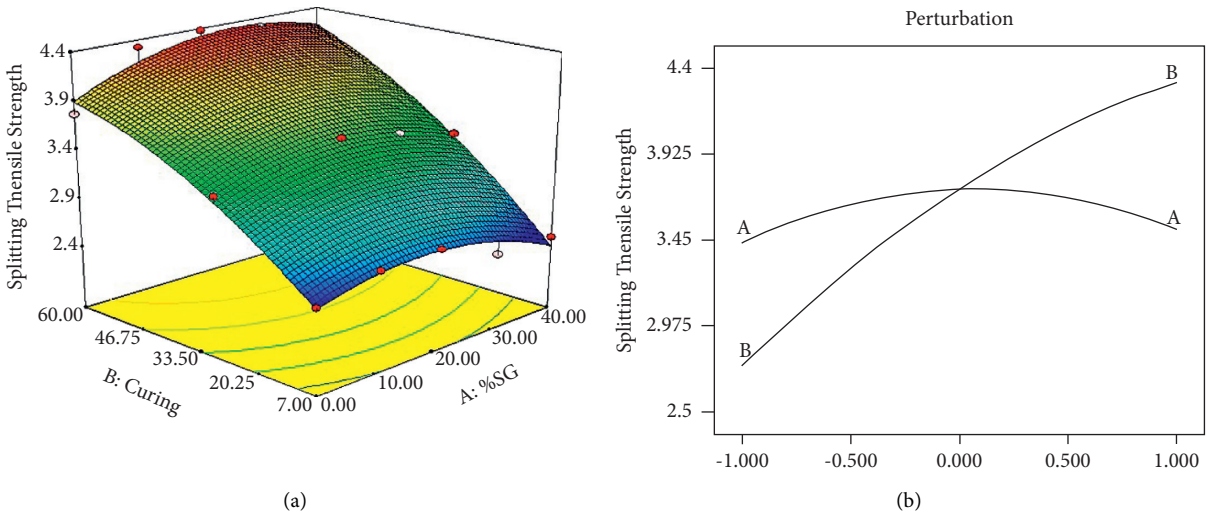

Figure 14: Response surface plots (a) and perturbation plots (b) indicating the relationship between spent garnet content and curing days with respect to splitting tensile strength.

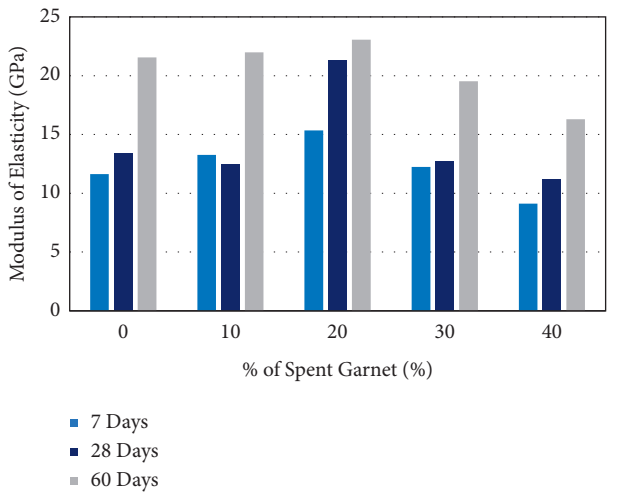

Figure 15: Modulus of elasticity of POC LWAC containing spent garnet.

that Curve A (spent garnet content) showed more curvy nature as compared to Curve B (curing days). Therefore, Curve A shows that response was sensitive, indicating that increment in MOE of POC decreased the content of spent garnet in POC mixes. The empirical relationship between compressive strength and multiples factors (% spent garnet and curing days) is expressed in Equation (4). It is observed that there is a potential relationship between the compressive strength and its modulus of elasticity with an adjustment around $R^2 = 0.54$ as shown in Figure 17.

$$MOE = -0.0108A^2 + 0.0020B^2 - 0.0014AB + 0.398A + 0.049B + 10.568, \quad (4)$$

where MOE is modulus of elasticity, A is percentage of spent garnet, and B is curing day.

3.7. Water Absorption. The effect of spent garnet as a partial fine aggregate replacement on the water absorption of POC LWAC is shown in Figure 18. According to the 28-day results, water absorption was 2.8%, 2.7%, 2.0%, 2.5%, and 2.6% for 0%, 10%, 20%, 30%, and 40% replacement of spent garnet in POC concrete, respectively. All POC LWAC specimens were categorized as good quality concrete as the water absorption was less than 4%. According to Neville [38], concrete with water absorption of less than 10% is classified as good quality concrete. The integration of 20% spent garnet, which resulted in the lowest water absorption value than other replacements, could be associated with the spent garnet fine particles acting as filler, thus forming a more compact structure. Figure 19 proves that concrete with 0% spent garnet had more void and less density, resulting in the highest water absorption compared with mix formed using 20% of spent garnet replacement, as shown in Figure 20. According to Zhang et al. [37], the decrease in water absorption was mostly due to the inner structure gradually densifying. However, excessive use of spent garnet at 30% and 40% caused rise in water absorption value. When too much of spent garnet was used, the packing level of aggregate may be inadequate, resulting in voids inside the concrete specimens. These unfilled voids allowed water to infiltrate and fill the voids. Therefore, a 20% replacement of sand with spent garnet was regarded as optimum and created the best specimen of all. Figure 21 show that water absorption has no clear relationship with compressive strength.

3.8. Acid Resistance. As illustrated in Figure 22, the usage of spent garnet affects the durability of POC LWAC that has been immersed in a 10% hydrochloric acid solution for 28 and 60 days, respectively. Generally, as the immersion duration increased, all concrete specimens undergo higher mass loss and strength. Figure 23POC LWAC containing up to 30% of spent garnet exhibit lower mass loss and strength

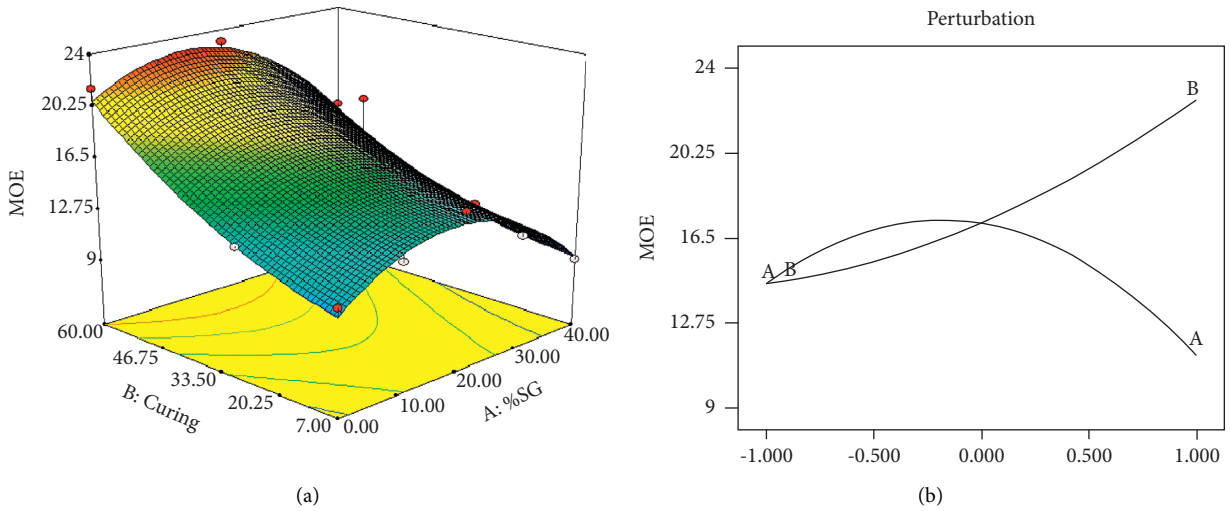

Figure 16: Response surface plots (a) and perturbation plots (b) indicating the relationship between spent garnet content and curing days with respect to modulus of elasticity (MOE).

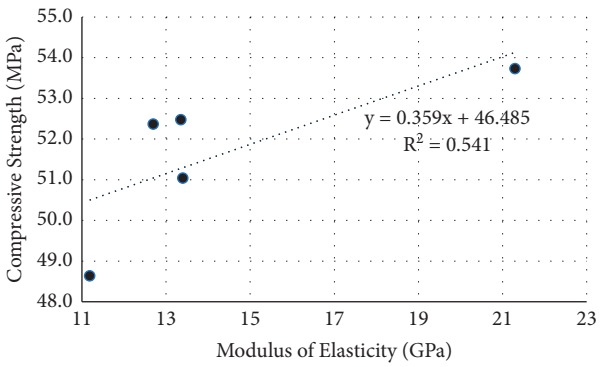

Figure 17: Fitted line plots of regression analysis for the relationship between compressive strength and modulus of elasticity on 28-day curing.

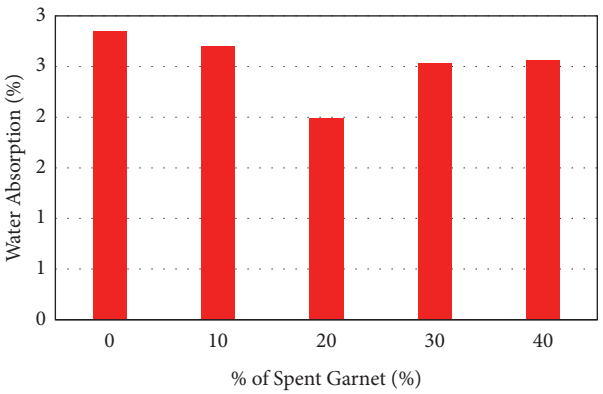

Figure 18: Water absorption of POC LWAC containing spent garnet.

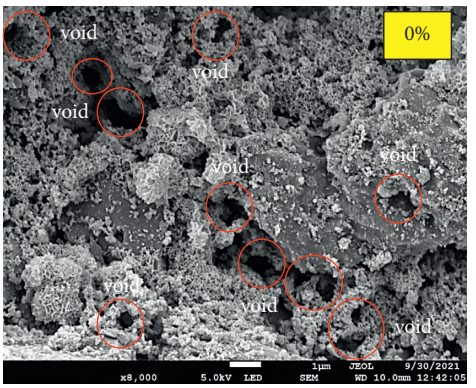

Figure 19: Appearance of many voids in the POC LWAC specimens containing 0% spent garnet.

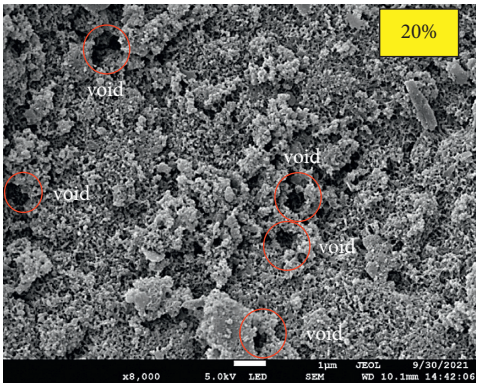

Figure 20: Appearance of lesser void in the POC LWAC specimens containing 20% spent garnet.

reduction as compared to plain concrete. The mix produced using 20% spent garnet demonstrates the least mass loss and strength reduction across the various immersion durations compared to other specimens. After 60 days of hydrochloric acid, the mass loss and strength reduction of 20% spent garnet are 0.57% and 10.8%, respectively, compared to the control specimen, 1% and 19.3%, respectively. The ability of POC LWAC sample with 20% of spent garnet replacement to withstand the acidic attack is related to the filler effect

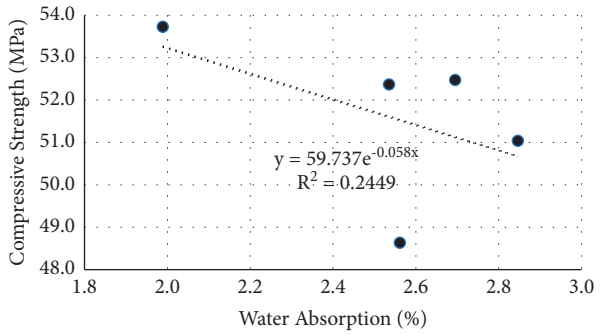

Figure 21: Fitted line plots of regression analysis for the relationship between compressive strength and water absorption.

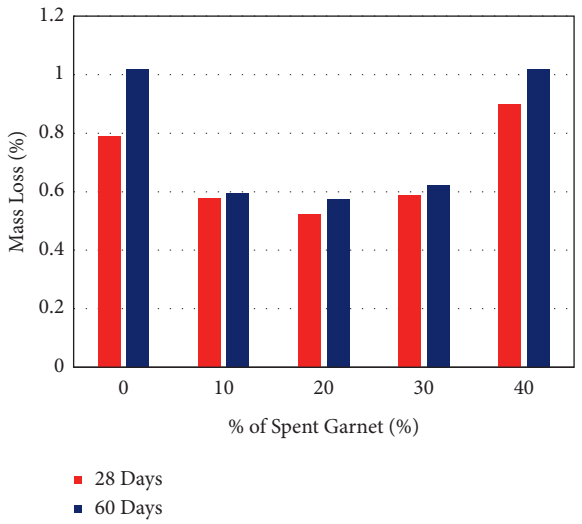

Figure 22: Mass loss of POC LWAC due to acid attack.

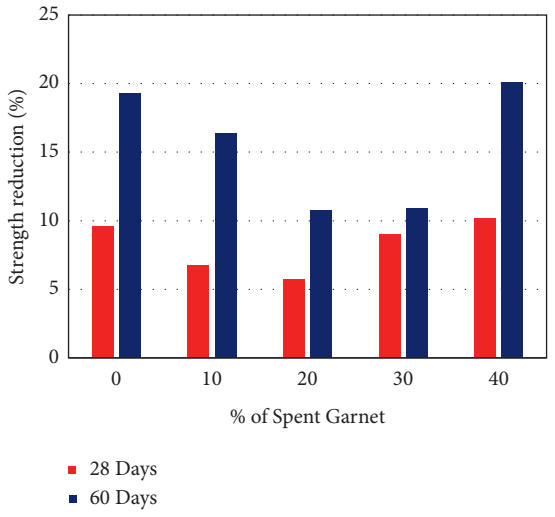

Figure 23: Strength reduction of POC LWAC due to acid attack.

provided by the spent garnet, which contributed to the densification concrete by reducing the voids. This condition makes the durability of POC LWAC with 20% of spent garnet in acidic environment is higher compared to control

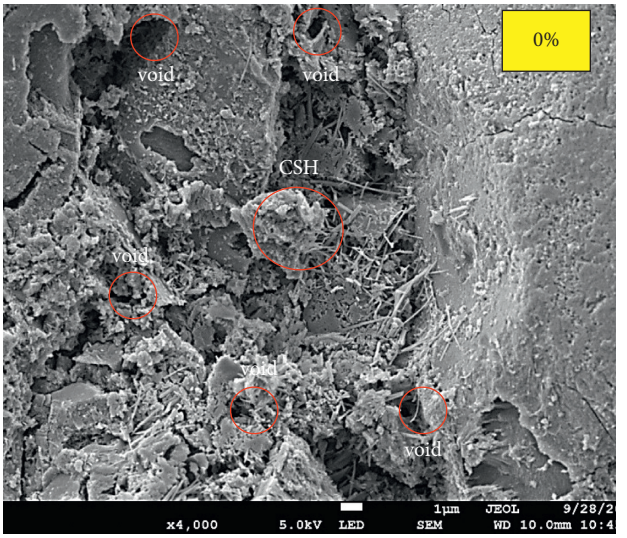

Figure 24: Microstructure of POC LWAC containing 0% spent garnet after exposure to hydrochloric solution at 28 days.

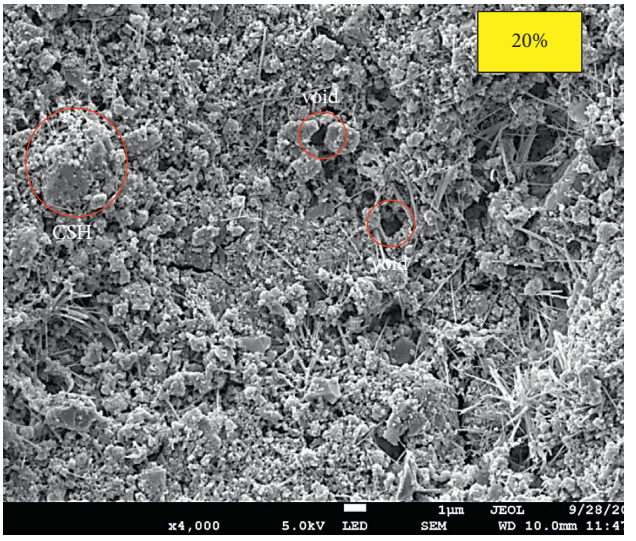

Figure 25: Microstructure of POC LWAC containing 20% spent garnet after exposure to hydrochloric solution at 28 days.

specimen. The scanning electron microscope image of the samples after acid resistance test shows control specimen (Figure 24) with the surface texture that has been exposed to leaching and the presence of large voids in contrast to mix with 20% spent garnet (Figure 25) with lesser voids. Zivica and Bajza [43] stated that the acidic resistance of cement-based materials is significantly dependent on pore size distribution. The resistance of the concrete was increased when its content of finer pores decreased. Extreme use of spent garnet of 40% significantly reduces the durability of concrete to acid attack. Due to the hydrochloric acid attack, the concrete matrix weakened, and the specimen's weight decreased due to the loss of cement paste. Calcium hydroxide is soluble in water and tends to get leached out from the concrete surface upon exposure to acidic environment. Conclusively, inclusion of 20% spent garnet improved the

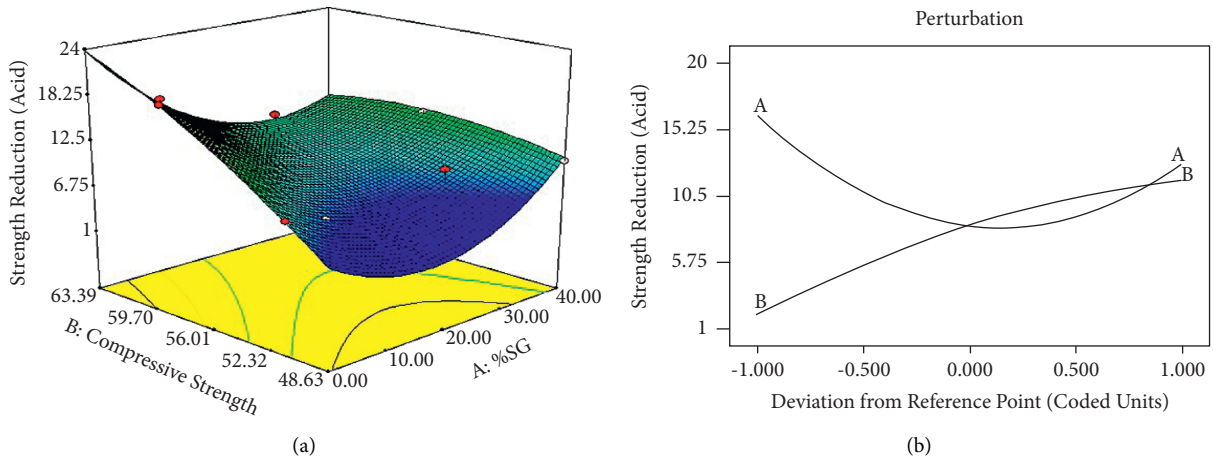

Figure 26: Response surface plots (a) and perturbation plots (b) indicating the relationship between spent garnet content and strength reduction with respect to strength reduction (acid resistance).

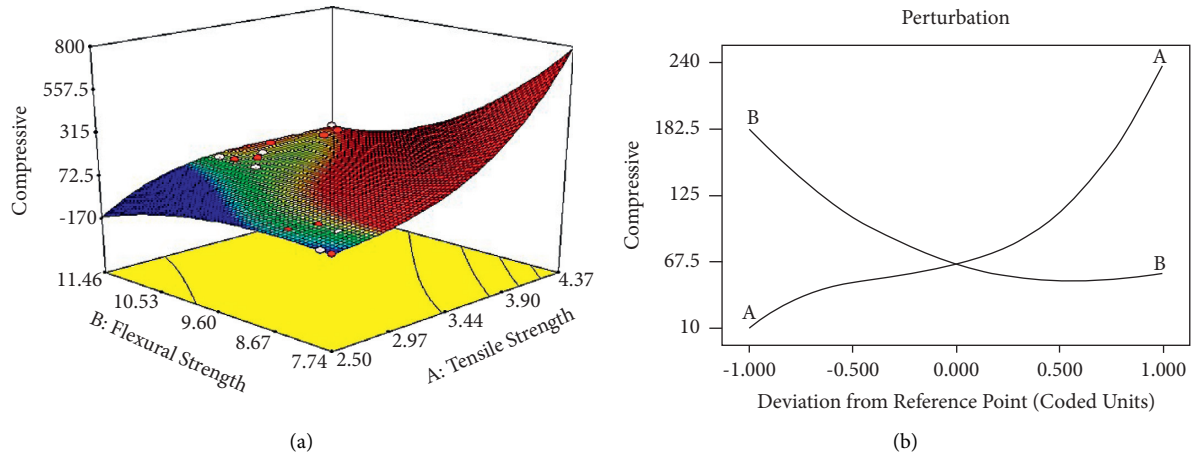

Figure 27: Response surface plots (a) and perturbation plots (b) indicating the relationship between compressive, flexural, and splitting tensile strength.

internal microstructure of the concrete by filling internal spaces and resistance to acid attack.

The verification was performed to confirm the effect of spent garnet in POC LWAC to acid resistance, as shown in Figure 26. The RSM plots indicated the relationship between spent garnet content and compressive strength towards strength reduction when the POC LWAC specimens were immersed in acid solution at Day 28 and Day 60. The 3D surface plots in Figure 26(a) illustrate that the spent garnet and compressive strength of plain POC specimens and a series of spent garnet-based POC specimens significantly affected the strength reduction. It can be noted that when the spent garnet content was increased, the compressive strength of POC LWAC decreased consequently, influencing the reduction in strength. Figure 26(b) shows the perturbation plots to compare the individual effect (% spent garnet and compressive strength) on the strength reduction (acid resistance). It shows that, with the curvature in the levels of percentage spent garnet, Curve A seemed to be much curved than Curve B, indicating that Curve A was more sensitive to the strength reduction. Therefore, POC LWAC containing 20% spent garnet provided positive effect. Inclusion of 20% spent garnet in POC LWAC exhibited an increase in strength and good resistance when exposed to acid solution. The quadratic model was the best fit for the analysis, and the value of R^2 obtained was found to be 0.961. R^2 obtained showed strong correlation for the model. This means that about 96.10% variation in the strength reduction could be explained by the spent garnet content in POC concrete.

4. Relationship between Compressive, Flexural, and Splitting Tensile Strength

Figure 27 illustrates the relationship between compressive, flexural, and splitting tensile strength of the POC LWAC containing spent garnet. As suggested from the response surface method (RSM), the cubic model was the best fit to maximize the relationship. The results described that the compressive strength for POC LWAC was influenced by flexural strength. It can be observed from the regression model that a strong relation was existing in between compressive, flexural, and splitting tensile strength having R^2

greater than 90%. Figure 27(b) shows the perturbation plots to compare the individual effect (flexural strength and splitting tensile strength) on the compressive strength. It shows that the curvature in levels of flexural strength Curve B seemed to be much more curved than Curve A, indicating that Curve B was more sensitive to the compressive strength.

5. Conclusion

The following conclusions can be drawn from this investigation:

(1) POC concrete mixes had a slump value in the range of 40 mm–185 mm. As the spent garnet content increased, the workability of concrete increased.

(2) The density of POC concrete increased with the increase of spent garnet in the concrete mix. It ranged from 2091 kg/m^3 to 2220 kg/m^3 because the bulk density of spent garnet was higher than that of river sands.

(3) The highest compressive strength was 63.4 MPa with spent garnet replacing 20% of the sand. At Day 60 of water curing, the lowest compressive strength recorded was 57 MPa with 40% replacement of spent garnet as sand.

(4) The flexural strength, splitting tensile strength, and modulus of elasticity of concrete mixtures prepared with 20% spent garnet were higher than those of the corresponding control concrete.

(5) By substituting 20% spent garnets for river sand, the durability properties such as water absorption and resistance to hydrochloric acid attack were enhanced.

(6) The viability of integrating spent garnet as an acceptable substitute for river sand in POC concrete was demonstrated in this research.

(7) The response surface plots clearly displayed that the inclusion of 20% spent garnet in POC mix enhanced the performance of spent garnet based POC. The regression coefficient (R^2) derived from the ANOVA analysis also indicated that the relationship between factors and those variables is strong. The robust relation verifies the effectiveness of 20% spent garnet as partial fine aggregate replacement towards compressive strength, flexural strength, and splitting tensile strength. The prediction model can be used as reference model for future testing on spent garnet in POC concrete. [42].

Data Availability

The data used to support the findings of this study are included within the article.

Conflicts of Interest

The authors state that they have no known conflicting financial or personal interests that might seem to have influenced the work presented in this study.

Acknowledgments

The authors would like to thank University Malaysia Pahang (UMP) for funding the research (Research Grant RDU190342 and RDU213306).

References

[1] United Nations Department of Economic and Social Affairs, "Ensure access to affordable, reliable, sustainable and modern energy for all," *UN DESA*, vol. 51, no. 4, pp. 17-18, 2015.

[2] A. Opoku, "Biodiversity and the built environment: implications for the sustainable development Goals (SDGs)," *Resources, Conservation and Recycling*, vol. 141, pp. 1–7, 2019.

[3] K. Thunga and T. Das, "An experimental investigation on concrete with replacement of treated sea sand as fine aggregate," *Materials Today Proceedings*, vol. 27, pp. 1017–1023, 2020.

[4] S. A. Zareei, F. Ameri, N. Bahrami, P. Shoaei, H. R. Moosaei, and N. Salemi, "Performance of sustainable high strength concrete with basic oxygen steel-making (BOS)slag and nano-silica," *Journal of Building Engineering*, vol. 25, Article ID 100791, 2018.

[5] McGill University, "Global sand and gravel extraction conflicts with half of UN Sustainable Development Goals," *One Earth*, vol. 4, no. 8, pp. 1095–1111, 2021.

[6] W. Liu and C. Song, "Effect of post injection strategy on regulated exhaust emissions and particulate matter in a HSDI diesel engine," *Fuel*, vol. 185, pp. 1–9, 2016.

[7] L. Koehnken and M. Rintoul, *Impacts of Sand Mining on Ecosystem Structure*, Process & Biodiversity in Rivers, WWF, Rue Mauverney 28, 1196 Gland, Switzerland, 2018.

[8] M. Kuhar, *World Aggregates Market*, pp. 2–4, Denver, Co, USA, 2014.

[9] S. W. Danielsen and E. Kuznetsova, "Environmental impact and sustainability in aggregate production and use," *Eng. Geol. Soc. Territ. - Urban Geol. Sustain. Plan. Landsc. Exploit.,* vol. 5, pp. 1–1400, 2015.

[10] Z. Qin, Q. Chen, X. Ji, S. Ming, and Q. Du, "Biodiversity protection and ecological restoration of Guilin Karst quarry," *E3S Web of Conferences*, vol. 194, Article ID 04025, 2020.

[11] U.S, "Geological Survey," *"GARNET (INDUSTRIAL)," Miner. Commod. Summ.,* vol. 1, no. 703, pp. 2019-2020, 2019.

[12] G. F. Huseien, A. R. M. Sam, K. W. Shah, A. M. A. Budiea, and J. Mirza, "Utilizing spend garnets as sand replacement in alkali-activated mortars containing fly ash and GBFS," *Construction and Building Materials*, vol. 225, pp. 132–145, 2019.

[13] M. A. Ab Kadir, M. I. Khiyon, A. R. M. Sam et al., "Performance of spent garnet as a sand replacement in high-strength concrete exposed to high temperature," *Journal of Structural Fire Engineering*, vol. 10, no. 4, pp. 468–481, 2019.

[14] H. L. Muttashar, M. W. Hussin, J. M. Mohd Azreen Mohd Arriffin, N. Hasanah, and A. U. Shettima, "Mechanical properties of self-compacting geopolymer concrete containing spent garnet as replacement for fine aggregate," *J. Teknol.,* vol. 3, pp. 23–29, 2017.

[15] K. R. Usman, M. R. Hainin, M. K. I. M. Satar et al., "A comparative assessment of the physical and microstructural properties of waste garnet generated from automated and manual blasting process," *Case Studies in Construction Materials*, vol. 14, Article ID e00474, 2021.

[16] H. L. Muttashar, M. A. M. Ariffin, M. N. Hussein, M. W. Hussin, and S. Bin Ishaq, "Self-compacting geopolymer

concrete with spend garnet as sand replacement," *Journal of Building Engineering*, vol. 15, pp. 85–94, 2018.
[17] D. Workman, "World ' s top exports palm oil exports by country palm," *oil exports by country*, pp. 1–6, 2020.
[18] Malaysia Palm Oil Board, "Overview of the Malaysian oil palm industry," *No. January*, vol. 1, pp. 1–6, 2020.
[19] K. H. Mo, U. J. Alengaram, P. Visintin, S. H. Goh, and M. Z. Jumaat, "Influence of lightweight aggregate on the bond properties of concrete with various strength grades," *Construction and Building Materials*, vol. 84, pp. 377–386, 2015.
[20] H. A. Ibrahim and H. Abdul Razak, "Effect of palm oil clinker incorporation on properties of pervious concrete," *Construction and Building Materials*, vol. 115, pp. 70–77, 2016.
[21] M. A. Sulaiman, M. I. Ali, M. Y. Al-Amri et al., "Properties of concrete containing crushed palm oil clinker as partial fine aggregate replacement," *IOP Conference Series: Materials Science and Engineering*, vol. 712, no. 1, 2020.
[22] H. M. Hamada, G. A. Jokhio, A. A. Al-Attar et al., "The use of palm oil clinker as a sustainable construction material: a review," *Cement and Concrete Composites*, vol. 106, Article ID 103447, 2020.
[23] A. R. G. De Azevedo, M. Teixeira, B. A. Tayeh, D. Cecchin, A. Camposo, and S. Neves, "Technological performance of açaí natural fibre reinforced cement-based mortars," *Journal of Building Engineering*, vol. 33, Article ID 101675, 2021.
[24] J. Kanadasan, A. Fauzi, H. Razak, P. Selliah, V. Subramaniam, and S. Yusoff, "Feasibility studies of palm oil mill waste aggregates for the construction industry," *Materials*, vol. 8, no. 9, pp. 6508–6530, 2015.
[25] Mida, "Sustainable waste management in Malaysia : opportunities and challenges," *Malaysian Invest. Dev. Auth.*, pp. 1–14, 2019.
[26] Bs En 12350-2, *Testing Fresh concrete — Part 2: Slump Test*, The British Standards Institution, London, UK, 2009.
[27] ASTM C642, *Standard Test Method for Density, Absorption, and Voids in Hardened Concrete*, ASTM International, West Conshohocken, PA, USA, 2013.
[28] BS EN 12390-3, *Compressive Strength of Test Specimens*, The British Standards Institution, London, UK, 2001.
[29] B. S. En 12390-5, *Testing Hardened concrete - Part 5: Flexural Strength of Test Specimens*, The British Standards Institution, London, UK, 2009.
[30] ASTM C 496, *Standard Test Method for Splitting Tensile Strength of Cylindrical Concrete*, ASTM International, West Conshohocken, PA, USA, 1996.
[31] BS 1881, *Part 121, Method for Determination of Static Modulus of Elasticity in Compression*, The British Standards Institution, London, UK, 1983.
[32] BS 1881-122, *Method for Determination of Water Absorption*, The British Standards Institution, London, UK, 1983.
[33] M. Sarıdemir and S. Çelikten, "Investigation of fire and chemical effects on the properties of alkali," *Activated Lightweight Concretes Produced with Basaltic Pumice Aggregate*, vol. 260, 2020.
[34] A. M. A. Budiea, W. Z. Sek, S. N. Mokhatar, K. Muthusamy, and A. R. M. Yusoff, "Structural performance assessment of high strength concrete containing spent garnet under three point bending test," *IOP Conference Series: Materials Science and Engineering*, vol. 1144, no. 1, Article ID 012018, 2021.
[35] N. H. Abdul Shukor Lim, N. F. N. Alladin, H. Mohammadhosseini, N. F. Ariffin, and A. N. Mazlan, "Properties of mortar incorporating spent garnet as fine aggregates replacement," *Int. J. Integr. Eng.*, vol. 12, no. 9, pp. 96–102, 2020.
[36] Bs En 1992-1-1, "Euro code 2: design of concrete structures - Part 1-1," *General rules and rules for buildings*, vol. 1, 2004.
[37] W. Zhang, X. Gu, J. Qiu, J. Liu, Y. Zhao, and X. Li, "Effects of iron ore tailings on the compressive strength and permeability of ultra-high performance concrete," *Construction and Building Materials*, vol. 260, Article ID 119917, 2020.
[38] A. M. Neville and J. J. Brooks, *Concrete Technology*, Longman, London, UK, 2012.
[39] K. Soman, D. Sasi, and K. A. Abubaker, "Strength properties of concrete with partial replacement of sand by bottom ash," *Int. J. Innov. Res. Adv. Eng.*, vol. 1, no. 7, pp. 2349–2163, 2014.
[40] H. K. Kim and H. K. Lee, "Use of power plant bottom ash as fine and coarse aggregates in high-strength concrete," *Construction and Building Materials*, vol. 25, no. 2, pp. 1115–1122, 2011.
[41] N. Saikia and J. De Brito, "Mechanical properties and abrasion behaviour of concrete containing shredded PET bottle waste as a partial substitution of natural aggregate," *Construction and Building Materials*, vol. 52, pp. 236–244, 2014.
[42] V. Zivica and A. Bajza, "Acidic attack of cement-based materials-a review Part 2. Factors of rate of acidic attack and protective measures," *Construction and Building Materials*, vol. 16, no. 4, pp. 215–222, 2002.

Hindawi
Advances in Civil Engineering
Volume 2023, Article ID 9856964, 1 page
https://doi.org/10.1155/2023/9856964

Retraction

Retracted: Study on Seismic Performance of Recycled Steel Fibers Locally Reinforced Cruciform Concrete Frame Beam-Column Joint

Advances in Civil Engineering

Received 10 October 2023; Accepted 10 October 2023; Published 11 October 2023

This article has been retracted by Hindawi following an investigation undertaken by the publisher [1]. This investigation has uncovered evidence of one or more of the following indicators of systematic manipulation of the publication process:

(1) Discrepancies in scope
(2) Discrepancies in the description of the research reported
(3) Discrepancies between the availability of data and the research described
(4) Inappropriate citations
(5) Incoherent, meaningless and/or irrelevant content included in the article
(6) Peer-review manipulation

The presence of these indicators undermines our confidence in the integrity of the article's content and we cannot, therefore, vouch for its reliability. Please note that this notice is intended solely to alert readers that the content of this article is unreliable. We have not investigated whether authors were aware of or involved in the systematic manipulation of the publication process.

Wiley and Hindawi regrets that the usual quality checks did not identify these issues before publication and have since put additional measures in place to safeguard research integrity.

We wish to credit our own Research Integrity and Research Publishing teams and anonymous and named external researchers and research integrity experts for contributing to this investigation.

The corresponding author, as the representative of all authors, has been given the opportunity to register their agreement or disagreement to this retraction. We have kept a record of any response received.

References

[1] Y. Li, R. Zhao, D. Li, and C. Qu, "Study on Seismic Performance of Recycled Steel Fibers Locally Reinforced Cruciform Concrete Frame Beam-Column Joint," *Advances in Civil Engineering*, vol. 2022, Article ID 8155038, 19 pages, 2022.

Hindawi
Advances in Civil Engineering
Volume 2022, Article ID 8155038, 19 pages
https://doi.org/10.1155/2022/8155038

Research Article

Study on Seismic Performance of Recycled Steel Fibers Locally Reinforced Cruciform Concrete Frame Beam-Column Joint

Yan Li, Rong-Hua Zhao, Dong-Yi Li, and Chang Qu

School of Civil Engineering, Jilin Jianzhu University, Changchun, Jilin Province, China

Correspondence should be addressed to Dong-Yi Li; lidongyi@student.jlju.edu.cn

Received 16 December 2021; Revised 7 January 2022; Accepted 30 January 2022; Published 25 March 2022

Academic Editor: Ramadhansyah Putra Jaya

At present, concrete frame structures are widely used, and the frame beam-column joints are the key parts of the whole frame in seismic resistance. In previous studies, recycled steel fiber-reinforced concrete is a new type of environment-friendly reinforcement material, which can also be widely used in the construction industry. Therefore, in this paper, MTS electrohydraulic servo loading systems were used to carry out low-cycle reciprocating cyclic loading tests to study the seismic performance of five 1/2 scale cruciform concrete frame beam-column joint specimens with plain concrete, normal steel fiber-reinforced concrete, and three recycled steel fiber-reinforced concrete with different fiber contents in the joint core area. The results show that the addition of normal steel fibers can improve the bearing capacity, ductility, energy dissipation capacity, and shear strength of concrete frame joint specimens and delay the stiffness degradation of joint specimens, recycled steel fibers can improve the seismic performance of the cruciform concrete frame joints better than normal steel fibers, and the seismic performance increases gradually with the increases of volume ratio of recycled steel fibers. Moreover, with the recycled steel fiber content from 0.5% to 1.0% and then to 1.5%, the increased amplitude of the seismic performance of joint specimens increases. Considering the reinforcing effect of recycled steel fibers on concrete matrix and based on the design formula of shear capacity of reinforced concrete joints, the design formulas of shear capacity of recycled steel fiber-reinforced concrete beam-column joints were established by using the statistical analysis method and the baroclinic rod-truss model, and the calculation results were in good agreement with the test results. This study can provide references for seismic performance research of steel fiber-reinforced beam-column joints and the recycling of steel wire from waste tires.

1. Introduction

Reinforced concrete frame structure has been widely used in various fields of construction industry because of its good seismic performance. It is found that, under earthquake load, the frame beam-column joints are subjected to complex stress and are prone to brittle shear failure [1]. Adding normal steel fibers into the frame joint core area can improve the bonding strength between longitudinal bars and concrete and enhance the ductility and energy dissipation capacity of frame joints [2, 3]. The industrial recycled steel fibers formed by cutting high-quality steel wire extracted from waste tires also have higher hardness, breaking force, elongation, torsion strength, tensile strength, and yield strength [4]. It can be mixed into concrete according to a certain volume ratio to prepare a new hybrid high-performance environmental protection composite material, which will have a good application prospect in construction industry. In foreign countries, the steel wire from waste tires has been made into high-performance wire mesh, spring, and so on for housing construction, water conservancy, and other construction projects. And although the price of industrial recycled steel fibers is similar to or slightly higher than that of normal steel fibers and because the volume of normal steel fibers is small, the amount of normal steel fibers under the same volume rate is much more than that of recycled steel fibers, so the use of recycled steel fibers in engineering is more economic and reasonable than normal steel fibers. And according to statistics, in recent years, the production of waste tires in China and the world has been huge [5]; the wire accounts for 15~20% of the total weight of a waste tire. Therefore, making recycled steel fibers from waste tires as a reinforcement

material can not only save resources and protect the environment but also provide a new research direction for the improvement of the harmless utilization rate of waste tires and the green and sustainable development of the country [6, 7].

2. Research Background

Kheni et al. [8] studied the ductility of fiber-reinforced concrete beam-column joints, and the results showed that adding hybrid fibers into the joint part of the specimen could effectively improve the displacement ductility and energy dissipation capacity of the specimen. Liang et al. [9] studied the seismic performance of fiber-reinforced concrete interior beam-column joints, and the results showed that steel fibers can effectively improve the seismic performance of concrete beam-column joints. Shang. [10] conducted an experimental study on the seismic performance of steel fibers locally reinforced high-strength concrete frame joints, and the results show that steel fibers can improve the shear strength of frame joints, and with the increases of the volume ratio of steel fibers in the frame joints, the ductility and energy dissipation capacity of specimens are significantly improved, and the degradation of bearing capacity and stiffness is delayed.

However, the research mainly focused on the performance of normal steel fiber-reinforced frame beam-column joints, and the research on the performance of recycled steel fiber-reinforced frame joints is also less, so in this paper, five cruciform reinforced concrete frame beam-column joint specimens were designed, and three of the specimens were mixed with recycled steel fibers of different volume rate in their joints. The low-cycle reciprocating cyclic loading test was carried out on the specimens, and the seismic performance of beam-column joints was theoretically analyzed and experimentally studied. Under the condition of considering the reinforcing effect of recycled steel fibers on concrete matrix, a calculation model of shear capacity of recycled steel fiber-reinforced concrete frame joints was established by using the design formula of shear capacity of reinforced concrete joints. This study can provide references for the engineering application of concrete beam-column joints and the recycling of steel wire from waste tires.

3. Experimental Programs

3.1. Experimental Materials. In this test, copper-coated microwire steel fibers were selected as normal steel fibers, bending 100% without fracture and tensile strength more than 2850 MPa. The recycled steel wire was selected from straight round steel wire from waste tires of a company, which was manually polished and cut. To ensure the effective bonding length between recycled steel fibers and concrete [11], many experts and scholars have conducted in-depth studies and found that recycled steel fibers with a length-diameter ratio above 30 can play the bridging role with concrete better. Therefore, recycled steel fibers with a length-diameter ratio above 40 were adopted in this experiment. The basic characteristic parameters of recycled steel fibers are shown in Table 1 and the sheared recycled steel fibers are shown in Figure 1. The longitudinal bars of the beams and columns are HPB300 grade rebars, and the stirrups are HRB400 grade rebars. Concrete material properties of the five specimens are shown in Table 2.

3.2. Design of Specimens. In order to simplify the test, the cruciform concrete frame beam-column joint was selected for the specimen as shown in Figure 2 [12], and the reinforcement of the specimen is shown in Figure 3, with only horizontal or vertical force at the boundary. According to relevant regulations, the size of the frame joint specimen in the quasistatic loading test should be greater than or equal to 1/4 of the prototype [13], so the specimen adopted a 1/2 scale according to the actual situation of the laboratory. The beam in the specimen is 3.1 m long, the section size is 250×400 mm, the column height is 2.8 m, and the section size is 300×300 mm. The axial compression ratio was selected as 0.2. Among the five specimens, specimen SJ-1 is an ordinary reinforced concrete specimen. According to various theories of fiber reinforcement mechanism, such as fiber spacing theory and composite material theory [14, 15], fiber volume ratio is one of the main factors affecting the fiber reinforcement effect. According to relevant research data on the flexural performance of recycled steel fibers, adding 0.5%~1.5% industrial recycled steel fibers into concrete can effectively improve the mechanical properties of concrete [16]. Therefore, specimens SJ-2, SJ-3, and SJ-4 are recycled steel fiber-reinforced concrete specimens with a fiber volume ratio of 0.5%, 1.0%, and 1.5%, respectively. Specimen SJ-5 is a reinforced concrete specimen mixed with 0.5% normal steel fibers. The steel fibers were uniformly distributed in the concrete beam-column joints, and the mixing position of recycled steel fibers and normal steel fibers was 1.5 times the height of the beam from the column edge [17].

3.3. Loading System and Measurement Content and Method. During the earthquake, the damage of the general high-rise building is mainly caused by horizontal vibration, while the damage of the concrete frame beam-column joints in the low-rise building is generally caused by the vertical load. Therefore, the vertical low-cycle reciprocating cyclic loading test is adopted in this test to simulate the earthquake load. In the test, the large reaction walls, a reaction beam, and a 100 T hydraulic Jack were used to apply 500 kN vertical axial pressure on the top of the column, and the top and bottom of the column are fixed by hinge supports. Two symmetric MTS electrohydraulic servo loading systems with stroke of ±250 mm and maximum range load of 650 kN were used to carry out a low-cycle reciprocating cyclic loading test on the beam end of the specimen, as shown in Figure 4.

Displacement loading method was used in the test. Before the test, the axial force of an axial compression ratio of 0.2 was gradually applied on the top of the specimen column. At this time, the MTS actuator retained a certain distance from the beam end to ensure that the beam end was free and no internal force was generated before the test began. The vertical force remained constant during the test.

Table 1: Material performance parameters of recycled steel fibers.

Type	Average length (mm)	Effective diameter (mm)	Fusibility (C)	Specific gravity (kg m^2)	Tensile strength (MPa)
Round straight	60	1.5	258	40	1800

Figure 1: Recycled steel fibers.

Table 2: Material properties of concrete.

No.	The compressive strength of a prism (MPa)	Axial compressive strength (MPa)	Elasticity modulus (MPa)
SJ-1	40.34	35.07	3.27×10^5
SJ-2	45.25	42.15	3.29×10^5
SJ-3	47.53	43.23	3.29×10^5
SJ-4	50.14	45.37	3.31×10^5
SJ-5	44.05	40.55	3.28×10^5

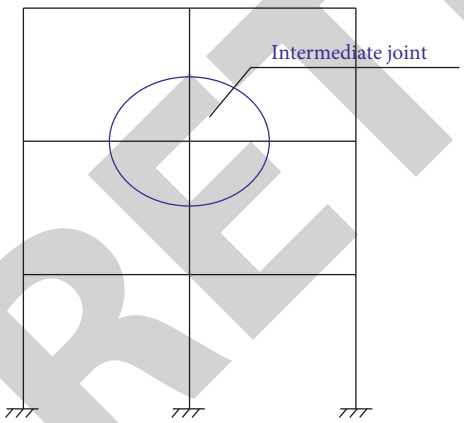

Figure 2: Captured schematic diagram of the frame joint.

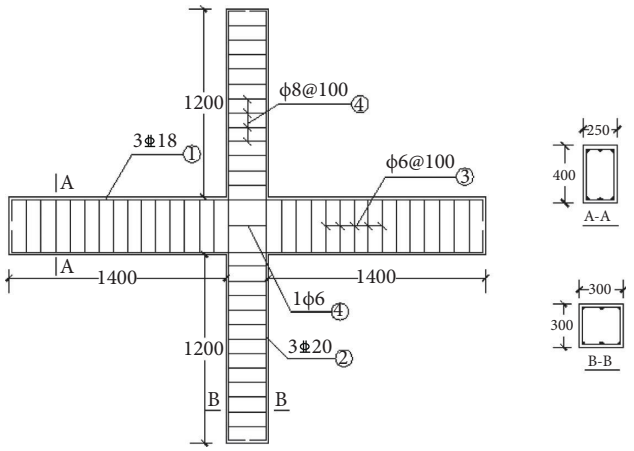

Figure 3: Reinforcement diagram of the specimen.

Then, the displacement-controlled loading was carried out according to the loading method in Figure 5. In the process of testing, one MTS actuator applied an upward force, while the other applied a downward force, then returned to zero at the same time, then acted in the opposite direction, and finally returned to zero at the same time, thus forming a low-cycle reciprocating loading. The pre-pasted resistance strain gauge was used to connect the IMP acquisition plate to measure the strain of beam-column joint core areas, the beam longitudinal reinforcements, the column longitudinal reinforcements, and the column stirrups. The layout of longitudinal strain gauges is shown in Figure 6, and the layout of stirrup strain gauges is shown in Figure 7. The column end displacement and angle of beam end plastic hinge area near the joint were measured by the displacement meter arranged in Figure 8. The development of cracks was observed visually, and the crack width was measured by the ZBL-F103 Fazhibolian crack width meter independently developed by Beijing.

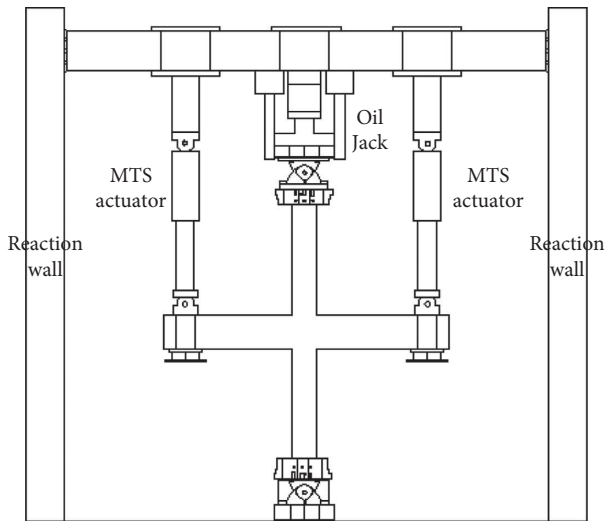

Figure 4: Schematic diagram of test equipment and loading.

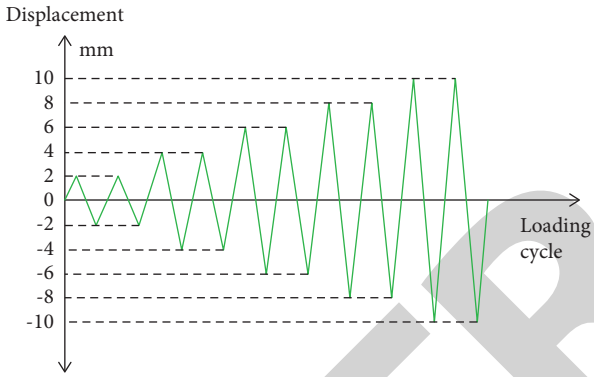

Figure 5: The loading system of specimens.

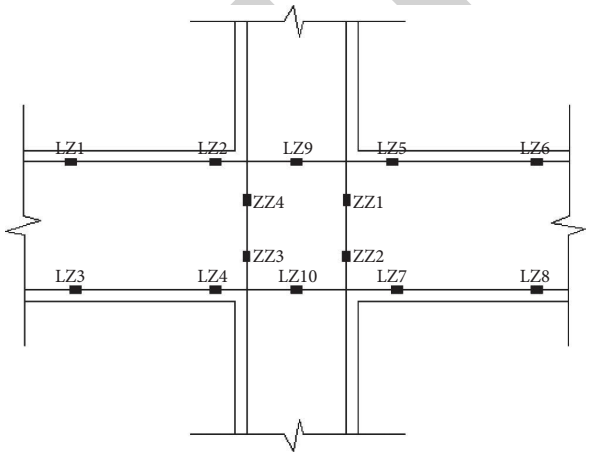

Figure 6: Layout of longitudinal reinforcement strain gauges.

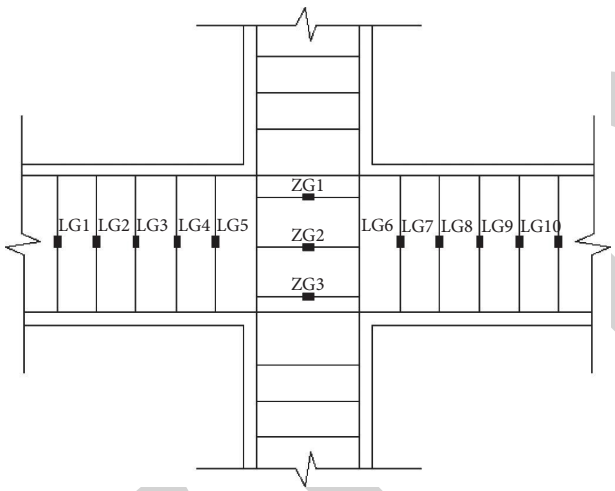

Figure 7: Layout of stirrup strain gauges.

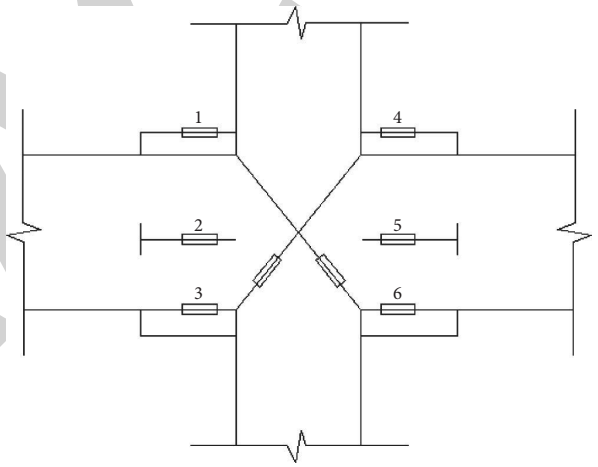

Figure 8: Layout of displacement meter.

4. Failure Phenomenon and Result Analysis of Specimens

4.1. Failure Phenomenon of Specimens. Specimen SJ-1 was ordinary reinforced concrete. When the displacement cycle reached +10 mm, the first inclined crack appeared in the joint area, with a width of 0.01 mm and a length of 37 cm, and several tiny cracks appeared near the beam end of the joint area. When the displacement cycle reached −16 mm, an inverted inclined crack with a width of 0.01 mm and a length of 35 cm appeared in the joint area. When the cycle reached +22 mm, the peak load reached 97.68 kN, and a tiny crack parallel to the main inclined crack appeared in the joint area. When the displacement cycle reached +24 mm, the specimen had a clicking sound, the main inclined crack deepened, and the crack widened to 0.42 mm. When +28 mm, the two main cracks in the core area along the diagonal direction widened to 1.36 mm, and the width of tiny cracks increased obviously. A small area of concrete spalled on the surface of the joint area at −32 mm. When the displacement cycle reached −34 mm, the bearing capacity of the specimen decreased to below 80%. The final failure mode of specimen SJ-1 is shown in Figure 9(a).

Specimen SJ-4 is a reinforced concrete specimen mixed with 1.5% recycled steel fibers. When the displacement cycle reached +18 mm, the first main inclined crack with a width of 0.01 mm and a length of 15 cm appeared in the joint area,

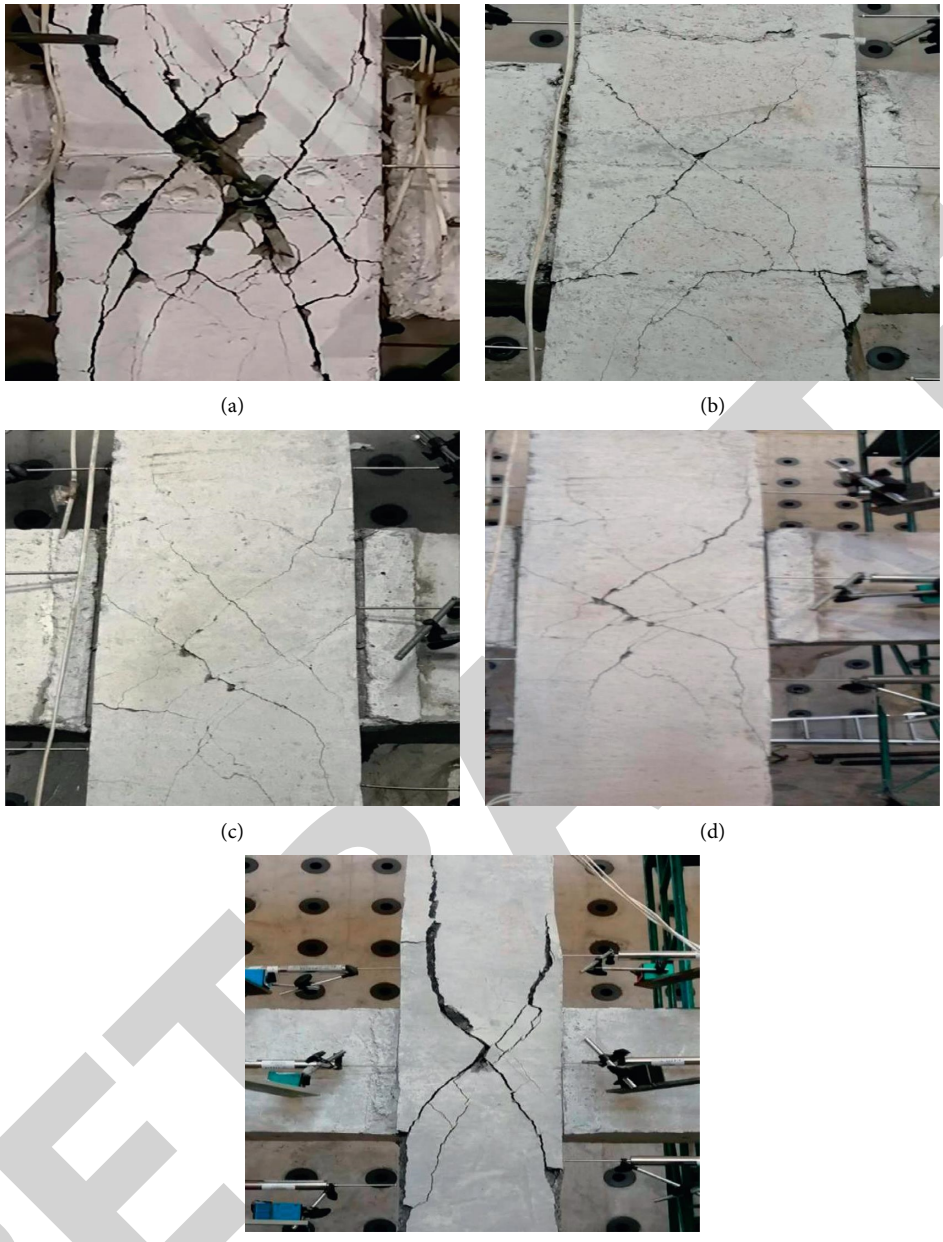

Figure 9: Final failure mode of specimens. (a) SJ-1. (b) SJ-2. (c) SJ-3. (d) SJ-4. (e) SJ-5.

and a horizontal crack with a length of 15 cm appeared in the lower side of the column. An oblique tiny crack appeared in the beam end near the left side of the joint area, 30 cm away from the beam end. At +24 mm, "X-shaped" cracks appeared in the joint area, accompanied by tiny cracks parallel to the main cracks. When the displacement cycle reached +28 mm, the ultimate load of the specimen reached 100.87 kN, the main crack in the joint area widened to 0.67 mm, and the horizontal cracks at the column end formed a small through-crack. At +32 mm, two small tiny cracks appeared near the column end of the joint area, and the soil mass on the concrete surface fell off. At +38 mm, the tiny cracks in the joint area increased, the tiny cracks near the joint area lengthened, and the crack width reached 1.65 mm. When the displacement circulated to −44 mm, there was a large area of soil spalled near the column end of the joint core area. The final failure mode of specimen SJ-4 is shown in Figure 9(d).

Specimen SJ-5 was a reinforced concrete specimen mixed with 0.5% normal steel fibers. When the displacement cycle reached +12 mm, inclined cracks appeared in the plastic hinge area on the left side of the joint 40 cm from the beam end, with a length of 35 cm. At +16 mm, another crack appeared in the opposite direction to the main crack, forming a cross crack with it, and short fine cracks appeared on both sides of the column end at the joint. When the displacement cycle reached −20 mm, the tiny crack perpendicular to the oblique crack was extended to 28 cm, and other small cracks were still extended continuously. At

−22 mm, the peak load of the specimen reached 98.31 kN, a tiny crack with a length of 30 cm parallel to the second main crack appeared in the joint area, and the number of tiny cracks in the joint area increased. When the displacement cycle reached −38 mm, the main crack in the joint area extended to the column end, and the width of the crack increased to 1.45 mm. A small area of soil spalled occurred in the joint area, and many tiny cracks perpendicular to the main crack appeared. When the bearing capacity of the specimen decreased to below 80% of the peak load, the test stopped. The final failure mode of specimen SJ-5 is shown in Figure 9(e).

The macroscopic test phenomenon of specimens SJ-2 and SJ-3 is basically similar to that of specimen SJ-4. The failure modes of joints are different due to the different volume ratios of recycled steel fibers. Compared with SJ-4, the number of cracks in the joint core area of specimens SJ-2 and SJ-3 increased significantly, and their widths increased significantly when specimens SJ-2 and SJ-3 were destroyed. The situation of cracks development and failure of specimen SJ-3 are better than that of specimen SJ-2. See Figure 9(b) and Figure 9(c) for their final failure patterns. Referring to relevant literature and test results [18], the failure modes of five joint specimens can be obtained as shown in Table 3.

4.2. Result Analysis

4.2.1. Hysteretic Curves Analysis of Specimens. Under the quasistatic action, load-displacement curves of steel fiber-reinforced concrete beam-column joint specimens with different fiber types and fiber volume contents and ordinary reinforced concrete beam-column joint specimens are shown in Figure 10.

According to Figure 10, the hysteretic curves of five joint specimens are all close to S shape. In the early stage of the test displacement cycles, the specimens were in the elastic working stage, and the load-displacement curves changed linearly. The hysteretic curves were approximately a straight line, almost no residual deformation occurred, and stiffness degradation was not obvious. However, as the number of displacement cycles increased, cracks began to appear in the specimen. At this time, the load-displacement curves began to show nonlinear changes, the hysteretic curves were no longer linear, and their area was also increasing. The specimens began to show large residual deformation, and stiffness degradation became obvious. As the specimens reached the ultimate loads and then the failure loads, the fullness of the hysteretic curve of specimen SJ-1 was worse than that of the other four specimens, the number of displacement cycles was relatively less, and stiffness degradation was obvious. For specimens SJ-2~SJ-4, the cracking loads, yield loads, ultimate loads, and their corresponding displacement of specimens all gradually increase with the increases of recycled steel fiber content. Moreover, when the recycled steel fiber content increases from 0.5% to 1.0% and then to 1.5%, the increased amplitude of the three kinds of load and their corresponding displacement of joint specimens all becomes larger. However, the ultimate load of specimen SJ-2 was slightly smaller than that of specimens SJ-1 and SJ-5, which may be caused by nonuniform mixing during pouring concrete or uneven watering during curing. It can also be seen from the hysteretic curves of all specimens that the overall slope of the hysteretic curve of specimen SJ-1 is the smallest; that is, the stiffness of specimen SJ-1 is the smallest. However, from specimen SJ-5 to SJ-2 to SJ-4, the slope of the hysteretic curves is gradually increased; that is, the stiffness of the specimens is gradually increased. In addition, it can be seen that the stiffness of the four specimens gradually degrades, and compared with specimen SJ-1, the capacity of dissipation earthquake and deformation of specimens SJ-2~SJ-4 is gradually improved; that is, the ductility of specimens is gradually improved.

(1) Under the action of low-cycle reciprocating cyclic loading, the cross-cracks appeared in the joint core area of specimen SJ-1 for a very short time, there were many cracks in the joint core area, and the crack width was the largest. The joint core areas of specimens SJ-2~SJ-5 have good toughness and multiple cracking properties under load. The initial cracking of the joint surface was later than that of SJ-1, and the joint core area mixed with recycled steel fibers showed a large number of tiny cracks, indicating that the crack resistance of specimens has been improved to a certain extent.

(2) From the hysteresis curves of specimens SJ-2 to SJ-4 (Figures 10(b)–10(d)), it can be seen that the ultimate bearing capacity of three specimens increases gradually, but there is little difference. The stiffness degradation of specimen SJ-4 was slower than that of SJ-2 and SJ-3. Therefore, the increase of recycled steel fiber content does not significantly improve the bearing capacity of specimens [19] but has a relatively obvious improvement in the ductility and the delay of stiffness degradation of specimens [20].

(3) Specimen SJ-2 and specimen SJ-5 are used as comparison specimens; it can be seen that the bearing capacity and stiffness degradation capacity of specimen SJ-2 are slightly stronger than that of specimen SJ-5, and specimen SJ-2 has fewer cracks than specimen SJ-5, indicating that recycled steel fibers can improve the seismic performance of joint specimens better than normal steel fibers.

4.2.2. Skeleton Curves Analysis of Specimens. As can be seen from the comparison diagrams of skeleton curves of specimens in Figure 11, the ultimate loads and ultimate displacements of the joint specimens mixed with steel fibers in the joint core area are increased to varying degrees. Before yielding, the specimens were in the elastic stage, and the skeleton curves were approximately a straight line. When the inflection point of the skeleton curve of specimen SJ-1 appeared, the curves of specimens SJ-2~SJ-5 continued to rise with the increase of the displacements. The time of inflection point of the curve of specimen SJ-4 is the latest, and the ultimate load value is the largest. Comparing specimen SJ-2 and SJ-5, specimen SJ-2 showed better

Table 3: Test results.

No.	Cracking load (kN)	Cracking displacement (mm)	Yield load (kN)	Yield displacement (mm)	Ultimate load (kN)	Ultimate displacement (mm)	Failure mode
SJ-1	78.14	10	84.75	16.18	97.68	21.94	Shear and bending failure
SJ-2	79.78	13	85.59	17.82	96.71	25.59	Shear and bending failure
SJ-3	81.26	15	88.24	18.31	98.67	25.73	Shear failure
SJ-4	84.49	18	95.68	19.23	100.87	25.95	Shear failure
SJ-5	79.21	12	85.31	16.68	98.31	22.21	Shear and bending failure

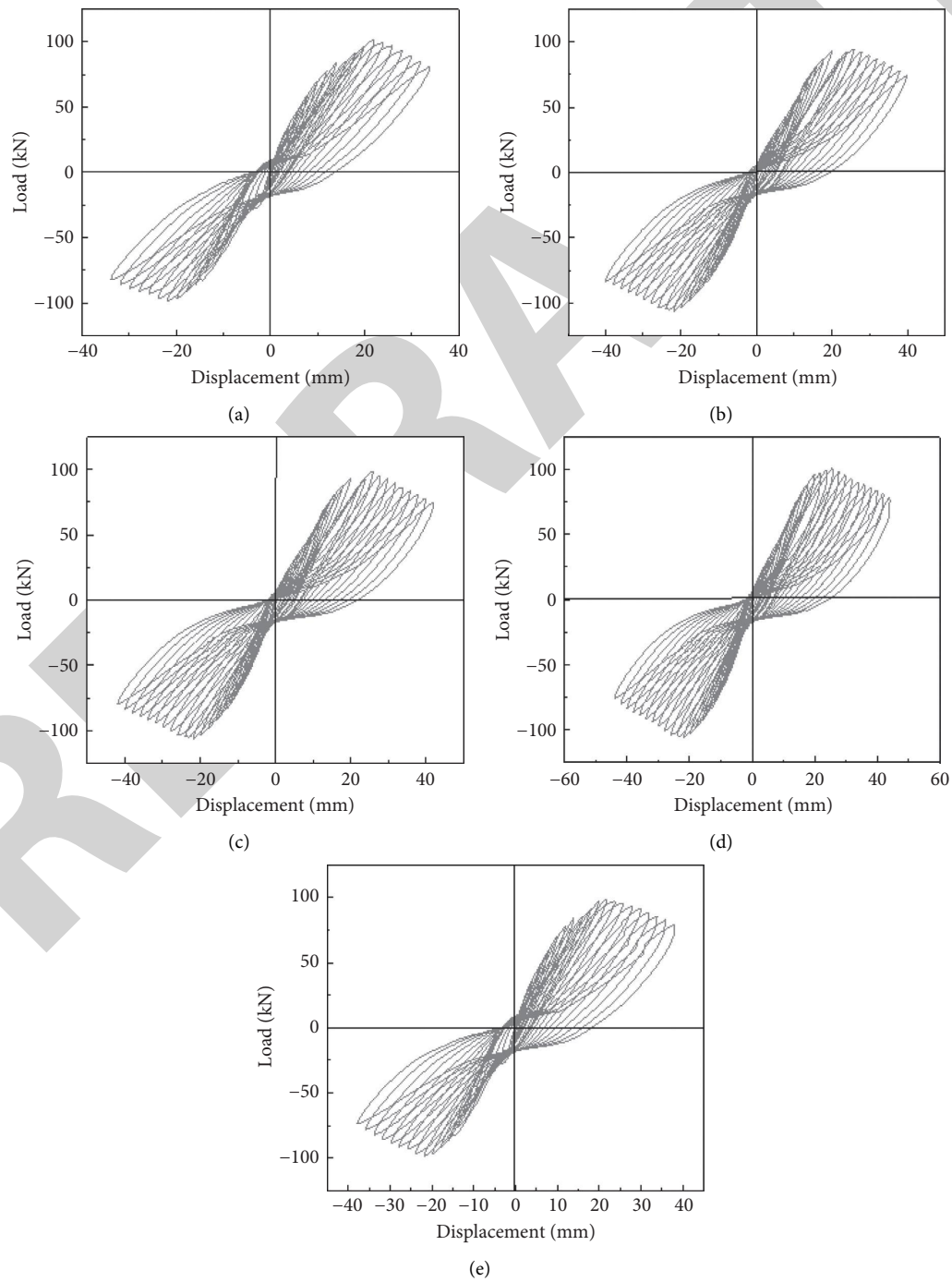

Figure 10: Hysteretic curves of specimens. (a) SJ-1. (b) SJ-2. (c) SJ-3. (d) SJ-4. (e) SJ-5.

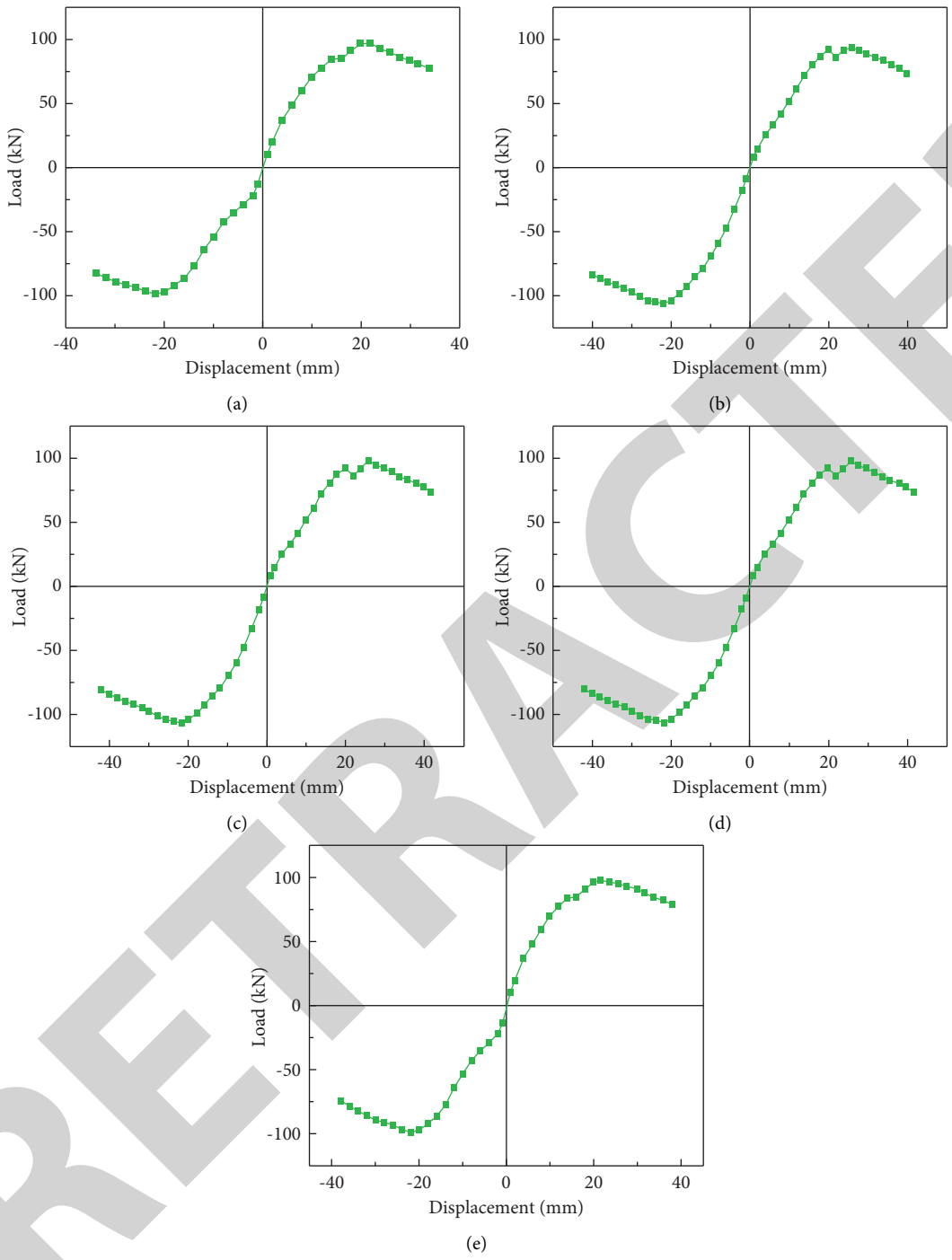

Figure 11: Skeleton curves of specimens. (a) SJ-1. (b) SJ-2. (c) SJ-3. (d) SJ-4. (e) SJ-5.

strength. Based on the skeleton curve analysis, it can be concluded that the seismic bearing capacity of specimens can be improved by adding steel fibers in the joint area, and except the ultimate load of specimen SJ-2, the cracking loads, yield loads, ultimate loads, and their corresponding displacements of the joint specimens mixed with recycled steel fibers in the joint core area are increased to a greater extent; that is, the effect of recycled steel fibers on strengthening the crack resistance of specimens is better than that of normal steel fibers.

4.2.3. Ductility Analysis of Specimens. The ductility discussed in this paper is the deformation capacity that the bearing capacity remains in a relatively stable state after the beam end section near the joint area rises from the yield to the maximum bearing capacity. The good ductility of the specimen can show that it still has the ability to consume earthquake after yielding or reaching the ultimate bearing capacity and can avoid the occurrence of brittle failure of the specimen.

In this paper, the characteristic values of bearing capacity and displacement ductility of specimens were obtained by the "energy equivalence method," the principle of which is shown in Figure 12. The yield load P_y and yield displacement Δ_y of specimens were determined according to the skeleton curve of each specimen, the failure load was set as $P_u = 0.8P_{max}$, and the failure displacement Δ_u was the corresponding displacement value of the failure load. The ductility of specimens is calculated according to the ratio of failure displacement to yield displacement of specimens, as shown in formula (1). The characteristic values of bearing capacity and ductility coefficient of specimens are shown in Table 4.

$$\mu = \frac{\Delta_u}{\Delta_y}, \tag{1}$$

where μ is the displacement ductility coefficient; Δ_u is the failure displacement (mm); Δ_y is the yield displacement (mm).

It can be seen from the table that the addition of normal steel fibers can improve the ductility of specimens, the recycled steel fibers can improve the ductility of specimens better than normal steel fibers, and the ductility of specimens gradually improves with the increase of the volume ratios of recycled steel fibers. Moreover, with the recycled steel fiber content from 0.5% to 1.0% and then to 1.5%, the increased amplitude of the ductility performance of joint specimens increases.

4.2.4. Stiffness Degradation Analysis of Specimens. The stiffness degradation is mainly caused by the bonding degradation between rebars and concrete after the cracking of beam-column joints and the cumulative development of some tiny cracks in the macroscopic expression of specimen damage. Stiffness degradation can reflect the fatigue damage and the whole process from the beginning of loading to yield to failure of the specimen under cyclic loading [21].

The index used in this paper to evaluate stiffness degradation of specimens under low-cycle reciprocating cyclic loading is secant stiffness. The specimens in the test in this paper are evaluated and analyzed according to secant stiffness. The design formula is as follows:

$$K_i = \frac{\left|V_i^+\right| + \left|V_i^-\right|}{\left|\Delta_i^+\right| + \left|\Delta_i^-\right|}, \tag{2}$$

where K_i is the secant stiffness in the i cycle; V_i^+ and V_i^- are the ultimate load of the specimen in the i cycle; Δ_i^+ and Δ_i^- are the displacement value corresponding to the peak load in the i cycle.

According to the comparative analysis of stiffness curves of all specimens in Figure 13, it can be seen that, compared with the reinforced concrete specimens mixed with recycled steel fibers in the joint core area, the initial stiffness of both the ordinary reinforced concrete specimen and the concrete specimen mixed with normal steel fibers is slightly higher. However, the slope of the curve is also very high, which is mainly affected by the early shear failure at the joint. The ductility of the joint is greatly enhanced by the addition of recycled steel fibers, so the slope of the curves of specimens

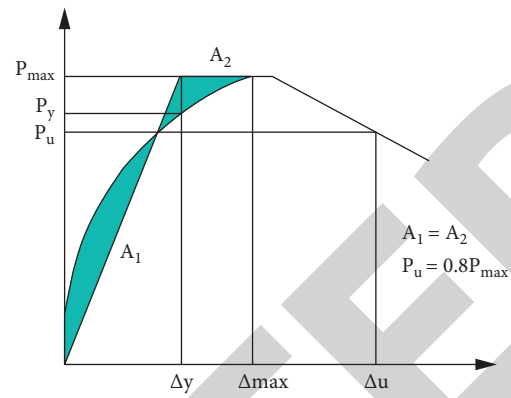

Figure 12: Principle of energy equivalence method.

SJ-2~SJ-4 is much lower, and with the recycled steel fiber content from 0.5% to 1.0% and then to 1.5%, the amplitude of the stiffness degradation of joint specimens decreases. After the inflection point of the curves, the decreasing rate of stiffness degradation curves of all specimens slows down and tends to a gentle state.

4.2.5. Energy Dissipation Capacity Analysis of Specimens. Under the action of earthquake, the structure has the ability to absorb and dissipate seismic energy, and the calculation of the fixed value of the energy dissipation capacity of the specimen should be realized by using the equivalent viscous damping coefficient and power ratio index [22], and the larger the value is, the stronger the energy dissipation capacity of the structure is. In this paper, the energy dissipation performance of the structure is evaluated in general by calculating the energy dissipation coefficient and equivalent viscous damping coefficient.

In general, the dissipated energy of a structure usually refers to the area enclosed by the closed curve formed by the hysteretic curve. As shown in Figure 14, the structure energy dissipation coefficient (formula (3)) and equivalent viscous damping coefficient (formula (4)) are obtained by calculating the area of the hysteretic curve. See Table 5 for the results.

$$E = \frac{S_{(ABD+CDB)}}{S_{(OCE+OAF)}}, \tag{3}$$

where E is the structural energy dissipation coefficient; $S_{(ABD+CDB)}$ is the area enclosed by the hysteretic curve closed curve; $S_{(OCE+OAF)}$ is the area of triangle OCE and triangle OAF.

$$h_e = \frac{1}{2\pi} \cdot \frac{S_{(ABD+CDB)}}{S_{(OCE+OAF)}}, \tag{4}$$

where h_e is the equivalent viscous damping coefficient.

As can be seen from Table 5, the energy dissipation coefficient and equivalent viscous damping coefficient of specimens mixed with steel fibers in the joint core area are higher than the ordinary reinforced concrete specimen; especially, the specimen with recycled steel fibers content of 1.5% has the largest value. Compared with specimen SJ-2

Table 4: Characteristic values of bearing capacity and ductility coefficients of specimens.

No.	Yield point		Limit point		Breaking point		Displacement ductility
	P_y/kN	Δ_y/mm	P_{max}/kN	Δ_{max}/mm	P_u/kN	Δ_u/mm	μ
SJ-1	84.75	16.18	97.68	21.94	76.78	33.87	2.09
SJ-2	85.59	17.82	96.71	25.59	76.95	40.24	2.26
SJ-3	88.24	18.31	98.67	25.73	77.41	42.23	2.31
SJ-4	95.68	19.23	100.87	25.95	78.58	46.11	2.40
SJ-5	85.31	16.68	98.31	22.21	76.97	36.13	2.17

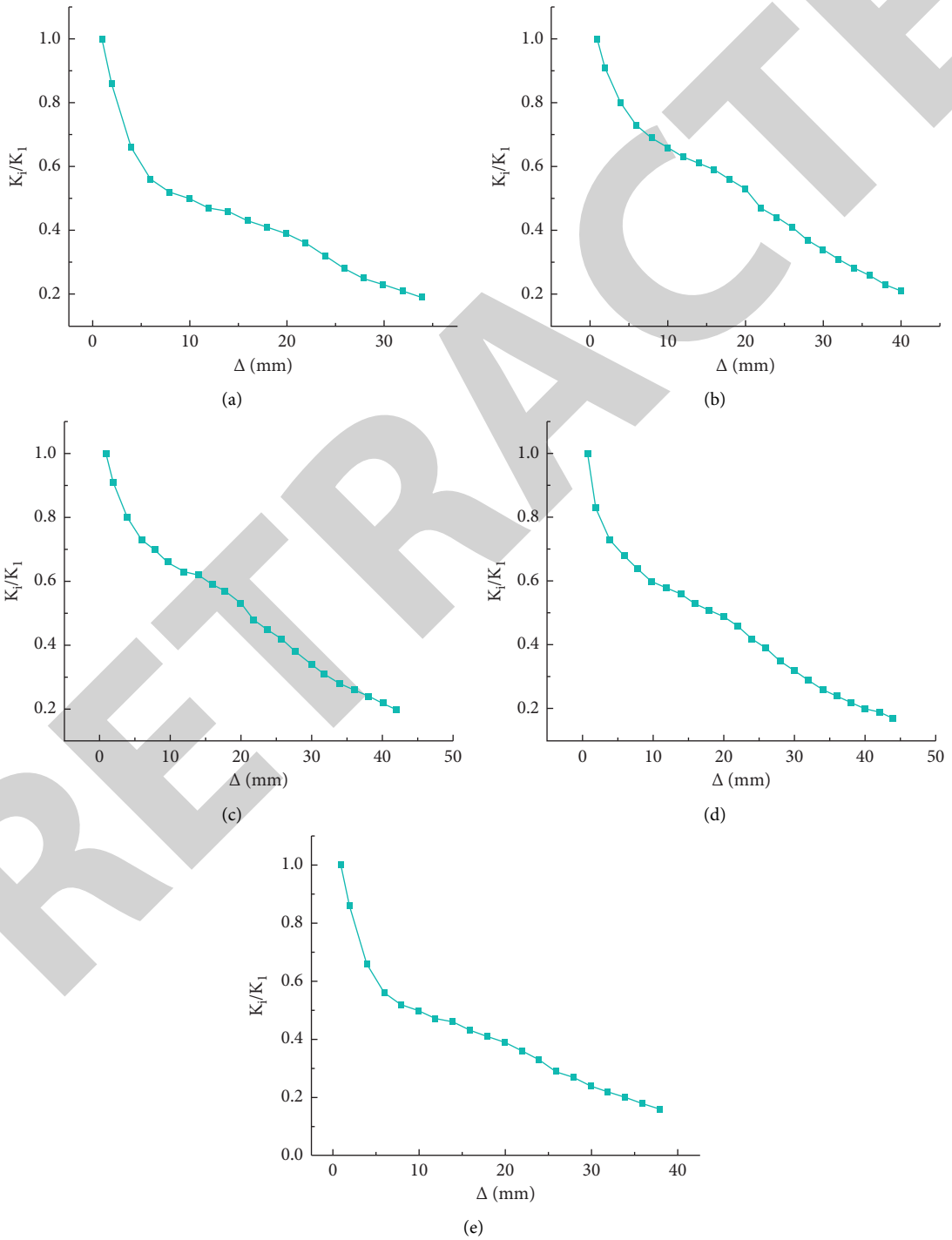

Figure 13: Stiffness degradation curves of specimens. (a) SJ-1. (b) SJ-2. (c) SJ-3. (d) SJ-4. (e) SJ-5.

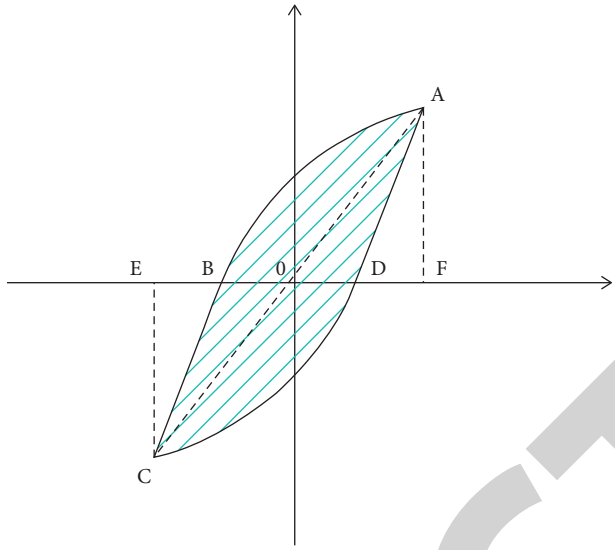

Figure 14: The area of the hysteretic curve.

Table 5: Equivalent viscous damping coefficient and energy dissipation coefficient of specimens at structural yield.

No.	Area enclosed by the hysteretic curve	Energy dissipation coefficient	Equivalent viscous damping coefficient (%)
SJ-1	528.91	0.41	6.53
SJ-2	541.75	0.47	7.48
SJ-3	576.48	0.54	8.59
SJ-4	663.83	0.66	10.50
SJ-5	533.84	0.43	6.84

and SJ-5 under the same content, specimen SJ-2 has a better effect than specimen SJ-5. According to the energy dissipation coefficient, equivalent viscous damping coefficient, and the above analysis, the energy dissipation capacity of specimens with steel fibers mixed in the joints and plastic hinge areas at both ends is greatly improved compared with the ordinary concrete specimen, the effect of recycled steel fibers on enhancing energy dissipation capacity is stronger than normal steel fibers, and the energy dissipation capacity of specimens increases with the increase of volume ratios of recycled steel fibers. Moreover, with the recycled steel fiber content from 0.5% to 1.0% and then to 1.5%, the increased amplitude of the energy dissipation capacity of joint specimens increases.

4.2.6. Shear Deformation Analysis of Specimen Joints. Under the action of quasistatic loading, there are two diagonal angles at the specimen joint area. Under the influence of the bidirectional pressure transmitted by the beam end and the column end and the tension transmitted by the bonding stress of the rebars, a group of cross diagonal tension pressures are formed at the joint. Under the joint influence of the two forces, the shear deformation in the joint core area is shown in Figure 15, resulting in the decline of the overall stability of the structure. The shear angle of the joint core area can be calculated by geometric analysis, as shown in Figure 15.

The shear deformation angle formula (5) is obtained from the geometric relationship in Figure 15:

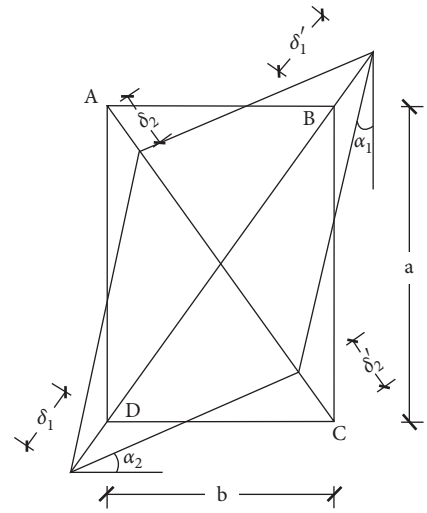

Figure 15: Geometric relation diagram of shear deformation in joint core area.

$$\gamma = \alpha_1 + \alpha_2 = \frac{\sqrt{a^2 + b^2}}{2ab}\left[\left(\delta_1 + \delta_1'\right) - \left(\delta_2 + \delta_2'\right)\right], \tag{5}$$

where γ is the sum of shear deformation angles in joint core area; α_1 and α_2 are the deformation angles of the two diagonal directions at the joint; a and b are the joint area dimensions (height and width); δ_1, δ_1', δ_2, and δ_2' are the

change values of the diagonals in the joint core area (stretching and compression).

The shear deformation angle value of each specimen under the first yield state and limit state is shown in Figures 16 and 17.

For specimens SJ-2~SJ-5, both the deformation angle under the first yield state and the deformation angle under the first limit state decrease compared with specimen SJ-1. In other words, under the condition of the same stirrup ratio, the concrete constraint ability in the joint core area was significantly improved after the recycled steel fibers were added, and the development of concrete inclined cracks in the joint core area was alleviated. As the shear deformation angle of specimen SJ-4 is 0.5 times that of specimen SJ-1, it can be seen that the recycled steel fibers with a high volume ratio have better crack resistance in the joint core area and can improve the overall stability of the structure. That is to say, with the increases of the volume ratio of recycled steel fibers, the shear angles of the specimen joint decrease gradually, and the stiffness and shear strength increase.

The beam end deflection δ_j caused by shear deformation at the joint is

$$\delta_j = l \cdot \gamma, \tag{6}$$

where l is the distance between the free end of the beam and the end of the joint and is taken as $l = 1500$ mm.

The calculated deflection value δ_j of the beam end is shown in Table 6.

5. Derivation of Design Formulas of Shear Capacity of Recycled Steel Fiber-Reinforced Cruciform Concrete Frame Joints

5.1. Action Mechanism of Shear Capacity of Recycled Steel Fiber-Reinforced Concrete Frame Joints. Frame joints play an important role in the stability of the whole structure. They are subjected to forces in multiple directions, as shown in Figure 18(a). The baroclinic bar mechanism is shown in Figure 18(b), and the truss mechanism is shown in Figure 18(c).

At the initial stage of loading, when the stirrups could not bear the shear force, the recycled steel fiber-reinforced concrete baroclinic bar formed in the joint core area played a central role. When the shear force at the beam-column joints exceeds the tensile strength of the recycled steel fiber-reinforced concrete, the surface of the joint core area shows the first crack. However, due to the incorporation of recycled steel fiber-reinforced concrete, the tensile strength at the specimen joints is obviously improved, making the initial crack appear later. In the middle of loading, the capacity of the baroclinic bar to bear the baroclinic pressure decreases due to the increase of the displacement and load. At this time, the truss mechanism composed of stirrups, vertical rebars, and recycled steel fiber-reinforced concrete in the joint core area mainly bears the baroclinic tension, and the baroclinic pressure is borne by the baroclinic bar. At the end of loading, the baroclinic pressure is mainly borne by the

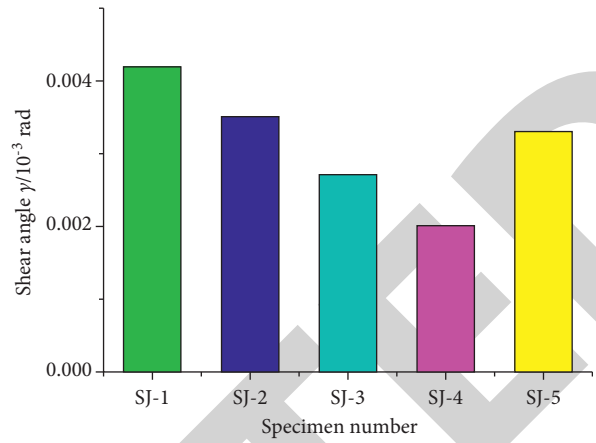

Figure 16: Deformation angles of specimens under the first yield state.

frictional resistance between the cracks at the joints and the bonding force between the recycled steel fiber-reinforced concrete and the rebars.

For ordinary reinforced concrete joint specimens and reinforced concrete joint specimens mixed with normal steel fibers, the anchorage bond between cement mortar, stirrups, longitudinal reinforcements, and recycled steel fibers in recycled steel fiber-reinforced concrete beam-column joints is obviously stronger. The shear force at the joints can be transferred by the bonding force between the rebars and the recycled steel fiber-reinforced concrete so that the shear capacity of the truss mechanism can be better played. Therefore, the action mechanism of the shear capacity of the recycled steel fiber-reinforced concrete frame beam-column joints is the joint action of the barocline bar-truss mechanism.

5.2. Constitutive Relations of Recycled Steel Fibers. Compared with the brittle material (concrete), the constitutive relationship of steel wire recycled from industrial waste tires is not complicated. The nature of recycled steel fibers belongs to steel, and some classical constitutive relations proposed by previous researchers can be adopted and used. So the bilinear follow-up strengthening model is directly adopted in this paper. Therefore, the stress-strain relationship of recycled steel fibers is shown in Figure 19. The initial elastic modulus is E_0, and the plastic modulus (E_1) entering the plastic stage after yielding is 1.0% of the initial elastic modulus, namely,

$$E_1 = 0.01E_0. \tag{7}$$

5.3. Calculation Model of Shear Capacity of Recycled Steel Fiber-Reinforced Concrete Frame Joints. In the calculation of shear capacity of joints, the influence of concrete, column axial pressure, and stirrups at joints is considered in the Chinese code [23], and the design formula is as follows:

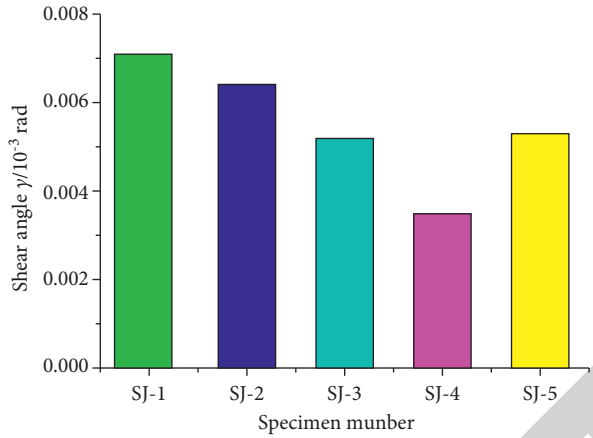

Figure 17: Deformation angles of specimens under the first limit state.

Table 6: Beam end deflection caused by shear deformation in the joint core area.

No.	SJ-1	SJ-2	SJ-3	SJ-4	SJ-5
Beam end deflection under first yield state/mm	6.34	5.29	4.22	3.05	5.01
Beam end deflection under first limit state/mm	10.69	9.65	7.86	5.29	7.99

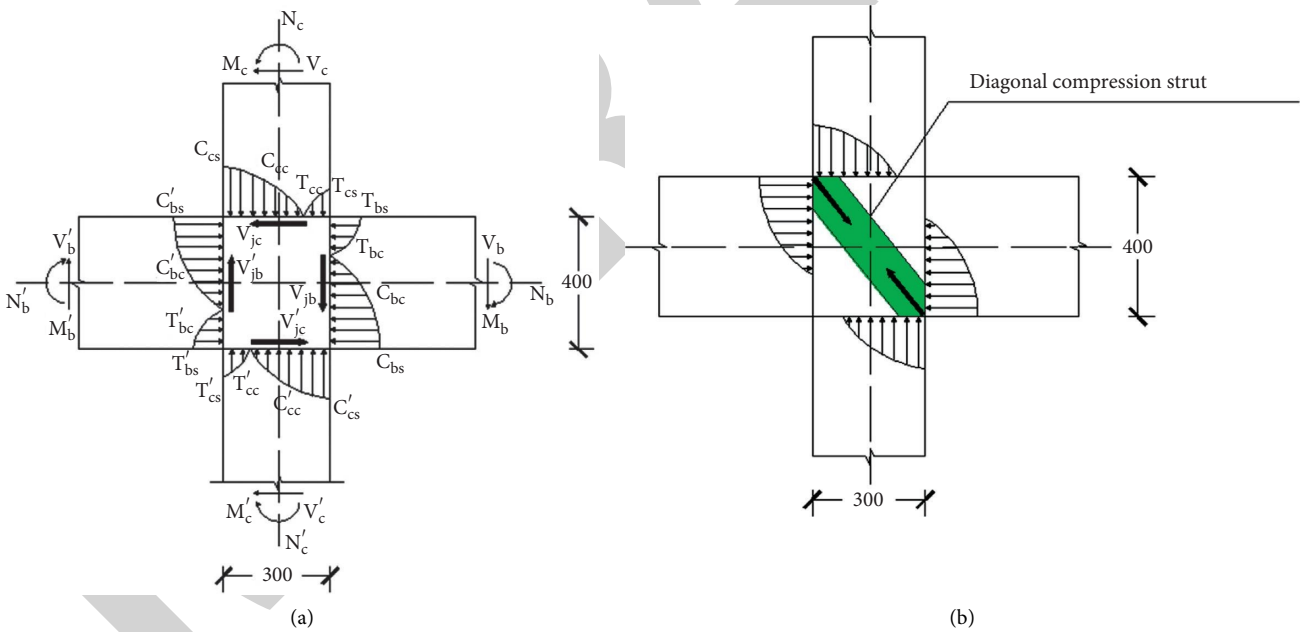

Figure 18: Continued.

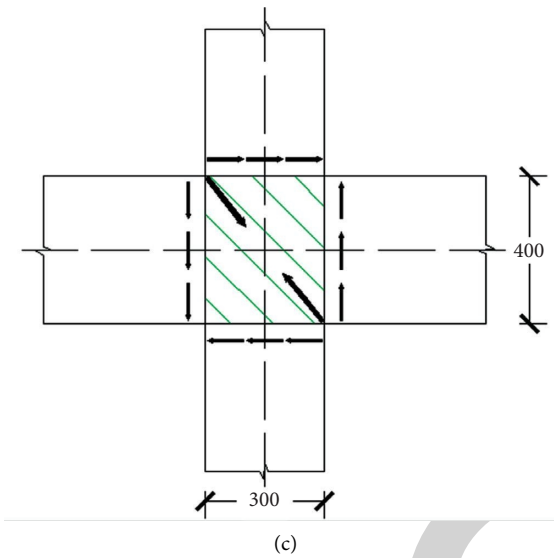

Figure 18: Force diagram of beam-column joints. (a) The force on the joint. (b) Baroclinic bar mechanism. (c) Truss mechanism.

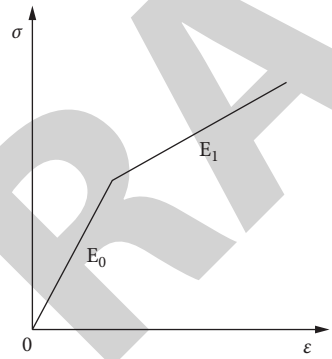

Figure 19: Stress-strain relationship of recycled steel fibers.

$$V_j \leq \frac{1}{\gamma_{RE}}\left[1.1\eta_1 f_t b_j h_j + 0.05\eta_j N\frac{b_j}{b_c} + f_{yv}A_{svj}\frac{h_{bo}-a_s'}{s}\right], \tag{8}$$

where V_j is the shear strength of joints; η_j is the constraint influence coefficients of orthogonal beams on joints; N is the design value of axial force at column end; h_{bo} is the effective height of beam section.

The shear strength design formula of joints specified in the American code is based on the baroclinic bar mechanism, and its design formula is as follows:

$$V_j = 0.083\gamma\sqrt{f_{ck}}b_j h_c, \tag{9}$$

$$b_j = \min\left(\frac{b_j + b_c}{2}, b_b + \sum\frac{mh_c}{2}, b_c\right), \tag{10}$$

where γ is the influence coefficient of joints; f_{ck} is the concrete compressive strength; b_j is the section width of joint core area; m is the coefficient ($m = 0.3$ when the eccentricity of the center of the beam-column joint exceeds $b_c/8$; $m = 0.5$ in other cases).

The stress and shear mechanism of beam-column joint core areas are relatively complex. After referring to the design formula of shear capacity of ordinary reinforced concrete joints, the calculation model of shear capacity of recycled steel fiber-reinforced cruciform concrete frame joints is established, as shown in Figure 20:

$$V_{rj} = V_c + V_s + V_{rf}, \tag{11}$$

where A_{str} is the shear capacity of concrete; θ is the shear capacity of stirrups; V_{rf} is the shear capacity of recycled steel fibers.

(1) Shear capacity V_c of concrete joints. Concrete shear bearing capacity V_c in the baroclinic bar model is determined by the following formula (12):

$$V_c = f_c A_{str}\cos\theta, \tag{12}$$

where A_{str} is the cross-section area of the baroclinic bar; θ is the angle between the baroclinic bar and

bottom longitudinal bar ($\theta = \arctan(h'_b/h'_c)$, h'_b, and h'_c are the spacing of longitudinal bars in the protective layer of beam and column, respectively)

It is found that compressive stress diffusion exists in the process of force transmission of steel fiber-reinforced concrete baroclinic bar [24]. To simplify the calculation, the effective cross-sectional area of the baroclinic bar is determined by the following formula:

$$A_{str} = \frac{kb_s h_c}{\cos\theta}, \tag{13}$$

where k is the comprehensive influence coefficient of effective area of the baroclinic bar; b_s is the cross-section width of the baroclinic bar ($b_s = b_j$, b_j is the joint width); h_c is the height of column end section. For reference, value k is determined by the following formula [25]:

$$k = 0.168(1 + 0.263n)\left(1 + 0.492\lambda_f\right)\left(1 + 6.054\lambda_s\right), \tag{14}$$

where n is the axial compression ratio of column end; λ_f is the characteristic value of steel fiber content ($\lambda_f = \rho_f(l_f/d_f)$); λ_s is the stirrup characteristic value of the joint core area ($\lambda_s = 0.08$).

Softening coefficient λ_{str} ($\lambda_{str} = 0.4$)introduced for barotropic bar mechanism was softened because of cyclic tension and compression [26]. The following formula (15) can be obtained by combining (12) (14):

$$V_c = \lambda_{str} f_c k b_s h_c. \tag{15}$$

(2) Shear capacity of the joint stirrup V_s. In this paper, the shear capacity of the joint stirrups is calculated by using the calculation formula 16 of shear capacity of ordinary reinforced concrete beam-column joint:

$$V_s = f_{yv}\frac{A_{sv}}{S}(h_0 - a'_s), \tag{16}$$

where f_{yv} is the design value of tensile strength; $A_{sv} = nA_{sv1}$, A_{sv} is the total section value of stirrups, n is the total number of stirrups in the same section, and A_{sv1} is the sectional area of the stirrup of a single leg [27]; h_0 is the effective height of joint section; S is the stirrups spacing (the direction is along the beam length and column height); a'_s is the distance between the resultant point of longitudinal reinforcement and the edge of concrete.

According to the experimental analysis, the loss of bearing capacity of joints is due to the existence of the compression area at the beam end and column end, which limits the development of inclined cracks, leading to the stirrups in the joint core area failure to yield completely [28], so the coefficient δ is introduced; assume that the stress within the 2/3 height range in the middle of the joint core area reaches yield, taking $\delta = 2/3$, and obtain the following formula (17):

$$V_{js} = {}_{\delta} f_{yv}\frac{A_{sv}}{S}(h_0 - a'_s). \tag{17}$$

(3) The shear capacity V_{rf} of recycled steel fibers at the joint. There are usually two formulas for calculating the shear capacity of steel fiber-reinforced concrete (SFRC): one is to take SFRC as composite material and use the property that steel fibers can improve the tensile strength of concrete matrix to calculate. The other is to take steel fibers as a separate reinforcement to calculate. Based on the two design formulas of steel fiber-reinforced concrete, the design formulas of shear capacity of recycled steel fibers under different conditions are established, respectively, in this paper:

(1) As composite materials, according to relevant literature [29], the shear capacity of recycled steel fibers is determined by formula (18):

$$V_{rf} = V_{jc}\alpha_f\frac{f_{ft}}{f_t}, \tag{18}$$

where α_f is the influence coefficient of steel fibers on tensile strength of concrete matrix, combining with the test [30], taking $\alpha_f = 0.53$; f_t is the tensile strength of concrete matrix; f_{ft} is the tensile strength of recycled steel fiber-reinforced concrete, and its expression is shown in formula (19).

$$f_{ft} = f_t\left(1 + 1.177\rho_f\left(l_f/d_f\right)\right), \tag{19}$$

where ρ_f is the volume content of steel fibers; l_f/d_f is the length-diameter ratio of steel fibers. Substitute formula (19) into formula (18) to obtain

$$V_{rf} = 0.53V_{jc}\left(1 + 1.177\rho_f\left(l_f/d_f\right)\right). \tag{20}$$

Substitute formulas (15), (17), and (20) into formulas (11) to obtain the design formula (21) for shear capacity of recycled steel fiber-reinforced concrete frame joints:

$$V_{rj} = 0.4f_c k b_s h_c\left[1 + 0.53\left(1 + 1.177\lambda_f\right)\right] + \frac{2}{3}f_{yv}\frac{A_{sv}}{S}(h_0 - a'_s). \tag{21}$$

(2) As an independent reinforcement, considering the bonding stress between steel fibers and concrete mortar when steel fibers are used as independent reinforcement for calculation, the shear bearing capacity of recycled steel fibers can be determined by the following formula:

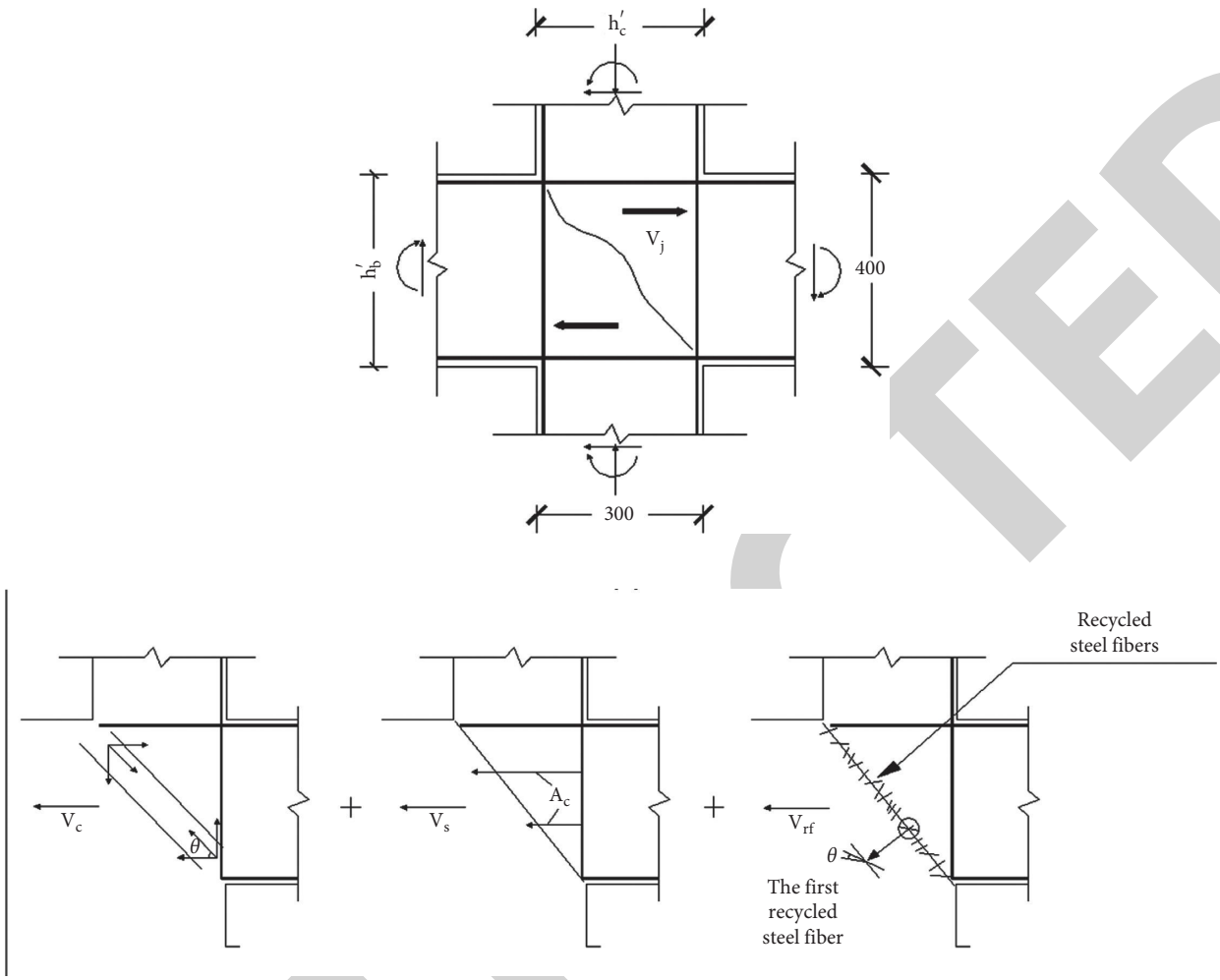

Figure 20: Calculation model of shear capacity of beam-column joints.

$$V_{rf} = \sum_{i=1}^{n_f} \pi \, d\tau_{fi} \cos \theta_i, \tag{22}$$

where n_f is the number of equivalent steel fibers on inclined crack surfaces; τ_{fi} is the bonding stress of the ith steel fiber at inclined crack. The number of steel fibers n_f in the cross crack can be determined by the following formula:

$$n_f = \frac{\alpha_1 \rho_f b_j h_j}{\pi d^2 \sin \theta_1}, \tag{23}$$

where θ_1 is the angle between inclined crack and horizontal axis; α_1 is the nonuniform influence coefficient of recycled steel fibers (approximately taking $\alpha_1 = 0.41$).

Assuming that τ_{fi} and θ_i of each steel fiber at inclined crack are the same, formula (24) can be obtained:

$$V_{rf} = \frac{\alpha_1 \cos \theta_2}{\sin \theta_1} \tau_f \lambda_f b_j h_j, \tag{24}$$

where τ_f is the bonding stress of steel fibers ($\tau_f = \eta_b f_{ft}$, η_b is theinterface bonding coefficient); θ_2 is the angle between steel fibers and horizontal plane.

In the finishing formula (24), taking $\mu = \alpha_1 \eta_b f_{ft} \cos \theta_2 / \sin \theta_1$, the shear capacity V_{rf} of recycled steel fibers is

$$V_{rf} = \mu \eta_b \lambda_f f_{ft} b_j h_j. \tag{25}$$

By inserting formulas (15), (15), and (27) into formulas (11), the calculation model of shear capacity of recycled steel fiber-reinforced concrete can be written:

$$V_{rj} = 0.4 f_c k b_s h_c + \frac{2}{3} f_{yv} \frac{A_{sv}}{S} (h_0 - a_s') + \mu \eta_b \lambda_f \left(1 + 1.177 \lambda_f\right) b_j h_j. \tag{26}$$

Combined with the relevant data in this paper, considering the different bonding effects between recycled steel fibers and concrete, the influence coefficient γ was added,

Table 7: The comparison between the test and calculated results of shear capacity of specimens.

No.	f_{cu}/MPa	f_c'/MPa	Beam size/mm × mm		n	Steel fibers		The stirrups at the joints		v_j^t/MPa	v_j^c/MPa		v_j^t/v_j^c	
			$b_c \times h_c$	$b_b \times h_b$		$\frac{l_f}{d_f}$	ρ_f /%	Number of stirrups	f_y /MPa		Formula (26)	Formula (27)	Formula (26)	Formula (27)
SF-1 [25]	21.3	—	250 × 350	200 × 350	0.32	66	1.20	0	0	325.2	304.2	284.3	1.069	1.144
SF-7 [25]	18.2	—	250 × 350	200 × 350	0.25	54	1.50	3 Φ 6	497	398.6	340.9	361.8	1.169	1.102
A-1 [26]	31.0	—	200 × 250	180 × 300	0.20	80	0.50	0	0	186.4	139.0	123.1	1.341	1.514
A-2 [26]	33.3	—	200 × 250	180 × 300	0.20	80	1.00	0	0	189.5	170.3	172.0	1.113	1.102
SF-1 [27]	21.3	—	250 × 350	200 × 350	0.32	61	1.20	0	0	189.5	298.6	273.7	1.089	1.188
SF-6 [27]	18.2	—	250 × 350	200 × 350	0.25	75	1.50	0	0	330.9	223.9	290.1	1.478	1.141
SF-7 [27]	18.2	—	250 × 350	200 × 350	0.25	75	1.50	3 Φ 6	497	398.6	360.6	426.8	1.105	0.934
SJ-1	30.01	—	300 × 300	250 × 400	0.20	60	0	1 Φ 6	168	200.5	191.6	170.8	1.046	1.174
SJ-2	30.13	—	300 × 300	250 × 400	0.20	60	0.5	1 Φ 6	168	204.6	225.2	190.5	0.909	1.074
SJ-3	31.14	—	300 × 300	250 × 400	0.20	60	1.0	1 Φ 6	168	209.8	244.4	256.1	0.858	0.818
SJ-4	32.35	—	300 × 300	250 × 400	0.20	60	1.5	1 Φ 6	168	213.7	271.6	301.8	0.787	0.708

and the coefficient of recycled steel fiber-reinforced cruciform concrete frame beam-column joints was set as $\gamma = 0.8$, while the coefficient of normal steel fiber-reinforced cruciform concrete frame beam-column joint was set as $\gamma = 0.9$.

In order to verify the rationality of the above design formula, the test data of seven steel fiber-reinforced concrete beam-column joint specimens in the literature [31–33] and the test data of four recycled steel fiber-reinforced concrete cruciform frame joint specimens in this paper are selected as shown in Table 7. According to formulas (21) and (26), the shear capacity of eleven joint specimens is statistically analyzed, and the calculation models of shear capacity of recycled steel fiber-reinforced cruciform concrete frame beam-column joints are fitted, respectively, as follows:

$$V_{rj} = \gamma\left[0.28nf_c b_j h_c\left(1 + 0.53 \times \left(1 + 1.177\lambda_f\right)\right) + \frac{2}{3}f_{yv}\frac{A_{sv}}{s}\left(h_0 - a_s'\right)\right], \tag{27}$$

$$V_{rj} = \gamma\left[0.35nf_c b_j h_c + 0.8\lambda_f\left(1 + 1.177\lambda_f\right)b_j h_j + \frac{2}{3}f_{yv}\frac{A_{sv}}{s}\left(h_0 - a_s'\right)\right]. \tag{28}$$

Table 7 shows the comparison between the shear bearing capacity test values and the calculated values based on formulas (27) and (28). The average value, standard deviation, and variation coefficient of shear capacity of eleven joint specimens are 1.088, 0.191, and 0.176, respectively, in the ratio between the test values and the calculated values of formula (4-27) (27). The average value, standard deviation, and variation coefficient are 1.082, 0.201, and 0.186, respectively, in the ratio between the test values and the calculated values of formula (4-28) (28). The results are in good agreement with each other.

6. Conclusions

In this paper, quasistatic tests were carried out on five cruciform reinforced concrete frame joint specimens to study their seismic performance. By comparing the test results with the formula calculation results, the following main conclusions are drawn:

(1) The addition of normal steel fibers can improve the bearing capacity, ductility, energy dissipation capacity, and shear strength of cruciform concrete frame joint specimens and delay the stiffness degradation of joint specimens, that is, improve the seismic performance of specimens, and the effect of recycled steel fibers is better than normal steel fibers in improving the seismic performance of joint specimens.

(2) With the increase of volume ratio of recycled steel fibers, the seismic performance of joint specimens is improved gradually. Moreover, with the recycled steel fiber content from 0.5% to 1.0% and then to 1.5%, the increased amplitude of the seismic performance of joint specimens increases.

(3) The calculation results of the calculation model of shear capacity of recycled steel fiber-reinforced concrete frame joints are in good agreement with the test results, which can provide references for the calculation of shear capacity of steel fiber-reinforced concrete frame joint specimens.

Data Availability

All the raw data used to support the findings of this study are included within the article. All the raw data are available from the corresponding author upon request.

Conflicts of Interest

The authors declare that they have no conflicts of interest.

Acknowledgments

This work was supported in part by the National Key Research and Development Program of China (no. 2017YFC0806100) and the Jilin Scientific and Technological Planning Project (no. 20210402073GH).

References

[1] L. P. Wang, W. W. Luo, S. W. Liu et al., "Experimental investigation of beam elongation effects on the mechanism and seismic performance of RC frame joints," *Engineering Mechanics*, vol. 37, no. 2, pp. 159–167, 2020.

[2] S. Qudah and M. Maalej, "Application of Engineered Cementitious Composites (ECC) in interior beam-column connections for enhanced seismic resistance," *Engineering Structures*, vol. 69, pp. 235–245, 2014.

[3] A. Aviram, B. Stojadinovic, and G. J. Parra-Montesinos, "High-performance fiber-reinforced concrete bridge columns under bidirectional cyclic loading," *ACI Structural Journal*, vol. 111, no. 2, pp. 303–312, 2014.

[4] G. F. Peng, X. J. Niu, and Q. Q. Long, "Experimental study of strengthening and toughening for recycled steel fiber reinforced ultra-high performance concrete," *Key Engineering Materials*, vol. 629-630, pp. 104–111, 2015.

[5] Z. Z. Kang and B. J. Zhang, "Scrap tires recycling in landscape engineering," *Advanced Materials Research*, vol. 374-377, pp. 1571–1575, 2011.

[6] J. Carrillo, J. Lizarazo-Marriaga, and F. Lamus, "Properties of steel fiber reinforced concrete using either industrial or recycled fibers from waste tires," *Fibers and Polymers*, vol. 21, no. 9, pp. 2055–2067, 2020.

[7] Y. Li, X. P. Wang, G. He Zh et al., "Experimental study on shear behavior of industrial waste fiber reinforced cement matrix composites," *Industrial Construction*, vol. 50, no. 12, pp. 88–92, 2020.

[8] D. Kheni, R. H. Scott, S. K. Deb et al., "Ductility enhancement in beam-column connections using hybrid fiber-reinforced concrete," *ACI Structural Journal*, vol. 112, no. 2, pp. 167–178, 2015.

[9] X.-w. Liang, Y.-j. Wang, Y. Tao, and M.-k. Deng, "Seismic performance of fiber-reinforced concrete interior beam-column joints," *Engineering Structures*, vol. 126, pp. 432–445, 2016.

[10] G. Sh, "Experimental study on seismic behavior of steel fibers locally reinforced high strength concrete frame joints," *Zhengzhou University*, vol. 36, p. 57, 2012 Zhengzhou, Henan Province, China.

[11] M. Ming, S. S. Zheng, H. Zheng et al., "Experimental study on bond slip performance of profile steel high performance fiber-reinforced concrete," *Engineering Mechanics*, vol. 37, no. 8, pp. 148–157, 2020.

[12] E. Eincina, Y. Lu, and R. S. Henry, "Axial elongation in ductile reinforced concrete walls," *Bulletin of the New Zealand Society for Earthquake Engineering*, vol. 49, no. 4, pp. 305–318, 2016.

[13] L. I. Zh, "Study on mechanical properties of steel fiber-reinforced concrete and its application in subway engineering," *Southwest Jiaotong University*, vol. 2018, 2017 Chengdu, Sichuan Province, China.

[14] N. Nourmohammadi, N. P. O'Dowd, and P. M. Weaver, "Effective bending modulus of thin ply fibre composites with uniform fibre spacing," *International Journal of Solids and Structures*, vol. 196-197, pp. 26–40, 2020.

[15] S. G. Liu, R. Bai, C. W. Yan et al., "Experimental study and theoretical calculation of bending stiffness of reinforced fiber reinforced cement matrix composite beams," *Journal of Building Structures*, vol. 39, no. S2, pp. 176–182, 2018.

[16] L. Liao, J. Zhao, F. Zhang, S. Li, and Z. Wang, "Experimental study on compressive properties of SFRC under high strain rate with different fiber content and aspect ratio," *Construction and Building Materials*, vol. 261, p. 119906, 2020.

[17] R. A. Raju, S. Lim, M. Akiyama, and T. Kageyama, "Effects of concrete flow on the distribution and orientation of fibers and flexural behavior of steel fiber-reinforced self-compacting concrete beams," *Construction and Building Materials*, vol. 262, p. 119963, 2020.

[18] Southeast University Tianjin University Tongji University, "Concrete structure," *China Building Industry Press*, China, Beijing, 2020.

[19] Z. H. B. Xu, "Study on seismic behavior of steel fiber-reinforced concrete plastic hinge beam-column joints at beam end," *Tongji University*, China, Shanghai, 2006.

[20] R. Siva Chidambaram and P. Agarwal, "Seismic behavior of hybrid fiber reinforced cementitious composite beam-column joints," *Materials & Design*, vol. 86, pp. 771–781, 2015.

[21] K. F. Gao, "Design and mechanical properties analysis of column-column-beam assembled steel frame joints, Harbin Institute of Technology," *Harbin, Heilongjiang Province, China*, 2018.

[22] H. Zhang, "Early capability and damage analysis of self-compacting, steel-fiber-reinforced lightweight aggregate concrete," *Materials Review*, vol. 31, no. 20, pp. 124–128, 2017.

[23] Code for Concrete Design Structures (GB 50010-2010), *Beijing*, China Building Industry Press, Beijing, China, 2017.

[24] D. Y. Gao, K. Shi, and B. Zhao Sh, "Calculation method of shear capacity of reinforced steel fiber concrete beam-column joints based on softened tension and compression bar model," *Journal of Civil Engineering*, vol. 47, no. 9, pp. 101–109, 2014.

[25] J. W. Zhang, "Study on mechanical properties of steel fiber concrete side joints and legs," *Zhengzhou University*, Zhengzhou, Henan Province, China, 2011.

[26] G. H. Xing, B. Q. Liu, and T. Wu, "Simplified calculation model of shear capacity of reinforced concrete frame joints," *Journal of Building Structures*, vol. 32, no. 10, pp. 130–138, 2011.

[27] L. S. Zhang, "Structural vulnerability evaluation considering elastic-plastic, parameter randomness and internal force contribution of component materials," *Fuzhou University*, Fuzhou, Fujian Province, China, 2018.

Hindawi
Advances in Civil Engineering
Volume 2023, Article ID 9865205, 1 page
https://doi.org/10.1155/2023/9865205

Retraction

Retracted: Experimental Study on Mineral Solid Waste Green Grouting Material Based on Electromagnetic Characteristic Detection

Advances in Civil Engineering

Received 10 October 2023; Accepted 10 October 2023; Published 11 October 2023

This article has been retracted by Hindawi following an investigation undertaken by the publisher [1]. This investigation has uncovered evidence of one or more of the following indicators of systematic manipulation of the publication process:

(1) Discrepancies in scope
(2) Discrepancies in the description of the research reported
(3) Discrepancies between the availability of data and the research described
(4) Inappropriate citations
(5) Incoherent, meaningless and/or irrelevant content included in the article
(6) Peer-review manipulation

The presence of these indicators undermines our confidence in the integrity of the article's content and we cannot, therefore, vouch for its reliability. Please note that this notice is intended solely to alert readers that the content of this article is unreliable. We have not investigated whether authors were aware of or involved in the systematic manipulation of the publication process.

Wiley and Hindawi regrets that the usual quality checks did not identify these issues before publication and have since put additional measures in place to safeguard research integrity.

We wish to credit our own Research Integrity and Research Publishing teams and anonymous and named external researchers and research integrity experts for contributing to this investigation.

The corresponding author, as the representative of all authors, has been given the opportunity to register their agreement or disagreement to this retraction. We have kept a record of any response received.

References

[1] X. Wang, J. Hu, X. Zhang, K. Wang, D. Shen, and C. Liang, "Experimental Study on Mineral Solid Waste Green Grouting Material Based on Electromagnetic Characteristic Detection," *Advances in Civil Engineering*, vol. 2022, Article ID 6261429, 19 pages, 2022.

Hindawi
Advances in Civil Engineering
Volume 2022, Article ID 6261429, 19 pages
https://doi.org/10.1155/2022/6261429

Research Article

Experimental Study on Mineral Solid Waste Green Grouting Material Based on Electromagnetic Characteristic Detection

Xiangpeng Wang,[1,2] **Jin Hu**,[2,3] **Xiang Zhang**,[1] **Kunpeng Wang**,[1] **Di Shen**,[1] **and Chuntao Liang**[1]

[1]*College of Geophysics, Chengdu University of Technology, Chengdu 610059, China*
[2]*Tsinghua University, Department of Civil Engineering, Sichuan Mianzhu New Building Materials Co., Ltd., High Performance Green Building Materials Joint Research and Development Center, Deyang 618200, China*
[3]*Sichuan College of Architecture Technology, Deyang 618000, China*

Correspondence should be addressed to Xiangpeng Wang; wangxiangpeng@stu.cdut.edu.cn and Jin Hu; 478428210@qq.com

Received 12 November 2021; Revised 27 December 2021; Accepted 11 January 2022; Published 18 March 2022

Academic Editor: Ramadhansyah Putra Jaya

The production processes for the gypsum- and cement-based materials, which are widely used in civil engineering projects, require the consumption of large amounts of energy and natural resources. At the present time, the main development directions of civil engineering material include realizing solid waste recycling and the applications of green building materials, which can be then used in the fields of disaster treatment and ecological restoration, such as grouting materials. In addition, the grouting quality is always difficult to detect. This study examined the gypsum- and cement-based green grouting materials made from mineral solid waste used in disaster and cloud detection by means of electromagnetic characteristics. According to the requirements of electrical testing of grouting quality, first we designed a material made with solid waste. Then, we studied the resistivity, strength, porosity, and other physical and mechanical properties of the material. The test results of the material and its soaking solution indicate that this material is a green material meeting the environmental safety standards. The experimental results show that the rapid detection of grouting quality can be realized. The following effects on electromagnetic characteristics and mechanical properties of the green materials of gypsum- and cement-based were analyzed. The results showed that the resistivity and strength were related to the ratios of the water content to the modified phosphogypsum; the percentages of cement content in the total amount of modified phosphogypsum and marble powder; the percentages of marble powder in the modified phosphogypsum; the percentages of steel fiber content in the phosphogypsum; and the fineness of the marble powder. The field test results also confirm that the green grouting material can be effectively applied in engineering repair imaging monitoring.

1. Introduction

The production processes for the gypsum- and cement-based materials, which are widely used in civil engineering projects, require the consumption of large amounts of energy and natural resources. At the present time, the main development directions of civil engineering material design include solid waste recycling and the applications of green building materials. A primary focus is to realize the recycling of solid waste materials, which can then be used in the fields of disaster treatment and ecological restoration.

In recent years, many countries throughout the world have made major progress in mining, metal smelting, coal power generation, and chemical production. However, at the same time, large quantities of industrial waste products have been discharged during the production processes. If industrial waste residue is not used, it will not only occupy valuable land resources but will also result in air pollution, soil pollution, and water pollution. However, it has been determined that industrial waste residue has utilization value. On the premise of meeting the requirements of environmental safety, industrial waste residue can be used as a

part of the cement- and gypsum-based materials applied to ecological restoration and disaster management projects, thereby reducing carbon emissions and improving some of the properties of civil engineering materials [1–3].

In the field of civil engineering, grouting is an important technical means for the rapid control of engineering disasters and the reinforcement of weak strata. It has been widely used in slope control, mining, and tunnel water shutoff emergencies [1–8]. At the same time, the backfill of mining goafs and reinforcement of urban underground spaces must be treated before construction can begin, in order to avoid damages to upper structures caused by uneven surface deformations. The most common treatment scheme involves grouting filling. For example, after construction is completed, the traditional detection methods include drilling, water pressure tests, surface deformation monitoring, and so on [9–11]. However, the monitoring of the construction processes cannot be effectively carried out, and only fixed-point detections can be completed for the detection points. These types of detections are not only time-consuming but also involve high cost and still may be unable to comprehensively grasp the grouting situation in a timely manner. Therefore, it can be seen that the workloads of detection and monitoring processes are large, and the original geological conditions may be seriously damaged.

To accurately understand the diffusion processes and scope of underground spaces from the aspect of slurry and visualize the relevant information, several geophysical methods can be adopted. Such combinations have the advantages of high efficiency and large-area detection results when detecting concealed work areas and can be combined with other detection methods to realize the "point surface combination" in three-dimensional detections [12]. The most commonly used geophysical detection methods include high-density electrical; transient Rayleigh waves; geological radar; transient electromagnetic; magnetotelluric; cross hole seismic wave CT; cross hole electromagnetic wave CT methods [13–17]. S. H. Adnan, R. Hamdan, and N. A. Roni introduced an alternative method, which reuses the RCA as a water filter medium to remove phosphorus from wastewater [18]. In addition, Sang L., Idowu T., and Okumu V. examined the viability of waste marble dust (WMD), an industrial waste produced during the shaping and polishing of marble blocks, as well as during its extraction from mines, as a mineral filler in hot-mix asphalt (HMA) concrete [19]. Hossain, M. B., Roknuzzaman, M., Biswas, M. A., and Islam, M., considered since there is a possibility of leaching by dumping a large quantity of fly ash in the pond, the use of fly ash from the power plants to improve soft cohesive soils for road subgrade may be an environment-friendly alternative to its disposal in the ponds [20]. Adewumi, J. R., Ajibade, T. F., and Ajibade, F. O., studied undertaken to assess the present status of on-site sanitation facilities in public places within Akure, to trace problems related to sanitation and solid waste management [21]. Kam, C. Z., and Kueh, A. B. H., discussed on the major existing methodologies in pursuing sustainable value of polymeric materials [22]. However, the previous studies had only detected the grouting treatment effects of mining goafs based on cement and fly ash materials. When compared with cement and fly ash materials, gypsum-based and cement-based composite materials have the advantages of high setting rates (close to 100%); easy transportation; easy control of the diffusion range; and no water separation during solidification. Therefore, such material can be gradually applied in goaf backfilling and other projects. In summary, at the present time, the grouting treatment effects of gypsum- and cement-based composites for mining goafs have become new research topics.

Previous studies [23, 24] have shown that when fluid flows and diffuses in the stratum, the movement of water and slurry in the rock soil spaces will transfer the electrical charges and cause changes in the geoelectric potential and currents, which are sensitive to changes in slurry diffusion. Many researchers have investigated the variations of electric fields during the process of groundwater seepage (Hamdi FAI et al., 2012; Rupesh et al., 2021) [25–27]. A large number of research studies have been carried out regarding the law of seepage, diffusion of grout, and the effects of grouting filling from the aspects of theoretical analysis, experimental research, and engineering practices both in China and internationally, and major achievements have been made [28–30]. It is generally believed that transient electromagnetic methods have the advantages of no primary field background interference; no high resistance shielding effects; no static effects; and minimal influencing effects of terrain. Such methods are also especially sensitive to low resistance. However, there have been few reports presented on whether natural electrical fields and artificial electrical fields can be used to reflect the infiltration and diffusion of slurry during the process of grouting in porous rock and soil. That is to say, slurry diffusion in geological structures [31–40].

The characteristics of the medium resistivity of cement and fly ash slurry after solidification have been thoroughly investigated. However, the changes in resistivity of gypsum-based and cement-based material slurry before and after solidification have rarely been studied. According to this study's experimental design, the correlations between the resistivity changes of different gypsum- and cement-based materials, and other properties of gypsum- and cement-based materials, were analyzed in depth. Then, based on the obtained experimental results, the feasibility of detecting the grouting effects of gypsum- and cement-based materials were deferred using electrical characteristics. In addition, tests of the application effects were performed in practical engineering scenarios. The goals of this study were to provide a new method for the detection of material grouting effects and to promote the resource utilization of solid waste in the construction of ecological environments. The research results of this study can potentially be used to detect filling conditions after grouting and to determine whether the conditions meet the physical and mechanical properties of the design requirements. The electrical differences between the grouting material and the surrounding rock, soil, or other materials can also be utilized to realize the monitoring and detection of disaster control grouting engineering processes.

2. Raw Materials

2.1. Cement. In the present investigation, 425 ordinary Portland cement was obtained from the Xi'an Yaobai cement plant. It was confirmed that its performance met the national standards (Table 1).

2.2. Phosphogypsum. In order to verify the different types of mineral admixtures, two different types of phosphogypsum were used in this experiment. The modified phosphogypsum used in this study was dihydrate phosphogypsum provided by Mianzhu Panlong Co. (Table 2). The modified phosphogypsum powder was hemihydrate gypsum produced by Mianzhu Co. (Table 3).

2.3. Steel Fiber. Hebei Zhitai Steel Fiber Manufacturing Co., Ltd., provided the steel fiber utilized in this study (Table 4).

2.4. Basalt Fiber. The basalt fiber was produced by Deyang Zhongxin Co. (Table 5).

2.5. Marble Powder. According to the details of previous related experiments, marble powder respectively milled for 1, 5, 30, and 120 minutes will exhibit different characteristics. The particle distributions and properties are shown in Figure 1 and Table 6. In this study's orthogonal experiment, these were represented by finenesses of 1, 2, 3, and 4, respectively.

2.6. Sand. The sand utilized in the experiments was obtained from Mianzhu Construction Investment Co. It was confirmed to meet the national requirements (Table 7). The gradation is shown in Table 8, which also met the requirements. The fineness modulus was 3.08, which was considered to be medium sand.

2.7. Water Reducing Agent. This study adopted a YSNF-A6 superplasticizer provided by Shanxi Yongsheng Building Materials Chemical Co., Ltd. The water reduction rate was 17%; bleeding rate was 45%; and gas content was 2.4%. The setting timeframe was 25 to 65 minutes. The compressive strength ratios were as follows: 1 d: 153%; 3 d: 143%, 7 d: 130%, and 28 d: 126%. Compressive strength ratio refers to the strength of the specimen with water reducing agent in the same age divided by the strength without water reducing agent.

2.8. Retarder. This study used SG-09 gypsum retarder produced by Suzhou Xingbang Chemical Building Materials Co., Ltd. The powder was white to yellowish in color. The water content was ≤3%, and the *pH* value (20% aqueous solution, 20°C) ranged between 10 and 13.

3. Experimental Testing Scheme

3.1. Compressive Strength. Some factors affecting resistivity and strength of concrete are studied, such as the ratio of cement content to the total amount of modified phosphogypsum and marble powder, and the ratio of steel fiber content to phosphogypsum. Therefore, a five-factor and four-level orthogonal test method was used in this research investigation to design the mix proportion, and the testing scheme is shown in Table 9.

In the present study, the marble powder with finenesses of 1, 2, 3, and 4, respectively, refers to marble powder D50 37.87 μm, 31.70 μm, 29.74 μm, and 20.42 μm. The compressive strength and flexural strength levels of mortar were tested by 40 * 40 * 40 mm, 70.7 * 70.7, and 100 * 100 * 100 mm molds for 3 days, 7 days, 28 days, and 3 months, respectively.

3.2. Resistivity Test Scheme. The resistivity changes observed from the beginning of the forming processes were tested by applying a resistance tester.

3.3. Porosity Test Scheme. The changes in the porosity levels were tested using a magnetic resonance instrument. A nonevaporating water content method was also tested.

3.4. Environmental Safety Detection Scheme. The material composition was tested using an electron scanning microscope/energy spectrometer (SEM/EDS), Fourier transform infrared spectrometer (FTIR), gas chromatography mass spectrometry (GCMS), and inductively coupled plasma emission spectrometer (ICP-OES). The test was performed according to standards GB/T6040-2019, GB/T9722-2006, GB/T17359-2012, and EPA6010D-2018. After the sample had been soaked for 24 hours, the composition of the soaking solution was tested in the same way.

4. Results and Analysis

4.1. Compressive and Flexural Strength. As shown in Figure 2, the strength levels of the 3 d, 7 d, and 28 d and 6 m (i.e., maintenance for 6 months) were observed to have increased. Group 8 had the highest strength on day 3, while Group 4 had the highest strength on days 7 and 28. The proportion of water in Group 9 was larger than that in Group 4, while the proportions of steel fiber and cement were smaller than that in Group 4. It was observed that the relationships among the early strength levels and the steel fiber content, cement content, and water cement ratios were minimal. However, the late strength level of Group 9 was observed to be lower than the others, which indicated that the previously mentioned factors had mainly affected the later strength levels. The ratio of water to solid material in Group 4 was 0.32, and that of Group 8 was 0.5, while the proportion of steel fiber in solid material was 0.12 in Group 4 and 0.083 in Group 8.

Table 1: Cement properties content and other natural requirements.

Chemical composition	SiO_2	Fe_2O_3	Al_2O_3	CaO	MgO	SO_3	Loss
Content (%)	22.63	3.83	5.71	58.95	1.89	2.62	4.37

	Chemical composition content (%)			Specific surface area	Water requirement of normal consistency (%)	Setting time (min)		Flexural strength (MPa)		Compressive strength (MPa)	
	Loss	MgO	SO_3	m^2/kg		Initial setting	Final setting	3 d	28 d	3 d	28 d
Index requirements	≤5.0	≤5.0	≤3.5	≥300		≥45	≤600	≥3.5	≥6.5	≥17.0	≥42.5
Experimental data	4.37	1.89	2.62	354	27.5	182	235	5.7	7.8	31.5	56.9
Single evaluation	Standard	Standard	Standard	Standard	Standard	Standard	Standard	Standard	Standard	Standard	Standard

Table 2: Modified phosphogypsum ($CaSO_4 \cdot 2H_2O$) properties.

Inspection items	Experimental data (%)
I.oss	—
SiO_2	—
Fe_2O_3	—
Al_2O_3	—
CaO	31.56
MgO	—
SO_3	42.68
Water soluble fluorine	Not detected
Water soluble phosphorus pentoxide	0.008
P_2O_3	0.36
F	Not detected
Attached water	—
Crystal water	16.98
C3A	—

Table 3: Modified phosphogypsum powder (CaSO4·1/2H2O) properties.

Inspection items		Unit	Index requirements			Experimental data	Single evaluation
			3.0	2.0	1.6		
B-CaSO4·1/2H2O		%		>60.0		68.7	Standard
Fineness (0.2 mm square hole sieve residue)		%		≤10		3	Standard
Setting time	Initial setting time	min		≥3		4	Standard
	Final setting time	min		≤30		8	Standard
2 h flexural strength		Mpa	≥3.0	≥2.0	≥1.6	3.4	Standard
2 h compressive strength		Mpa	≥6.0	≥4.0	≥3.0	7.0	Standard
Radioactivity	IRa	—		≤1.0		—	—
	Ir	—		≤1.0		—	—
Restricting element	K_2O	%	Agreed by both parties			0.16	—
	Na_2O	%	Agreed by both parties			0.11	—
	MgO	%	Agreed by both parties			0.96	—
	P_2O_5	%	Agreed by both parties			1.80	—
	F	%	Agreed by both parties			0.10	—

Table 4: Steel fiber properties.

	Diameter (mm)	Length (mm)	Aspect ratio	Tensile strength (MPa)	Bending performance, bending core 3 mm
Index requirements	0.55 ± 0.055	35 ± 3.5	60 ± 6	≥1000	Cold bend 90°, 9/10continuous
Experimental data	0.55	35.10	64	1265	20/20 continuous
Single evaluation	Standard	Standard	Standard	Standard	Standard

Table 5: Basalt fiber properties.

	Diameter (μm)	Length (mm)	Breaking strength (MPa)	Elongation at break (%)	Elastic modulus (MPa)	Alkali resistance (%)	Density (g/cm^3)	Appearance
Index requirements	9–25	—	≥1200	≤3.1	≥8.0 * 103	≥75	2.60–2.80	Uniform color and no pollution
Experimental data	16.5	18	1354	3.1	57.3 * 103	95.4	2.62	Uniform color and no pollution
Single evaluation	Standard	—	Standard	Standard	Standard	Standard	Standard	Standard

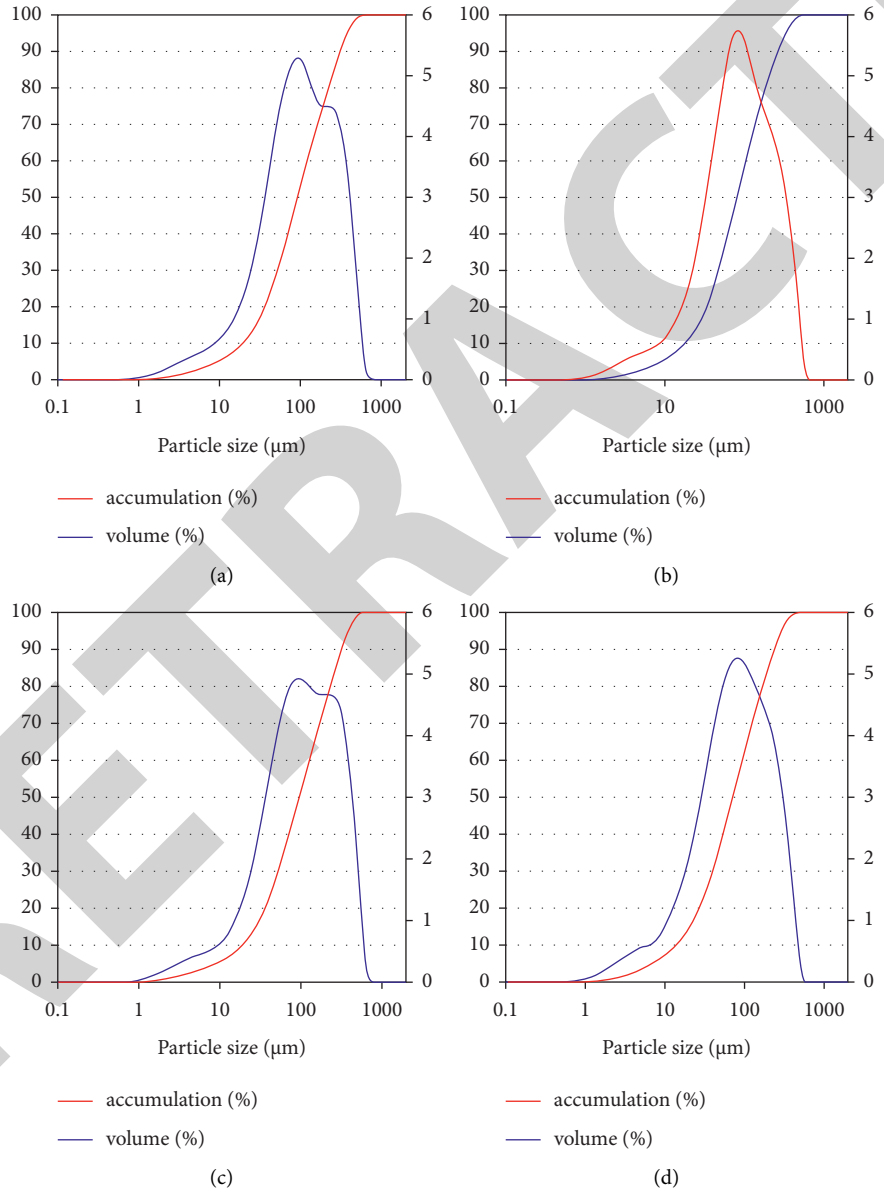

Figure 1: Particle size distributions of marble powder under different grinding time: (a) particle distribution grinding for 1 minute; (b) particle distribution grinding for 5 minutes; (c) particle distribution grinding for 30 minutes; (d) particle distribution grinding for 120 minutes.

Group 4, which had a large steel fiber proportion and small water proportion, had the highest strength in the later stage. It can be seen that the ratio of steel fiber and water was more important in the later stage, while Group 8, which had small steel fiber and large water proportion, had higher strength in the early stage. It can also be seen that the ratio of water to

Table 6: Marble powder properties.

	CaO + MgO (%)	Color	Free water (%)	Volume stability
High-class index requirements	≥70	—	0.4–2	Qualified
Experimental data	100	Higher white interference co]our	0	Qualified
Single evaluation	Standard	—	Standard	Standard

Table 7: Sand properties.

Mesh size(mm)	4.75	2.36	1.18	0.6	0.3	0.15	Sieve bottom	—
Cumulative percentage retained (%)	5.99	23.13	48.27	73.91	83.54	90.21	94.27	—
Apparent density (g/cm^3)	2.651	Mud content (%)	1.0	Clay content (%)			0.1	
Fineness modulus	3.08	Soundness (%)	2	Mica content (%)			0.21	
0rganic matter content		—		SO3 content (%)			0.12	

Table 8: Material grading table.

Aperture (mm)	5	2.5	1.25	0.625	0.31	0.16	<0.16
Cumulative sieve residue percentage (%)	5.99	23.13	48.27	73.91	83.54	90.21	100

Table 9: Experimental scheme.

Serial number	Ratio of water to modified phosphogypsum A	Percentage of cement content in total amount of modified phosphogypsum and marble powder B (%)	Percentage of marble powder in modified phosphogypsum D (%)	Percentage of steel fiber content in phosphogypsum E (%)	Fineness of marble powder
1	0.55	5	10	20	1(1)
2	0.55	15	0	10	3(30)
3	0.55	20	20	5	4(120)
4	0.55	25	40	40	2(5)
5	0.6	5	20	40	3
6	0.6	15	40	5	1
7	0.6	20	10	10	2
8	0.6	25	0	20	4
9	0.65	5	40	10	4
10	0.65	15	20	20	2
11	0.65	20	0	40	1
12	0.65	25	10	5	3
13	0.7	5	0	5	2
14	0.7	15	10	40	4
15	0.7	20	40	20	3
16	0.7	25	20	10	1

solid materials and the proportion of steel fiber were not the most important factors affecting the strength at the late age.

As can be seen in Figure 3, the compressive strength increased with age, with Group 13 being the slowest. The fastest increase was observed in Group 4. The compressive strength of Group 13 was also low and increased slowly in the three ages. However, since the marble powder dosage was 0, it was indicated that the marble powder had not degraded the strength. The intensity of Group 4 increased rapidly, so that it became much higher than the other groups other than Group 3, and it was the highest after 28 d. The special proportion of the fourth group is the use of 6% naphthalene water reducer. It can be seen from the SEM photograph shown in Section 4.2 that the crystal structure and density of Group 4 with water reducing agent are completely different from those without water reducing agent. It is speculated that this is the result of its chemical reaction, and further research is in progress.

The strength measured after soaking for 3 d in proportioning 4 is only 0.401 MPa, but it reaches 8.7907 Mpa after 28 d and 8.8075 Mpa after soaking for 7 d. The strength of standard curing is also 0.6521 and 1.1612 MPa after 3 and 7 d, respectively, while it reaches 14.5133 MPa after 28 d. The strength in the later stage is greatly improved. It is quite different from the intensity growth mode of other groups. In addition, at 6 months, the compressive strengths of Groups 1 and 6 were lower than at 28 d.

As mentioned in Figure 4, the flexural strength had not increased with age, and the flexural strength levels of Groups

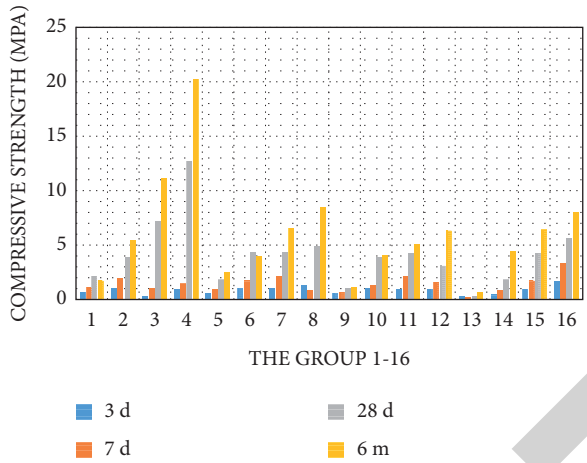

Figure 2: 3 d, 7 d, 28 d, and 6-month compressive strength.

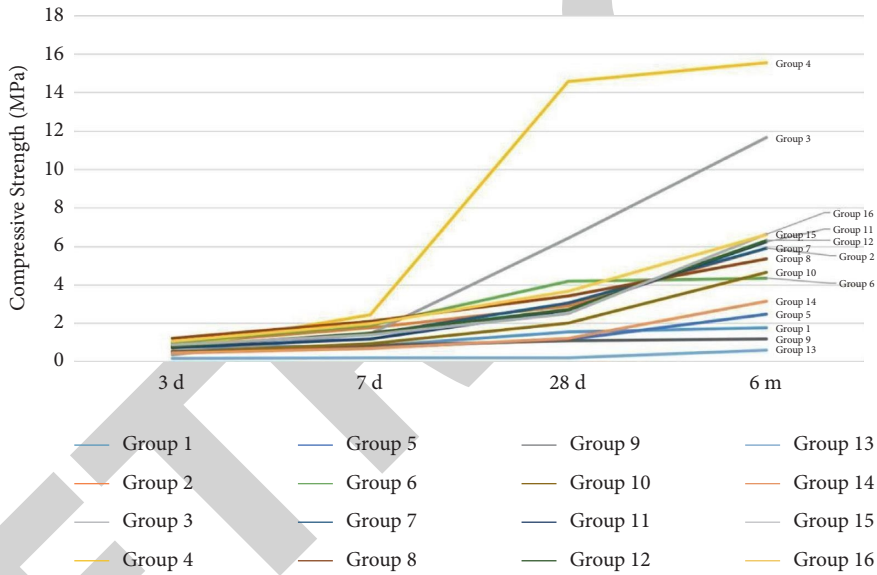

Figure 3: Variation trends of the compressive strength levels.

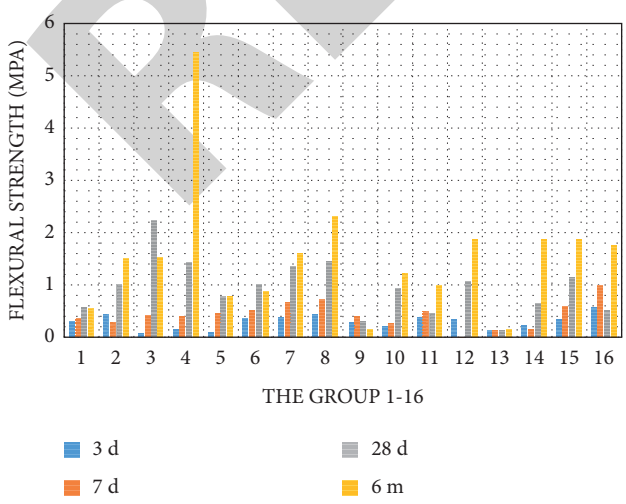

Figure 4: 3 d, 7 d, 28 d, and 6-month flexural strength.

9, 11, 13, and 16 decreased on day 28. In particular, the strength levels of Group 9 and Group 13 were the lowest at 28 d, which was similar to the compressive strength. Groups 1, 3, 6, and 9 had intensities of less than 28 d after 6 months. The 28 d resistivities of Groups 1, 6, 9, and 13 are higher, which shows that there is some connection among them, and the reason behind this is being further studied.

As can be seen in Figure 5, the change trends of the compressive strength and flexural strength were not the same. The flexural strengths at 3 d and 7 d were the highest in Group 16, and the flexural strength at 6 months was the highest in Group 4. The compressive strength at 3 d was the highest in Group 8, and the flexural strengths at 7 d and 6 months were the highest in Group 4. The compressive strength increases from 3 d to 6 months, while the flexural strengths of Groups 1, 6, and 9 of three months were even lower than that of 7 d. Therefore, the underlying mechanism requires further studied.

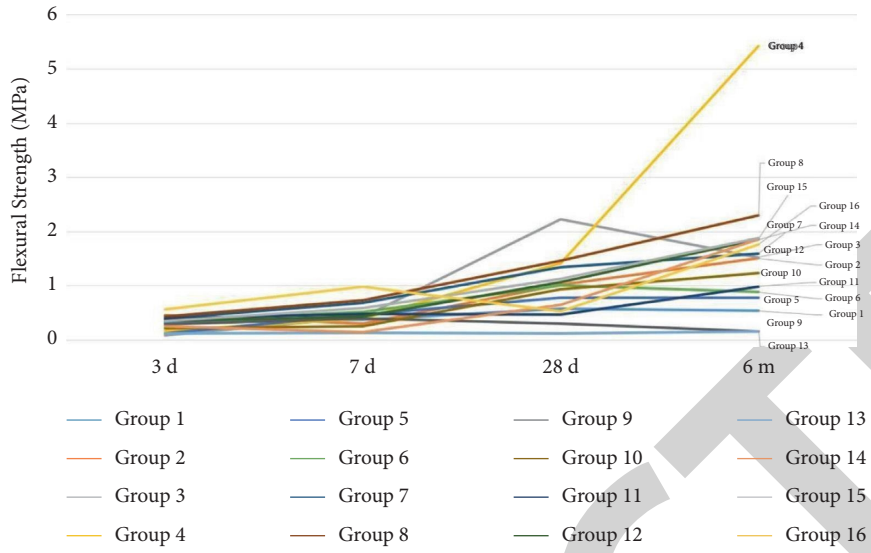

Figure 5: Change trends of the flexural strength levels.

4.2. Micromorphology. The reason for which SEM images are selected for comparison is that the later flexural strengths of Groups 1, 6, and 9 are lower than those in the early age, while the strength of Group 4 is very high, and the strength increases significantly compared with that in the early age.

The microscopic imagery of Group 4's observations showed that the crystal was much more highly dense than the other groups, and the crystal shape was clear (Figure 6–11). Its high strength is also likely related to this.

The strength of ratio 3 is only second to 4, while the crystal density of ratio 3 is also second only to 4.

4.3. Element Content. According to the element content shown in Table 10, the highest strength of ratios 3 and 4 is likely due to the absence of P. P is the element phosphorus, which has a retarding effect on concrete, and its enrichment easily causes the eutrophication of environmental water. The reason for the lowest strength of ratio 13 is likely the highest content of S.

4.4. Resistivity Changes. The testing data are detailed in Figure 12. We can see that the sample with high resistivity in three days has high resistivity in seven days. This characteristic can help us to quickly detect the properties of materials.

As shown in Figure 13, the change trends of the resistivity were not consistent with the that of the compressive strength. However, there were some similarities observed with the change rules of the flexural strength.

4.5. Porosity Changes. When the results shown in Figure 14 were compared with those shown in Figure 12, it can be seen that the variation trends of the porosity were contrary with those of the resistivity. In addition, as shown in Figure 13, the change trends of the porosity were basically the same during all the different ages. Also, the change trends of the strength during the different ages were basically the same, and the smaller the resistance was, the greater the porosity would be. The change trend of nonevaporated water content is shown in Figure 15. It can be seen that it is highly consistent with the change trend of resistivity shown in Figure 12, thus indicating that the nonevaporated water content is directly related to resistivity.

4.6. Environmental Safety Detection Results. The component test results of the material and its soaking solution are shown in Tables 11 and 12. No substances affecting environmental safety appear in the soaking solution, indicating that this material is a green material, which meets environmental safety standards.

5. Analysis of the Data

5.1. Analysis of the Influencing Factors of the Optimal Strength. According to the calculation and analysis rules of the orthogonal experiment, the following results are determined based on the table. Due to the large size of the table and space constraints, combined with the fact that the data are reflected in the previous figure, the process is omitted from the table.

It can be seen from Tables 13 and 14 that the main and secondary influencing factors of the compressive strength were the proportions of cement content in the total amount of modified phosphogypsum and marble powder; fineness of the marble powder; proportions of steel fiber content in the phosphogypsum; proportions of water and modified phosphogypsum; and proportions of marble powder in the modified phosphogypsum.

5.2. Analysis of the Influencing Factors of the Resistivity Optimization. As detailed in Tables 15 and 16, the primary and secondary influencing factors of the resistivity were the percentages of steel fiber content in the phosphogypsum.

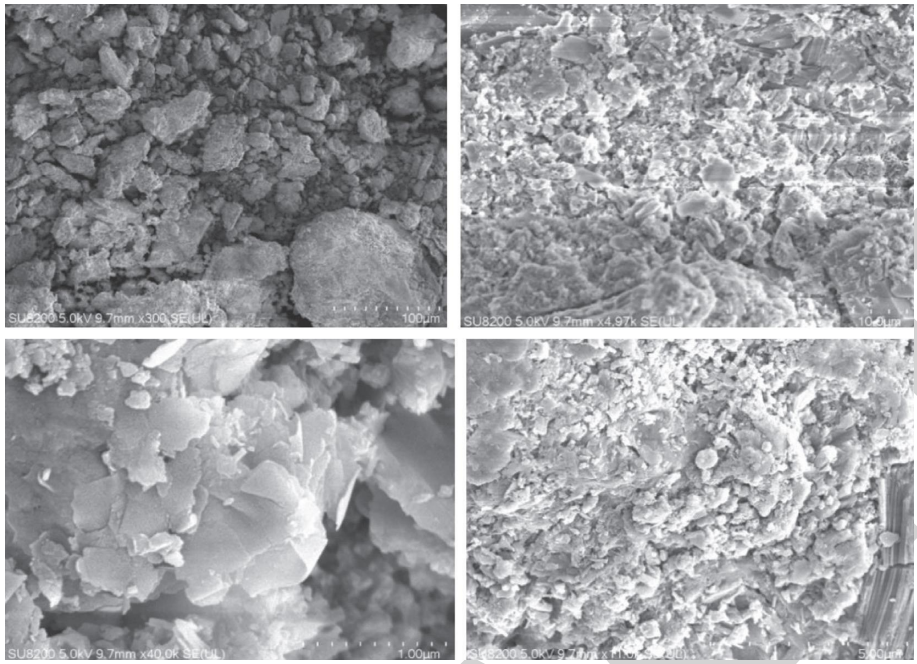

Figure 6: Microstructure of Group 4.

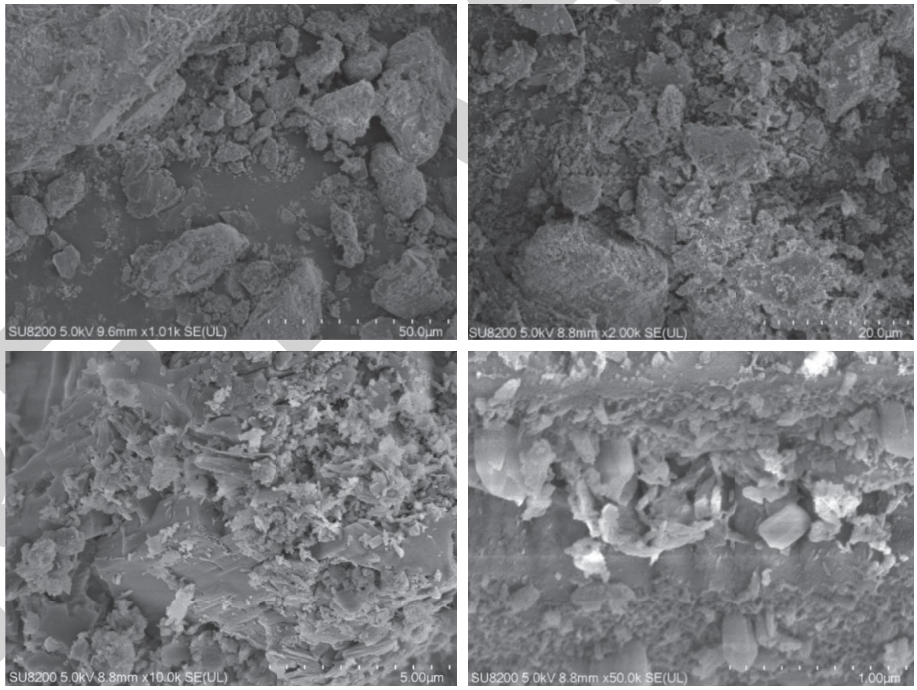

Figure 7: Microstructure of Group 1.

This was followed by the proportions of water and modified phosphogypsum; percentage of marble powder in the modified phosphogypsum; fineness of the marble powder; and the percentage of cement content in the total amount of modified phosphogypsum and marble powder.

5.3. Parallel Tests and Analysis of the Optimal Strength Ratios. The parallel experiment mentioned here refers to that performed under the condition of the same amount of other materials, except for the fact that the amount of marble powder is changed to compare the influence of the change of

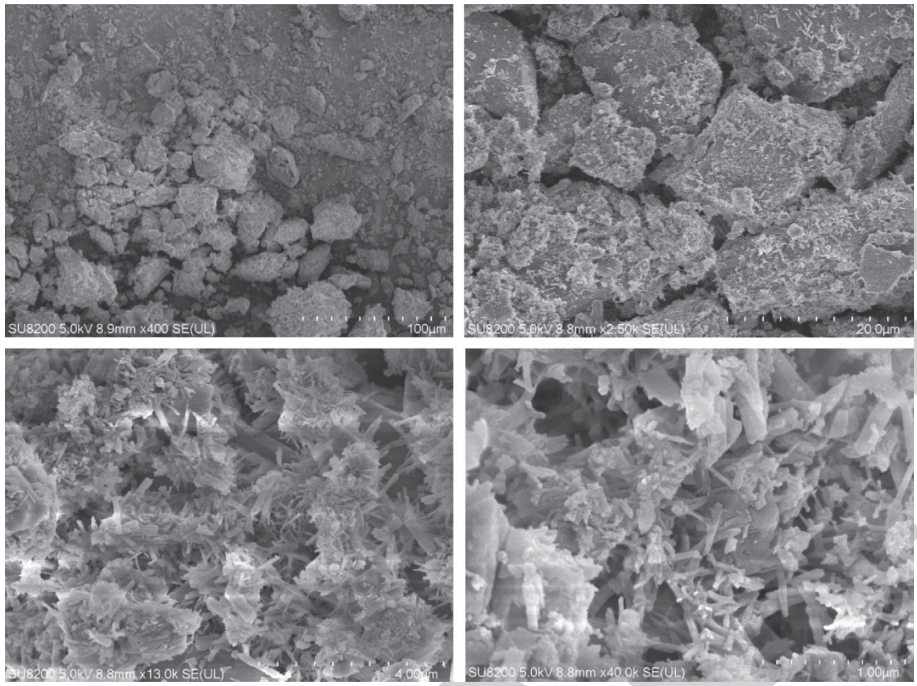

Figure 8: Microstructure of Group 6.

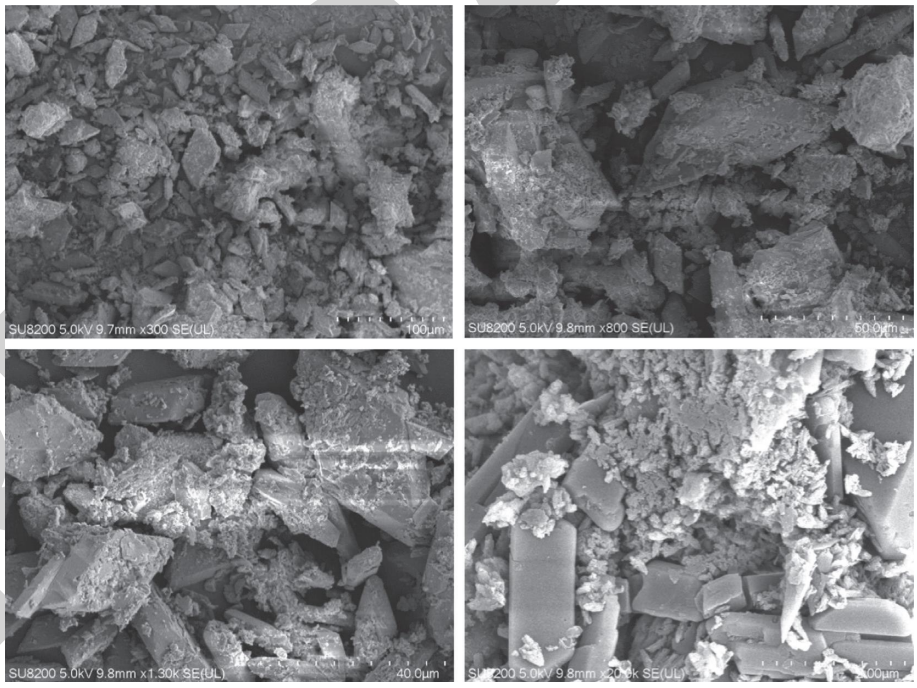

Figure 9: Microstructure of Group 13.

single conditions, which is different from the above orthogonal experiment.

In this study, in accordance with the identified influencing factors and the analysis of the optimal ratios, the parallel test ratio of the optimal ratio was obtained, as shown in Table 17.

The strength test results of the optimal ratio are shown in Table 18.

It was determined that the most effective dosage of marble powder for the 3 d strength was 100. For the 7 d compressive strength, the most effective marble powder content was 50, while the flexural strength was the best when

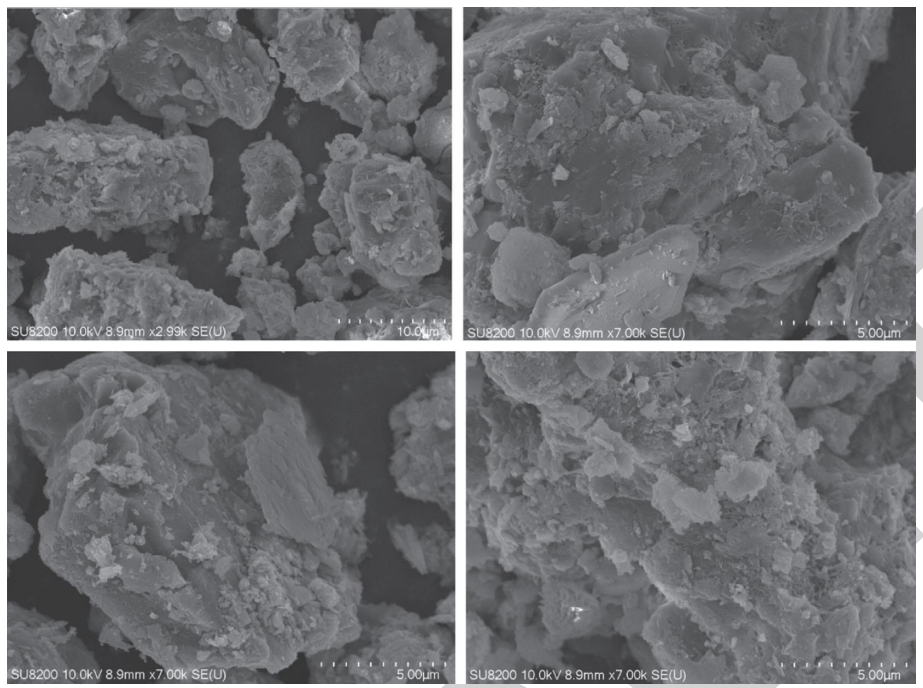

Figure 10: Microstructure of Group 3.

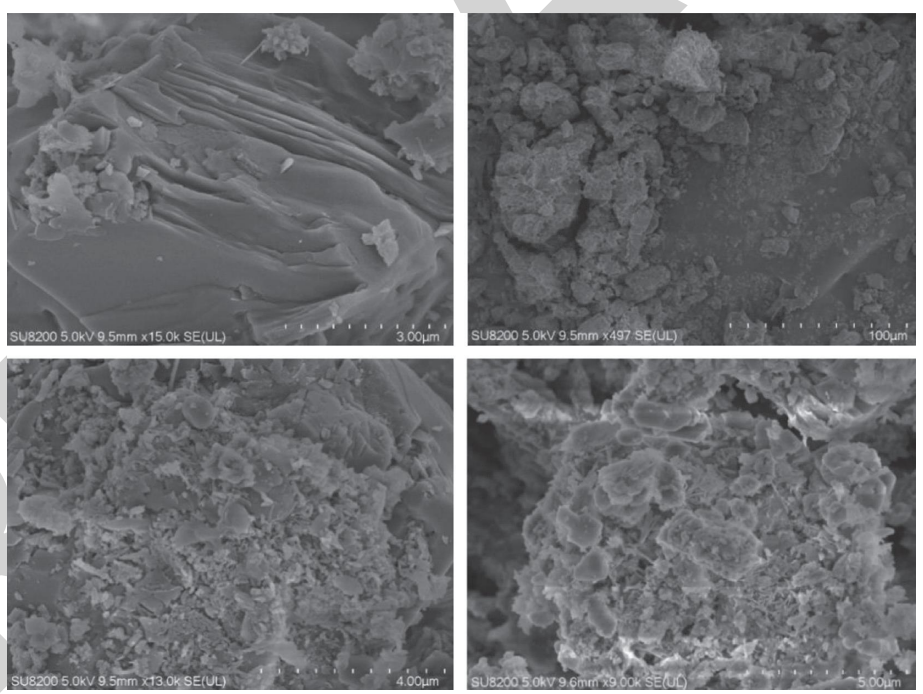

Figure 11: Microstructure of Group 9.

Table 10: Element content.

Element content(%)	C	O	Na	Mg	Al	Si	P	S	K	Ca	Fe	Au
Group 1	21.82	51.87			1.63	3.08	0.79	5.24	0.24	6.52		8.81
Group 3	43.05	32.97	0.12	0.1	0.69	1.51		4.9	0.11	12.08	0.36	4.11
Group 6		49.47		0.71	1.82	7.39	0.46	6.32	0.7	21.48	1.29	10.35
Group 9	6.04	24.95	0.31	0.25	1.72	3.41	0.93	9.74	0.42	41.97	1.6	8.67
Group 13		46.91	0.31	0.28	1.72	6.06	0.83	14.27	0.26	20.41	1.72	7.24
Group4		49.81		0.57	1.21	3.59		10.87	0.32	28.33	1.74	3.56

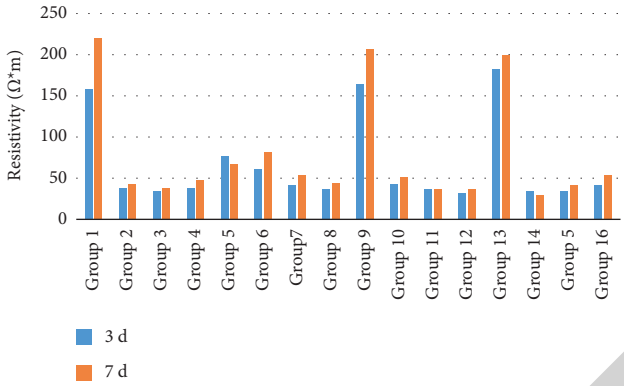

Figure 12: Resistivity.

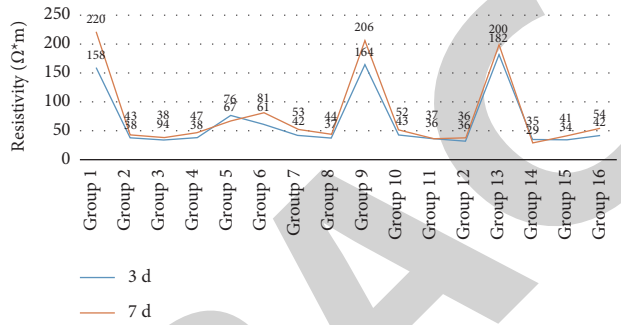

Figure 13: Change trends of the resistivity.

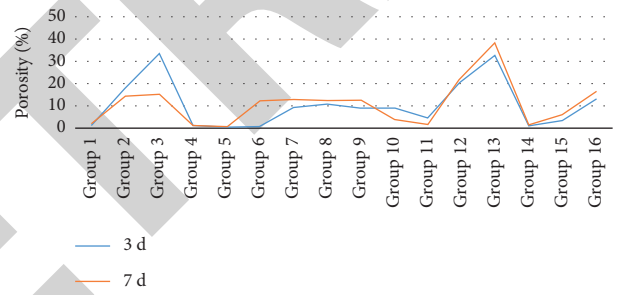

Figure 14: Change trends of the porosity.

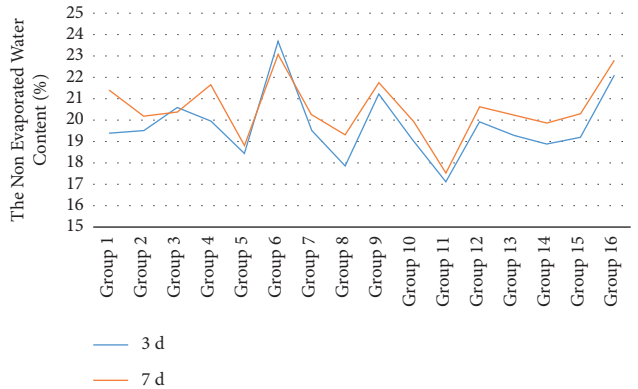

Figure 15: Change trends of the nonevaporated water content.

Table 11: Material composition.

Component	Content (%)
$CaCO_3$	46.3
$CaSO_4$	29.8
Al_2O_3	3.4
Fe_2O_3	1.1
$MgCO_3$	3.9
Phosphate	0.6
TiO_2	0.1
SiO_2	11.8
Water	3.0

Table 12: Soaking solution composition.

Component	Content(ppm)
Al	5
Ca	603
K	9
Na	19
SO42-	1222

Table 13: Statistical table of the influencing factors of the 3 d strength levels.

	Ratio of water to modified phosphogypsum powder *A*	Percentage of cement content in total amount of modified phosphogypsum and marble powder *B* (%)	Percentage of marble powder in modified phosphogypsum powder *C* (%)	Percentage of steel fiber content in phosphogypsum powder *D* (%)	Fineness of marble powder E
Primary and secondary order			*B* > *E* > *D* > *A* > C		
Optimal level	*A*2	*B*4	*C*1	*D*2	
Optimal combination			*A*2 *B*4 *C*1 *D*2*E*1		

Table 14: Statistical table of the influencing factors of the 7 d strength levels.

	Ratio of water to modified phosphogypsum powder A	Percentage of cement content in total amount of modified phosphogypsum and marble powder B (%)	Percentage of marble powder in modified phosphogypsum powder C (%)	Percentage of steel fiber content in phosphogypsum powder *D* (%)	Fineness of marble powder E
Primary and secondary order			*B* > *E* > *D* > *A* > C		
Optimal level	*A*2	*B*4	*C*1	*D*2	
Optimal combination			*A*2 *B*4 *C*1 *D*2*E*1		

Table 15: Statistical table of the influencing factors of the 3 d electrical characteristics.

	Ratio of water to modified phosphogypsum powder *A*	Percentage of cement content in total amount of modified phosphogypsum and marble powder *B* (%)	Percentage of marble powder in modified phosphogypsum powder *C* (%)	Percentage of steel fiber content in phosphogypsum powder *D* (%)	Fineness of marble powder E
Primary and secondary order			*D* > *A* > *C* > *E* > B		
Optimal level	*A*4	*B*1	*C*4	*D*1	
Optimal combination			*A*4 *B*1 *C*4 *D*1*E*2		

Table 16: Statistical table of the influencing factors of the 7 d electrical characteristics.

	Ratio of water to modified phosphogypsum powder *A*	Percentage of cement content in total amount of modified phosphogypsum and marble powder *B* (%)	Percentage of marble powder in modified phosphogypsum powder *C* (%)	Percentage of steel fiber content in phosphogypsum powder *D* (%)	Fineness of marble powder E
Primary and secondary order	$D > A > C > E > B$				
Optimal level	*A*1	*B*1	*C*4	*D*3	
Optimal combination	*A*1 *B*1 *C*4 *D*3*E*1				

Table 17: Parallel tests of the optimum ratios affecting the compressive strength levels.

	Water(W)	Cement (C)	Modified phosphogypsum (MPG)	Modified phosphogypsum powder(MPCG)	Marble powder (WMP)	Steel fiber (SF)	Sand (S)
ZA1	2700	1060	2250	2025	0	210	10350
ZA2	2700	1060	2250	2025	50	210	10350
ZA3	2700	1060	2250	2025	100	210	10350
ZA4	2700	1060	2250	2025	200	210	10350

Table 18: Strength level results of the parallel tests.

	ZA1	ZA2	ZA3	ZA4
3-day compressive strength	1.102	1.0988	1.3173	1.2175
7-day compressive strength	1.5058	1.9373	1.6037	1.915

Table 19: Resistivity test results (Ω·m).

	ZA1	ZA2	ZA3	ZA4
3d/r	32	23	38	30
7d/r	47	58	57	46

the marble powder content was 200. Resistivity tests were carried out for each ratio of the parallel tests, and the results are shown in Table 19.

Figure 16(a) shows the compressive strength of the sample and Figure 16(b) shows the resistivity of the same sample. The data change trend of Figure a and Figure b was completely similar. At the same time, according to the test results, the strength levels were high when the resistivity was high (Figures 16(a) and 16(b)). Therefore, the qualitative situation of the strength could be obtained by directly measuring the resistance, and the construction quality could be controlled for rapid detections.

6. Field Tests

The reason for testing the mechanical properties, environmental safety properties, and resistivity properties of the above material is to develop a material with environmental safety, mechanical requirements, and easy-to-use resistivity properties for on-site detection and monitoring. Section VI of this paper aims to apply this developed material for on-site detection, and the results show that this material can detect the grouting effect quickly and effectively through resistivity, thereby meeting our expected requirements.

The resistivity acquisition instrument used in this study's testing processes was a WDZJ-4 high-density electrical instrument produced by the Chongqing Geological Instrument Factory. In addition, RES2DINV software was utilized for the data processing and inversion imaging, and a least square method was used for the inversion. Due to the fact that the measurements of landslides are affected by terrain, terrain inversion was adopted in the inversion process. Then, the data were calculated according to formulas (1)–(3). In order to meet the depth of the slip section, the distance between the on-site measurement points was set as 10 m. Since the terrain of this study's soft soil reinforcement experiment was flat, a topographic survey was not carried out during inversion imaging, and the distance between the on-site measurement points was 1 m, as shown in Figures 17 and 18. We conducted field tests using proportions ZA2 and ZA3.

The expression of potential difference was calculated as follows:

$$U_M^{AB} = \frac{I\rho}{2\pi}\left(\frac{1}{AM} - \frac{1}{BM}\right) \tag{1}$$

$$\Delta U_{MN} = U_M^{AB} - U_N^{AB} = \frac{I\rho}{2\pi}\left(\frac{1}{AM} - \frac{1}{BM} - \frac{1}{AN} + \frac{1}{BN}\right) \tag{2}$$

The calculation formula of resistivity was performed as follows:

$$\rho = K\frac{\Delta U_{MN}}{I} \tag{3}$$

6.1. Field Test No. 1. The test results of the landslide after the disaster treatment point are shown in Figure 19. As can be seen in the figure, the landslide was caused by the tensile fracturing of the red bed rock trailing edge as a result of continuous rainfall. In accordance with the previously mentioned testing results, grouting materials were prepared,

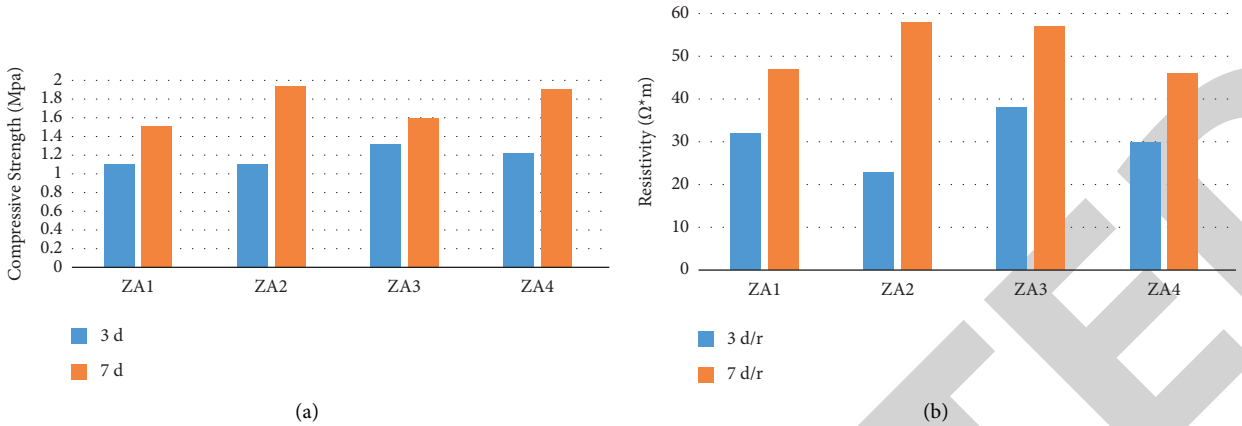

Figure 16: Comparison of strength level results.

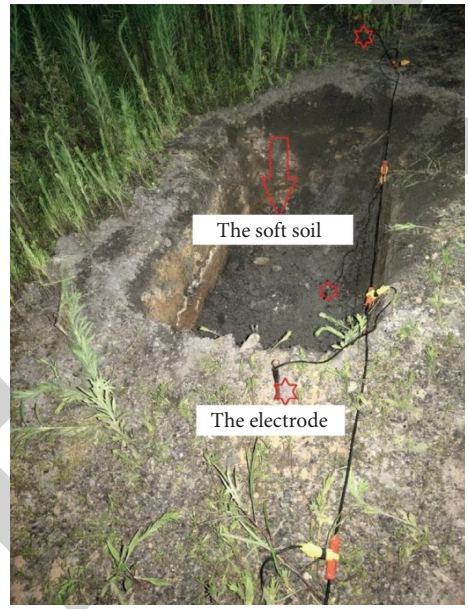

Figure 17: Experimental site images.

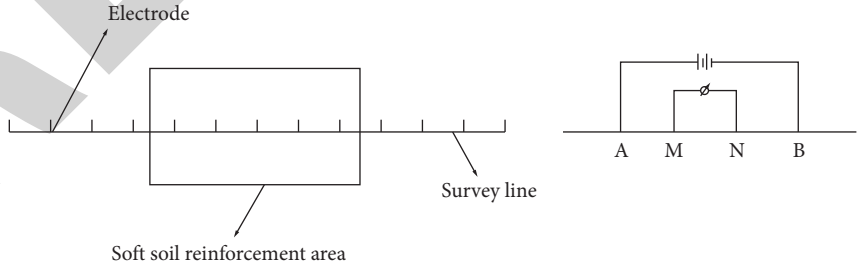

Figure 18: Schematic diagram of the experimental site.

and the strength design met the requirements of the engineering reinforcements. In addition, the electrical characteristics were taken as the detection factors of reinforcement effects. Prior to the grouting process, the rear edge of the slope body was filled with water due to rainfall and the development of cracks, which exhibited the characteristics of anomaly low resistance (indicated position before grouting). High resistance mortar was prepared according to the previously mentioned experiments and was tested three days after grouting. The original low resistance abnormal area showed high resistance anomaly (indicated position after grouting), and the resistivity of the surrounding rock was

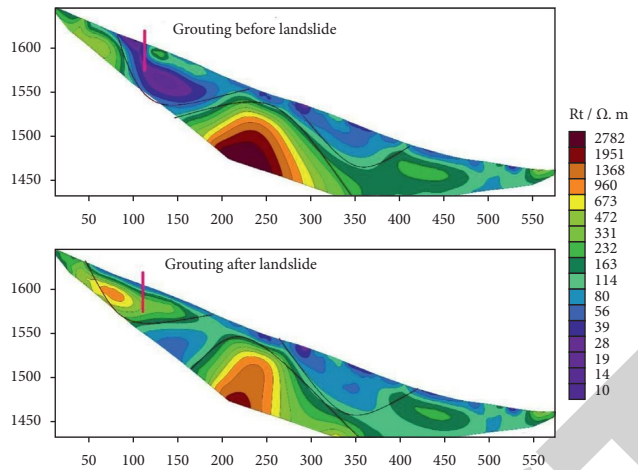

Figure 19: Experimental results of the grouting reinforcement treatment of a landslide area.

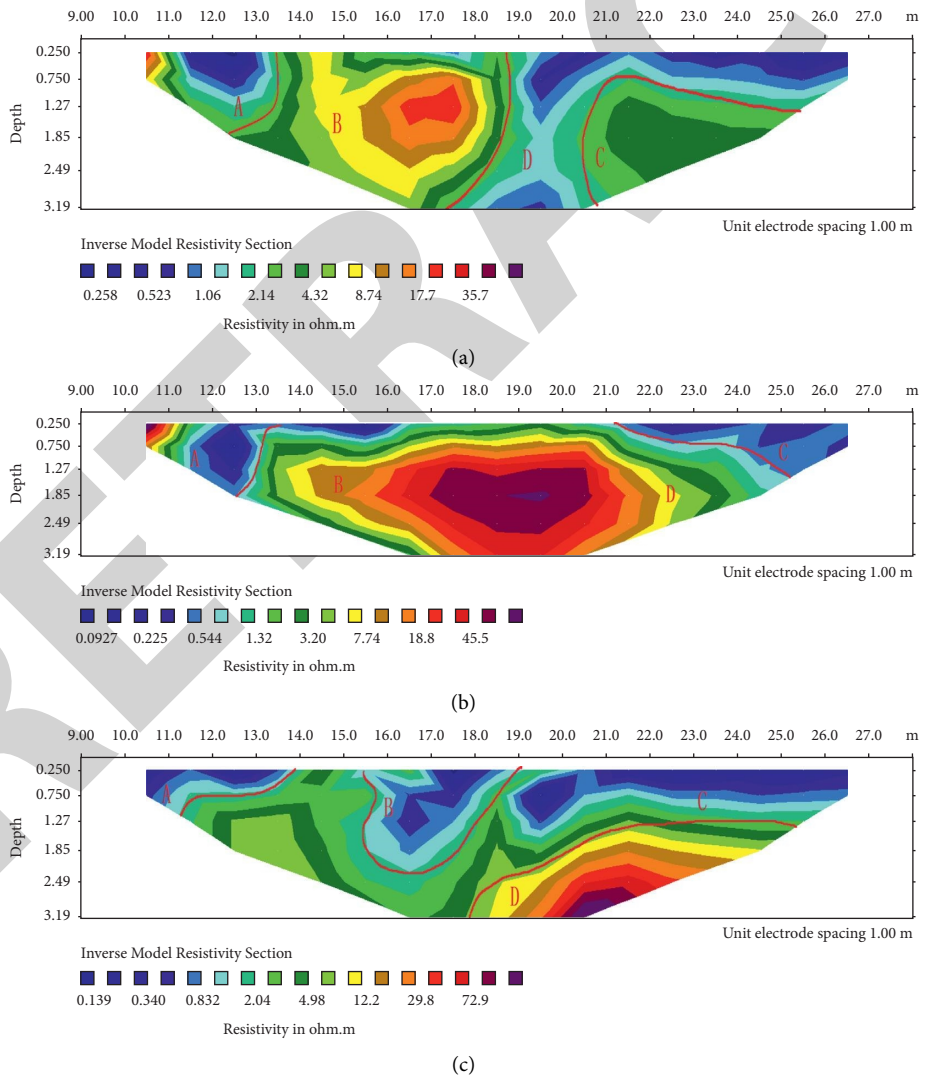

Figure 20: Soft soil reinforcement experiment: (a) electrical structure information of undisturbed stratum, (b) electrical structure information when half of the mortar is filled, and (c) formation electrical structure information after filling.

significantly increased. Therefore, the results indicated that the mortar also penetrated into the surrounding rock by filling the cracks, a good overall reinforcement of the landslide site had been formed. In summary, this field test confirmed that it was feasible to use materials with electromagnetic characteristics as the quality inspection and detection for grouting engineering.

6.2. Field Test No. 2. This study used the ZA2 ratios to prepare grouting material for the second field test. It can be seen in Figure 20(a) that ZA2 is selected, as its strength is moderate and quite representative. The resistivity of the undisturbed formation was abnormal and the structure was stable. The high resistivity anomaly at Point B was inferred to be an accumulation layer of landfill macroporous slag soil. Points *D* and C were determined to be the relatively low resistivity anomalies since the soil stratum had been affected by rainfall. Figure 20(b) shows the measurement results during the process of pouring grouting material ZA2 underground. Affected by manual excavation, Points C and *D* showed high resistance anomalies and symmetrical distributions, which indicated that the measurement results during the filling process were affected not only by the differences between the electrical properties of the grouting materials and surrounding rock but also by the surface shallow excavation process. Figure 20(c) shows that the measurement results after the slurry was fully filled. As can be seen in the figure, the original high resistance anomaly at Point B had disappeared, indicating that the injected slurry was basically filled. A small area of a high resistivity anomaly can be seen in the lower right corner, which may have been due to large fractures or high resistivity bodies in that area.

Through field experiments, it can be seen that the grouting materials based on mineral admixtures can be effectively applied to the ecological environment fields, such as geological disaster prevention and soft soil reinforcement. By altering the ratio of grouting materials and measuring the change of resistivity, the dynamic monitoring of grouting process and the evaluation of grouting effect can be realized.

7. Conclusions and Further Research Ideas

According to the previously mentioned test results, the following conclusions were drawn. (1) The resistivity was determined to be related to the proportions of water to modified phosphogypsum; percentages of cement content in the total amount of modified phosphogypsum and marble powder; percentages of marble powder in the modified phosphogypsum; percentages of steel fiber content in the phosphogypsum; and the fineness of the marble powder. Among these, the proportions of steel fiber content in the phosphogypsum were determined to be the most important factor. This was followed by the proportions of water to modified phosphogypsum; proportions of marble powder in the modified phosphogypsum; fineness of the marble powder; and the proportions of cement content in the total amount of modified phosphogypsum and marble powder. (2) According to this study's test results, the influencing factors of the resistivity and strength levels were not the same. However, the changing trend of strength and resistivity of the 3 d and 7 d samples were found to be consistent and could be used for early monitoring and detection of grouting material construction effects. (3) The component test results of the material and its soaking solution indicate that this material is a green material, which meets environmental safety standards. (4) The field test results show that the materials studied in the experiment can be used as grouting materials, and the proportion of materials can be adjusted according to the geological environmental conditions to achieve the dynamic monitoring of the grouting process and the evaluation of the effect. In the future, we will further verify the monitoring and detection advantages of grouting materials based on electromagnetic characteristics in the fields of disaster control and ecological restoration. Therefore, it was considered that the results obtained in this investigation will provide an important basis for further theoretical research and production practices.

Data Availability

The data used to support the findings of this study are included within the article.

Conflicts of Interest

The authors declare that they have no conflicts of interest.

Acknowledgments

Thanks are due to Suzhou Niumag Analytical Instrument Corporation's help in NMR Experiment and analysis. This project was supported by Key R & D project of Sichuan Science and Technology plan under grant nos. 2020YFS0472 and 2019ZYZF0065.

References

[1] H. Jin, "Late-age properties of concrete with different binders cured under 45°C at early ages," *Advances in Materials Science and Engineering*, vol. 2017, Article ID 8425718, 13 pages, 2017.

[2] H. Jin, "Comparison between the effects of superfine steel slag and superfine phosphorus slag on the long-term performances and durability of concrete," *Journal of Thermal Analysis and Calorimetry*, vol. 128, no. 10, pp. 1251–1263, 2017.

[3] H. Jin, Y. Yulei, R. Xiaojiang, Y. Kui, and L. Changkun, "Application progress of phosphorus slag in green concrete," *Commercial concrete*, vol. 5, no. 3, pp. 79–81, 2015.

[4] R. Alaie, R. Jamshidi Chenari, and M. Karimpour-Fard, "Shaking table study on sand-EPS beads-mixtures using a laminar box," *Geosynthetics International*, vol. 28, no. 3, pp. 224–237, 2021.

[5] J. G. Zornberg and G. H. Roodi, "Use of geosynthetics to mitigate problems associated with expansive clay subgrades," *Geosynthetics International*, vol. 28, no. 3, pp. 279–302, 2021.

[6] J. Zhang, Z. Yang, Q. Yang, G. Yang, G. Li, and J. Liu, "Liquefaction behavior of fiber-reinforced sand based on cyclic triaxial tests," *Geosynthetics International*, vol. 28, no. 3, pp. 316–326, 2021.

[7] S. H. Liu, J. Liao, and K. W. Fan, "Repeated loading of soilbag-reinforced road subgrade," *Geosynthetics International*, vol. 28, no. 2, pp. 113–124, 2021.

[8] H. J. Kim, T. W. Park, P. R. Dinoy, and H. S. Kim, "Performance and design of modified geotextile tubes during filling and consolidation," *Geosynthetics International*, vol. 28, no. 2, pp. 125–143, 2021.

[9] C. Lv, C. Zhu, C.-S. Tang, Q. Cheng, L.-Y. Yin, and B. Shi, "Effect of fiber reinforcement on the mechanical behavior of bio-cemented sand," *Geosynthetics International*, vol. 28, no. 2, pp. 195–205, 2021.

[10] L. Zhe, W. Yan-Qing, and Z. Jian-Shan, "Mathematical model of high pressure injection cement liquid and its application," *Rock and Soil Mechanics*, vol. 26, no. 12, pp. 1972–1976, 2005.

[11] H. Hong-Yuan and R. Yao, "Analysis of driving water permeation grouting of saturated sand seam," *Rock and Soil Mechanics*, vol. 30, no. 7, pp. 2016–2020, 2009.

[12] Y. Ping, T. Yi-Qun, P. Zhen-Bin, and A. Chen, "Study on grouting simulating experiment in sandy gravels," *Chinese Journal of Geotechnical Engineering*, vol. 28, no. 12, pp. 2134–2138, 2006.

[13] S. Hui, W. Zai-Quan, and W. Jing-Jie, "Test study on seepage permeability of limestone grouting wall system," *Chinese Journal of Underground Space and Engineering*, vol. 5, no. 5, pp. 956–959, 2009.

[14] Z. Gai-Ling, Z. Kai-Yu, and S. Wang-Hua, "Experimental investigation of the impact of flow velocity on grout propagation during chemical grouting into a fracture with flowing water," *Journal of China Coal Society*, vol. 36, no. 3, pp. 403–406, 2011.

[15] M.-Q. Zhang, W.-Q. Zhang, and G.-Q. S, "Evaluation technique of grouting effect and its application to engineering," *Chinese Journal of Rock Mechanics and Engineering*, vol. 25, no. S2, pp. 3109–3118, 2006.

[16] Z. Ping-Song, W. Jian-Sheng, and L. Sheng-Dong, "Prospecting possibility with high density resistivity for quality of concrete behind segment in tunnel," *Chinese Journal of Underground Space and Engineering*, vol. 4, no. 2, pp. 331–335, 2008.

[17] P. Hu, G.-R. Zhu, and Q.-R. Wang, "Application of high density electrical resistivity method in the monitoring survey of high pressure jet-grouting project," *Geological Journal of China Universities*, vol. 16, no. 3, pp. 375–382, 2010.

[18] S. H. Adnan, R. Hamdan, and N. A. Roni, "Removal of phosphorus from synthetic wastewater using recycled concrete aggregates as a filter medium," *Journal of civil engineering, science and technology*, vol. 9, no. 1, pp. 13–26, 2018.

[19] L. Sang, T. Idowu, and V. Okumu, "Evaluation of the performance of waste marble dust as a mineral filler in hot-mix asphalt concrete," *Journal of Civil Engineering, Science and Technology*, vol. 12, no. 1, pp. 1–14, 2021.

[20] M. B. Hossain, M. Roknuzzaman, M. A. Biswas, and M. Islam, "Evaluation of engineering properties of thermal power plant waste for subgrade treatment," *Journal of Civil Engineering, Science and Technology*, vol. 12, no. 2, pp. 112–123, 2021.

[21] J. R. Adewumi, T. F. Ajibade, and F. O. Ajibade, "Appraisal of on-site sanitation facilities and solid waste management in public places within akure municipality, Nigeria," *Journal of Civil Engineering, Science and Technology*, vol. 11, no. 1, pp. 8–21, 2020.

[22] C. Z. Kam and A. B. H. Kueh, "Towards sustainable polymeric materials: zero waste, green and self-healing," *Jurnal Teknologi*, vol. 74, no. 4, 2015.

[23] H. Xin, *Study on Grouting Effect Detection of Goaf under Subgrade of New Dongdu-Pingyi Railway*, Southwest Jiaotong University, Chengdu, China, 2013.

[24] C. Zilong, *Model Test Study on Detecting Grouting Effect of Karst Subgrade by High Density Electrical Method*, Southwest Jiaotong University, Chengdu, China, 2014.

[25] Z. Xuan, *Study on Grouting Treatment Effect of Comprehensive Geophysical Detection Method in Goaf of Nanqin Line*, Southwest Jiaotong University, Chengdu, China, 2014.

[26] L. Xueliang, L. Shuzhi, and H. Jinbo, "Application of EH-4 conductivity imaging system in detection of grouting effects in goaf area," *Safety In Coal Mines*, vol. 43, no. 11, pp. 139–142, 2012.

[27] F. A. I. Hamdi and G. Morelli, "Application of cross-hole resistivity tomography in the detection of underground cavities and weak zones," in *Proceedings of the Near Surface Geoscience 2012–18th European Meeting of Environmental and Engineering Geophysics*, Paris, France, September 2012.

[28] T. P. Rupesh and S. P. Sharma, "High-resolution quasi-3D electric resistivity tomography for deciphering groundwater potential zones in lateritic terrain," *Natural Resources Research*, vol. 30, pp. 3339–3353, 2021.

[29] D. Yu, F. Guangming, and W. Chengzhen, "Experimental research on basic properties of superhigh-water packing material," *Journal of China Coal Society*, vol. 36, no. 7, pp. 1087–1092, 2011.

[30] F. Guangming, J. Kaijun, and S. Baobao, "Application and prospect of super-high-water packing material in mining engineering," *Coal Science and Technology*, vol. 43, no. 1, pp. 5–9, 2015.

[31] G.-B. Zhang, J.-L. Liu, and M. Aubert, "Interpretation of self-potential anomalies in hydrogeological exploration of volcanic areas," *Earth Science - Journal of China University of Geosciences*, vol. 21, no. 3, pp. 109–116, 1996.

[32] S.-C. Liu, X.-M. Liu, Z.-H. Jiang, T. Xing, and M. Chen, "Research on electrical prediction for evaluating water conducting fracture zones in coal seam floor," *Chinese Journal of Rock Mechanics and Engineering*, vol. 28, no. 2, pp. 348–356, 2009.

[33] L. Sheng-Dong, W. Bo, Z. Guan-Qun, S. Yang, and M. Chen, "Experimental research on mine floor water hazard early warning based on response of geoelectric field in groundwater seepage," *Chinese Journal of Rock Mechanics and Engineering*, vol. 28, no. 2, pp. 267–272, 2009.

[34] Z. Can-Tang, "The technique to detect the leakage of dam by applying the spontaneous electric field," *Progress in Geophysics*, vol. 20, no. 3, pp. 854–858, 2005.

[35] H. Zhe, W. Jieqiang, and L. Bin, "Theoretical study of osmotic grou-ting in rock mass," *Chinese Journal of Rock Mechanics and EngiNeering*, vol. 20, no. 4, pp. 492–496, 2001.

[36] L. Zhe, W. Yanqing, and Z. Jianshan, "Mathematical model of high pressure injection cement liquid and its application," *Rock and Soil Mechanics*, vol. 26, no. 12, pp. 1972–1976, 2005.

[37] Z. Minqing, Z. Wenqiang, and S. Guoqing, "Evaluation technique of grouting effect and its application to engineering," *Chinese Journal of Rock Mechanics and Engineering*, vol. 25, no. S2, pp. 3109–3118, 2006.

Hindawi
Advances in Civil Engineering
Volume 2023, Article ID 9898510, 1 page
https://doi.org/10.1155/2023/9898510

Retraction

Retracted: Energy Evolution Characteristics and Performance Parameter Degradation of Rubber-Mixed Concrete in Sulfate Attack Environment

Advances in Civil Engineering

Received 10 October 2023; Accepted 10 October 2023; Published 11 October 2023

This article has been retracted by Hindawi following an investigation undertaken by the publisher [1]. This investigation has uncovered evidence of one or more of the following indicators of systematic manipulation of the publication process:

(1) Discrepancies in scope
(2) Discrepancies in the description of the research reported
(3) Discrepancies between the availability of data and the research described
(4) Inappropriate citations
(5) Incoherent, meaningless and/or irrelevant content included in the article
(6) Peer-review manipulation

The presence of these indicators undermines our confidence in the integrity of the article's content and we cannot, therefore, vouch for its reliability. Please note that this notice is intended solely to alert readers that the content of this article is unreliable. We have not investigated whether authors were aware of or involved in the systematic manipulation of the publication process.

Wiley and Hindawi regrets that the usual quality checks did not identify these issues before publication and have since put additional measures in place to safeguard research integrity.

We wish to credit our own Research Integrity and Research Publishing teams and anonymous and named external researchers and research integrity experts for contributing to this investigation.

The corresponding author, as the representative of all authors, has been given the opportunity to register their agreement or disagreement to this retraction. We have kept a record of any response received.

References

[1] X. Chen, "Energy Evolution Characteristics and Performance Parameter Degradation of Rubber-Mixed Concrete in Sulfate Attack Environment," *Advances in Civil Engineering*, vol. 2022, Article ID 5692655, 10 pages, 2022.

Hindawi
Advances in Civil Engineering
Volume 2022, Article ID 5692655, 10 pages
https://doi.org/10.1155/2022/5692655

Research Article

Energy Evolution Characteristics and Performance Parameter Degradation of Rubber-Mixed Concrete in Sulfate Attack Environment

Xiu-ling Chen

School of Architectural Engineering, Ma'anshan University, Ma'anshan 243000, China

Correspondence should be addressed to Xiu-ling Chen; chenxl_1990@126.com

Received 21 December 2021; Revised 12 January 2022; Accepted 13 January 2022; Published 30 January 2022

Academic Editor: Ramadhansyah Putra Jaya

In order to study the sulfate resistance of rubber concrete (RC), the compressive strength test of RC with different contents (0%, 5%, 10%, and 15%) was carried out, and the proportion of RC with standard curing for 28 days was optimized. Sulfate attack test was carried out on the selected RC and compared with normal concrete (NC). The degradation degree was measured from the effective porosity, relative dynamic elastic modulus, SO_4^{2-} concentration, and SEM microstructure observation after different attack times. The energy analysis method is used to study the evolution law of total strain energy, elastic strain energy, and dissipated strain energy of NC and RC in the process of deformation and failure after different attack times, and the influence of sulfate attack on concrete is explored from the perspective of energy. The results show that with the progress of sulfate attack, the effective porosity of NC and RC both decreases first and then increases, and the relative dynamic elastic modulus increases first and then decreases. Rubber is beneficial to improve the sulfate resistance of concrete, delay the attack of SO_4^{2-} on concrete, and improve the ductile deformation of concrete. This study can provide a theoretical reference for the application of RC in practical engineering.

1. Introduction

As the most widely used and most basic building material, concrete is increasingly applied into the fields of civil engineering, transportation, water conservancy and hydropower, etc. Its durability has become a key engineering issue and has received widespread attention [1, 2]. Among them, sulfate erosion is one of the important factors. Essentially, sulfate ions react with cement hydrates to produce expansions that result in concrete damage and destruction, which affects the durability of concrete and reduces the strength of concrete. There are high concentrations of sulfate ions in the saline soil environment, and the long-term sulfate erosion of concrete reduces the structural safety of concrete and also shortens the service life [3, 4].

Currently, many scholars have done researches on the reduction of concrete durability caused by sulfate attack. Wang et al. [5] conducted an experimental study on the law and mechanism of concrete durability degradation, whose results showed that the durability damage of sulfate attack on concrete was much greater than compound salt attack. Wu et al. [6] carried out researches on the durability of concrete under sulfate erosion environment based on the theory of damage mechanics and found that with the increase of erosion time, the coexpansion of ettringite and gypsum caused microcracks and the number continued to increase. Wang et al. [7] studied the changing characteristics of concrete pore structure under sulfate attack and analyzed the microstructure and mineralogical composition. Jin et al. [8] conducted an experimental study on the damage process of concrete in a sulfate attack environment, and the results showed that sulfate attack caused the expansion of concrete and formed a large number of cracks, which deteriorated the performance of concrete. Zhao et al. [9] studied the acoustic emission and physical and mechanical properties of concrete under the two sulfate erosion conditions of continuous

soaking and dry-wet cycle. They found that the dry-wet cycle accelerated the deterioration of concrete. The pores inside the concrete increased the strength of the concrete to a certain extent.

In order to improve the resistance of concrete to sulfate corrosion and extend the service life of the building, Sharma and Khan [10] used copper slag to replace parts of the fine aggregate in concrete to study the sulfate corrosion resistance and found that the copper slag replaces 40% of the fine aggregate, which was beneficial to improve the compressive strength of concrete and the resistance to sulfate attack. Wang et al. [11] studied the performance degradation of basalt fiber concrete under sulfate erosion environment and found that basalt fiber had a certain increase in the bearing capacity and deformation capacity of concrete and could delay the increase of concrete porosity. Lv et al. [12] studied the sulfate corrosion resistance and mechanism of silica fume-reinforced cement mortar. Vishwakarma et al. [13] separately incorporated fly ash and nano-TiO_2 into concrete to compare and analyze the sulfate erosion resistance and found that the fly ash concrete had better sulfate erosion resistance.

With the rapid development of the global economy, the rapid growth of annual automobile sales has caused a sharp increase in the amount of discarded rubber tires each year. As discarded tires are solid wastes that are not easily degradable, they have caused serious pollution [14, 15]. Studies have shown [16–18]: substituting rubber particles for part of the fine aggregate in concrete can not only solve the environmental pollution caused by discarded tires and save resources, but also make the concrete have good toughness, excellent impermeability, and antipermeability, together with good freezing performance and high ductility. Strukar et al. [19] conducted a uniaxial compression test on RC to explore the influence of rubber content on the mechanical behavior of concrete, conducted a comprehensive study on its stress-strain curve, and found that rubber could enhance the ductility of concrete. Ridgley et al. [20] used acoustic emission technology to study the abrasion resistance of NC and RC, and found that the quality loss and wear depth of RC were significantly lower than that of NC. Zhang et al. [21] studied the effect of rubber on the frost resistance of concrete and found that rubber could effectively reduce the damage of concrete in a freeze-thaw cycle environment and improve its freeze-thaw cycle resistance. Alwesabi et al. [22] found that rubber can enhance the fracture toughness of concrete.

In this paper, rubber is mixed into concrete, and the rubber dosage is optimized to carry out the sulfate corrosion test and use NC as a reference, and reveals the law of rubber to improve the sulfate corrosion resistance of concrete, providing theoretical support for related engineering practice.

2. Experiment

2.1. Raw Materials. The raw materials are as follows—cement: P·O 42.5 grade ordinary Portland cement; stone: continuous graded crushed stones with particle sizes of 5~15 mm; sand: medium sand with a fineness modulus of 2.55; rubber: particle sizes of 1~3 mm with a density of 1050 kg/m^3; sulfate: analytically pure AR-type anhydrous sodium sulfate; water reducing agent: HPWR-type high-performance water reducing agent; and water: tap water.

2.2. Design of Mix Proportion. The purpose of the experimental design in this paper is to reveal the degradation law of RC performance under sulfate attack. According to the National Standard of the People's Republic of China GB/T 50082-2009 *Standard for Test Methods of Long-term Performance and Durability of Ordinary Concrete*, the sulfate solution concentration is selected as 5%. Referring to the National Standard of the People's Republic of China JGJ 55-2011 *Specification for Mix Proportion Design of Ordinary Concrete,* the design of the concrete mix proportion was carried out. In this experiment, the rubber contents are 0%, 5%, 10%, and 15% of the sands quality, respectively. The specific mix proportions are listed in Table 1.

According to the relevant provisions of the National Standard of the People's Republic of China GB/T 50081-2019 *Standard for Test Methods of Concrete Physical and Mechanical Properties*, CSS-YAN 3000 press is used for compressive strength test, and the test results are shown in Figure 1. It can be summarized that with the increase of rubber content, the compressive strength of concrete increases first and then decreases. When the rubber content is less than 10%, the strength of rubber concrete is improved, compared with that of NC. But with the further increase of rubber content, the concrete strength begins to decrease. When the rubber content is 10%, the strength growth rate is the largest, and compared with NC, it is increased by 22.20%. It can be seen from Figure 1(b) that the stress-strain curves of NC and RC are similar on the whole. With the increase of rubber content, the stress-strain curve's rising speed is more rapid than that of NC, and the decline rate of the curve after the peak stress decreases, which shows that the addition of rubber into concrete is conducive to improving the ductility and deformation of concrete. This is mainly because rubber improves the gradation of sands, enhances the adhesion between cement and sands, and improves the workability of concrete. However, too much rubber will reduce the cement hydration reaction of concrete, and the amount of sands will be greatly reduced, resulting in the decrease of strength, which is consistent with relevant studies [23].

2.3. Sulfate Erosion Experiment Schemes. In the sulfate erosion test, the RC content is 10%, that is, the mix proportion of RC_2 group. The size of the concrete specimen is 100 mm × 100 mm × 100 mm, which has been cured for 28 days at a relative humidity of 95% or so under a temperature zone from 18°C to 22°C. With the concentration of the sulfate solution being 5%, the experiment is carried out to test the performance degradation process of RC in a sulfate erosion environment and compare it with NC by following alternating dry and wet methods. The specific operation process is in accordance with the National Standard of the People's Republic of China GB/T 50082-2009 *Standard for Test Methods of Long-term Performance and Durability of*

Table 1: Mix proportion (kg/m^3).

Specimen	Cement	Stone	Sand	Rubber	Water	Water reducing agent
NC	425	1185	650	0	195	5.25
RC_1	425	1185	617.5	32.5	195	5.25
RC_2	425	1185	585	65	195	5.25
RC_3	425	1185	552.5	97.5	195	5.25

Ordinary Concrete. The drying temperature was 85°C, and the alternating time was 72 hours. The dry and wet ratio was 3 : 1, and the number of dry and wet alternates was set to 15 times, 30 times, 45 times, 60 times, 75 times, and 90 times, respectively. In view of the fact that SO_4^{2-} will react with the calcium silicate hydrate in the concrete during the erosion process, the SO_4^{2-} of the erosion solution will decrease. Therefore, the sulfate solution was changed every 30 days.

After reaching the predetermined number of dry and wet alternations, the saturated mass and dry mass of the test piece were weighed to calculate the effective porosity of the test piece. The calculation formula shall be carried out according to formula (1); the HC-U81 nonmetal ultrasonic detector was applied to detect the ultrasonic sound of the test piece at each predetermined number of dry and wet alternations. When calculating the relative dynamic elastic modulus of the test piece, Equation (2) was carried out.

$$w = \frac{m_s - m_d}{m_d}, \tag{1}$$

where w is the effective porosity; m_s is the saturated mass (kg); and m_d is the dried mass (kg).

$$E = \left(\frac{T_0}{T_t}\right)^2, \tag{2}$$

where E is the relative dynamic modulus of elasticity; T_0 is the uncorroded ultrasonic duration (s); and T_t is the ultrasonic duration (s) when eroded t times.

2.4. Principle of Energy Conversion. Energy conversion is the essential feature of the physical process of matter. The deformation and failure process of concrete under load is essentially the process of energy evolution inside concrete and energy exchange with the outside world. With the continuous action of the load, the energy input from the outside is gradually transformed into elastic strain energy, dissipation energy, electromagnetic energy, radiation energy, and so on of concrete. Since the proportion of electromagnetic energy and radiant energy is very small under static action, the main energy conversion relationship of concrete under load is seen in

$$U = U_e + U_d, \tag{3}$$

where U is the total strain energy per unit volume; U_e is the elastic strain energy per unit volume; and U_d is the dissipated strain energy per unit volume.

According to the stress-strain relationship, the total strain energy and elastic strain energy input by external force of concrete specimen per unit volume are seen in.

$$U = \int \sigma d\varepsilon, \tag{4}$$

$$U_e = \frac{\sigma^2}{2E}, \tag{5}$$

where σ is the axial stress; ε is the axial strain; and E is the initial elastic modulus.

Therefore, the dissipated strain energy per unit volume is

$$U_d = U - U_e. \tag{6}$$

It should be pointed out that the initial defects inside the specimen have been closed to a certain extent because the concrete specimen has been repeated preloading and unloading before formal loading. Therefore, E is taken as the slope of the straight line between 10% and 30 of the peak stress at the initial stage of the stress-strain curve of the specimen.

3. Experimental Results and Analysis

3.1. Stress-Strain Curve. The stress-strain curves of NC and RC in the sulfate attack environment are shown in Figure 2. It can be seen that with the progress of sulfate erosion, the stress-strain curves of NC and RC have undergone significant changes, but on the whole, the changes of NC are more obvious; as the dry-wet cycles' times increase, the stress-strain curve moves toward the right direction that deviates from the Y-axis. The stress and strain peaks of NC and RC increase first and then decrease as a whole, and the stress peak of RC increases rapidly in the early stage of erosion and then the speed being slower. The deformation of RC in the linear elastic stage is lighter. After 30 times' dry-wet cycles, the peak stress of NC came to the biggest. Compared with the uneroded specimen, the peak stress increases by 7.24%. After 60 times' dry-wet cycles, the peak stress of RC is the largest. Compared with the uneroded specimen, the peak stress increases by 11.66%. After 90 times' dry-wet cycles, the stress and strain peaks of NC and RC decrease at the same time in different levels. Compared with the uneroded specimen, the peak stress of NC and RC decreases by 28.04% and 8.6%, respectively.

The change rules of compressive strength with sulfate erosion are shown in Figure 3. Based on Figure 3, it can be seen that at the same sulfate attack time, the compressive strength of RC is greater than that of NC. As the erosion progresses, the compressive strength of RC is comparable to that of the predetermined number of dry-wet cycles. Compared with NC, it increased by 22.20%, 21.88%, 22.66%, 38.84%, 52.48%, 48.50%, and 55.19%, respectively. It can be seen that in the environment of sulfate erosion, rubber is beneficial to increase the compressive strength of concrete, improve the deterioration performance of concrete, and enhance the sulfate erosion resistance. The longer the erosion time is, the more obvious the effects are.

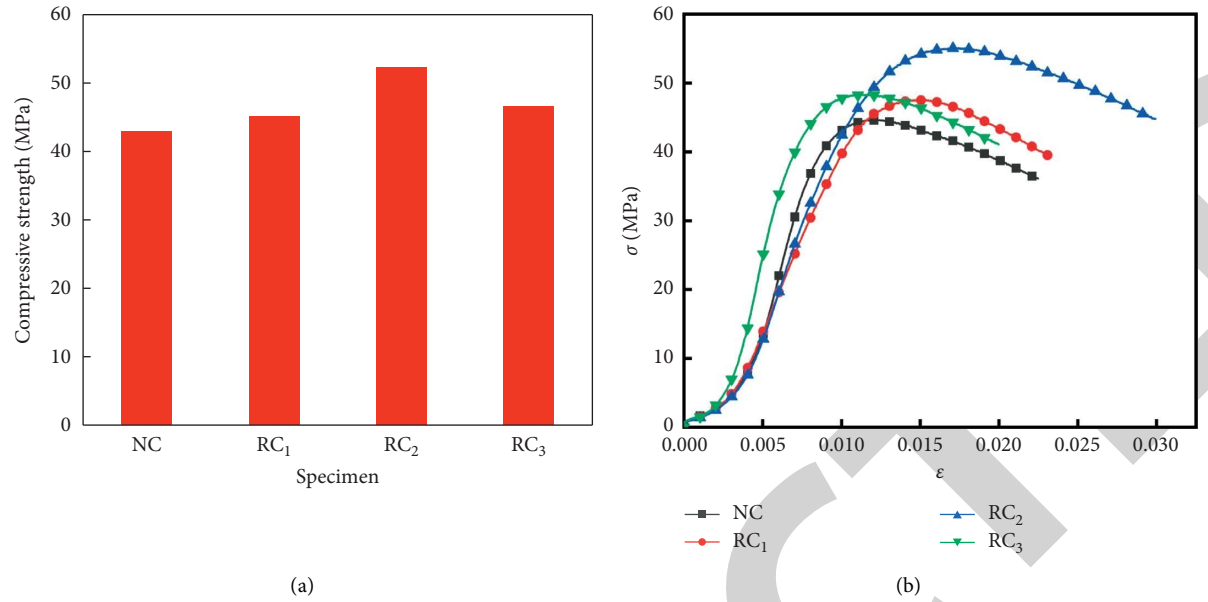

Figure 1: Test results. (a) Compressive strength. (b) Stress-strain curves.

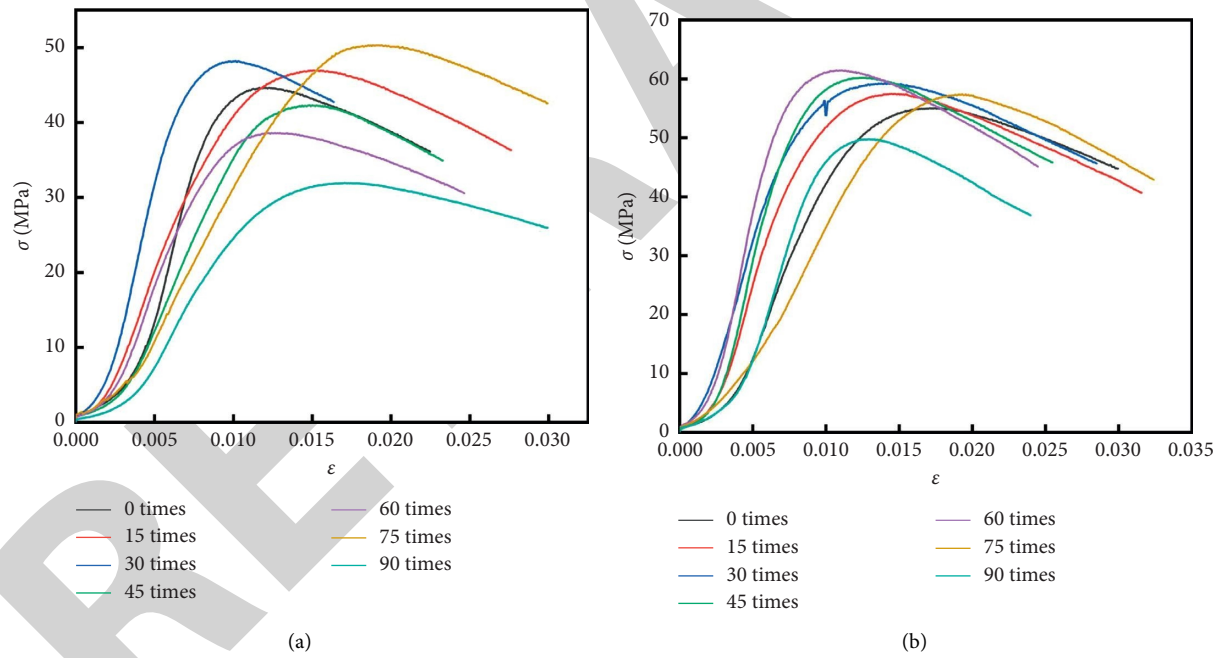

Figure 2: Stress-strain curve. (a) NC. (b) RC.

If it is assumed that the change in compressive strength with sulfate erosion is continuous, the following formula, as shown in equation (7), could be set up under the guidance of the least square method [24].

$$f = a + bt + ct^2, \tag{7}$$

where f is the compressive strength; a, b, and c are fitting parameters; and t is the number of dry-wet cycles. The fitting result is shown in Figure 4. The strength damage evolution equation is shown as follows:

$$\begin{aligned} f_{cn} &= 43.54 + 0.08296t - 0.00261t^2 \left(R^2 = 0.92\right), \\ f_{cr} &= 51.38 + 0.31714t - 0.00383t^2 \left(R^2 = 0.86\right), \end{aligned} \tag{8}$$

where f_{cn} and f_{cr}, respectively, represent the compressive strength of NC and the compressive strength of RC.

3.2. Energy Evolution. Figure 5 shows the evolution of the total strain energy of NC and RC in a sulfate attack environment. Figure 6 shows the evolution of the dissipated

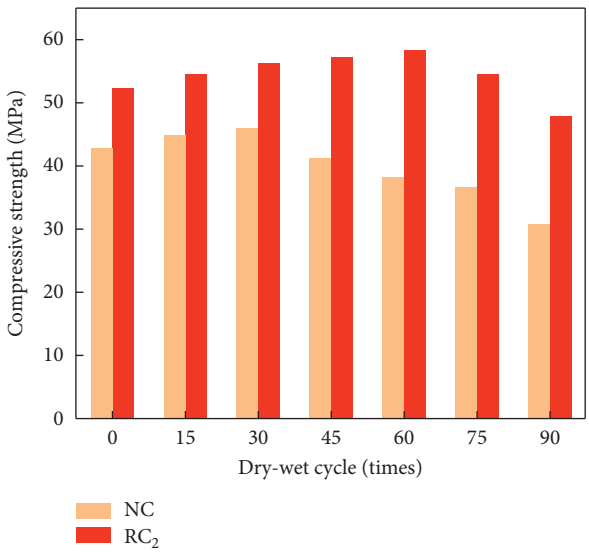

Figure 3: Compressive strength.

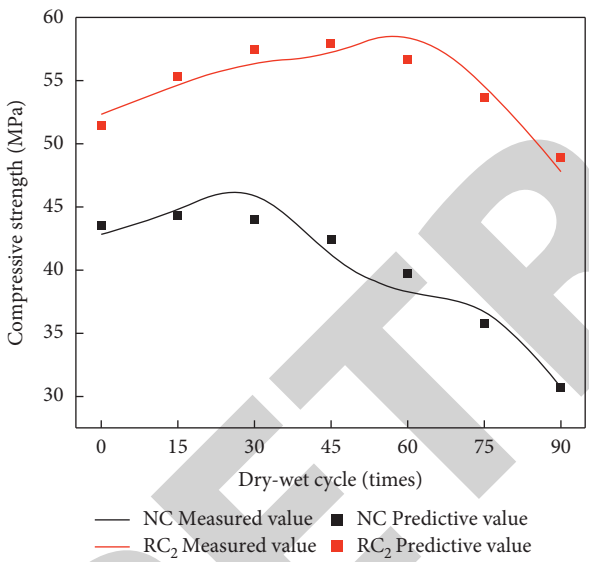

Figure 4: Compressive strength damage evolution fitting curve.

strain energy of NC and RC in the sulfate erosion environment. It can be seen from Figures 5 and 6 that the total strain energy and dissipation strain energy of NC and RC increase firstly and then decrease. Under the same number of dry-wet cycles, the total strain energy and dissipated strain energy of RC are greater than that of NC. In the early stage of erosion, the growth rate of total strain energy and dissipated strain energy of RC is greater than that of NC. In the later stage of erosion, the rate of decrease of total strain energy and dissipated strain energy of RC is lower than that of NC. With the increase in deformation, the incorporation of rubber into concrete can obviously speed up the rate of total strain energy and dissipated strain energy. When the specimen finally fails, the total strain energy of RC is increased by 41.21%, 52.36%, 60.64%, 68.39%, 69.80%, 22.85%, and 17.84%, respectively, compared with NC under the same number of dry-wet cycles. Bulk strain energy is increased by 37.98%, 43.72%, 49.79%, 54.28%, 60.34%, 33.39%, and 22.15%, respectively.

Figure 7 shows the evolution law of elastic strain energy of NC and RC in a sulfate attack environment. It can be seen that the change law of rubber to concrete elastic strain energy is similar to the total strain energy and dissipation energy. At the same predetermined number of dry-wet cycles, the elastic strain energy of NC decreases faster than RC as a whole when reaching its peak value, showing more obvious brittle failure, while RC shows more obvious ductile failure. This is mainly because rubber improves the gradation of sands, which can inhibit coupling, crack penetration speed and propagation speed, and improve the toughness and failure characteristics of concrete [25].

3.3. Deterioration of Performance Parameters. In order to deeply explore the internal damage of NC and RC by sulfate, the effective porosity and relative dynamic elastic modulus of concrete are used as performance parameters. The effective porosity and relative dynamic elastic modulus changes are shown in Figures 8 and 9.

It can be seen from Figure 8 that both NC and RC show a trend of first decreasing and then increasing with the progress of sulfate erosion. This is related to the above-mentioned compressive strength test; that is, as the effective porosity of concrete decreases, the interior of the concrete is dense. The higher the degree, the higher the intensity is. For NC, the effective porosity is the lowest when the dry-wet cycles being 45 times, and the lowest effective porosity of RC appears when the dry-wet cycles being 60 times; the effective porosity of NC is basically lower than that of RC, which shows that in sulfuric acid in a salt-eroded environment, the internal porosity of NC increases, while RC optimizes the particle gradation of cementing materials due to the rubber, which makes the concrete cement hydration reaction more sufficient and the density is improved.

It can be seen from Figure 9 that the relative dynamic elastic modulus of NC and RC increases first and then decreases with the progress of sulfate erosion. The peak value of the relative dynamic elastic modulus of NC appears at 45 times of dry-wet cycle, and then the relative dynamics elastic modulus drops rapidly. When the dry-wet cycles mounting to 90 times, the relative dynamic elastic modulus is lower than 0.75, which indicates that NC has reached the damage limit at this time; the relative dynamic elastic modulus of RC changes more slowly than NC. The peak value of the relative dynamic elastic modulus appeared at 60 times of dry-wet cycle and then began to decrease. When dry-wet cycles mounting to 90 times, the relative dynamic elastic modulus of RC was higher than 0.75, which did not reach the damage limit.

3.4. SO_4^{2-} Concentration Distribution Law. Figure 10 shows the change of SO_4^{2-} content in NC and RC after 45 times' dry-wet cycles. It can be seen that the SO_4^{2-} concentration of each group of specimens shows a downward trend, and as the depth deepens, the decreasing rate becomes faster and

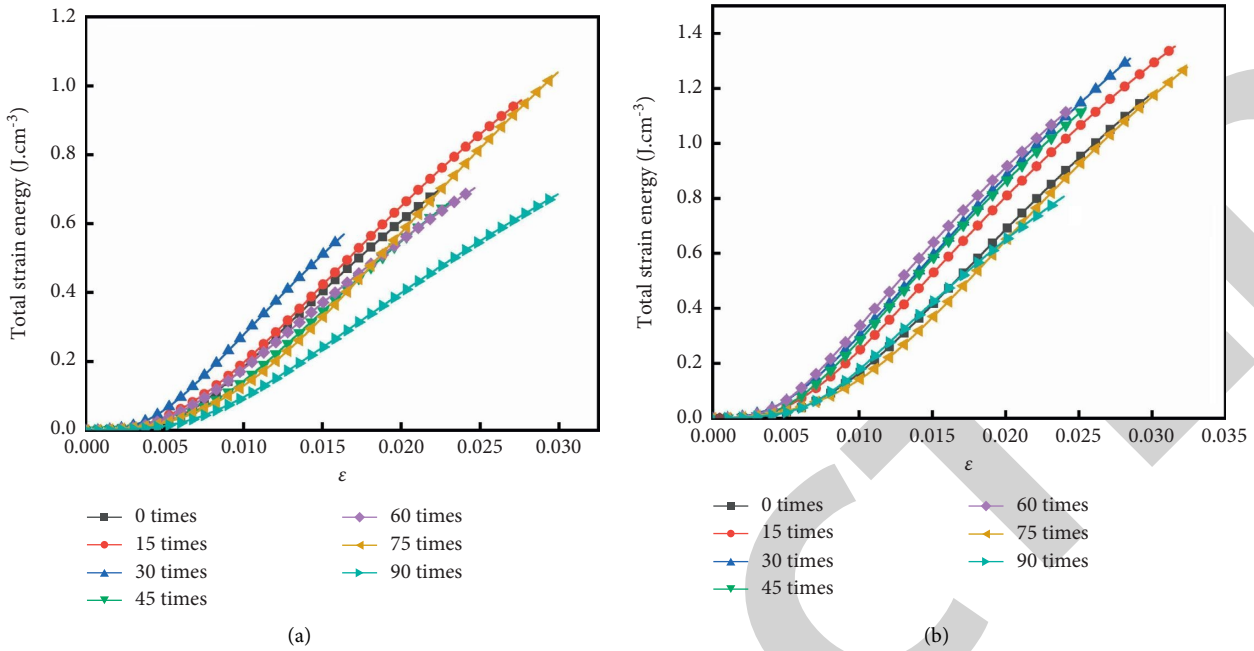

Figure 5: Total strain energy. (a) NC. (b) RC.

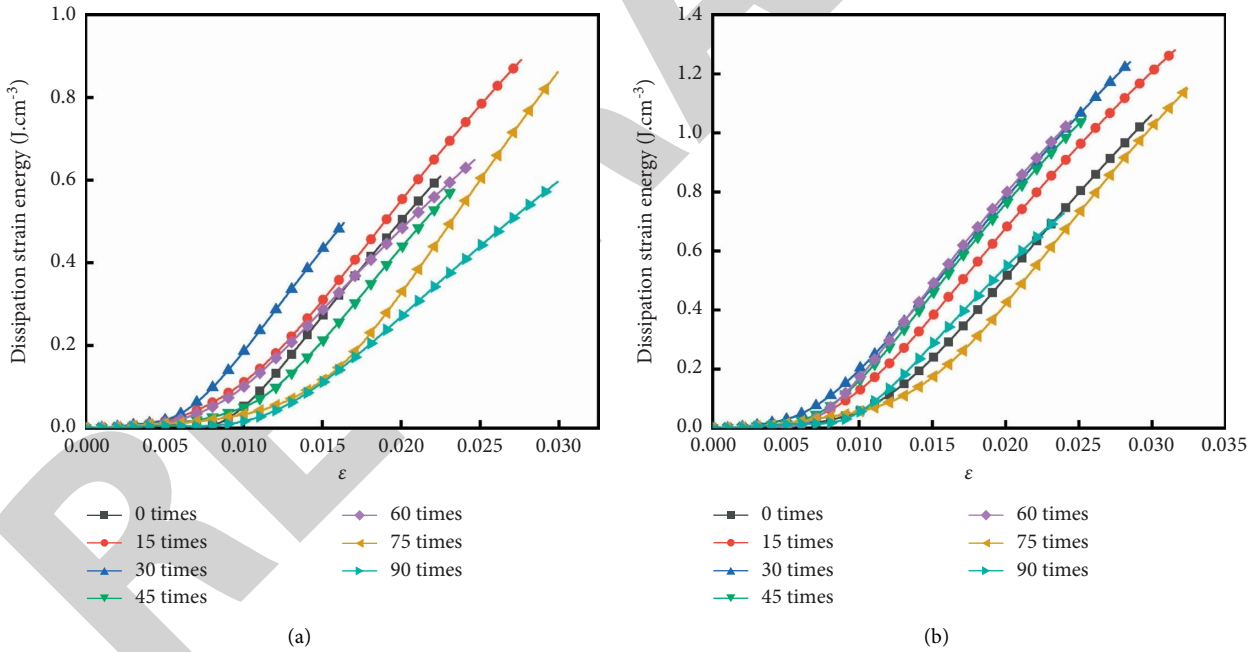

Figure 6: Dissipation strain energy. (a) NC. (b) RC.

faster. The SO_4^{2-} content gradually decreases with the increase of the penetration depth; because the surface concrete is in the influence depth range, a large amount of solution is sucked inside, so that SO_4^{2-} has a relatively high concentration on the surface of the concrete; as the depth increases, the migration rate of SO_4^{2-} decreases, and the concentration decreases accordingly.

Figure 11 shows the change of SO_4^{2-} content in NC and RC after 90 times' dry-wet cycles. It can be seen that the SO_4^{2-} concentration of each group of test pieces still shows a downward trend. The decrease is slower in the early stage and faster in the later stage. After 90 times' dry-wet cycles, the SO_4^{2-} concentration of each group of test pieces is compared with that of dry-wet cycles. It was higher at 45 times, and the SO_4^{2-} mass fraction from the outer layer to the inner layer also gradually decreased.

According to Figures 10 and 11, it can be seen that the incorporation of rubber into concrete significantly reduces

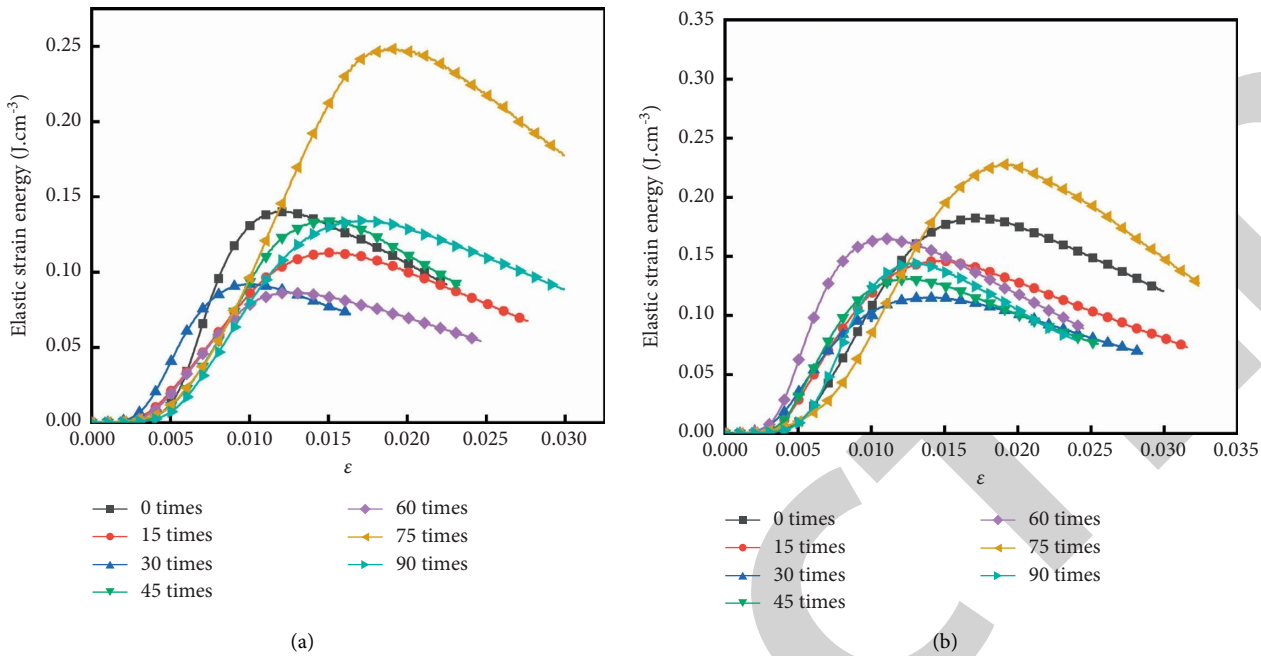

Figure 7: Elastic strain energy. (a) NC. (b) RC.

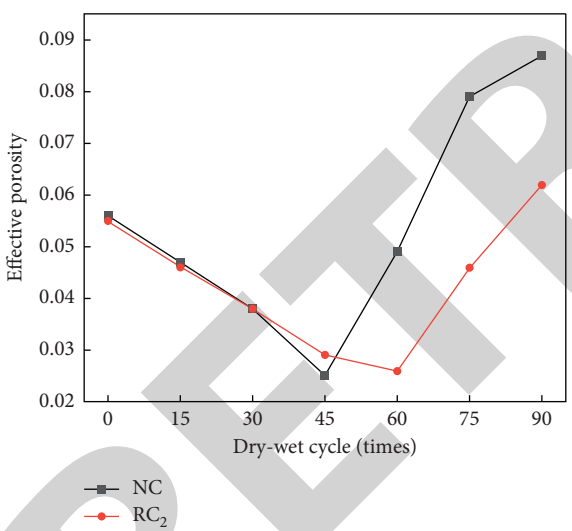

Figure 8: Effective porosity.

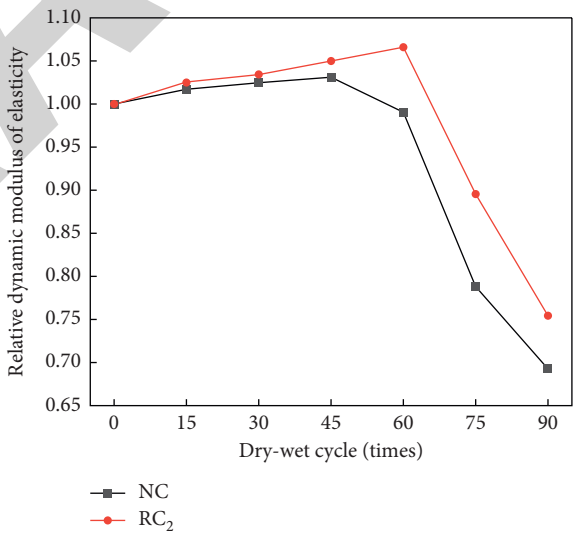

Figure 9: Relative dynamic modulus of elasticity.

the SO_4^{2-} concentration at different depths in the concrete, and the SO_4^{2-} corrosion resistance is in the order of RC group > NC group, which shows that rubber can improve the concrete's SO_4^{2-} corrosion resistance, to reduce the invasion of SO_4^{2-}.

4. SEM Microanalysis

The deterioration process of concrete in sulfate attack environment can be divided into two stages. In the first stage, due to the difference of SO_4^{2-} concentration between the inside and outside of the concrete sample in the attack solution, the SO_4^{2-} in the solution is continuously transferred to the inside of the concrete, and a series of chemical reactions occur with the $Ca(OH)_2$ and C-S-H gel inside the concrete to form ettringite and gypsum, which fills the pores inside the concrete and effectively reduces the effective porosity of the concrete. In the second stage, as the corrosion progresses, ettringite and gypsum continue to accumulate and fill the internal pores of the concrete to produce expansion force. The expansion force is greater than the tensile strength of the concrete to produce cracks. The gradual increase of cracks accelerates the SO_4^{2-} intrusion to generate more ettringite and gypsum, which eventually leads to structural expansion failure and sharp decline in mechanical properties [9, 26].

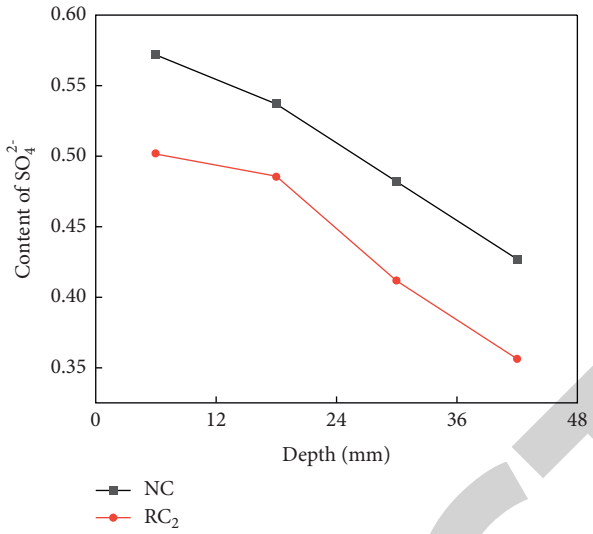

Figure 10: SO_4^{2-} content of NC and RC when dry-wet cycle being 45 times.

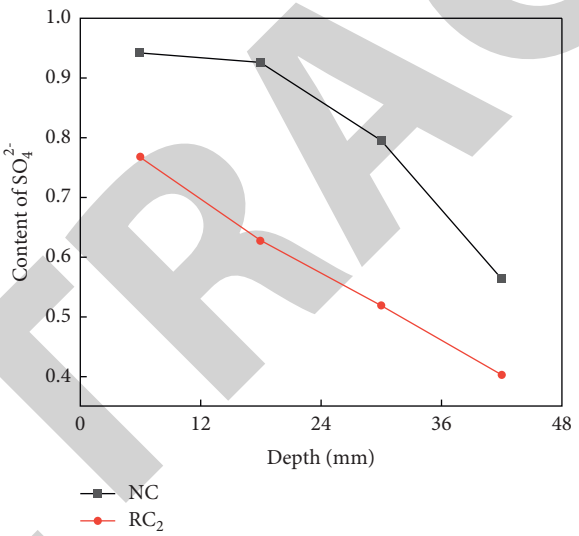

Figure 11: SO_4^{2-} content of NC and RC when dry-wet cycle being 90 times.

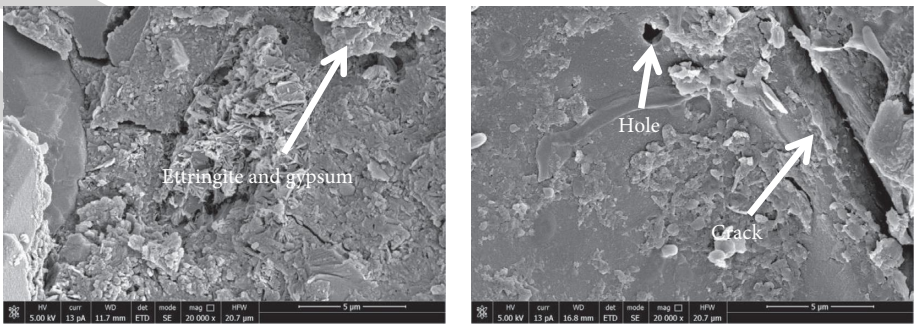

(a) (b)

Figure 12: The microstructure of ordinary concrete under sulfate erosion environment. (a) Dry-wet cycle 45 times. (b) Dry-wet cycle 90 times.

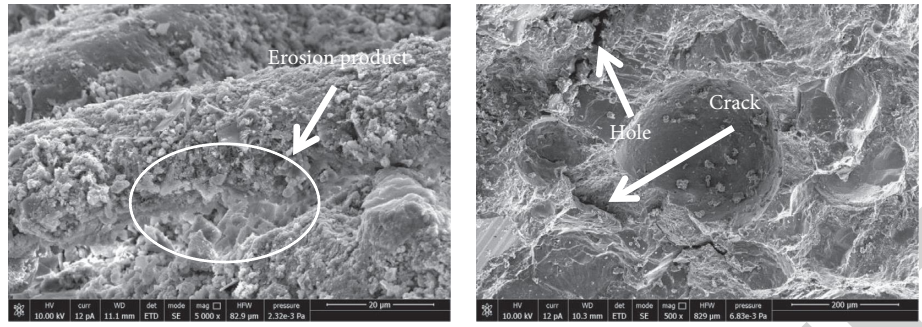

(a) (b)

Figure 13: The microstructure of rubber concrete under sulfate erosion environment. (a) Dry-wet cycle 45 times. (b) Dry-wet cycle 90 times.

The SEM microstructures of ordinary concrete and rubber concrete under sulfate attack environment are shown in Figures 12 and 13, respectively. As the corrosion progresses, there are obvious pores on the surface of ordinary concrete and rubber concrete. In contrast, the pore structure of ordinary concrete is looser. Both types of concrete have a large amount of corrosion products attached inside, indicating that SO_4^{2-} is transferred into the concrete for chemical reaction to produce gypsum. This chemical reaction rapidly consumed the hydroxide radicals inside the concrete and decomposed the C-S-H gel. Hence, the concrete pore increased and gradually developed into cracks, and reduced the concrete density and structural stability. Comparing Figures 12 and 13, it can be found that compared with rubber concrete, ordinary concrete higher content of adhesive mortar, weaker bonding at the interface, large internal holes, and wide cracks, which accelerates the transmission of SO_4^{2-} in the concrete, resulting in the interior structure of ordinary concrete is more loose. By contrast, due to the workability of rubber particles, the particle gradation of aggregate is optimized and the structure is more dense. Therefore, the sulfate resistance of rubber concrete is improved compared with ordinary concrete.

5. Conclusion

(1) Mixing a proper amount of rubber particles into concrete can effectively improve the compressive strength of concrete, and the rubber replaces the 10% mass of fine aggregate that is the optimal, which is 22.20% higher than that of ordinary concrete. In sulfate attack environment, the peak stresses of ordinary concrete and rubber concrete all show a trend of increasing first and then decreasing.

(2) Rubber can increase the dissipated strain energy of concrete and reduce the release rate of elastic strain energy of concrete, that is, increase the total strain energy of concrete, thereby improving the ductile deformation and toughness of concrete. It can delay the deterioration of concrete by sulfate, inhibit the penetration and expansion speed of cracks, and improve the sulfate resistance of concrete.

(3) The addition of rubber into concrete significantly reduces the concentration of SO_4^{2-} at different depths inside concrete, improves the sulfate attack resistance of concrete, and reduces the invasion of SO_4^{2-}. Due to the workability of rubber particles, the particle gradation of aggregate is optimized and the structure is relatively dense.

(4) The microscopic analysis of concrete samples after sulfate attack is carried out. At the initial stage of corrosion, the surface and internal pores of the concrete provide conditions and channels for sulfate attack. As the corrosion progresses, ettringite and gypsum are generated to fill the internal pores. After further corrosion, a large amount of ettringite produces structural damage and a large number of cracks and holes are generated.

Data Availability

The data used to support the findings of this study are included within the article.

Conflicts of Interest

The author declares that there are no conflicts of interest regarding the publication of this paper.

Acknowledgments

This study was financially supported by Major Natural Science Research Projects of Universities in Anhui Province (KJ2016SD08) and Natural Science Research Projects of Universities in Anhui Province (KJ2019A0917).

References

[1] K. Chen, D. Wu, L. Xia, Q. Cai, and Z. Zhang, "Geopolymer concrete durability subjected to aggressive environments-a review of influence factors and comparison with ordinary Portland cement," *Construction and Building Materials*, vol. 279, Article ID 122496, 2021.

[2] H. A. Gamal, M. S. El-Feky, Y. R. Alharbi, A. A. Abadel, and M. Kohail, "Enhancement of the concrete durability with hybrid nano materials," *Sustainability*, vol. 13, no. 3, p. 1373, 2021.

[3] H. Cheng, T. Liu, D. Zou, and A. Zhou, "Compressive strength assessment of sulfate-attacked concrete by using